JOINT-PATTERNS, MECHANICAL PROPERTIES AND WEATHERING CARACTERISTICS OF SELECTED, ARID, CONTINENTAL DEPOSITS OF THE COLORADO PLATEAU

Linn Therese Heienberg

Thesis for Master’s Degree
in Geodynamics

Department of Earth Science
University of Bergen
Bergen, Norway
June 2015

ACKNOWLEDGEMENTS

This thesis is the result of my studies during my master degree in geodynamics at the Department of Earth Science at the University of Bergen. Looking back at these two years working on my master project and the last year writing my master thesis, some gratitude are in order.

First and most foremost, I want to thank the Department of Earth Science (UIB) for allowing me to work on this exciting project and to spend three weeks in the amazing and spectacular nature of Utah during the field work. I want to thank Ragnhild Tunheim for a good collaboration and for very good company during our stay in Utah.

Further, I want to thank my main supervisor Haakon Fossen and my co-supervisor John Howell for all the help and constructive criticism I have received this past year. Allowing me (and Ragnhild) to present the result of our project on the NGF winter conference in Stavanger January 2015 was highly appreciated.
Working on this project has definitely been a very meaningful, exciting and a truly positive experience!

I also want to thank my amazing family and friends for their love and support these past two years (and all years before that). Further, thanks to Ivan Hjelmeland for helping me and Ragnhild with ArcGIS software.

ABSTRACT

The Colorado Plateau contains a stratigraphic sequence spanning from Precambrian to Tertiary in age, including a thick succession of Permian and Mesozoic strata that are well displayed in outcrops throughout southeastern Utah, USA. The appearances of these units, which are controlled by their weathering history, are all unique and pose the question: “Why should units with similar depositional environment and burial history look so different?” The most pronounced differences involve their erosional slopes, surface morphology, color and degree of fracturing. There are a number of possible factors that can contribute to the differences in weathering patterns: (1) depositional environment (2) different degree of lamination/stratification and thickness of bed units (3) different mineralogy and grain size/sorting (4) different degree of lithification/cementation and (5) different types of cement. Following in this thesis is a study of the erosional slopes, sedimentological- and mechanical properties and fracture-patterns of these seven stratigraphic units (listed in stratigraphic order from bottom to top with their average slope values in the brackets): the Cutler Formation (30-35°), the Chinle Formation (28-33°), the Wingate Sandstone (77-82°), the Kayenta Formation (65-70°), the Navajo Sandstone (43-48°), the Slick Rock Member (50-55°) and the Moab Member (78-83°). These formations also show different fracture-frequency distributions, which again relate to their mechanical properties and different degree of cementation. The joints in the study area post-date the deformation bands and faults and were most likely formed during the Tertiary uplift and exhumation of the Colorado Plateau. Both naturally occurring fractures in addition to fractures formed by hydraulic fracturing are essential for economic production of hydrocarbons in sandstone reservoirs. In this paper both sedimentological and mechanical properties have been investigated and analyzed in an attempt to explain the different appearances of these sandstone units.

Contents

1 Introduction

1.1 Aim of study

The formations included in this study are all formed in similar continental depositional environments but they show very dissimilar weathering characteristics. The most pronounced differences involve their erosional slopes, surface morphology, color and degree of fracturing (Figure 1.1). Figure 1.2 and Figure 1.3 illustrate differences between some of the formations from the area near Shafer Trail in Canyonlands National Park.

The main aim of this study has been to investigate which parameters that facilitate the cliff-forming formations in contrast to the more gently sloping formations. To what degree do primary features (mineralogy) in contrast to secondary features (cementation) influence the weathering patterns for sandstone formations? Do differences in sedimentological- and mechanical properties give a solid explanation for the dissimilar weathering characteristics of the formations? Further, one of the key questions attempted to address in this thesis is: what is the relation between joint-patterns and observed erosional signatures for the formations?

Joints (a type of extensional fractures) are the most dominating fracture type developed in the sandstone formations in the study area and are present to various degrees in the formations in this study. Such fracture-patterns are mapped and recorded for several of the formations. Both naturally occurring fractures and fractures formed by hydraulic fracturing are essential for economic production of hydrocarbons in sandstone reservoirs. In this study facies associations, sedimentological- and mineralogical properties, mechanical properties and fracture-patterns have been investigated in an attempt to explain the different appearances of these sandstone units.

The sedimentological- and mineralogical properties have been investigated by Ragnhild J. Tunheim (2015) whereas the study described in this thesis has a main focus on the structural geologic features and mechanical properties.

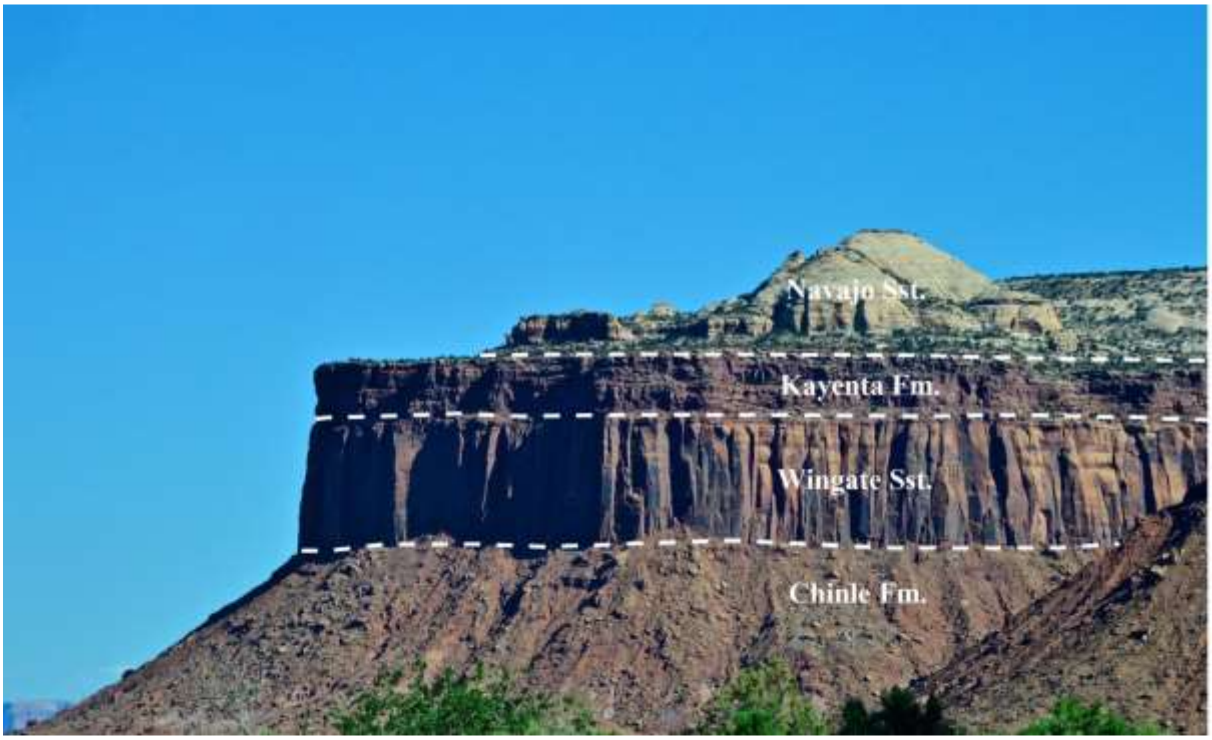

Figure 1.1: Image illustrating differences in erosional slopes and weathering characteristics for the Chinle Fm., Wingate Sst., Kayenta Fm. and the Navajo Sst. The undulating surface morphology of the light-colored Navajo Sst. stands out from the other formations in this stratigraphic sequence. Another striking difference is the highly fractured, cliff-forming Wingate Sst. in contrast to the underlying gently-sloping Chinle Fm. with almost no fractures developed. Photo by Haakon Fossen.

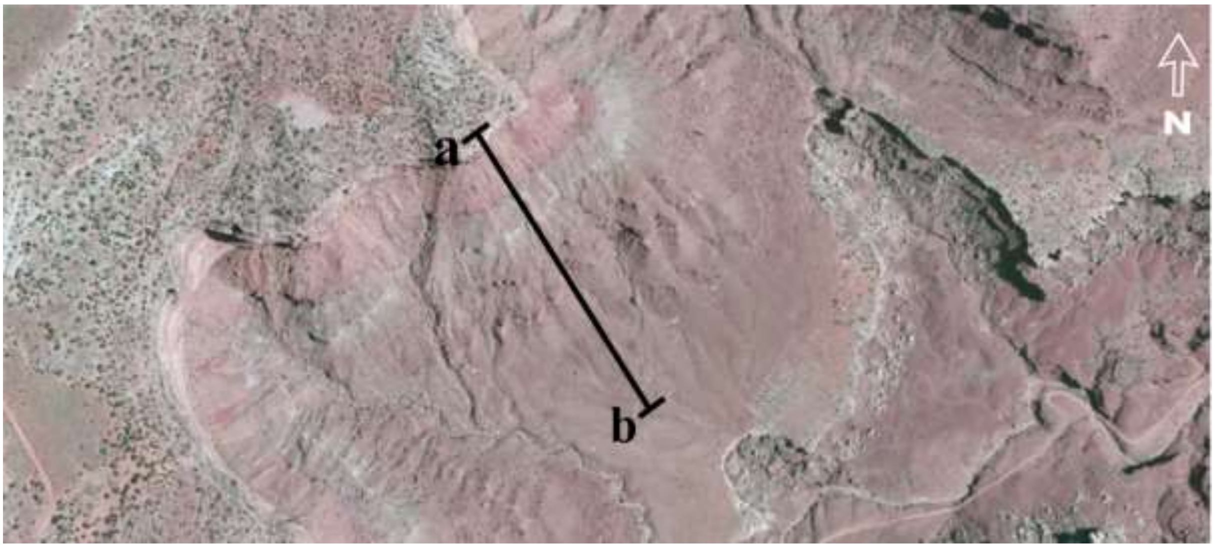

Figure 1.2: Aerial photo illustrating the location of the profile in Figure 1.2. The profile is located near Shafer Trail, Canyonlands National Park. UTM: 12S 604913 4258468.

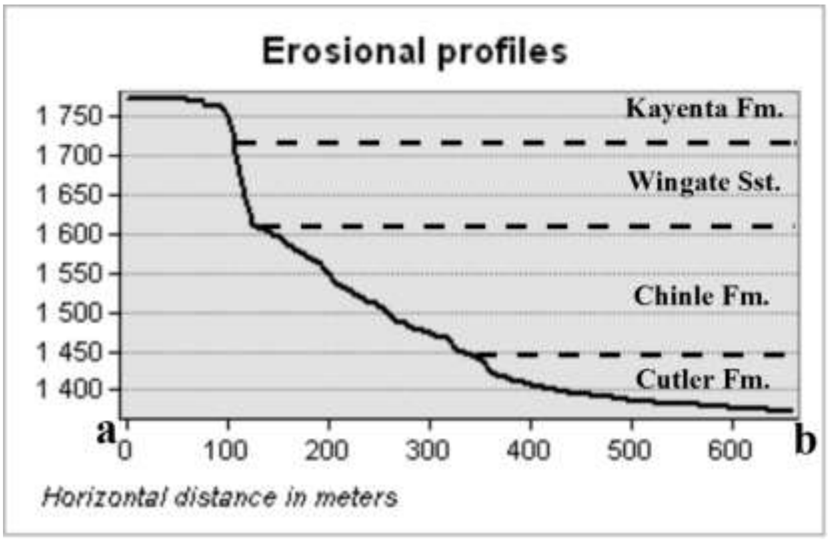

Figure 1.3: Cross section of the Cutler Fm., the Chinle Fm., Wingate Sst. and Kayenta Fm. at the location displayed in Figure 1.2. Cross section based on a DEM created in ArcGIS software.

1.2 Previous studies

The joints in the Entrada Sandstone have been explored in several studies. Dyer (1983), (1988) studied faulted joints in the Moab Member of the Entrada Sandstone at three locations: 1) on the southwestern limb of Salt Valley Anticline, 2) in the Garden area, and 3) in the area near Arches National Park campground on the east flank of the Salt Valley. He noted that the faulted joints in the Slick Rock Member have a very different orientation than those in the overlying Moab Member. Cruikshank, Zhao and Johnson (Cruikshank et al., 1991a, 1991b, Zhao and Johnson, 1991, Zhao and Johnson, 1992) studied joints, faulted joints and deformation bands (Aydin, 1978) within the Moab Member over an area of about 1 km^2. They established a sequence of deformation for the Garden area based on joint interaction features. This study enhances the importance of distinguishing between deformation bands (forming in shear with a few mm-cm shear displacement) and faulted joints (form as extension fractures but later slips a few mm-cm) in order to understand the deformation associated with fractures.

Cruikshank and Aydin (1995) explored three sets of joints developed in the Entrada Sandstone over an area of about 6 km^2 on the southwestern limb of Salt Valley Anticline, Arches National Park. They found a single joint set developed in the Moab Member in three distinct areas, and thus noted that a single joint set does not have to fill the entire area across which the stresses that formed the joints were acting. The first joint set is separated by a second set of joints at an angle of 35° to the first. The underlying Slick Rock Member contains a third joint set which is oriented with an angle of 5-35° to joints in Moab Member. The joints in the Slick Rock Member nucleated from the lower edges of joints of all orientations in the Moab Member and thus they note that the fracture-pattern has evolved both horizontally, within the same unit, and vertically between units. Further, they determined the sequence of jointing by establishing the relative age relation between each joint set, and interpreted each joint set orientation to represent a direction of maximum compression at the time of their formation. They found that the joints record a 95° counterclockwise rotation of the direction of maximum compression since the formation of an earlier set of deformation bands.

Alikarami et al. (2013) explored the distribution of deformation features (such as fractures and deformation bands) in the Navajo- and the Entrada sandstones in the fault core and damage zones of two faults in two localities (in southeast (Cache Valley) and central (San Rafael Swell) Utah). These two localities have a different degree of calcite cementation and the mechanical and petrophysical properties were thus investigated at each location in order to account for the impact of cementation on these properties and their possible relations. In-situ measurements by Tiny-Perm II and Schmidt Hammer were performed in order to examine the distribution of permeability and strength/ elasticity of rock within the damage zone of these faults. Statistical relations between Tiny-Perm II measurements and Schmidt Hammer values have been studied and the statistical results demonstrate that there are correlations between the studied parameters, but the dependencies vary with the degree of calcite cementation in mineralogically similar sandstones (quartz sandstone). Their statistical results demonstrate that the relation is best described by an exponential law for the non-cemented Navajo Sandstone whereas for the cemented Navajo Sandstone the relation is better approximated by a power law.

Based on work carried out in the area near Arches National Park, Antonellini and Aydin explored the effect of faulting on fluid flow in porous sandstones, both regarding geometry and spatial distribution (Antonellini and Aydin, 1995) and petrophysical properties (Antonellini and Aydin, 1994). They found that the number of deformation bands is proportional to the amount of slip on a single major fault and that deformation bands also have a very high density (>100 m^{-1}) in stepovers between slip planes. In such areas they found the largest anomalies in permeability (Antonellini and Aydin, 1995). Deformation bands were found to have a porosity about one order of magnitude less than the surrounding host rock and, on average, a permeability three orders of magnitude less than the surrounding host rock (Antonellini and Aydin, 1994). They conclude that deformation bands and slip planes can substantially modify fluid flow properties of a reservoir and have potential sealing capabilities.

Further, the microstructure of deformation bands were explored by Antonellini et al. (1994). At Arches National Park they distinguish 3 kinds of deformation bands on the basis of their distinctive microstructure: (1) deformation bands with little or no cataclasis; (2) deformation bands with cataclasis; and (3) deformation bands with clay smearing. They documented two generations of the deformation bands and relate the older generation (has little or no cataclasis and formed in relatively undisturbed sandstone probably under conditions of low confining pressure) to the growth of the salt structure and the younger generation to the collapse of the salt structure (exhibits cataclasis, appears to be localized in proximity to major faults and seems to have developed under high confining pressure).

1.3 Study area

The study area is located near the town of Moab in southeastern Utah, USA and covers an area of about 80x40 km^2. The formations included in this study have been investigated at different locations selected by how well the formations are exposed in the outcrops. In total 8 main localities have been explored, namely: Courthouse, Bartlett Wash, Hidden Canyon, Big Bend, Dead Horse Road, Indian Creek, Potash and Hunter Canyon (Figure 1.4). In addition, slope measurements have been recorded in Arches National Park and Canyonlands National Park. The rocks that dominantly outcrop in the study area are spanning from Precambrian to Tertiary in age, including a thick succession of Permian and Mesozoic strata that form characteristic erosion profiles (cliffs, slopes and ledges).

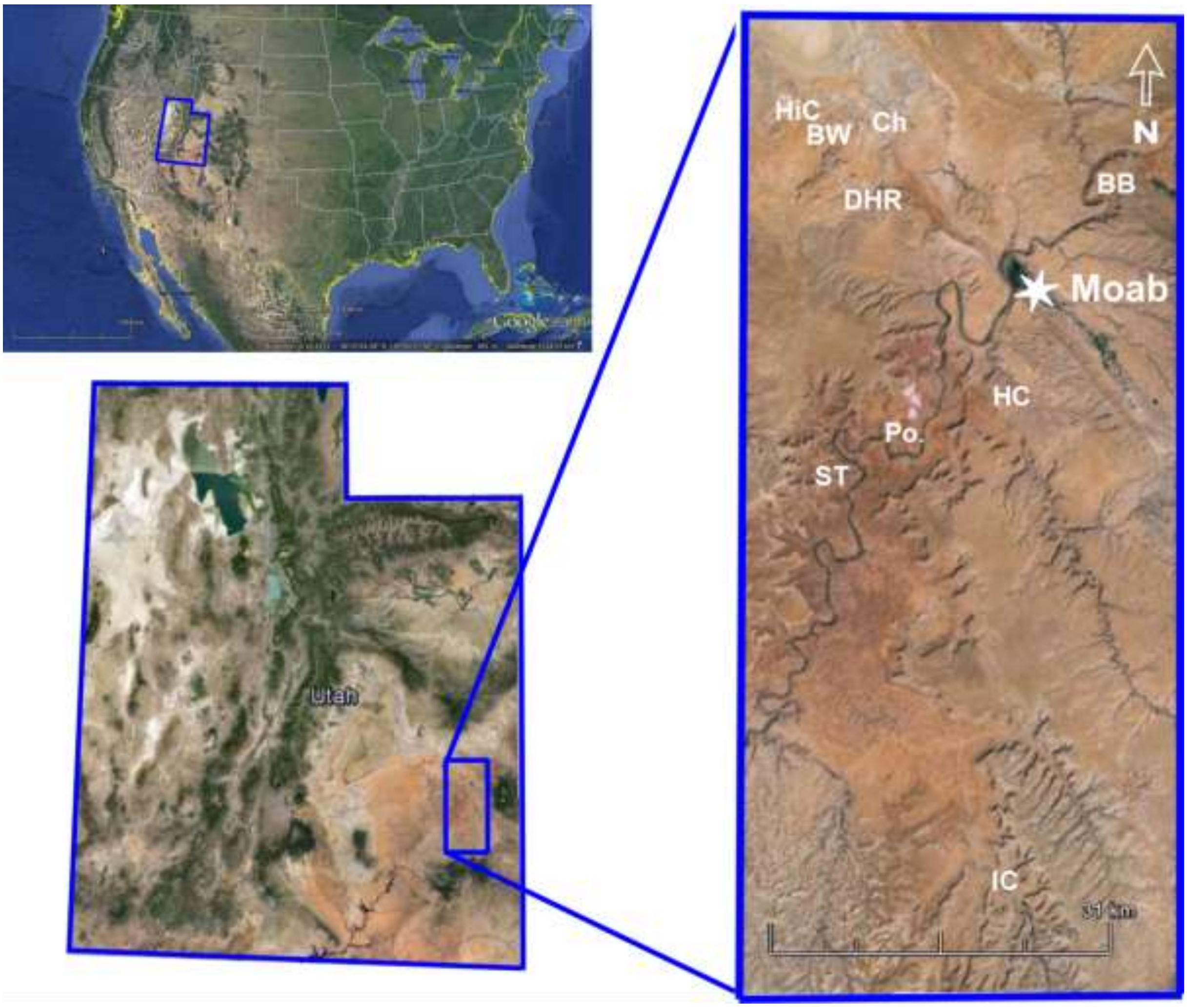

Figure 1.4: Map of the study area, based on aerial photos from Google Earth. The locality names and their geographic locations are indicated. HiC = Hidden Canyon, BW = Bartlett Wash, Ch = Courthouse, DHR = Dead Horse Road, BB = Big Bend, HC = Hunter Canyon, Po. = Potash and ST = Shafer Trail.

The Permian Paradox Basin underlies roughly half of the study area (Figure 1.5). It is a down-faulted basin that was formed by reactivation of deep-seated, northwest-trending Precambrian faults (Baars, 1993). The town of Moab is located in the eastern and deepest part of this basin. The water circulation in this sea was restricted which allowed for 1.2 – 2.4 km thick accumulations of salt to be deposited. The basin was asymmetrical so the salt accumulations are thickest in the NE part of the basin (below Arches National Park). Sediments of Late Carboniferous and Permian age overlie the salt in the basin. These sediments are erosional material that was shed from the adjacent Uncompahgre Uplift NE of the basin. Movements of the salt have had a great influence on the geological structures that developed in the Moab area.

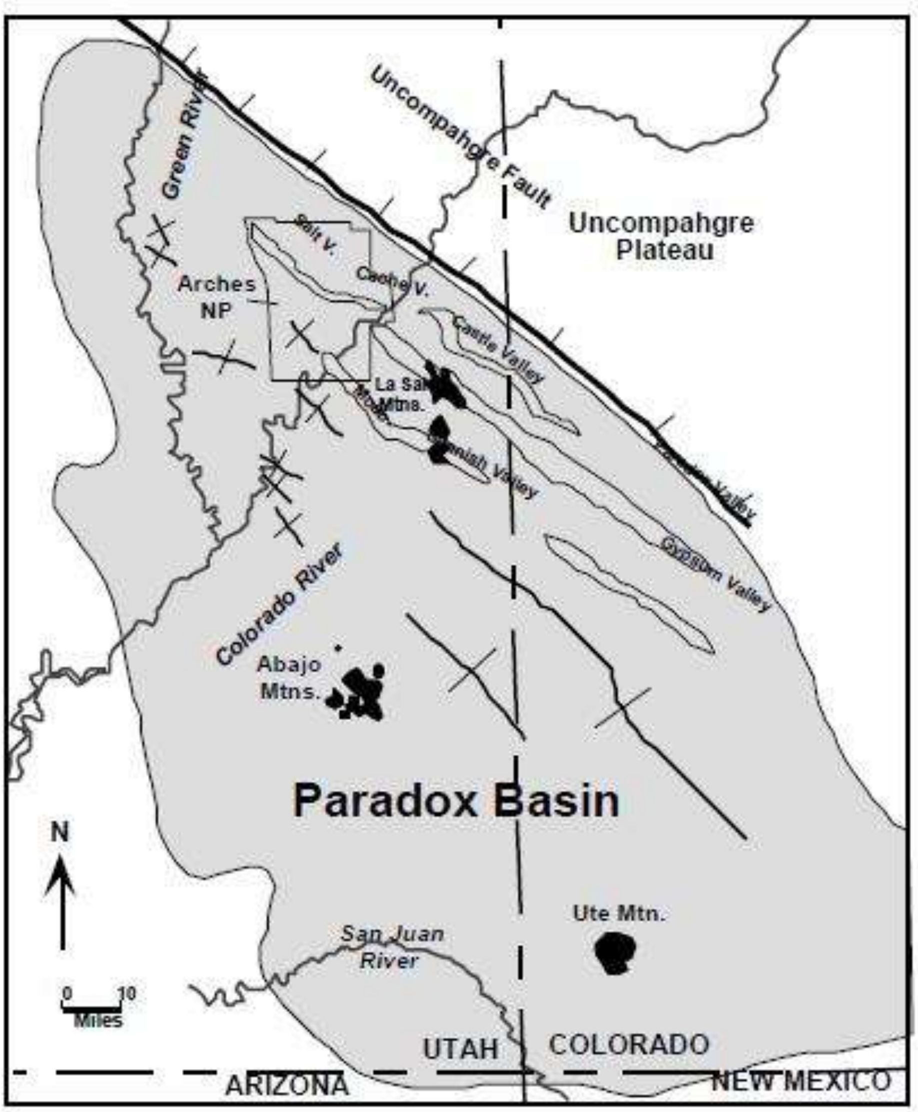

Figure 1.5: Map of the Paradox basin showing salt anticlines, and salt valleys formed by collapse of salt anticlines (stippled pattern). Also shown is the location of major laccoliths and volcanic centers: La Sal, Abajo and Ute Mountains. (Doelling, 1985).

The salt deposits deform plastically and have a low density relative to the sandstones. This caused the salt to rise upwards creating salt diapirs and deforming the overlying Mesozoic rock cover to form salt domes and salt anticlines. The salt likely started to move quite soon after deposition and continued through most of the Mesozoic Era, as indicated by the presence of angular unconformities and change in the thickness of sedimentary units (Baars, 1987). Examples of salt deformation structures in the study area are Moab Valley and Salt Valley which are both collapsed salt anticlines.

The rocks between the salt anticlines were downfolded into broad synclines and the basement faults were reactivated as a result of the compressional forces related to the Laramide orogeny (Baars, 1987). During the Tertiary, groundwater percolated through these fractures and along faults and dissolved underlying salt deposits. The overlying rocks would eventually collapse into the resulting voids to form salt valleys such as Moab- and Salt Valley. As a result of salt movements and corresponding deformation structures the deposition and erosion of sediments has been irregular along the salt anticlines. Along the Moab Valley salt anticline all of the Permian Cutler and Lower Triassic Moenkopi Formation and the lower part of the Upper Triassic Chinle Formation are missing in outcrop. The Colorado River, which crosses the study area from NE to SW, established its course prior to the collapse of the salt anticlines and sustained its route after the valley formed. The major drainage in the area hence flows across rather than down or parallel to the valleys (Baars, 1987).

Joints are spectacularly developed and displayed in many places throughout the study area. Joints in the Entrada Sandstone appear to be related to the salt-cored Moab- and Salt- Valley structures as they have an approximately parallel orientation and do not reflect a regional pattern (Kelley and Clinton, 1960), (Doelling et al., 1988). However, the Moab- and Salt Valley anticlines were well developed prior to the deposition of the Entrada Sandstone and it is important to realize that joints in this formation can only represent parts of the history of the anticlines (Cruikshank and Aydin, 1995). The timing of the propagation of the joints observed in the formations in this study is further discussed in the discussion chapter.

Cruikshank and Aydin (1995) identifies three stages of jointing in the Klondike Bluffs area in Arches National Park north of Moab. A period of deformation recorded in deformation bands and movement on the Klondike Bluffs fault postdates the jointing events. The joints in the Moab Member most likely formed prior to joints in the underlying Slick Rock Member. These joints nucleated from the lower edge of those formed in Moab Member in a response to a slightly different stress field.

Elongate rock fins is a common sight at locations subjected to much weathering along the joint-traces. In the “Devil’s Garden” area in Aches National Park, spectacular rock fins within the Entrada Sandstone can be observed. Other places however display very little sign of erosion along the joints. In many places the joint-patterns are quite simple with one dominating joint set developed, but there are also sites with multiple joint sets (Cruikshank and Aydin, 1995).

1.4 Methodology

1.4.1 Introduction

The aim of this study has been to give qualitative descriptions of how selected sandstone formations weather and to investigate possible explanations for their differences. The main focus of this study is related to the structural geologic parameters whereas the main focus of Tunheim (2015) has been on the sedimentological- and mineralogical properties. The methods that have been used to achieve the results presented in this thesis have been related to quantifying erosion profiles and making field observations and measurements of the mineralogy and structural geology.
These methods include:

1. Mapping the frequency of fractures along scanlines in the field.
2. Field measurements of permeability by using a Tiny-Perm II.
3. Field measurements of Young's Modulus by using a Schmidt Hammer.
4. Field descriptions and collection of hand specimens.
5. Field descriptions of erosion profiles.
6. Making fracture-maps and fracture-frequency analyses based on aerial photos.
7. Using ArcGIS software to create a DEM (Digital Elevation Model).
8. Studying thin sections from the collected hand specimens.
9. Performing statistical analyses and comparisons of the permeability- and Young's Modulus measurements.

The field work was located in the area near the town of Moab in southeastern Utah and was carried out in the period between 13th of May and June 3rd 2014.

1.4.2 Fracture scanlines

In order to obtain information about differences in degree of fracturing and layer-thickness/fracture-spacing ratio of the formations the fractures were mapped in selected outcrops in the field area. The methods used for mapping the fractures along scanlines included:

1. Finding a proper location to perform a fracture-frequency analysis.
2. Recording the GPS coordinates of the location.
3. Laying a measuring tape on the ground along the outcrop, making the scanline as horizontal as possible, (Figure 1.7).
4. Recording the spacing between- and orientation of the fractures that fully penetrated the layer in the outcrop. The strike and dip data of the fractures were obtained by using a compass.
5. Photographing the location and the fractures along the scanlines, using the other master student working in the area, Ragnhild J. Tunheim, as a scale for the pictures.
6. Subdividing the fracture orientations into joint sets and calculating the average thickness of the layers by examining the photos from the field and using Ragnhild's height as a scale.
7. Making tables (Appendix D, Table 8-12 – Table 8-37) and statistical analyses (Figure 4.34 - Figure 4.38) of the fracture-frequency distributions of the separate formations as well as comparisons with the other formations (Figure 4.43).

The numbers- and locations of the scanlines were limited by the accessibility of the formations. Along some of the formations it was not possible to find a proper reach of the scanlines due to topographic obstacles (trees, large rocks, steep slopes etc.).

Mapping of the fractures along scanlines can be performed in different ways. Considering that most formations have some fractures that penetrate the entire formation in addition to many fractures that reach a number of intermediate levels through the layers, it is important to be consistent in which types of fractures that get recorded. Only the fractures that fully penetrated the whole height of the formation in the outcrops were recorded during this field work (Figure 1.6). The proximity of the scanline relative to large structures such as fault zones may also influence the fracturing of the formations and produce local differences. This field work was generally carried out at great distances to such structures. A total of 26 fracture-frequency analyses were made during this study. Appendix E (Figure 8.27 – Figure 8.31) displays the locality for each of the 26 fracture-frequency distribution analyses.

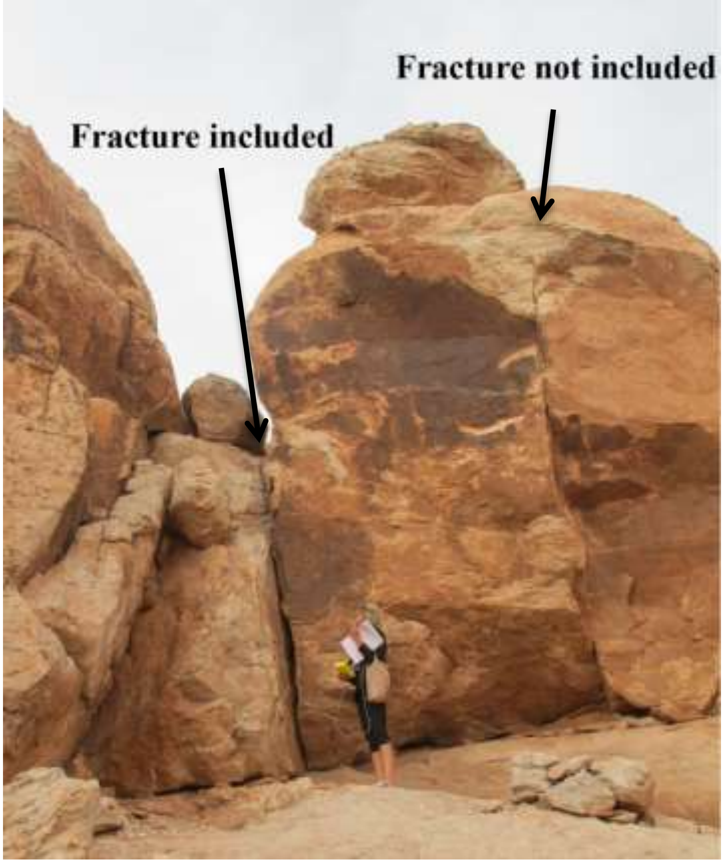

Figure 1.6: Example of fractures that are included and not included in fracture-frequency analyses.

Figure 1.7: Example of a scanline (measuring tape), Hammer for scale.

1.4.3 Field measurements of permeability

The permeability has been measured at a different number of localities for each formation as a result of limited accessibility of proper outcrops for some of the formations, and because some formations had a higher priority than others (18 for the Cutler Formation, 20 for the Chinle Formation, 39 for the Wingate Sandstone, 40 for the Kayenta Formation, 41 for the Navajo Sandstone, 54 for the Slick Rock Member and 35 for the Moab Member). The methods used for performing a Tiny-Perm II permeability measurement includes:

1. Finding a proper location for a measurement (finding a surface in the outcrop that not seemed too affected by weathering processes and that was not fractured).
2. Recording the GPS coordinates of the location.
3. Using a geology hammer to remove the outer-most weathered surface and the hammer and a chisel to make the surface as smooth and polished as possible. The Tiny-Perm II was thereafter used to remove the remaining small rock fragments and dust from the surface by blowing air on the surface.
4. Taking at least 3 consistent measurements with the Tiny-Perm II, excluding measurements that were affected by air leaking into the equipment during the sampling or similar influencing factors.
5. Naming and photographing the location.
6. Averaging the TP values from each location, calculating the permeability and making tables (Appendix B, Table 8-2 – Table 8-8) and statistical analyses (Figure 4.16) of the results for all the formation as well as comparisons of permeability measurements versus Young's Modulus measurements (Figure 4.18 – Figure 4.21) and erosional slopes (Figure 4.22). The equation used to calculate the permeability K (mD) based on the TP (Tiny-Perm II) measurements is the one recommended by the manufacturer (New England Research):

Equation 1.1: $TP = -0.8206 * \log(K) + 12.8737$

The correlation between Tiny-Perm values and standard plug evaluations (gas permeability) was evaluated by Fossen et al. (2011). These different methods provide values of permeability that are likely to differ to some extent. Tiny-Perm values are estimated based on an empirical calibration function that is provided by the manufacturer (NER) and may not be optimal for the sandstone formations explored in this study. Fossen et al. (2011) drilled plugs at the localities within the Navajo Sandstone where Tiny-Perm values were first obtained, and the result gave a positive correlation where Tiny-Perm is ~1.8 times the standard plug permeability values. They added data from Jurassic dune deposits from other localities in southern Utah which confirmed the correlation factor of 1.8 (Figure 1.8).

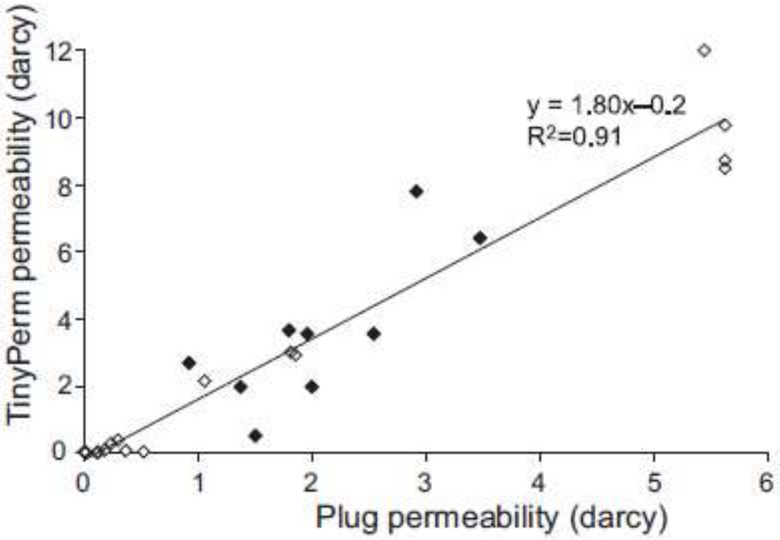

Figure 1.8: Graphical representation of the relationship between Tiny-Perm- and plug permeability (Fossen et al., 2011).

1.4.4 Field measurements of Young's Modulus

The Young's Modulus (σ/ε, a measure of the stiffness of a formation) has been measured at a different number of localities for each formation as a result of limited accessibility of proper outcrops for some of the formations and some formations had a higher priority than others (18 for the Cutler Formation, 20 for the Chinle Formation, 39 for the Wingate Sandstone, 40 for the Kayenta Formation, 41 for the Navajo Sandstone, 54 for the Slick Rock Member and 35 for the Moab Member). The methods used for performing a Young's Modulus measurement by using a Schmidt Hammer included:

1. Doing measurements on the same locations with the Schmidt Hammer on the smooth and polished surface that was left after performing the Tiny-Perm II measurements.
2. Performing at least 10 single impact readings with the Schmidt Hammer in addition to the discarded measurements that differed from the average by more than 10 units.
3. Averaging the HR (hammer rebound) values from each location, calculating the Young's Modulus and making tables (Appendix B, Table 8-2 – Table 8-8) and statistical analyses (Figure 4.17) of the results for all the formation as well as comparisons of Young's Modulus measurements versus permeability measurements (Figure 4.18 – Figure 4.21) and erosional slopes (Figure 4.23). The equation used to calculate the Young's Modulus *E* (GPa) based on the HR (Schmidt Hammer rebound) values is as follows:

Equation 1.2: $\ln(E) = -8.967 + 3.091 * \ln(HR)$ (+/- 0,101) (Katz et al., 2000)

Figure 1.9 illustrates the equipment used for performing Tiny-perm II and Schmidt Hammer measurements. Figure 1.10 is an example of a locality after Tiny-Perm II and Schmidt Hammer measurements have been recorded and the location is marked.

Figure 1.9: The equipment used for performing measurements with Tiny-perm II and Schmidt Hammer: a) Tiny-perm II, b) GPS recorder, c) compass, d) notepad, e) geology hammer, f) Schmidt Hammer, g) chisel and h) camera.

Figure 1.10: Locality I4 after performing Tiny-Perm II and Schmidt Hammer measurements.

1.4.5 Field descriptions and collection of hand specimens

Hand specimens were described and collected at some of the locations. The specimens were obtained by using a geology hammer to loosen a piece of the rock of a proper size for making a thin section. The rock sample was named, the location was photographed and the GPS coordinates of the location were recorded. Rock samples were obtained from rock volumes that displayed minimum evidence of weathering in order to secure that the samples could be as representable as possible of the whole formation. A total of 62 rock samples were collected during this field work.

1.4.6 Field descriptions of erosion profiles

A total of 70 erosion profiles were obtained from this study. The method used for carrying out the slope analyses included:

1. Finding a proper location for performing the slope analysis, where as many as possible of the formations included in the study were exposed at a not to great distance from our own position.

2. Recording the GPS coordinates of our position and the direction in which the profile was recorded.
3. Drawing sketches of the erosion profiles with names and descriptions of the formations, including characterizations of the transitions between the formations (i.e. step-like, gradual etc.).
4. Recording the general slope-value by measuring with a compass.
5. Photographing the slope profile.
6. Creating a 25th to 75th percentile boxplot illustrating the range, median and 25th to 75th percentiles of the data (Figure 4.3) and calculating the average slope-value of each formation (Appendix A, Table 8-1).

1.4.7 Fracture-maps and fracture-frequency analyses

Fractures have been recorded along scanlines based on aerial photos from Google Earth. The Wingate Sandstone, the Navajo Sandstone and the Moab Member all have well-developed, systematic fracture-patterns that are easily recognizable in map view from aerial photos and that have been recorded in this study. A total of 10 scanlines have been mapped for each of the mentioned formations (Figure 4.40 - Figure 4.42 and Appendix F, Table 8-38 – Table 8-67). Figure 1.11 is an example of a scanline in the Moab Member and the fractures recorded are marked with a white dot. The average orientation of the fractures, the number of fractures as well as the distance between the fractures have been recorded along these scanlines. In addition, fracture-maps based on aerial photos have been made of two different areas in order to illustrate the large-scale fracture orientations in the study area (Figure 4.28 and Figure 4.29).

Figure 1.11: Example of a scanline and the fractures recorded (marked by white dots) in the Moab Member, based on aerial photos from Google Earth.

1.4.8 DEM and slope profiles

A DEM (digital elevation model) of the study area has been made using ArcGIS software. Elevation data has been collected from http://gis.utah.gov/data/elevation-terrain-data/ and data from “5 Meter Auto-Correlated Elevation Models” has been imported to ArcMap 10.2.2. In ArcMap 10.2.2 the DEM has been created and different tools (including “slope” tool and “hillshade” tool) have been applied in order to highlight the differences in erosional slopes of the formations of the study area. The DEM model has been used to make a slope map, illustrating differences in erosional slopes between the formations (Figure 4.2). Further, slope profiles of the Cutler Formation, the Chinle Formation, the Wingate Sandstone and the Navajo Sandstone have been made from the area near Shafer Trail (Figure 1.3) and three slope profiles of the Slick Rock Member at Courthouse, Hidden Canyon and Bartlett Wash have been made using ArcMap 10.2.2 software (Figure 4.25).

1.4.9 Thin section description

Thin sections have been made of the rock samples collected during the field work. Using a microscope, the mineralogy, grain properties and petroleum properties of each thin section have been described and tables summarizing the descriptions have been made, (Table 4-1 – Table 4-3). The degree of cementation and pressure solution in the thin sections has been described qualitatively. The two properties are categorized into: very low-, low-, intermediate-, high-, and very high degree. There were often large differences within samples collected from the same formation regarding the degree of cementation and pressure solution visible in thin sections and the description of these two parameters are thus highly generalized. A total of 7 thin sections have been made of samples from the Cutler Formation, 8 from the Chinle Formation, 10 from the Wingate Sandstone, 5 for the Kayenta Formation, 11 for the Navajo Sandstone, 11 for the Slick Rock Member and 10 for the Moab Member. Images of thin sections from each formation have been captured by using a type of microscope with a camera attached (Figure 4.12 - Figure 4.15).

1.4.10 Statistical analyses

Statistical analyses of the erosional slope values, permeability- and Young’s Modulus measurements and fracture-frequency distributions have been performed using Excel software. Boxplots have been made, illustrating the spread of the data, the median value and the 25th to 75th percentile of the data (Figure 1.12). This type of boxplot (25th – 75th percentile) is used throughout this thesis. Further, a specific color (Figure 1.12) has been assigned to each formation and is used consistently in boxplots, fracture orientation analyses (stereonets and rose-diagrams) as well as for indicating fracture-frequency distribution localities (Appendix E, Figure 8.27 – Figure 8.31).

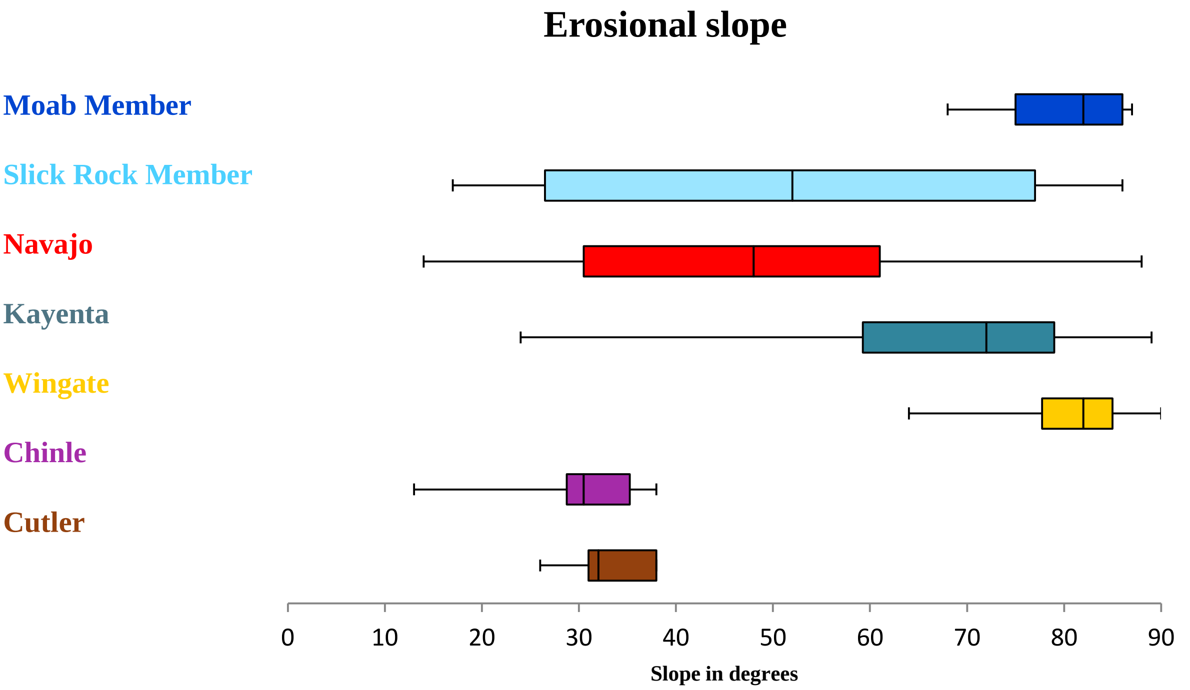

Figure 1.12: Example of a boxplot that illustrates the range, median and the 25th- and 75th percentiles of measured slope values of the formations in the field area. The horizontal black line illustrates the range of the values, the black vertical line in the middle of the box illustrates the median value whereas the box represents 25 to 75 percentiles of the data. A different color is assigned to each formation which is used consistently in this thesis.

2 Regional geology and stratigraphy

2.1 Regional geology

The state of Utah, USA, is made up of 4 major physiographic provinces; the Colorado Plateau, the Basin and Range, the Colorado Plateau/Basin-Range Transition and the Middle Rocky Mountains (Stokes, 1986) (Figure 2.1).

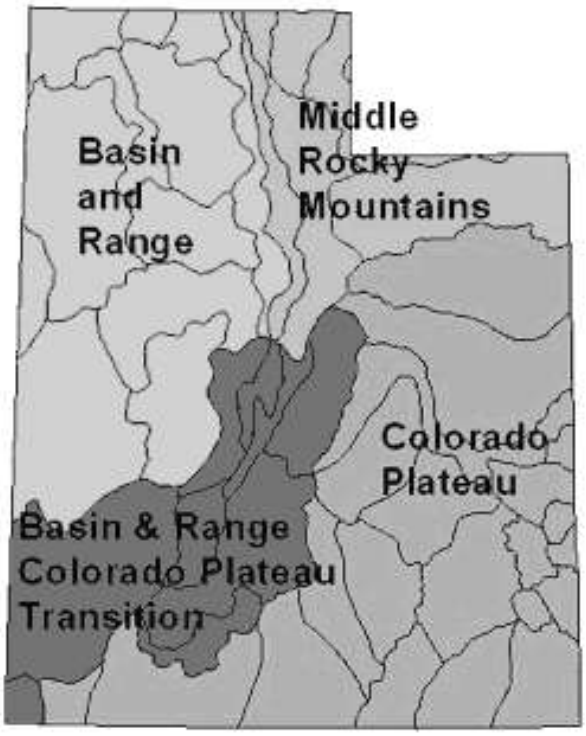

Figure 2.1: The four physiographic provinces of Utah (geology.utah.gov).

The *Colorado Plateau* has tectonically been a relatively stable part of the crust for the last 50 million years (Hintze, 2005), with little faulting and folding within the plateau. It is made up by predominantly continental sandstone and shale units, and geomorphic features of the plateau include mesas, domes, fins, chimney rocks, reefs, goblins and arches (Hintze, 2005).

A typical feature of the *Basin and Range Province* is alternating graben (basin) and horst (range) structures resulting in approximately 35 north-south trending narrow ranges separated by broad alluvial-fan-dominated valleys (Stokes, 1986). The Basin and Range Province was created as a result of crustal-thinning and extension that began about 17 million years ago (Stokes, 1986).

The *Colorado Plateau/Basin-Range Transition* is a broad zone of overlapping and merging features typical for the two provinces, including block faulting that extends tens of kilometers into the adjacent provinces (Stokes, 1986).

The Uinta Mountains and the Wasatch Range compose the alpine *Middle Rocky Mountains*. The Uinta Mountains trend east-west and it is Utah’s highest and largest range. It is composed of metasedimentary rocks of Neoproterozoic age, which were uplifted during the Laramide orogeny (Hintze and Kowallis, 2009). The Wasatch Range on the other hand, trends north-south and consists of rocks with a mixture of sedimentary, metamorphic and igneous origin (Hintze, 2005). The Wasatch Range is the result of displacement along the Wasatch fault, which comprise a 386 kilometer long fault zone in the Earth’s crust. The Middle Rocky Mountains include landforms such as deep canyons and cirque lakes sculpted by glaciers during the latest Ice Age (Hintze, 2005).

The state of Utah is divided into distinct eastern and western provinces by the Wasatch Line, which stretches from the northeast to the southwest, defining a big curving arc (Stokes, 1986). This arc represents an area of mountains and plateaus and marks the eastern limit of the collapsed Basin and Range province. It originated as a rift that defined the western margin of North America in late Precambrian time (Stokes, 1986). In Paleozoic time, the rift widened to become the Cordilleran geosyncline. The eastward-directed compressional forces that accompanied the tectonic activity along North America's western margin during the Mesozoic and Early Cenozoic eras resulted in big thrust faults. This geosyncline acted as a buttress along which the big stacks of sedimentary strata was shoved and overthrust (Stokes, 1986).

In north-central Utah, the Wasatch Line crosses the east-trending Uinta axis. Several large normal faults have been mapped along the Wasatch Line. From north to south, the largest faults are the Wasatch Fault, the Sevier Fault and the Hurricane Fault. These faults developed during the Basin and Range extension of the crust, about 17 million years ago. There are a great number of normal faults in Utah, along with many mappeable lineaments (Stokes, 1986). A number of large earthquakes are mapped along the Wasatch Line and the boundary between the Colorado Plateau and the Basin and Range Province is the most active area (Figure 2.2).

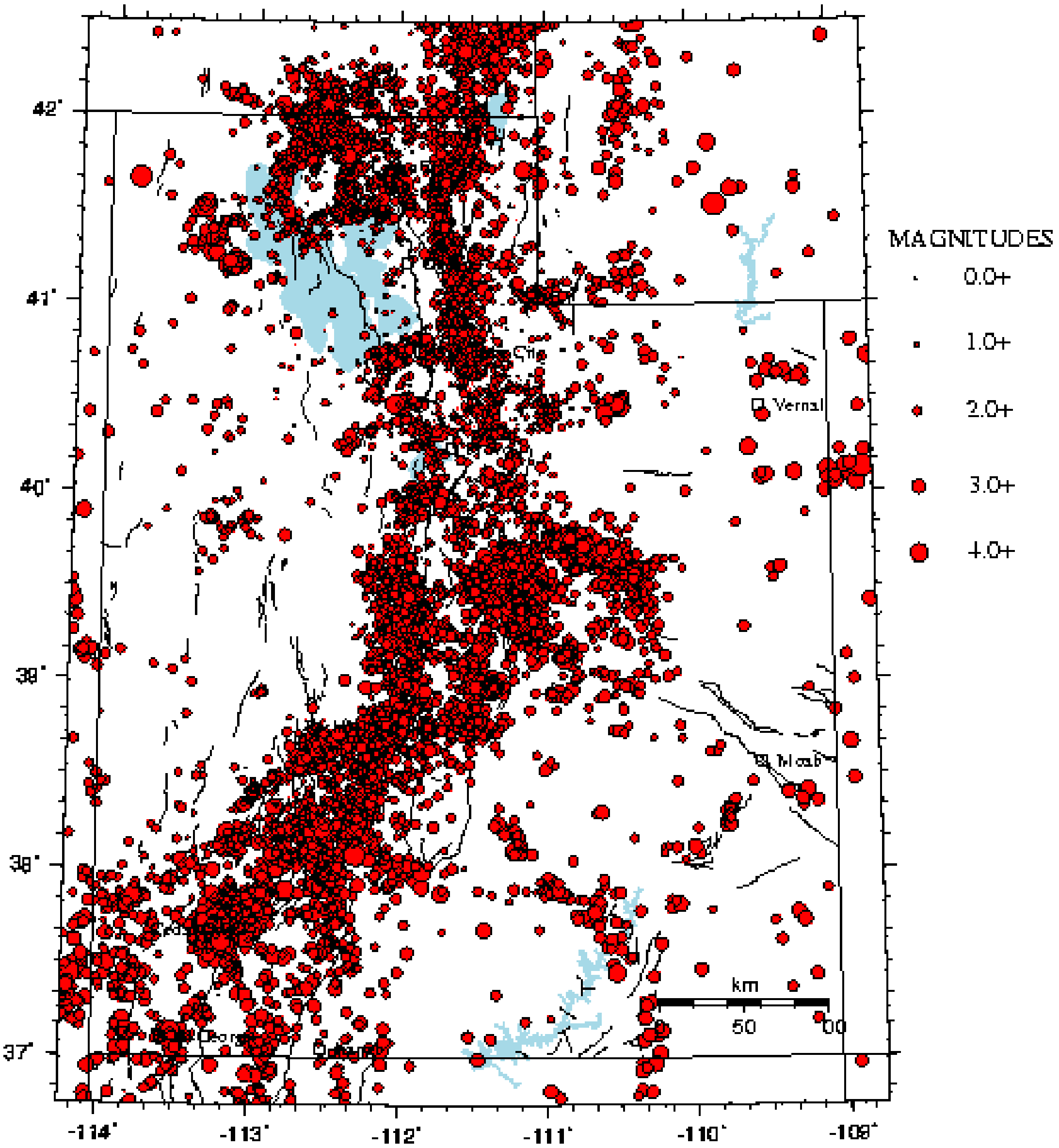

Figure 2.2: Earthquakes in Utah between July 1, 1962 – December 31, 1998. Earthquake epicenters are located by the University of Utah Seismograph Stations (http://www.seis.utah.edu).

Laccoliths and salt anticlines have caused special geological features to form in the Moab area (Hintze and Kowallis, 2009) (Figure 2.3).The laccoliths are Tertiary in age, and have pushed the overlying rocks into anticlinal and mushroom-shaped structures. The La Sal-, Henry- and Abajo Mountains represent large topographic features that can be seen in Utah today. They each consist of a swarm of laccolithic domes and were formed between 29 and 23 million years ago (Hintze, 2005). The evaporites of the salt anticlines were deposited in the Late Carboniferous Paradox Basin. Salt flowage has caused salt walls to form, resulting in deformation of the Mesozoic age rock cover (Hintze and Kowallis, 2009).

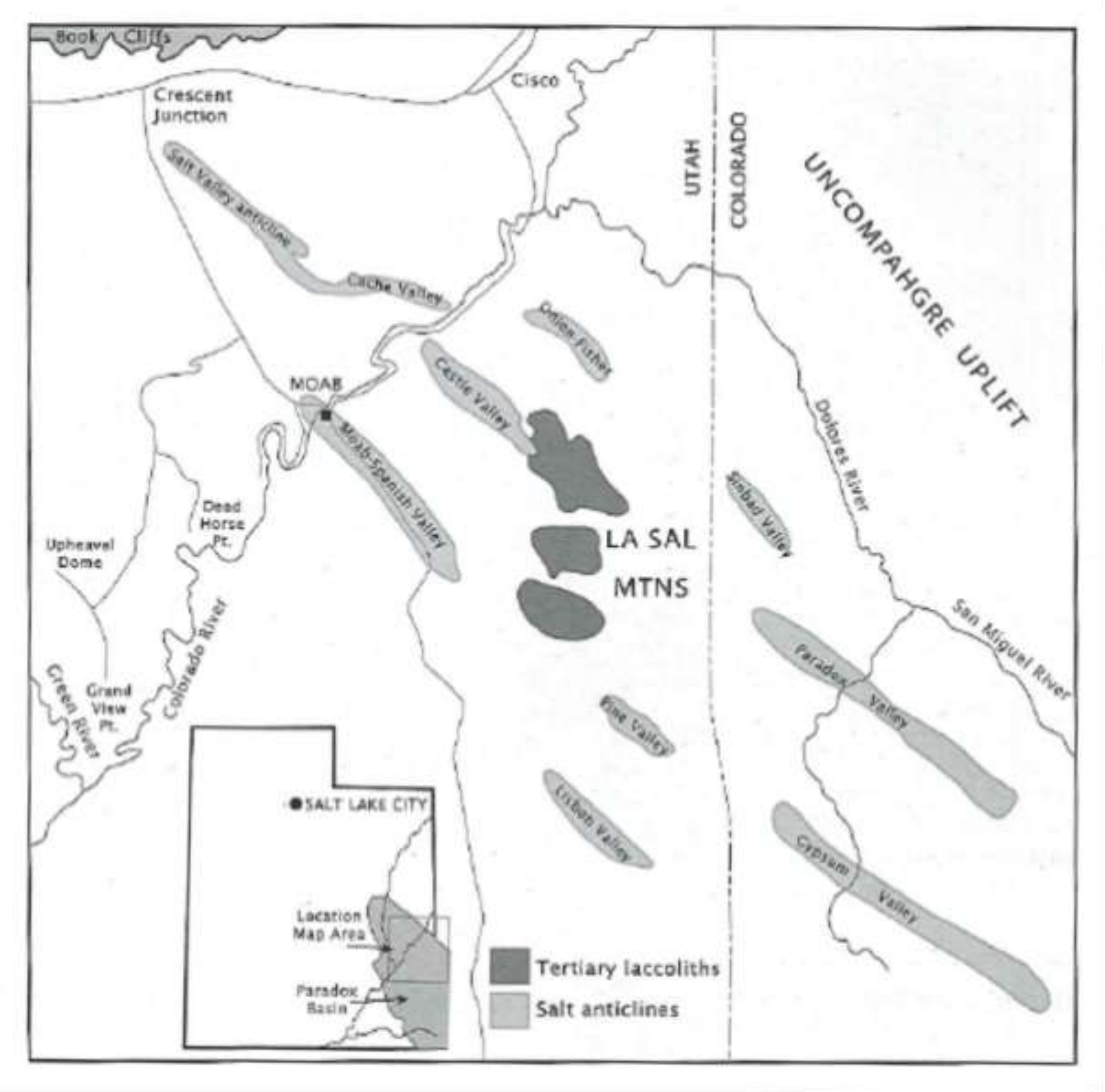

Figure 2.3: The location of two types of intrusive structures that produce unusual geologic features in the Moab area: 1) Tertiary laccoliths (dark grey color) and 2) Salt anticlines (light grey color) (Hintze and Kowallis, 2009).

2.2 Geological evolution

2.2.1 The Precambrian

The underlying basement rocks of the Colorado Plateau are of Early Proterozoic age, and were formed about 1750 million years ago (Blakey and Ranney, 2008). The basement is composed of both metamorphic rocks, such as gneiss, amphibolite and schist, and igneous rocks, including granite, pegmatites and quartz dikes. An unconformity (the so-called “great unconformity”) makes up the top of the crystalline basement, which represents a hiatus of 650 million years from 1650 to 1000 million years ago (Hintze, 2005). This extensive and long-lasting erosion produced the raw material for many succeeding deposits, most of which were transported large distances out of what is today Utah.

Movements of Earth’s major plates resulted in the buildup of the supercontinent Rodinia, by the continuous addition of small continents and island arcs to the continental margin. Rodinia existed between 1100 and 750 million years ago, and involved the amalgamation of Proto-Australia, proto-Antarctica and western North America (Hintze, 2005) (Figure 2.4). A rift developed in Rodinia a little more than a million years ago, which with time would separate the proto-Australia and later-to-be North America (Hintze, 2005). Three aulocogens, elongate subsiding basins, developed along North America’s new continental margin after the breakup of Rodinia in Neoproterozoic time (Hintze, 2005). The greatest accumulations of strata of this age found in Utah today, lie along the Uinta axis, which by Late Proterozoic time made up one of these aulocogenic basins. The basin rapidly subsided and filled with sand, gravel and mud derived from the mid-continental shield areas (Hintze and Kowallis, 2009).

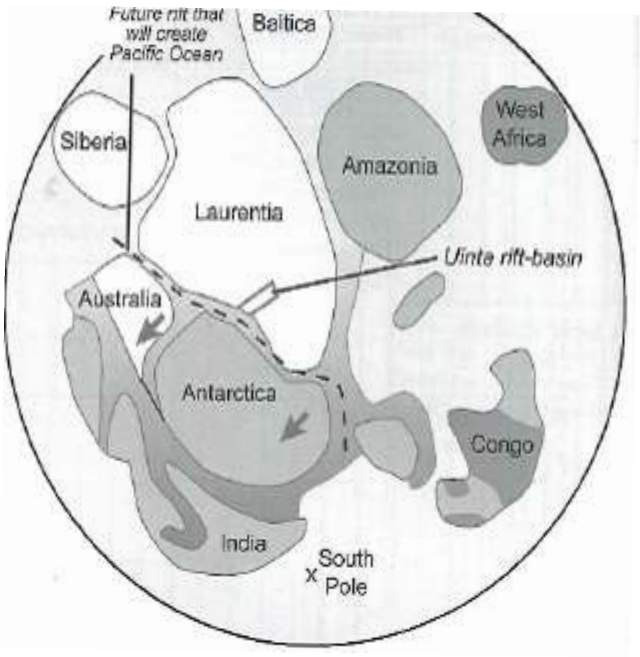

Figure 2.4: A Possible reconstruction of the supercontinent Rodinia, illustrating the arrangement of major continental areas in Neoproterozoic time and the splitting away of Antarctica and Australia from Laurentia (early North America). (Hintze and Kowallis, 2009).

Glacial deposits of Neoproterozoic age, such as tillites, found around the world today provides evidence of a period where the Earth’s surface has been covered with ice. The Earth’s greatest glaciation period extended from 850 to 630 million years ago (Hintze and Kowallis, 2009). This event is referred to as “Snowball Earth” and involved at least three prolonged glaciation periods (Hintze and Kowallis, 2009).

A great quantity of sediments was produced in late Precambrian time. The resulting rocks have not been greatly metamorphosed or deformed and are exposed in several places in Utah today (Stokes, 1986). A period of erosion is marked by an unconformity found in between latest Proterozoic- and earliest Cambrian strata in Utah (Hintze and Kowallis, 2009).

2.2.2 The Paleozoic Era

At the beginning of the Paleozoic Era, the North American continent was a low-lying shield commonly covered with shallow seas as a response to fluctuations of the sea level (Hintze and Kowallis, 2009) (Figure 2.5).

Through the Late Paleozoic time, shallow marine conditions dominated the deposition across most of the North American continent, leaving deposits such as limestones, sandstones and mudstones (Hintze, 2005). By the end of the Paleozoic time, most of Earth's continents were assembled in the supercontinent Pangaea (Hintze and Kowallis, 2009) (Figure 2.6 a)).

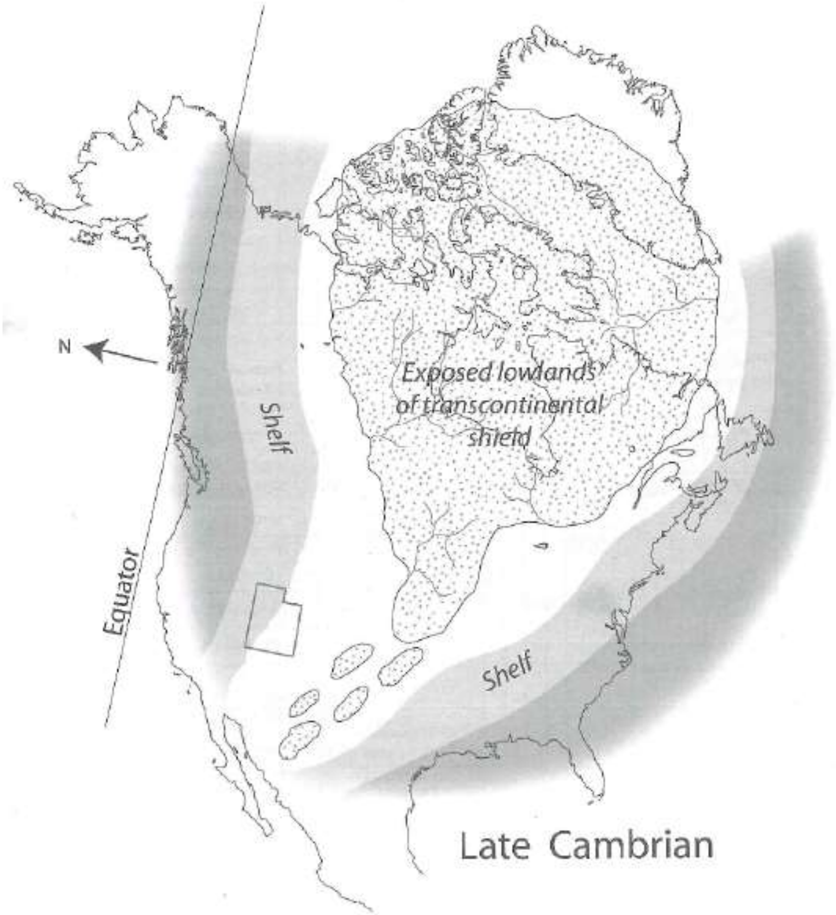

Figure 2.5: Paleogeography of North America at the end of the Cambrian Period, with an outline of Utah. Note that Utah was entirely covered by a shallow sea. As the Canadian Shield slowly subsided during the Cambrian Period the beaches moved inland and the outer margins were covered with shallow-water limestone deposits. The present-day outline of North America is shown for convenience of reference. The gray shading on this map shows the increase in water depth. (Hintze and Kowallis, 2009).

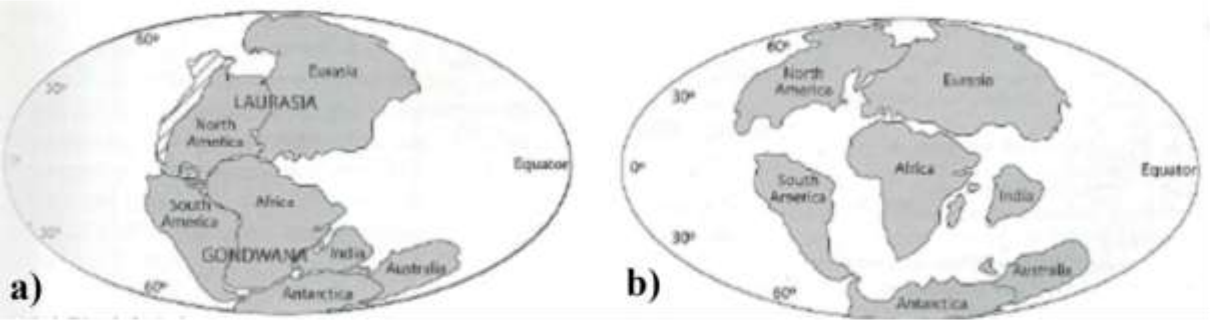

Figure 2.6: The supercontinent Pangaea a) before and b) after its breakup. The cross-hatched area of western North America on the Early Triassic map was accreted to North America during later Triassic and Jurassic time. (Hintze and Kowallis, 2009).

Different uplifts and basins that were a part of the Ancestral Rocky Mountain chain controlled the erosion and deposition in Utah throughout the Carboniferous and Permian periods. Two large depositional basins, the Paradox- and Oquirrh Basin, developed in opposite corners of Utah (Hintze, 2005). In addition, the Uncompahgre Uplift dominated the topography of eastern Utah throughout the Permian period (Stokes, 1986). During most of Permian time, shallow lakes, alluvial fans, and sand dunes dominated the landscape in Utah (Stokes, 1986).

The subduction activity along the southwestern margin of North America combined with the collision with Gondwanaland to the south, led to a complex deformation of the continental interior in Late Carboniferous time. This tectonic activity resulted in intraplate compression and an uplift of the Ancestral Rocky Mountains with accompanied development of a series of foreland basins (including the Paradox Basin) (Trudgill, 2011). The NW-SE trending Uncompahgre uplift was a ~4.6 km high and 50 km wide extension of the Ancestral Rocky Mountains. It is bounded by 200-300 km long fault zones to the northeast and southwest (Barbeau, 2003). The Paradox Basin represents an intraforeland flexural basin which formed on the southwestern flank of this uplift during the Late Carboniferous through Early Permian time (Barbeau, 2003).

Several large salt walls and salt diapirs have developed in The Paradox Basin and salt tectonics have played a major role in the structural deformation within the basin through geologic time. The salt diapirs formed when the overlying sedimentary rock cover was thinned and weakened, either as a result of extension of the crust or by differential loading. Once the salt emerged at the surface, the diapirs continued to grow by the process of passive diapirism (Trudgill, 2011). The diapirs created a relief on the basin floor surface, which the sedimentation patterns would adjust to. As a consequence, the sedimentary units confined within the Paradox Basin in Utah vary in thickness along the surface of the salt diapirs (Trudgill, 2011) (Figure 2.7).

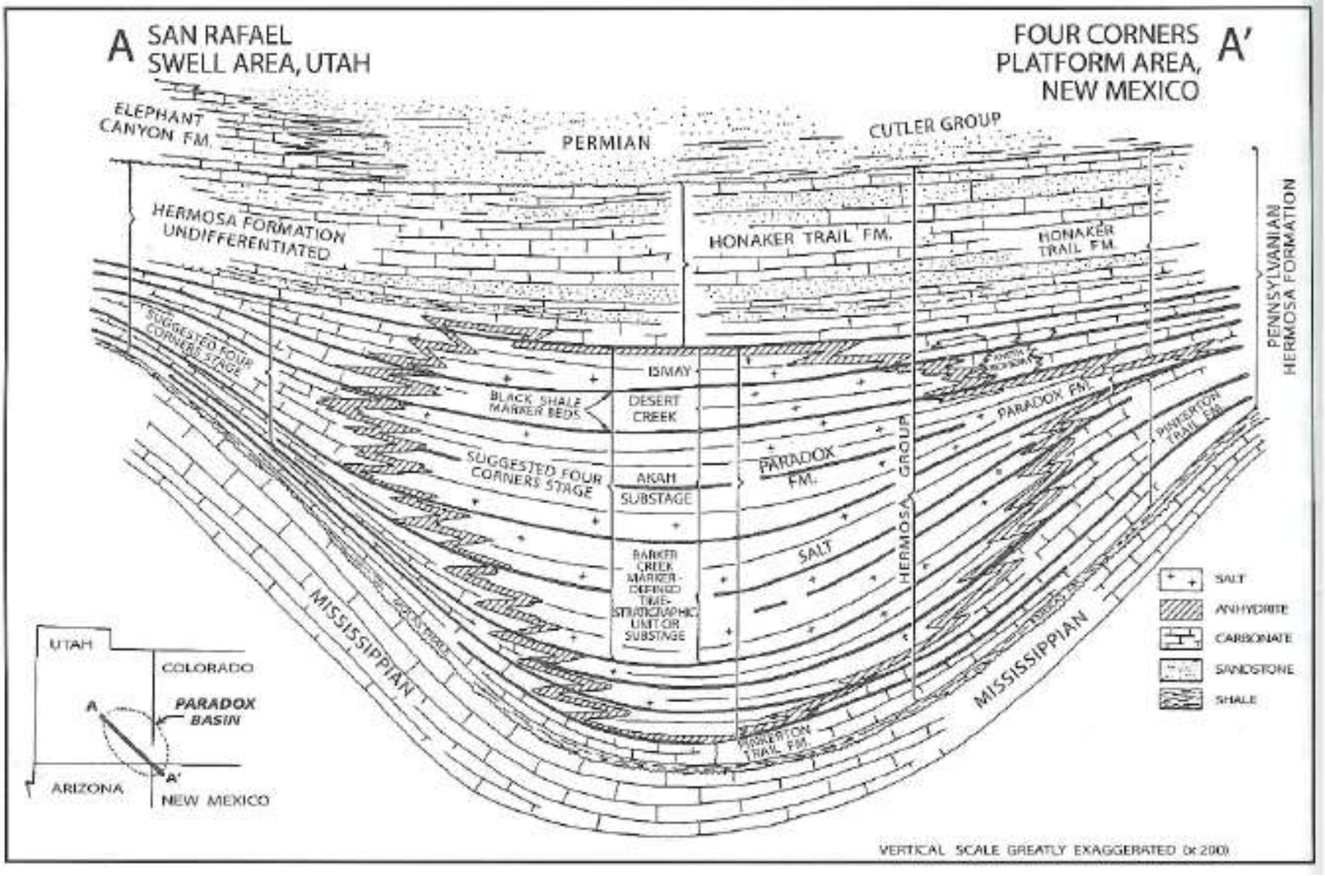

Figure 2.7: Schematic cross section illustrating facies relationships through the subsurface of the Paradox Basin. (Baars, 1983).

The red, arkosic, Cutler Formation of Permian age constitutes the uppermost part of the Paradox basin-filling (Hintze, 2005). A high content of feldspar in the Cutler Formation is consistent with a short transport distance of the sand grains. The source of these feldspar grains is Precambrian granites that were exposed in the Uncompahgre Uplift located less than 50 km east of Moab (Hintze, 2005). The Paradox Formation, which make up the lower part of the Paradox basin-fill, consists mainly of thick stacks of salt, gypsum, dolomite and shale

(Hintze, 2005). Salt flowage in the Paradox Basin has had a great influence on the structures that developed in the Moab area with time (Figure 2.8).

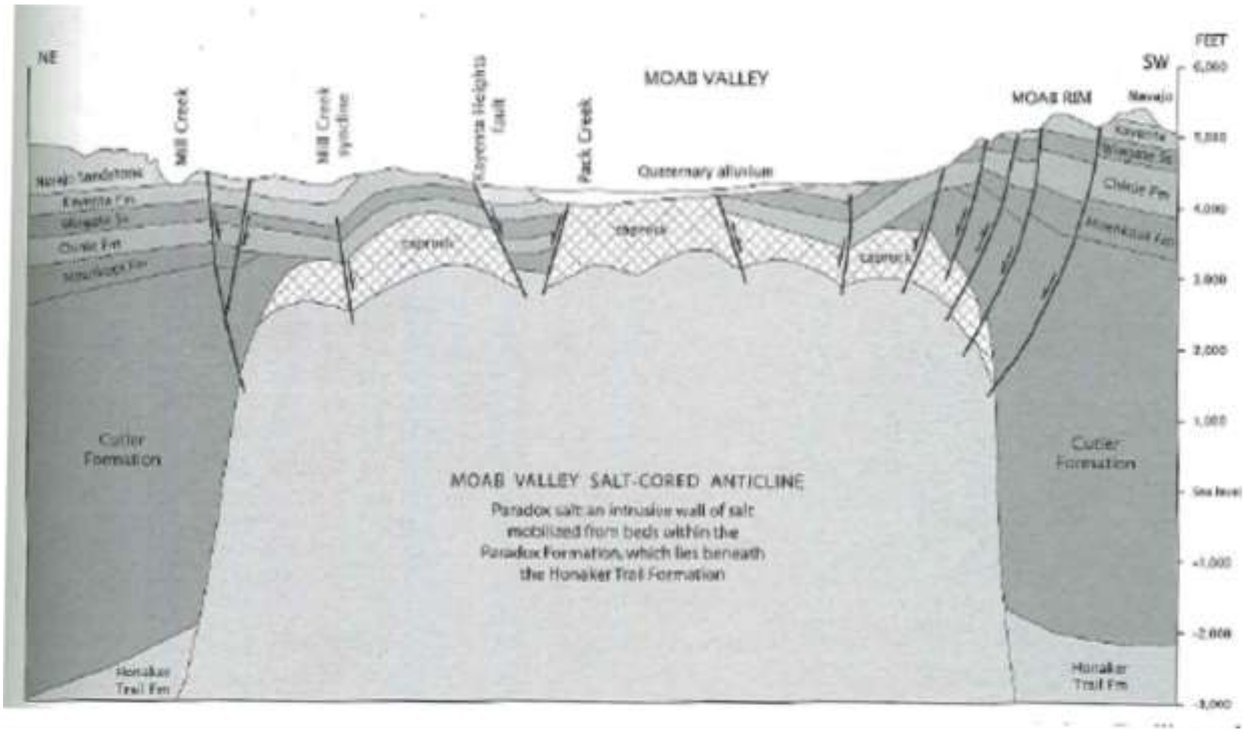

Figure 2.8: Northeast to southwest cross section across Moab Valley, illustrating the enormous salt wall that underlies Moab Valley. Horizontal and vertical scales are the same. (Doelling et al., 2002).

2.2.3 Palaeogeography in the Mesozoic Era

At the beginning of the Mesozoic era, all of Earth’s continents were assembled in the supercontinent Pangaea (Blakey and Ranney, 2008). A big landmass like Pangaea would trap the heat rising from the Earth’s interior towards the surface, leading to the central parts being uplifted and rifted. The fragmentation of Pangaea initiated great geologic changes in the western United States during the Triassic Period. The separation between Laurasia and Gondwana during the Triassic, ultimately forming the Atlantic Ocean (Figure 2.6 b)), was followed by the rifting separating North America and South America during the Late Triassic and Early Jurassic (Hintze and Kowallis, 2009). A steeply dipping subduction zone developed along the western margin of the North American continent as it started its westward drift towards the Farallon plate, which led to the accretion of island arcs and micro continents onto the margin (Stokes, 1986). The simultaneous rising of the Mesocordilleran High, which most likely is directly linked to the splitting of the Atlantic (Stokes, 1986), would be dominating the geology of Utah throughout the Jurassic period. Continued subduction along this zone would later create the Sevier fold and thrust belt during Jurassic and Cretaceous time, creating compressional forces eastward that resulted in overthrusting (Hintze, 2005). These compressional forces induced a broadly subsiding trough on the eastern part of the North American continent (Figure 2.9). The rising sea level due to the Cretaceous warm climate, would divide the continent into two land areas; one western, younger, growing mountain belt, and one older, eastern inactive landmass (Hintze, 2005).

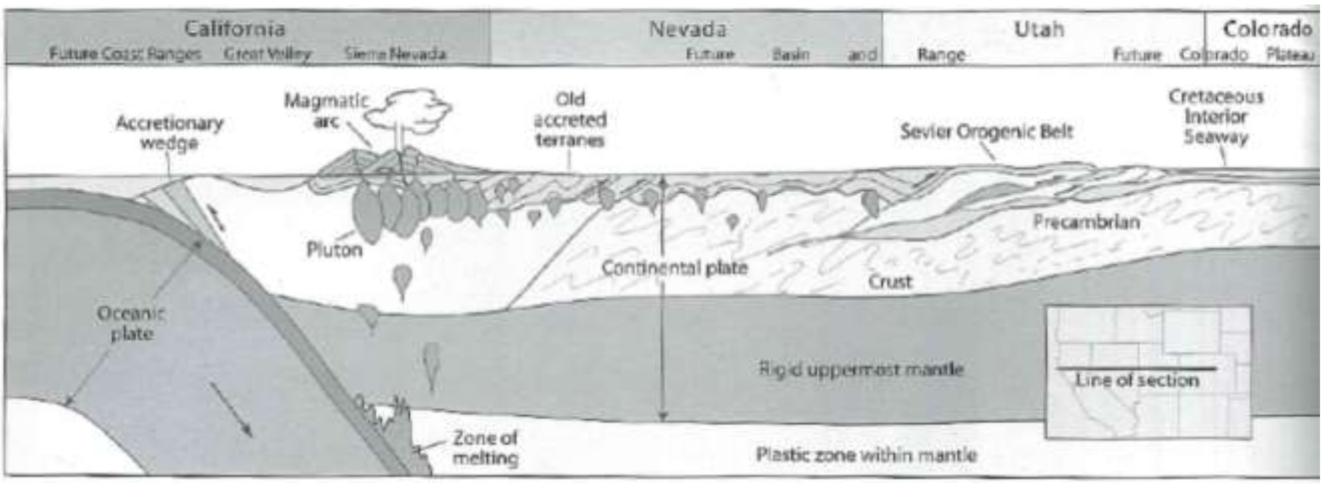

Figure 2.9: Generalized deep crustal cross-section illustrating an oceanic plate subducting beneath the west edge of North America. The Sevier orogenic belt and Cretaceous Interior Seaway were products of this compressional plate interaction on the west coast (Hamblin, 2004).

2.2.4 The Triassic Period

An unconformity representing a hiatus of about 15 million years is separating Permian from Early Triassic strata in Utah (Hintze and Kowallis, 2009). In Utah, Triassic strata are divided into an Early Triassic and a Late Triassic part (Hintze, 2005). Throughout Utah, all of the Middle Triassic deposits were removed by erosion due to uplift events related to the Sevier Orogeny (Hintze and Kowallis, 2009). An erosive surface is cut into the underlying Permian strata, and this surface represents a hiatus of about 10 million years (Hintze, 2005). The Colorado Plateau was a flat-lying plain in the Triassic time. This low gradient caused widespread deposition along the coastal plain, even with small sea level changes. A great portion of the Triassic sediments in Utah was derived from erosion of the Ancestral Rockies to the east (Stokes, 1986). The sediments accumulated inland from the tectonic activity, in a gently subsiding basin (Hintze and Kowallis, 2009). Early Triassic rocks were mostly deposited in environments such as tidal-flats, coastal-shelf and shallow-marine while Late Triassic rocks are continental in origin.

A drainage configuration that would persist well into the Jurassic developed in the Colorado Plateau region in the Early Triassic (Blakey and Ranney, 2008). Using modern coordinates, this trended from the south and east towards the north and west (Figure 2.10). The deposition of the Moenkopi Formation started in the Early Triassic and came to an end during the Middle Triassic, as weathering and erosion once again became the dominating processes on the plateau. This is marked by an erosional surface that is cut into the top of the Moenkopi Formation, representing a hiatus of about 10 million years (Hintze, 2005). The overlying Chinle Formation is divided into the Shinarump- and the Petrified Forest Member. Shinarump deposits filled the incised valleys that had been cut down into the underlying Moenkopi Formation at the beginning of the Late Triassic. The Shinarump streams were more vigorous than the Moenkopi streams and the deposits included very coarse sandstone and pebble conglomerate (Blakey and Ranney, 2008). The fluvial setting was dominating during the Triassic time, but a higher proportion of mudstone was preserved in the overlying units. The Petrified Forest Member is made up of mostly varicolored, soft mudstone with occasional lenses of coarser material such as sandstone and conglomerate. These lenses represent the location of the sinuous river channels (Blakey and Ranney, 2008). Erupting, explosive volcanoes that existed to the far south and west of the plateau contributed with volcanic ash to the overall fluvial Chinle deposits, and left blankets of volcanic ash interbedded with the sand and mud (Blakey and Ranney, 2008).

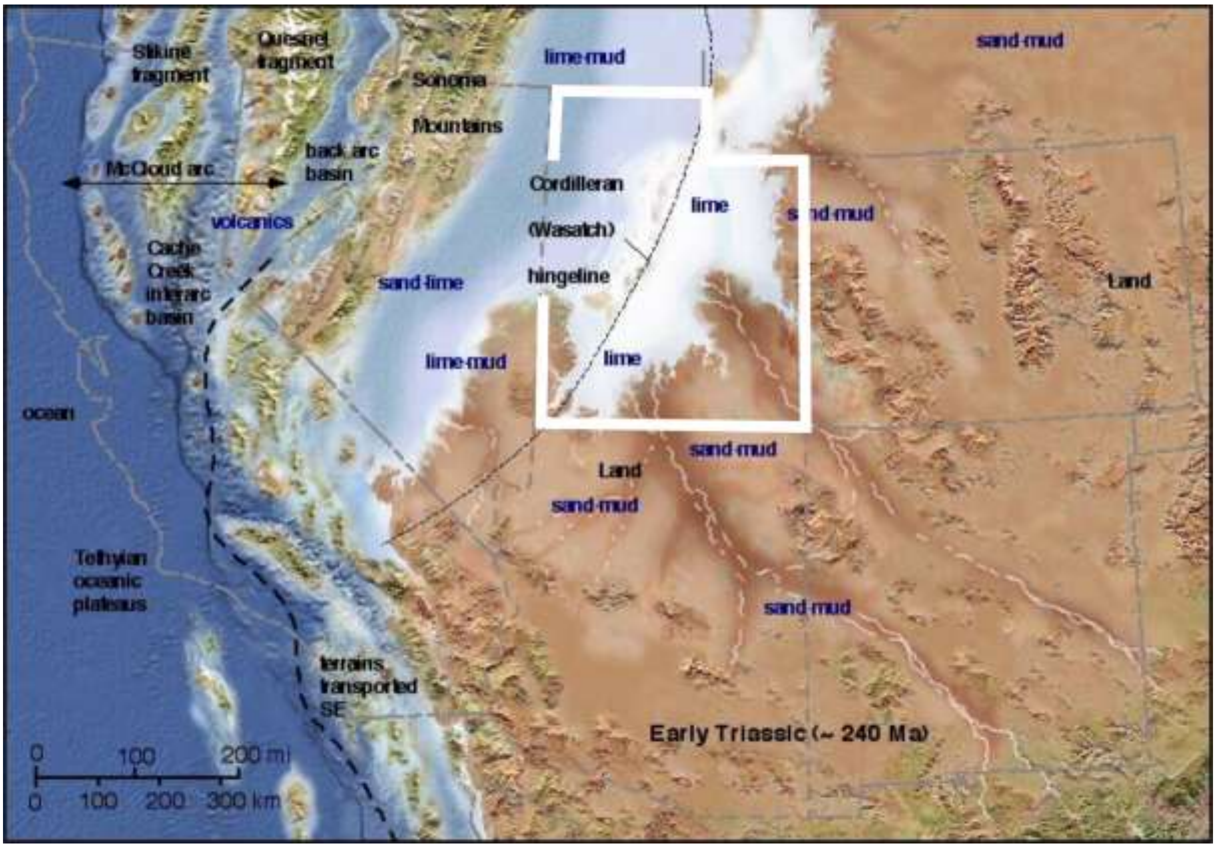

Figure 2.10: Early Triassic paleogeography. The state of Utah is outlined in white. URL: https://www2.nau.edu/rcb7/tripaleo.html.

An abundance of animals and plants lived by the Chinle rivers, and many large, colorful tree trunks of petrified wood weather out from the Chinle rocks. The special conditions with large amounts of volcanic ash and other sedimentary flood deposits rapidly burying dead tree trunks may have ultimately caused the trunks to become petrified with silica (Blakey and Ranney, 2008).

The final scene of the Triassic time was quite different. The streams became more ephemeral as the conditions became drier on the plateau and windblown sand started to dominate the landscape (Figure 2.11). Local aeolian dunes are hence preserved in the uppermost parts of the Chinle Formation (Blakey and Ranney, 2008). The typically cliff-forming Wingate Sandstone overlying the Chinle Formation is another Late Triassic deposit of aeolian origin. The Wingate Sandstone is a relatively homogenous formation and represents the remnants of about 200 million year old, windblown sand-dunes (Stokes, 1986).

Figure 2.11: Late Triassic paleogeography. The state of Utah is outlined in white. URL: https://www2.nau.edu/rcb7/tripaleo.html.

2.2.5 The Jurassic Period

In Utah, the formations of Jurassic age were deposited in a basin-like depression located between the Mesocordilleran High in central Utah and the remnants of the Ancestral Rockies in western Colorado (Stokes, 1986) (Figure 2.12). The Mesocordilleran High influenced Utah in different ways during the Jurassic Period. The arid, desert climate on the Colorado Plateau would be intensified due to the blocking of moisture-bearing winds on the windward side of the obstacle (Stokes, 1986). Further, it acted as a barrier for the seas invading the continent in Late Jurassic time, making them invade from the north through Canada. The Mesocordilleran High also became a source for rivers carrying sediments that were transported towards the east (Stokes, 1986).

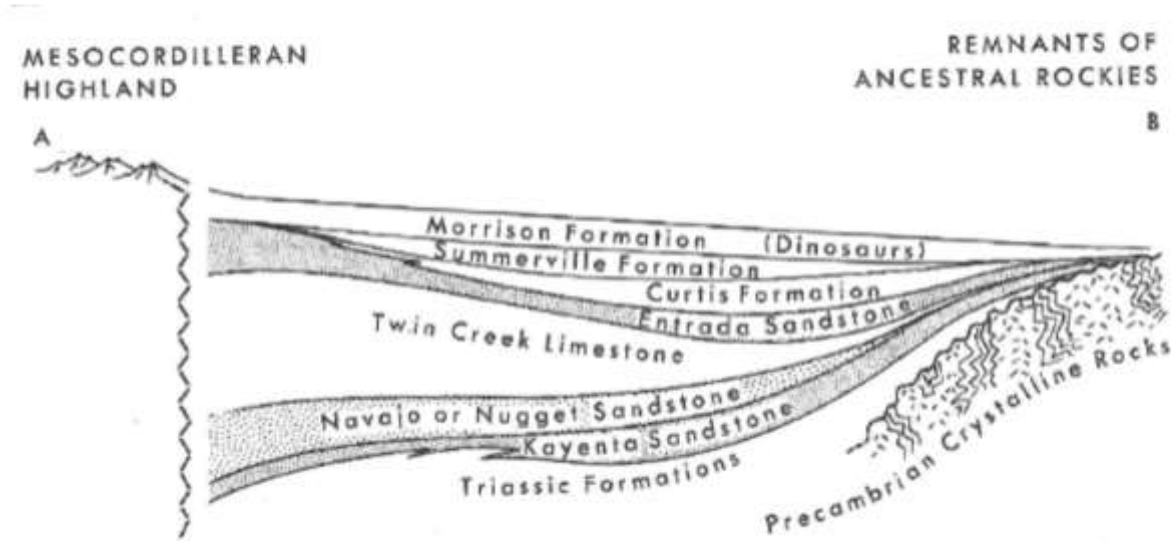

Figure 2.12: Simplified cross-section of Jurassic formations between central Utah and western Colorado. (Stokes, 1986).

The arid conditions that prevailed in the Colorado Plateau region during the latter part of the Late Triassic period, continued throughout the Jurassic period. Three different dominating environments that succeeded each other influenced the deposits from Jurassic time (Stokes, 1986).

The first of these environments, a sandy, desert environment, left deposits such as the Wingate Sandstone and the widespread aeolian Navajo Sandstone. The lower part of the Wingate Sandstone may be of Late Triassic age (Blakey and Ranney, 2008). In many places in Utah today, it constitutes sheer vertical cliffs, often seen with a metal-blue or black varnish, which is formed partly by metabolic processes of bacteria on the rock wall over a period of thousands of years (Blakey and Ranney, 2008). The Kayenta Formation, a sandy, braided fluvial system, overlies the Wingate Sandstone. Subsidence of the Kayenta fluvial basin created the accommodation place necessary to preserve the Wingate Sandstone (Blakey and Ranney, 2008). A coeval uplift of the Ancestral Rockies may have caused the slightly wetter conditions that were introduced to the Colorado Plateau in Early Jurassic time. In addition, this elevated land mass probably became a source for the Kayenta rivers (Blakey and Ranney, 2008). With time, the arid, desert conditions re-appeared on the plateau, and great sand-dunes were formed on the widespread Kayenta floodplain (Blakey and Ranney, 2008). The overlying Navajo Sandstone was deposited by winds blowing mostly from the northwest, in a scenery that probably resembled the Sahara Desert of modern times (Hintze, 2005). These three characteristic formations, the Wingate Sandstone, the Kayenta Formation and the Navajo Sandstone are often collectively referred to as the "Glen Canyon Group" (Hintze, 2005). The boundary between Early- and Middle Jurassic deposition is marked with an erosional surface that is cut down into the top of the Navajo Sandstone (Blakey and Ranney, 2008).

The following paleo-environment involved episodes of shallow marine invasions in Utah. Shallow seas entered from the North through Canada, spreading over wide areas of Utah, Montana and Wyoming (Stokes, 1986). The Colorado River marks the approximate eastern extent of the marine waters in Utah (Stokes, 1986). This seaway, in which the Carmel Formation was formed, may have been a back-bulge basin related to compressional forces spreading eastward from the subduction zone along North America’s western margin (Hintze, 2005). Different types of plate tectonic features were related to this subduction of the Farallon oceanic plate, including an east-vergent thrust belt, a foredeep basin, a forebulge high, and a back-bulge basin (Hintze, 2005). This tectonic activity is named the Nevadan orogeny, which caused a growth of the North American continent by the accretion of island arcs from the subducting oceanic plates (Hintze, 2005). The Nevadan orogeny was the forerunner to the more widespread Sevier orogeny of Cretaceous age.

The Entrada Sandstone was deposited in the latter part of the Middle Jurassic, as the arid, desert conditions once again started to dominate the plateau (Blakey and Ranney, 2008). Sabhka deposits are commonly found in the Entrada Sandstone, even though the overall deposits represent aeolian dunes. A relatively high water table created these sub-aerial, salt flat deposits (Blakey and Ranney, 2008).

The final, dominating environment on the Colorado Plateau during the Jurassic Period included rivers and fresh-water lakes (Stokes, 1986). It was during this last type of conditions that the overall fluvial Morrison Formation was formed in the interior non-marine Morrison basin. By Morrison time, there were only eroded remnants of the Ancestral Rockies left, which had been worn down during Jurassic time (Hintze, 2005) (Figure 2.13).

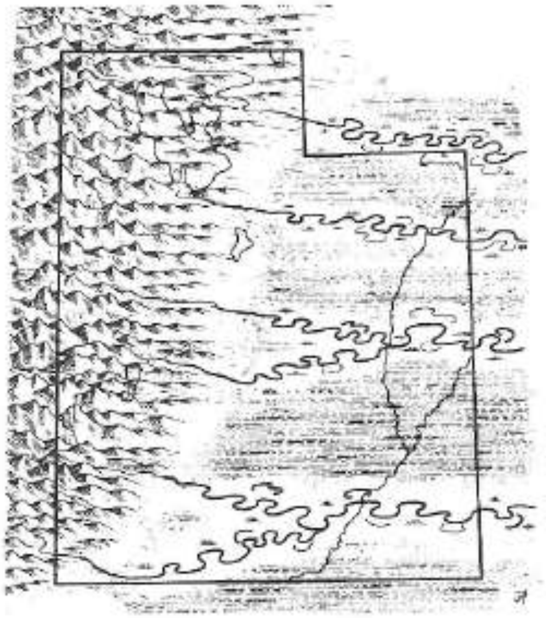

Figure 2.13: Paleogeography of Utah in late Jurassic time during deposition of the upper part of the Morrison Formation. The rivers running east-ward from the Mesocordilleran Highlands deposited fine-grained sediment over most of the western interior. (Stokes, 1986).

During the Jurassic time, the first intrusive igneous activity since the Precambrian appeared on the plateau (Stokes, 1986). The remnants of these granitic intrusions of Jurassic and Early Cretaceous age can be seen in Utah today. The subduction of the Farallon- and Kula oceanic plates beneath the southwestern edge of North America generated the heat which eventually melted surrounding rocks deep below the surface near the subduction zone (Hintze, 2005). The magmas were injected to the existing sedimentary bedrock.

2.2.6 The Cretaceous Period

Many of the most comprehensive effects of the breakup of Pangaea in the beginning of the Mesozoic Era were not felt until the Cretaceous time. As much of the heat that was trapped beneath the supercontinent escaped during the breakup, the newly formed continents would gradually subside closer to sea level (Blakey and Ranney, 2008). The resulting low elevation caused a series of major flooding events of all of Earth's continents during the Cretaceous (Blakey and Ranney, 2008).

During a period of about 10 million years, in the Late Jurassic and earliest Cretaceous, mild erosion most likely prevailed in southern Utah (Stokes, 1986). This part of the rock record hence seems to be missing. The Early Cretaceous Formations in Utah have a non-marine origin and were deposited in a continental interior environment a great distance from the oceans. Formations such as Cedar Mountain and Byrro Canyon were deposited on flat and broad floodplains east of the Mesocordilleran High at this time (Stokes, 1986).

The regional climate became much more humid during the Cretaceous, partly because of the drift of the North American continent towards the North and the mid-latitude belt of westerly winds (Blakey and Ranney, 2008).

Furthermore, major mountain building events greatly influenced the western part of North America throughout the Cretaceous time. The Sevier orogeny caused major uplifts in this region, and caused a tilting of previously deposited strata on the southwestern part of the Colorado Plateau (Blakey and Ranney, 2008). As the areas to the south and west were uplifted, the Colorado Plateau started to subside. The compressional forces related to the Sevier orogeny were directed towards the east. These forces caused great thrust faults to form deep beneath the Earth's surface, as big stacks of strata were tilted and pushed on top of each other (Hintze and Kowallis, 2009) (Figure 2.9). The thrust faults did however not have much impact on the Colorado Plateau region (Blakey and Ranney, 2008).

One of the greatest flooding events of all time, starting at the end of the Early Cretaceous, led to the invasion of seas that spread inwards from the north and south and divided the North American continent into two separate, big islands (Stokes, 1986). At this time, the Ancestral Rockies were torn down by erosion, allowing the marine waters to spread into Utah from the east. The Mesocordilleran High to the west, was on the other hand growing into a large Sevier mountain range (Stokes, 1986). The shoreline of the invading seas, which created the so-called *Cretaceous Interior Seaway*, was aligned parallel to the foothills of this rising land mass (Figure 2.14).

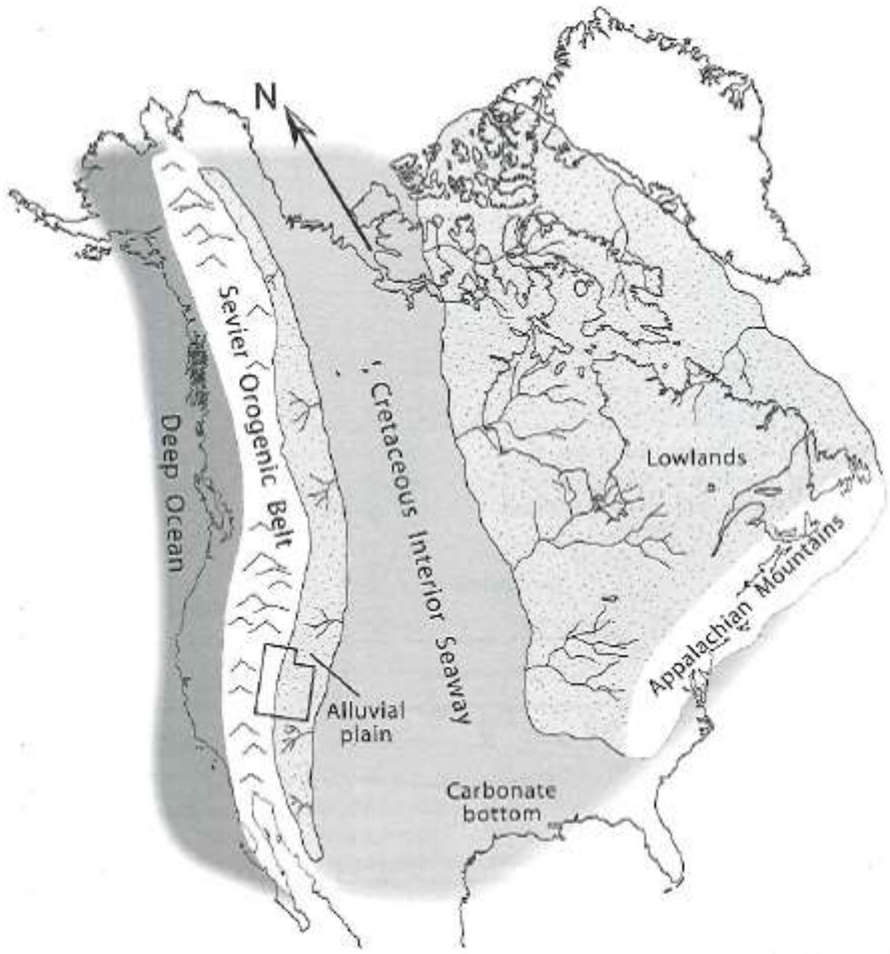

Figure 2.14: Geography of North America during the Cretaceous Period 80-100 million years ago with an outline of the location of Utah. The Sevier orogenic belt covered all of western Utah and eastern Nevada. (Hintze and Kowallis, 2009).

The tectonic situation that developed in Utah during the Middle Cretaceous time, with the uplift of the region west of the Wasatch Line and subsidence of the eastern region resulted in the production of large quantities of sediments (Stokes, 1986). These sediments were rapidly transported and deposited by powerful rivers in the adjacent basins.

The sediments were transported from the west to the east. The different grain-sizes of the sediments, including conglomerate, sand and mud, clearly reflect the distance across which they were transported from the source area (Stokes, 1986).

Different types of environments existed between the mountain range and the seaway, including alluvial fans, coastal plain and -swamps and beaches (Blakey and Ranney, 2008). These environments were aligned parallel to the foothills of the Mesocordilleran High, and they repeatedly shifted to the west or to the east as a response to fluctuations of the relative sea level. The location of the environments was also dependent on the rate of sediment influx, with uplift-periods resulting in a high sediment production and an eastward facies-shift (Blakey and Ranney, 2008). In addition to coal beds of Cretaceous age, other important deposits found in Utah today include the Dakota Sandstone, the Mancos Shale and the Mesaverde Group (Hintze, 2005). These units are mainly made up of inter-tongues of coarse beach- and fluvial sand and offshore muds, created during westward fluctuations of the retreating shoreline (Hintze, 2005).

The sea withdrew from the continental interior near the close of the Cretaceous Period (Stokes, 1986). Environments such as river systems, swamps, and alluvial plains were most likely dominating the deposition in eastern Utah at this time (Stokes, 1986).

2.2.7 The Cenozoic Era

The initiation of several uplift events in the latest Cretaceous time put an end to the invasions of shallow seas that were characteristic for the Cretaceous period in Utah (Stokes, 1986).
The Laramide orogeny was a series of events of mountain building and erosion in the Rocky Mountains region, resulting in the formation of the Uinta Mountain in Utah. It initiated in Late Cretaceous time about 90 million years ago and ended in Eocene time about 50 million years ago (Hintze and Kowallis, 2009). The Laramide orogeny closed the Cretaceous Interior Seaway and caused a great deal of uplifts, including several uplifts of the Colorado Plateau region. The Colorado Plateau in general was little affected by the compressional forces and was uplifted largely as a single block (Blakey and Ranney, 2008).

The compressional forces resulted in reactivation of pre-existing structural weaknesses of Precambrian age. The many small flexures that exist in the Colorado Plateau region today, were formed along such ancient faults and deeply buried structures (Hintze, 2005). During the Eocene time there was an expansion of fresh-water lakes, notably the Green River Lake system that extended from Wyoming and Colorado into Utah where it formed Lake Uinta (Stokes, 1986).

Igneous activity that had extended inward from the continental margin in California, reached northern Utah about 40 million years ago and by 30-20 million years ago it prevailed across the entire southern half of the state (Hintze and Kowallis, 2009). These Oligocene-Miocene igneous intrusions formed the foundations of the Henry- and La Sal Mountain in southeastern Utah (Hintze and Kowallis, 2009) (Figure 2.3). The subduction rate of the Pacific Plate along the southwestern margin of North America slowed down after the Laramide orogeny. This happened as the oceanic spreading ridge separating the Pacific Plate and the Kula Plate approached the subduction zone. The subducting plate detached and a transform plate boundary developed (Hintze and Kowallis, 2009). This event marked the beginning of the development of the San Andreas Fault system along the California coast (Stokes, 1986).

The Basin and Range Province, in addition to several large extensional faults, started forming in Miocene time and continued onwards (Hintze and Kowallis, 2009). About 17 million years ago, Utah began to expand westward ultimately forming the Great Basin (Hintze and Kowallis, 2009).

A major Miocene uplift and tilting of the Colorado Plateau led to the initiation of carving and sculpturing of the Canyonlands area, due to the increased gradient of the rivers (Hintze, 2005). This sculpturing is still going on. The Canyonlands are the northern extension of a broad swell called the Monument Uplift (Hintze, 2005). The Canyonlands National Park area lies entirely within the Paradox Basin and it contains very few faults.

During the humid climate of Pleistocene epoch, there were periodic glaciations in Utah. Lake Bonneville formed about 32 000 years ago, occupying a large part of central Utah (Hintze, 2005). The present day Great Salt Lake and the Utah Lake are the shrunken remnants of Lake Bonneville. The Pleistocene geologic record is almost completely missing on the Colorado Plateau, as a result of the extensive erosion and exhumation that has affected the region during the past few million years (Blakey and Ranney, 2008). The thickest deposits of Pleistocene age in Utah are the bottom sediments of Lake Bonneville (Stokes, 1986). The climate became warmer and dryer with the start of the Holocene epoch (Stokes, 1986).

Ongoing erosion and deposition continued to carve and sculpture the landscape to form Utah’s present day morphology.

2.3 Stratigraphy

2.3.1 Stratigraphic overview

The sedimentary rock column exposed in the study area near the town of Moab ranges from leached evaporites of the Late Carboniferous Paradox Formation upward to the Entrada Sandstone of Jurassic age. All of the formations that overlies the Paradox Basin in the area are in some way distorted and influenced by paleo-growth of the Moab salt-intruded anticline and/or later collapse of the structure (Baars, 1987). The sedimentary units included in this study are from bottom to top: the Cutler Formation, the Chinle Formation, the Wingate Sandstone, the Kayenta Formation, the Navajo Sandstone, the Slick Rock Member of the Entrada Sandstone and the Moab Member of the Entrada Sandstone (Figure 2.15).

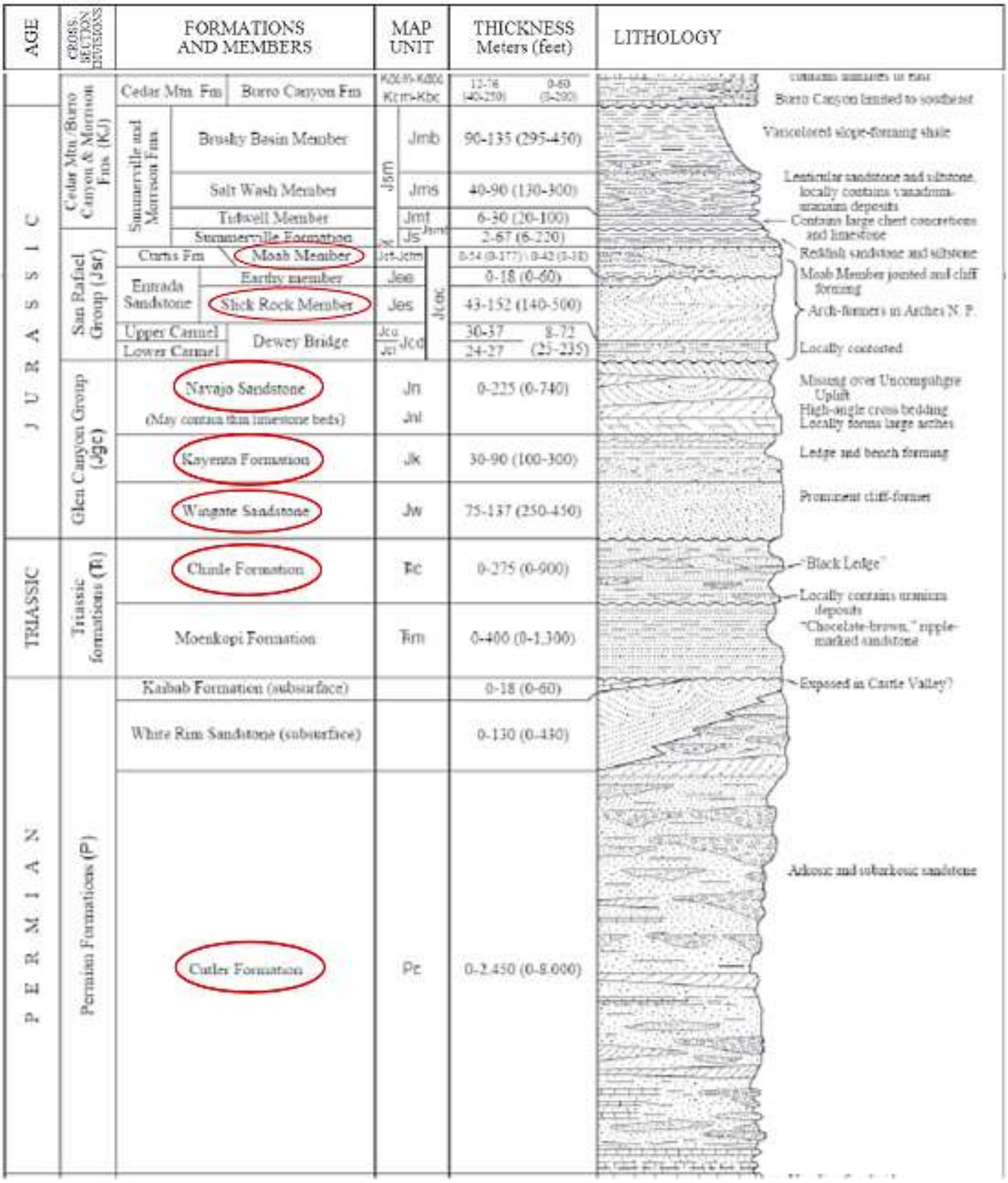

Figure 2.15: Stratigraphic overview of the formations included in this study (outlined in red). Modified after: Doelling et al. (2002).

2.3.2 The Cutler Formation

The Cutler Formation was formed during the Early Permian time (Figure 2.16 a)), and includes several subunits in Utah. It is made up of fluvial, red, arkosic sandstones and white marine sandstones, with interbedded dark-red micaceous siltstone, and gray cherty fossiliferous limestone and dolomite (Doelling, 2001). The clasts were derived from the Uncompahgre Uplift to the east and were transported by fluvial processes. The erosional slopes measured of the Cutler Formation ranges from 26-38° with a mean value of ~33° (Figure 4.3 and Appendix A, Table 8-1). The Cutler Formation generally have a low porosity (4%), a moderate degree of cementation (dominantly carbonate) and a low degree of pressure solution (Table 4-2 - Table 4-4). It is generally poorly/ moderately sorted and the grains have a subrounded/ subangular shape. The Cutler Formation thickens northward from a wedge-edge at the "West Portal" north of the Colorado River to more than ~360 m in about 6.5 km. It also thickens considerably in the subsurface on both flanks of the Moab anticline structure (Baars, 1987). It is exposed mostly in the east half and in the north-central part of the study area and forms alternating slopes and ledges.

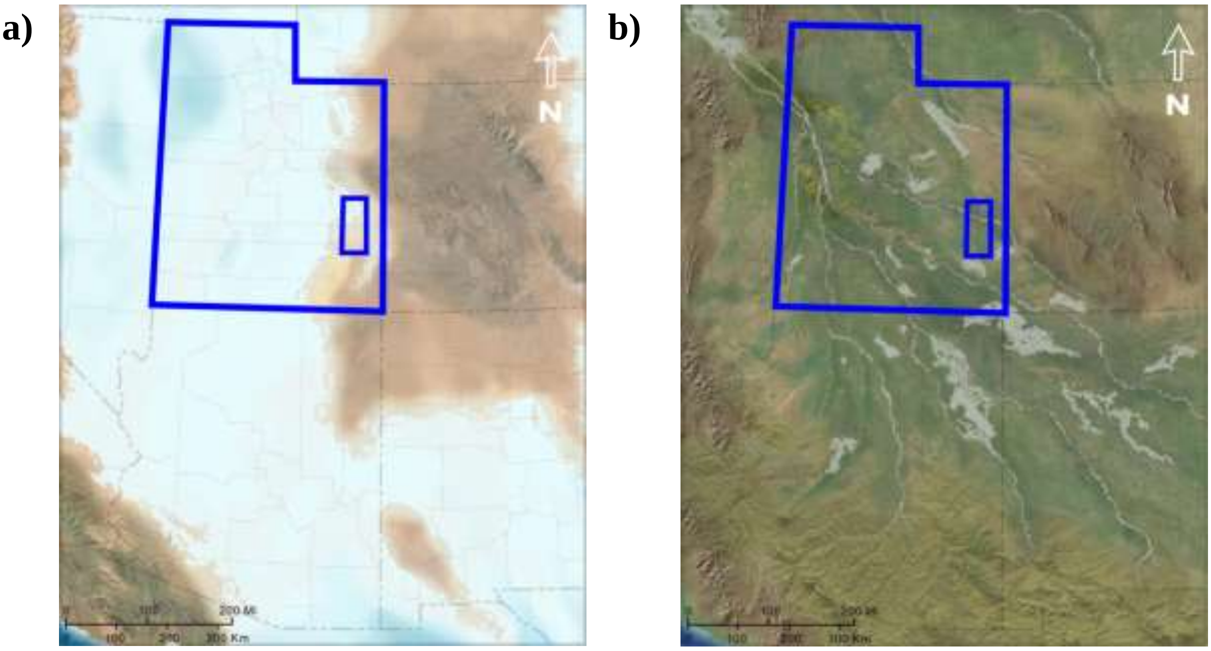

Figure 2.16: Palaeogeographic map of western North America in a) Early/Middle Permian time and in b) Late Triassic time. The state of Utah and the field area is outlined in a blue color. Based on map by Ron Blakey (https://www2.nau.edu/rcb7/ColoPlatPalgeog.html).

2.3.3 The Chinle Formation

The Chinle Formation is a varicolored (red, purple, green and yellowish) slope-forming shaly and ledgy unit of Triassic age (Figure 2.16 b)). It is made up by bentonitic clayey sandstones and siltones and locally contains scattered ledges of conglomeratic sandstones (Foos, 1999). The erosional slopes measured of the Chinle Formation ranges from 13-38° with a mean of ~31° (Figure 4.3 and Appendix A, Table 8-1). The Chinle Formation generally has a very low/ low porosity (6%), a high degree of cementation (dominantly carbonate) and a moderate degree of pressure solution (Table 4-2 - Table 4-4). It is generally moderatly/ well sorted and the grains have a subrounded/ rounded shape. The Chinle Formation forms a steep slope from the base of the overlying, massive Wingate Sandstone with the Moenkopi Formation below. The hiatus between the Moenkopi- and Chinle Formation represents all of Middle Triassic time, about 10 million years (Hintze and Kowallis, 2009). The base of the Chinle Formation is marked by a thin, white basal layer named Moss Back (Baars, 1987). The thickness of the Chinle Formation reach up to 275 meters or more with the greatest thickness in rim synclines adjacent to the salt-cored anticlines and are locally missing on anticlines.

2.3.4 The Wingate Sandstone

The Wingate Sandstone is a pale-orange to reddish-brown, massive cross-bedded sandstone. It is generally fine-grained and represents the remnants of widespread, aeolian sand-dunes that were deposited in Late Triassic to Early Jurassic time (Figure 2.17 a)). The erosional slopes measured of the Wingate Sandstone ranges from 64-90° with a mean of ~81° (Figure 4.3 and Appendix A, Table 8-1). The Wingate Sandstone generally has a relatively high porosity (13%), a high degree of cementation (dominantly carbonate and quartz) and a moderate degree of pressure solution (Table 4-2 - Table 4-4). It is generally moderatly/ well sorted and the grains have a rounded/ well rounded shape. Together with the overlying Kayenta Formation and Navajo Sandstone, this group of formations, referred to as the “Glen Canyon Group” can form immense vertical cliffs of up to 600 meters or more. The cliffs of the Wingate Sandstone are commonly stained with a dark blue to black desert varnish (Baars, 1987) and the thickness varies from about 75 to 137 meters.

2.3.5 The Kayenta Formation

The Kayenta Formation is a red-brown to lavender-gray, fine-to medium-grained, medium- to thick-bedded sandstone with subordinate silstone, limestone and shale interbeds. It contains some intraformational conglomerate and generally contains abundant slopeforming red siltsone in the upper third of the formation (Doelling, 2001). The erosional slopes measured of the Kayenta Formation ranges from 24-89° with a mean of ~69° (Figure 4.3 and Appendix A, Table 8-1). The Kayenta Formation generally has a moderately high porosity (9%), a moderate/ high degree of cementation (dominantly carbonate and quartz) and a moderate/ high degree of pressure solution (Table 4-2 – Table 4-4). The grains generally have a subrounded/ rounded shape. The lower surface is usually a scoured surface in the underlying Wingate Sandstone. It is generally divided into an upper slope-forming- and a lower cliff-forming unit. The Kayenta Formation was formed during Early Jurassic time (Figure 2.17 a)). It is fluvial in origin with a thickness that varies from 30 to 90 meters.

2.3.6 The Navajo Sandstone

The Navajo Sandstone is a pale orange, aeolian cross-bedded massive sandstone. It is well sorted, fine- to medium-grained and constitute the uppermost member of the cliff-forming “Glen Canyon Group” that can be observed throughout the study area in southeastern Utah. The erosional slopes measured of the Navajo Sandstone range from 14-88° with a mean of ~47° (Figure 4.3 and Appendix A, Table 8-1). The Navajo Sandstone generally has a relatively high porosity (13%), a moderate degree of cementation (dominantly carbonate and quartz) and a high degree of pressure solution (Table 4-2 – Table 4-4). The grains generally have a rounded shape. The lower third of the formation commonly weathers to a cliff, whereas the remainder weathers into domes and hummocky knobs (Doelling, 2001). It is best seen in Arches National Park, but it is also widely exposed along the margins of Moab Valley, high above the Moab fault north of the Colorado River and in the Colorado River canyons (Baars, 1987). The Navajo Sandstone was formed during Early Jurassic time (Figure 2.17 a)), deposited by wind in a vast desert that covered most of the Colorado Plateau. The thickness of the formation in the study area reaches up to 225 meters and it pinches out to the northeast over the Uncompahgre uplift.

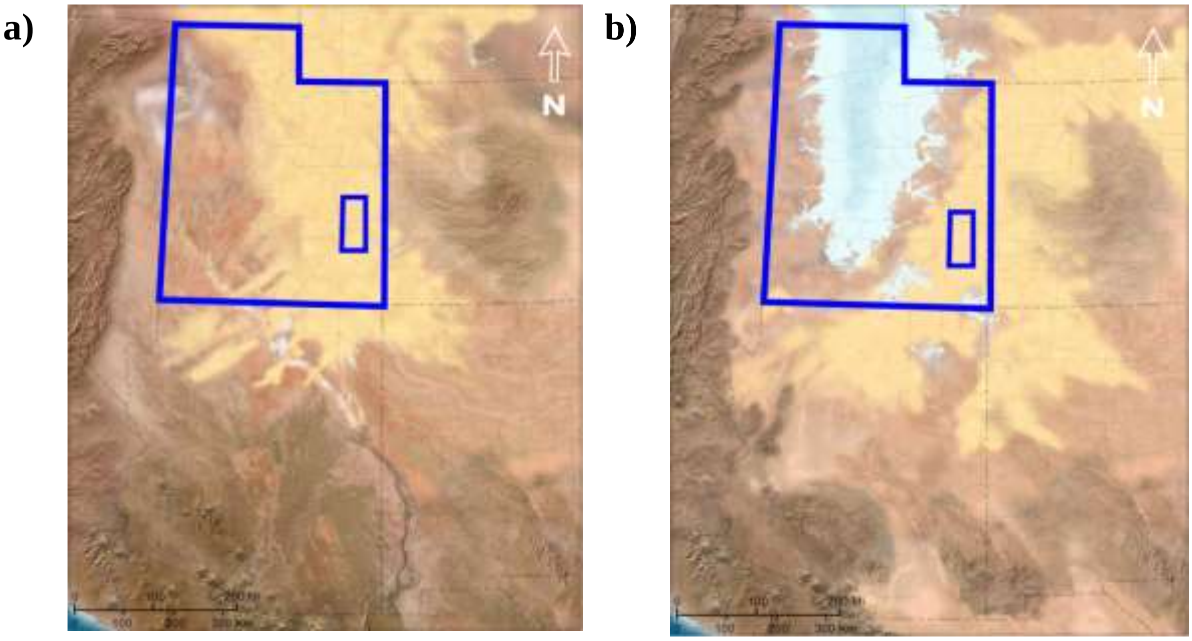

Figure 2.17: Palaeogeographic map of western North America in a) Early Jurassic time and in b) Middle Jurassic time. The state of Utah and the field area is outlined in a blue color. Based on map by Ron Blakey (https://www2.nau.edu/rcb7/ColoPlatPalgeog.html).

2.3.7 The Slick Rock Member of Entrada Sandstone

The Slick Rock Member is an orange-red or banded orange-red and white sandstone that constitutes the middle part of the Entrada Sandstone, located between the reddish basal Dewey Bridge Member and the highest massive sandstone cliffs of the Moab Member. The Entrada Sandstone is known as the massive cliffs containing the arches in Arches National Park, with many arches formed within the Slick Rock Member. It is a generally fine-grained, massive, aeolian cross-bedded sandstone. The erosional slopes measured of the Slick Rock Member ranges from 17-86° with a mean of ~53° (Figure 4.3 and Appendix A, Table 8-1). The Slick Rock Member generally have a moderately high porosity (11%), a moderate/ high degree of cementation (dominantly carbonate and quartz) and a moderate degree of pressure solution (Table 4-2 – Table 4-4). The grains generally has a subrounded/ rounded shape. The Slick Rock Member has a resistant and smooth weathering and is locally pocked with abundant small spherical holes (with diameters up to 10 cm) in outcrop (Doelling, 2001). It was deposited in a coastal dune environment by wind and streams in Middle Jurassic time (Figure 2.17 b)). It usually forms steep cliffs but at some localities in the study area (at

Bartlett Wash and Hidden Cannyon localities (Figure 1.4) it has weathered to form gentle slopes (Figure 4.25). The thickness of the formation varies from 43 to 152 meters and are thinning eastward.

2.3.8 The Moab Member of the Entrada Sandstone

The Moab Member of the Entrada Sandstone is a light-yellow-gray, fine- to medium-grained cross-bedded sandstone (Foos, 1999). It is massive and forms cliffs that rest directly on the underlying Slick Rock Member. The erosional slopes measured of the Moab Member ranges from 68-87° with a mean of ~80° (Figure 4.3 and Appendix A, Table 8-1). The Moab Member generally has a high porosity (19%), a low/ moderate degree of cementation (dominantly quartz) and a low/ moderate degree of pressure solution (Table 4-2 – Table 4-4). The grains generally have a rounded/ well rounded shape. The Moab Member was deposited during Middle Jurassic time (Figure 2.17 b)) and constitutes the upper member of the Entrada Sandstone. The thickness of this formation reaches up to 42 meters and pinches out towards the west.

3 Joints

3.1 Introduction

There are many reasons why it is important to study joints as they control the physiography of many landforms and play an important role in fluid flow. The study of joints provides information of the mechanical behavior of rocks. Such studies can also provide important tools for inferring paleo-stress- states and directions and different phases of a deformation history may be mapped by establishing relative age relationship with other structures (Pollard and Aydin, 1988). Further, as joints provide fracture permeability for fluids such as water, oil and gas in addition to ore-forming fluids, there are often large economic interests involved. Fracturing of rocks will efficiently weaken the host rocks which is an important factor to consider during construction planning and design of large structures such as highways, bridges and dams (Pollard and Aydin, 1988).

Deformation by fracturing is the most common brittle deformation mechanism that occurs in the Earth’s upper crust. Figure 3.1 displays joints developed in the aeolian Wingate Sandstone in Indian Creek, Utah, USA. Different types of fractures, such as shear- , extensional- and contractional fractures can be distinguished based on the mode of displacement along the fracture wall (Figure 3.2) (Fossen, 2010). Shear fractures have wall-parallel displacement that exceeds the wall-perpendicular extension. Extensional fractures include joints, fissures, veins and dikes and are “opening mode”/mode I fractures while contractional fractures, also known as anticracks, are “closing mode”/mode IV fractures (Fossen, 2010). Joints can be defined as planar tensile opening-mode fractures with little or no wall-perpendicular displacement (Narr and Suppe, 1991). They form perpendicular to the least principal stress (σ_3) and thus joints trace the maximum compressive stress (σ_1) at the time of the propagation.

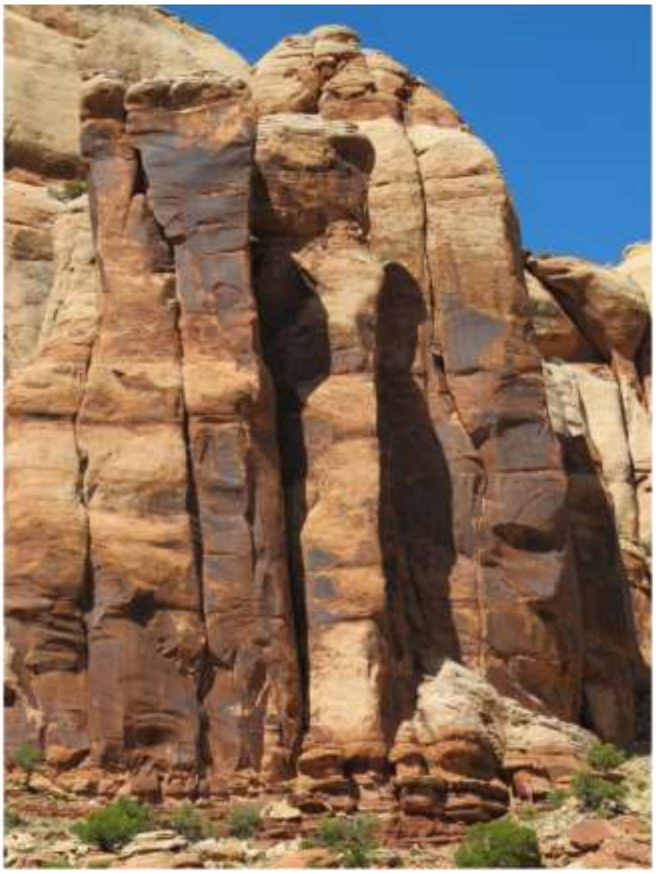

Figure 3.1: Nearly vertical joints formed in the Wingate Sandstone, Utah, USA. Coordinates: N38°02’23.2’’ W109°33’09.7’’.

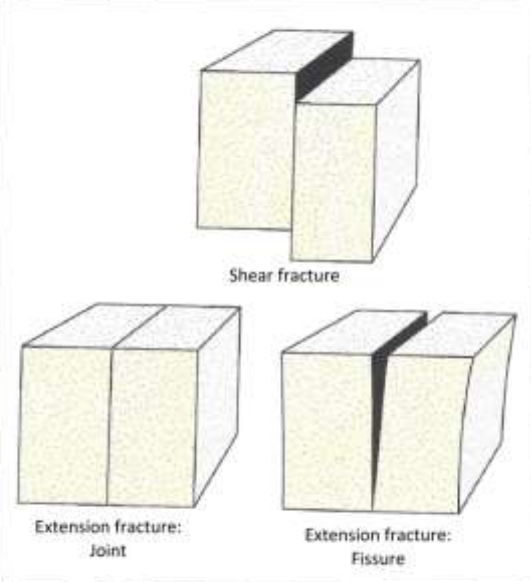

Figure 3.2: Three types of fractures. (Fossen, 2010).

3.2 Joint classification

Engelder (1985) suggested a distinction of different types of joints based on their different loading paths during a tectonic cycle. Based on an example from the Appalachian Plateau, USA, he distinguished between hydraulic, tectonic, unloading, and release joints. Different types of joints propagate at different times during the history of burial, lithification, deformation and denudation of the clastic basin-fill in sedimentary basins. Hydraulic and tectonic joints form prior to uplift as a result of an overpressure in the formation. Regarding hydraulic joints, the overpressure develops as a result of the weight of the overburden while the overpressure that causes tectonic joints to propagate is the result of tectonic compaction. Abnormal pore pressures as a result of tectonic compaction may develop at less than 3 km of burial, while overpressure as a result of the weight of the overburden most often requires a burial depth of 5 km or more (Engelder, 1985). In contrast, unloading and release joints form close to the surface by mechanisms such as thermal-elastic contraction accompanying removal of overburden weight. While the orientation of release joints is controlled by the rock fabric the orientation of the other types of joints is controlled by the contemporary or residual stress field.

3.3 Joint characteristics

Joints are associated with different types of characteristics compared to other fractures. Shear fractures form in the brittle/plastic transition zone and often develop in groups or clusters (Fossen, 2010). Joints, on the other hand, form at shallower depths in the brittle upper crust and have a tendency of spreading out with a spacing that is related to the thickness of the jointed layer. The proportionality of the layer thickness/joint spacing ratio was explored by Narr and Suppe (1991). Based on observations of joint spacing in the Monterey Formation in California they found a constant ratio of layer thickness to joint spacing of about 1.3. This fracture spacing index was approximately the same over a substantial region among different rock types and different structural locations. Thin layers thus develop a higher number of fractures than thicker layers of similar stiffness. Further they found that by adding the effect of microscopic flaws in the rocks to Hobbs (1967) model of the controls of joint spacing, it would predict a frequency distribution more similar in form to distributions based on actual observations in the field.

3.4 Mechanical conditions of jointing

Joints only form and propagate when the effective stress is tensile and the differential stress is high. Such conditions may appear in extensional as well as in contractional regimes. During layer parallel shortening in contractional regimes the outer arc experiences extension that may result in the formation of joints with an orientation that is parallel to the fold axis (Fossen, 2010). Cross-fold joints on the other hand develop with an orientation perpendicular to the fold axis as a result of the overpressure that builds up in a formation during the compression. Joints often develop perpendicular to the bedding in bedded sedimentary rock and occur with parallel fractures to form a joint set (Narr and Suppe, 1991). In homogenous rocks such as granites however, horizontal joints may form very close to the surface where the temperature is low and there is almost no overburden weight (Fossen, 2010). The result is referred to as “sheeting”.

The more competent or mechanically stiff layers will always develop more fractures than less competent or mechanically soft layers (Figure 3.3) (Fossen, 2010). This is because the stiffer layers can sustain and build up a higher level of differential stress before it fractures, which is required for joints to form. A softer layer would deform more easily and may not be able to build up a substantial differential stress to initiate joint formation.

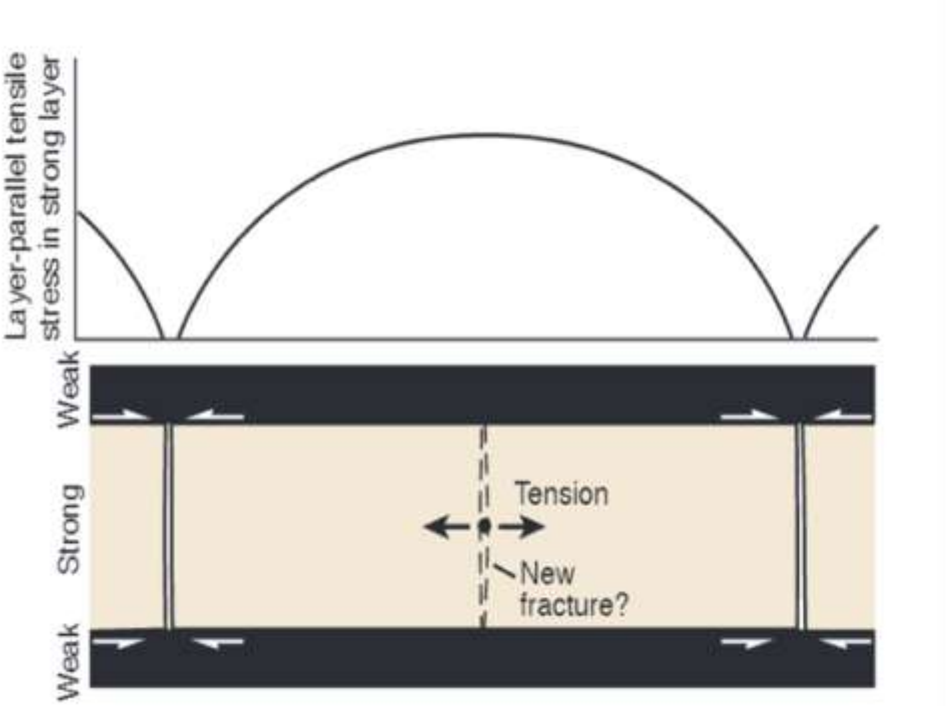

Figure 3.3: Illustration of deformation mechanisms in mechanically strong vs weak layers. Competent (strong) layers between weaker layers will preferentially fracture and the weaker layers will not. The weaker layers will thereby pull on the strong layer which creates tension between two existing joints. A new joint forms in the middle of the segment if the tensile stress exceeds the tensile strength of the layer. (Fossen, 2010).

3.5 Joint interaction

A single joint may have a planar (regular) or curviplanar (irregular) geometry. A distinction is also made between systematic and non-systematic joints, where parallel, straight joints with a relatively constant spacing are referred to as systematic. In contrast, non-systematic joints have an irregular geometry and orientation and do not make up joint sets (Fossen, 2010). Joints with parallel orientations confined within an area make up a joint set and are often of the same age –e.g. they are the result of the same tectonic event and propagated under the same stress field. Hence, different joint set orientations in an area are the result of tectonic events that occurred at different times during the Earth’s history. Figure 3.4 illustrates different types of intersections that may be observed in the field.

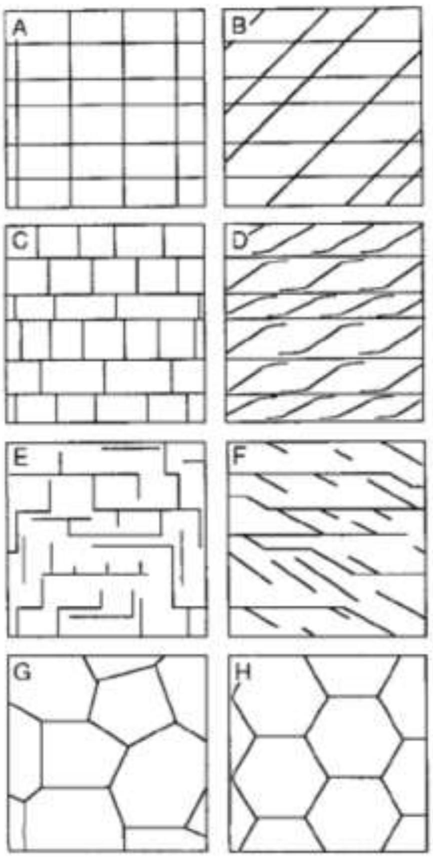

Figure 3.4: Schematic illustration of major multiple joint patterns. In A: Orthogonal and continuous (+ intersections), B: Nonorthogonal and continuous (X intersections), C: Orthogonal, one continuous and the other discontinuous (T intersections), D: Nonorthogonal, one continuous and the other discontinuous, E: Orthogonal, both sets being discontinuous, F: Nonorthogonal, both sets being discontinuous, G: Triple intersections with all joints discontinuous at various angles and H: Triple intersections at 120° angles. (Pollard and Aydin, 1988).

Examining the interactions between joint sets will often make it possible to establish relative age relationship between them (Figure 3.5). If the distance to neighboring joints is small the stress fields associated with the joints may interfere. This may have an important effect on the joint growth (Pollard and Aydin, 1988). T intersections indicate that an older, persistent set of parallel joints acts as a barrier to a younger joint set, which is arrested by the older set. Hook geometries develop when the tips of two joints interact. The tips of joints of similar age may curve towards each other, ultimately forming a double hook geometry (Figure 3.5 b)). The tip of a younger joint may curve towards an older, straight joint forming a single hook geometry (Figure 3.5 a)) (Cruikshank and Aydin, 1995).

In addition, the arrangement of twist hackles (seen as an echelon zone at the surface) reveals the propagation direction during the joint growth (Figure 3.5 c)) (Fossen, 2010). Shearing of an older joint may result in tail, wing, or horsetail fractures to form (Figure 3.5 d)). Such joints initiate from the tips of older joints or from roughness elements along the length of the older joint.

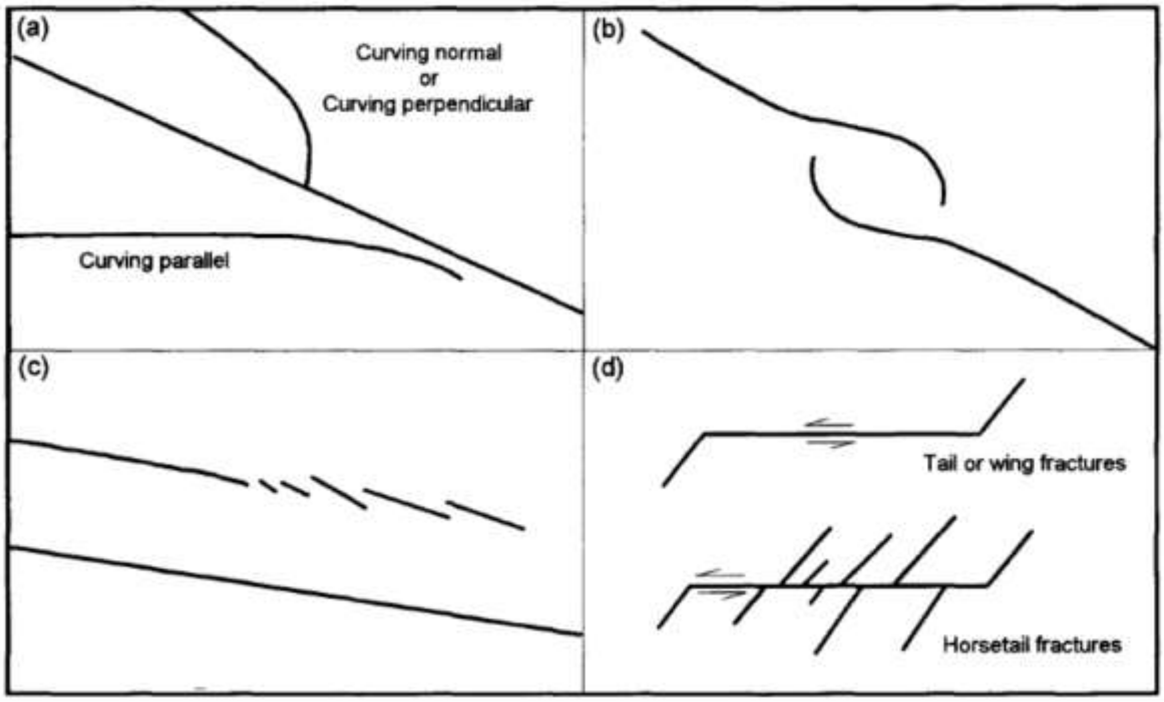

Figure 3.5: Relationships used to interpret relative ages of joints. In (a) the younger joints curve towards the older joint. In (b) the joints are of similar age and produce a hook-shaped geometry. In (c) the younger joint breaks down into a series of en enchelon segments that turn toward the older joint. In (d) tail-, wing- and horsetail fractures develop along the length of the older joint as a result of left-lateral shear displacement on the older joint. (Cruikshank and Aydin, 1995).

Further, the joint propagation trace may reveal information regarding the stress field during the joint growth. Olson (1989) introduced a method to interpret whether the remote stress field or the local stress field was dominating during the joint growth. He concluded that the curving paths of overlapping echelon fractures implied a predominance of a local stress over remote stress during propagation. A dominating remote compressive stress would on the other hand result in straight joint-traces.

4 Results

4.1 Introduction

In order to investigate possible explanations for the observed differences between the formations (Figure 4.1), figures and tables from studies of erosional slopes of the formations, facies associations, sedimentological-, mineralogical-, and mechanical properties, fracture-frequency distributions and layer thickness versus fracture spacing are presented in this chapter. These results will be used to support the observations described and discussed in the subsequent discussion chapter. Data presented in the facies associations- and sedimentological- and mineralogical properties subchapters are mainly based on the work of Tunheim (2015).

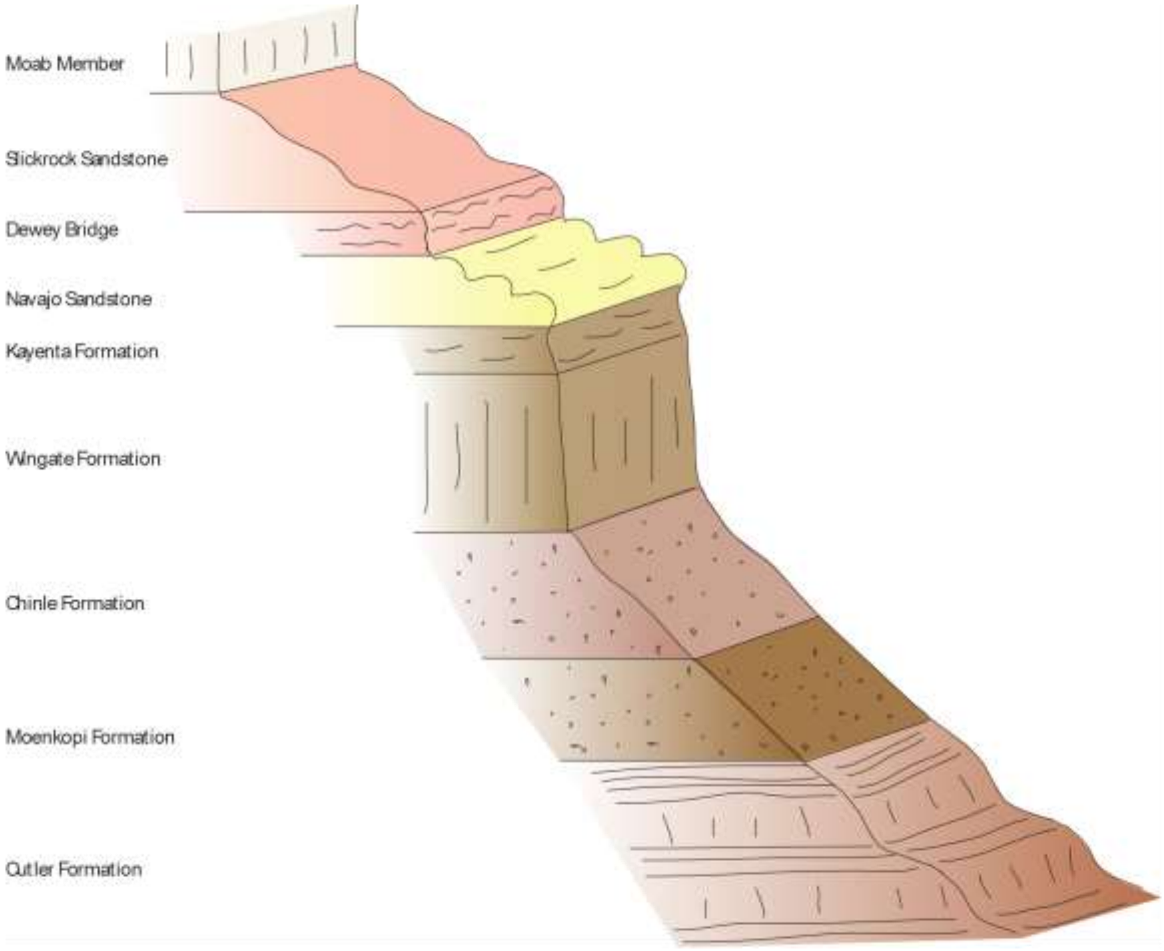

Figure 4.1: Simplified sketch illustrating the most pronounced differences in appearance of the formations (e.g. color, degree of fracturing and erosional slopes). Figure by Tunheim (2015).

4.2 Erosional slopes

The erosional slopes of the formations have been measured and recorded at in total 70 localities. The number of recorded slopes for the formations has been dependent on to what extent the formations were exposed in outcrops in the field area. While the gentle slopes of the Chinle Formation, overlain by the steep cliffs of the Wingate Sandstone are a common view in the area near Moab, the gently sloping Cutler Formation only crops out at a few localities. Figure 4.2 is a slope-map, illustrating differences in slope-values in a map view (with the Wingate Sandstone making up most of the red-colored, steep slopes).

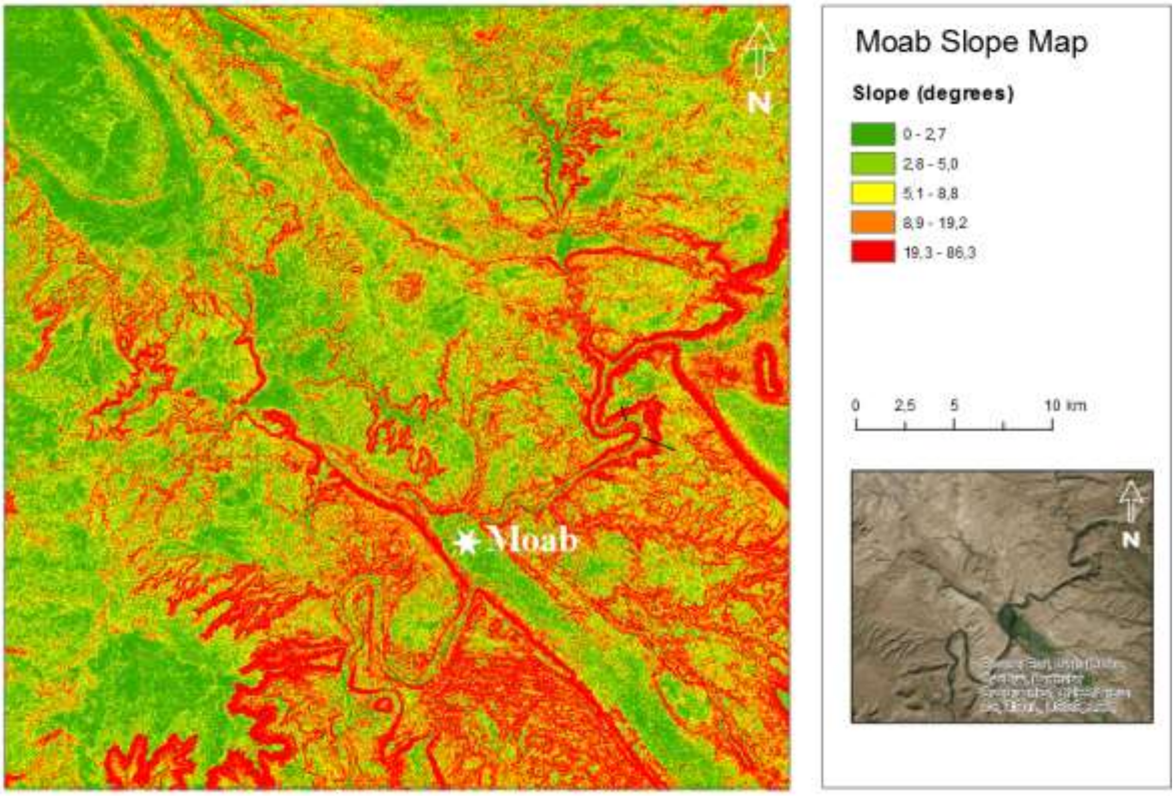

Figure 4.2: Slope-map illustrating differences in erosional slopes of the exposed formations in the area near Moab. The Wingate Sandstone constitutes the red color in parts of the area. The slope-map has been made based on a DEM created in ArcGIS software (the elevation data is collected from http://gis.utah.gov/data/elevation-terrain-data/).

Figure 4.3 displays measured slope values of each formation based on field observations. A list of all the recorded slope values can be found in Appendix A (Table 8-1). For the Cutler Formation the values range from 26-38° with a mean value of ~33°. For the Chinle Formation the values range from 13-38° with a mean value of ~31°. For the Wingate Sandstone the values range from 64-90° with a mean value of ~81°. For the Kayenta Formation the values range from 24-89° with a mean value of ~68°. For the Navajo Sandstone the values range from 14-88° with a mean value of ~47°. For the Slick Rock Member the values range from 17-86° with a mean value of ~53°. For the Moab Member the values range from 68-87° with a mean value of ~80°.

The variations in erosional slopes are clearly highest for the Slick Rock Member, the Navajo Sandstone and the Kayenta Formation. In contrast, the Cutler Formation, the Chinle Formation, the Wingate Sandstone and the Moab Member show significantly more uniform slope values throughout the study area (given by the relatively narrow 25th to 75th percentile boxes, Figure 4.3). Further, Figure 4.3 illustrates that the Moab Member, the Kayenta Formation and the Wingate Sandstone exhibit the steepest erosional slopes of the formations. The widespread undulating and hummocky surface morphology of the Navajo Sandstone results in the large range of measured slope values. The Cutler- and Chinle Formation are the most gently-sloping formations whereas the Slick Rock Member shows large lateral differences (e.g. gently-sloping at Hidden Canyon versus cliff-forming at Courthouse (Figure 4.24 and Figure 4.25)).

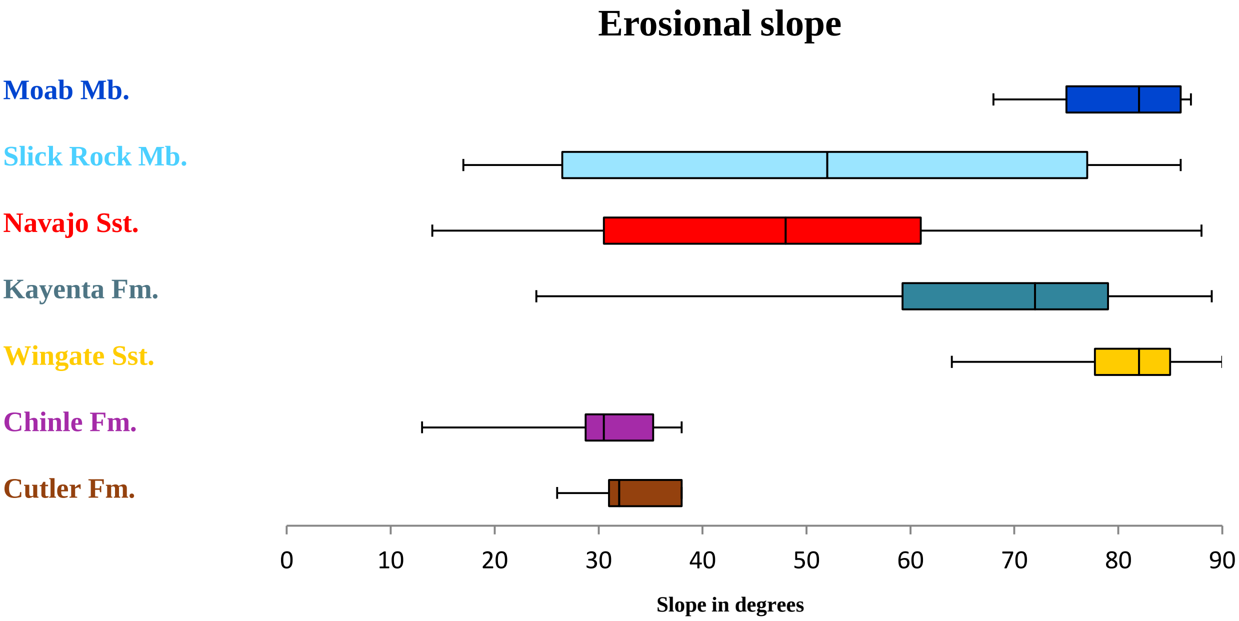

Figure 4.3: Boxplot illustrating the range, median and the 25th- and 75th percentile of measured slope values of the formations in the study area. The horizontal black line illustrates the range of the values, the black vertical line in the middle of the box illustrates the median value whereas the box represents 25 to 75 percentiles of the data. Note that the Wingate Sandstone, the Kayenta Formation and the Moab Member display relatively consistently steep erosional slopes in contrast to the generally gently-sloping Cutler-and Chinle formations.

4.3 Facies associations

The differences in depositional environments at the time the units were formed and their resulting facies associations are explored in this subchapter. Table 4-1 displays the sand- silt and clay content of each formation and Figure 4.4 illustrates measured bed thicknesses of each formation, both are based on sedimentological logs by Ragnhild J. Tunheim. Figure 4.5 – Figure 4.11 illustrate characteristic facies associations with images from outcrops as examples for each of the formations.

Table 4-1: Sand- silt and clay content (in %) of each formation. Data based on sedimentological logs by Ragnhild J. Tunheim.

Unit	Sand	Silt	Clay
Moab Mb.	98.9	1.1	-
Slick Rock Mb.	96.5	3.5	-
Navajo Sst.	100	-	-
Kayenta Fm.	90.1	8.5	1.3
Wingate Sst.	100	-	-
Chinle Fm.	75.4	22.3	2.3
Cutler Fm.	93.9	0.8	5.3

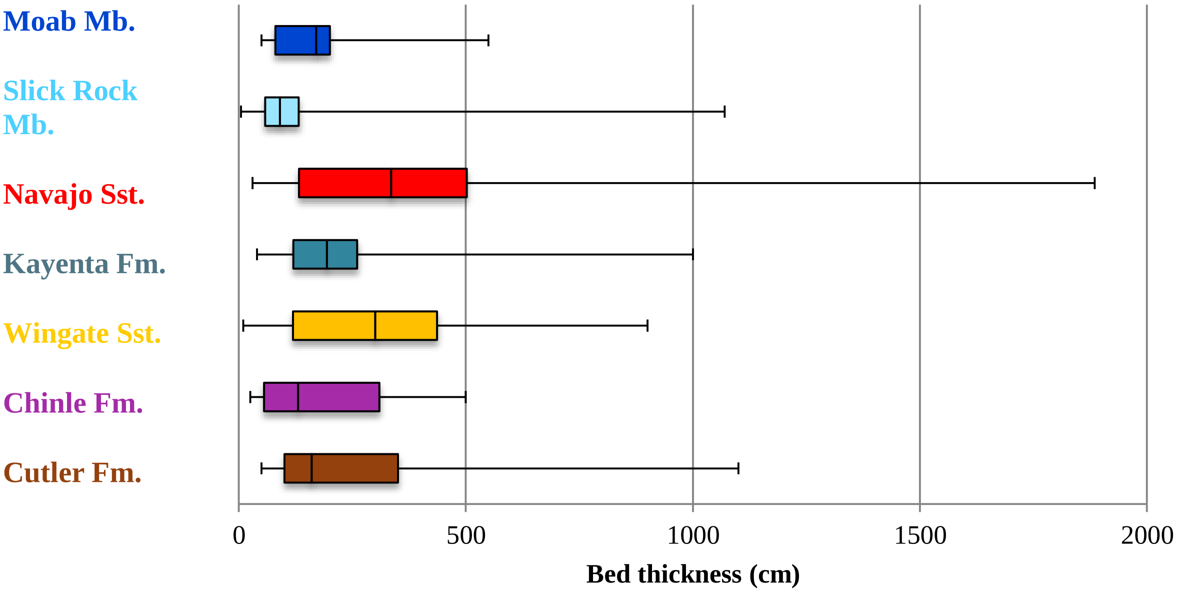

Figure 4.4: Boxplot illustrating the range-, median and 25th to 75th percentiles of measured thicknesses (in cm) of bed units of each formation based on sedimentological logs by Tunheim (2015) (25th to 75th percentile boxplot).

The Cutler Formation is characterized by large (up to ~11 m thick) through-cross- and planar-cross stratified dune units alternating with smaller interdunes and interbedded flash flood- and flood-plain units (Figure 4.5). The flood-plain facies contain fine-grained fractions of silt and clay (Figure 4.5, lowermost image). The Cutler Formation consists of ~93.8% sand, ~0.8% silt and ~5.3% clay (Table 4-1). These values correspond to the recorded values of the Chinle- and the Kayenta formations of similarly mixed-fluvial origin. However, the overlying Chinle Formation displays considerably larger proportions of the finer grained-fractions (silt and clay) than the other formations. The overall thicknesses of bed units in the Cutler Formation range from ~0.5- to ~11 m; however most of the beds have a thickness of ~1- to ~3.5 m (25th to 75th percentiles, Figure 4.4).

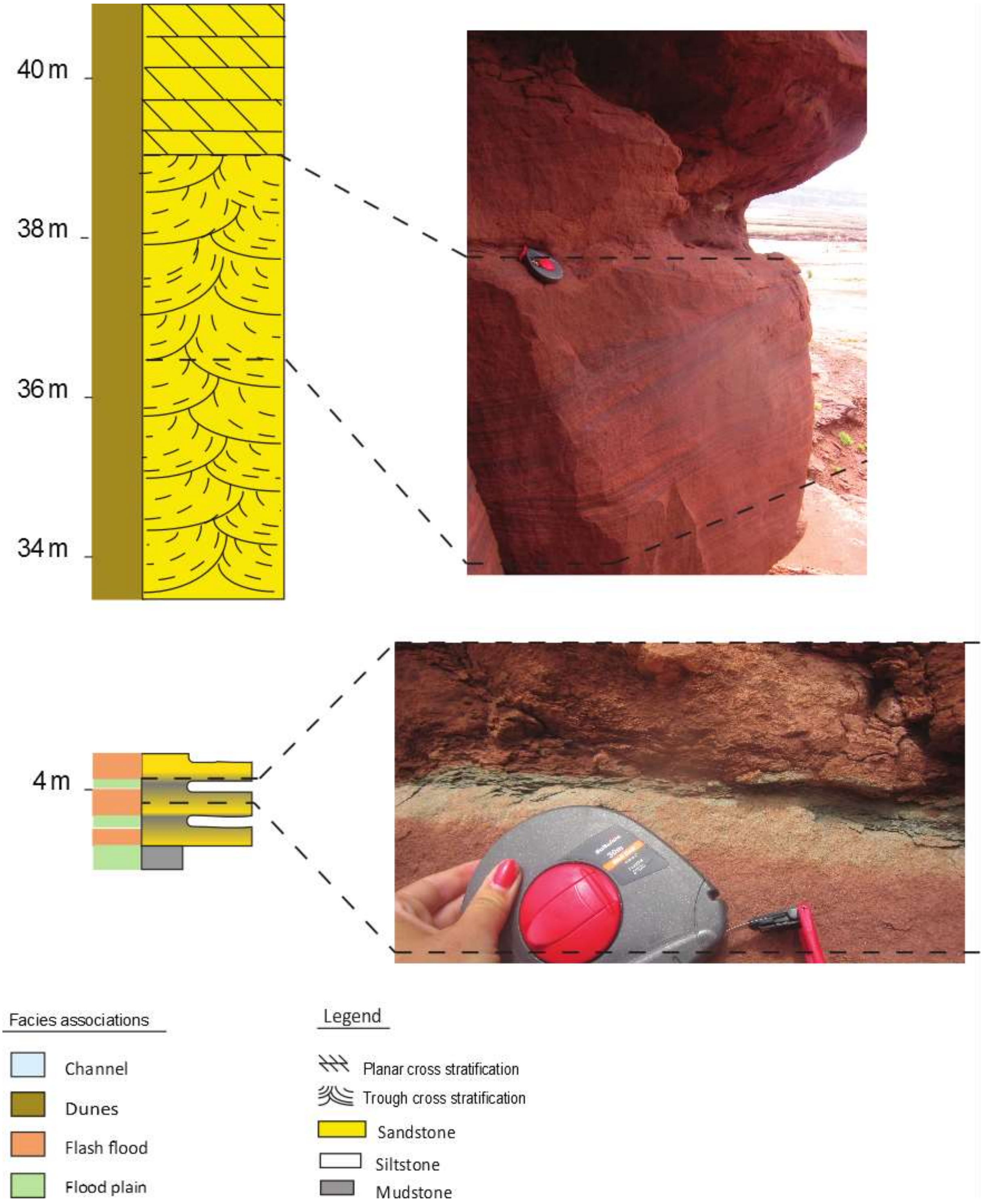

Figure 4.5: Characteristic facies associations (to the left) and example from outcrop (to the right, measuring tape holder for scale) of the Cutler Formation. Figure by Tunheim (2015).

The Chinle Formation is characterized by alternating flash-flood-, flood-plain- and channel facies of various thicknesses (Figure 4.6). The channel facies display low-angle cross-bedding and current-ripple cross-lamination with fining-upwards sequences. The flash-flood facies have a coarser grain-size and result in more resistant bedrock than the flood-plain facies. The flood-plain facies with smaller grain-sizes on the other hand, result in less resistant bedrock with screed-covered erosional surfaces (Figure 4.6, image to the right). The Chinle Formation consists of ~75.4% sand, ~22.3% silt and ~2.3% clay (Table 4-1). As mentioned, these values display considerably larger proportions of the finer grained-fractions (silt and clay) and less sand in comparison to the other formations. The overall thicknesses of bed units in the Chinle Formation range from ~0.25- to ~5 m; however most of the beds have a thickness of ~0.55- to ~3 m (25th to 75th percentiles, Figure 4.4). Generally, the thicknesses of the bed units are thus smaller in the Chinle Formation than in the underlying Cutler Formation.

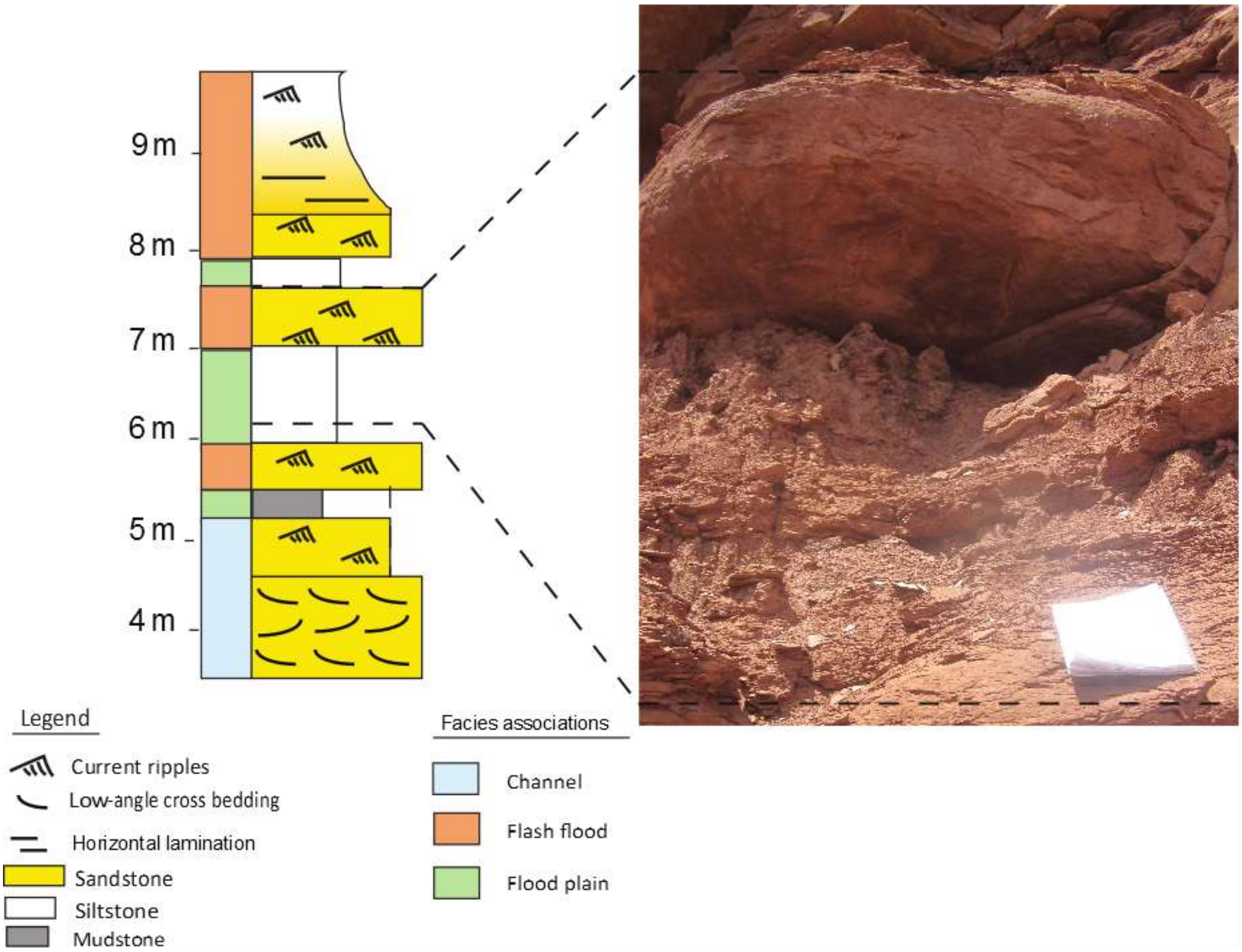

Figure 4.6: Characteristic facies associations (to the left) and example from outcrop (to the right, note pad for scale) of the Chinle Formation. Figure by Tunheim (2015).

The Wingate Sandstone is characterized by large (up to 9 m thick) trough-cross- and planar-cross stratified aeolian dune facies alternating with smaller interdune facies (with wavy, chaotic lamination) (Figure 4.7). The Wingate Sandstone consists of ~100% sand fractions (Table 4-1). The overall thicknesses of bed units in the Wingate Sandstone range from ~1- to ~9 m; however most of the beds have a thickness of ~1.2- to ~4.4 m (25th to 75th percentiles, Figure 4.4).

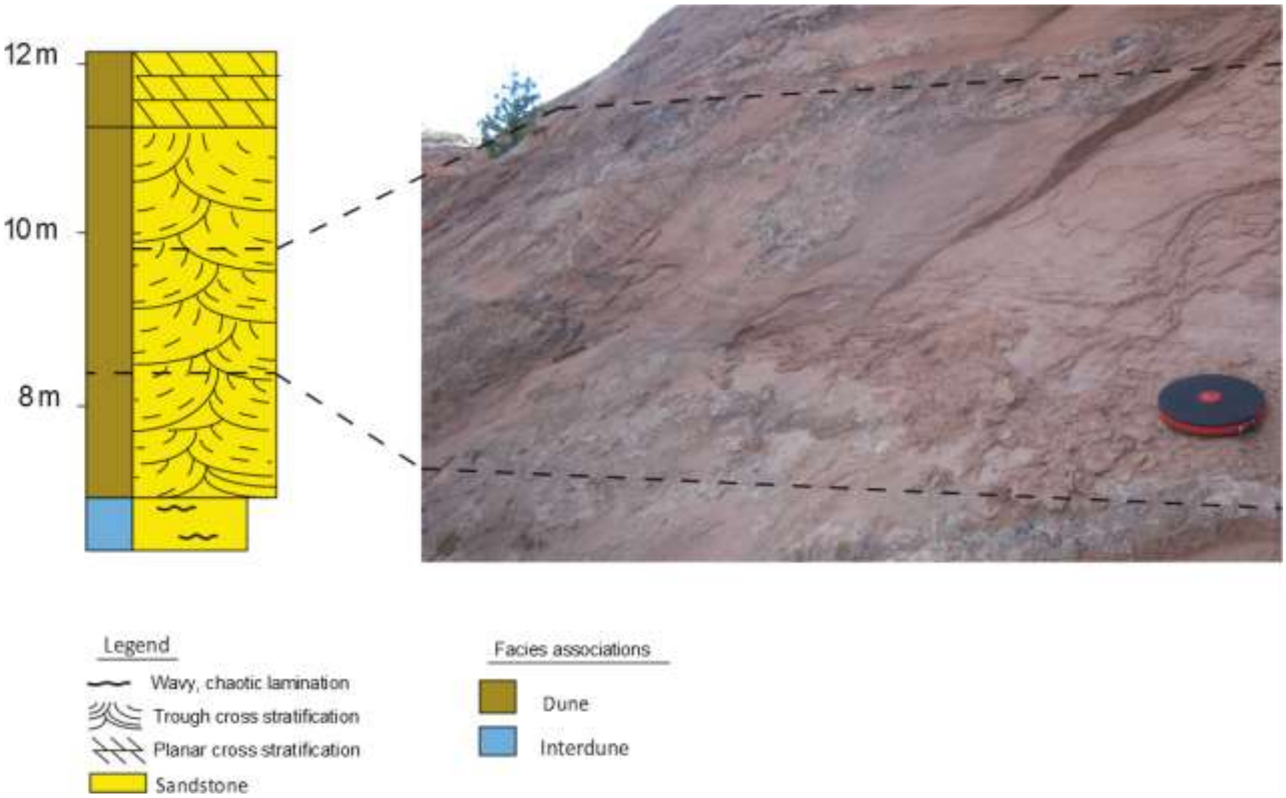

Figure 4.7: Characteristic facies associations (to the left) and example from outcrop (to the right, measuring tape holder for scale) of the Wingate Sandstone. Figure by Tunheim (2015).

The Kayenta Formation is characterized by through-cross stratified, fining-upward channel facies (up to ~10 m thick) with intervals of horizontal lamination, interbedded with smaller flood-plain facies dominantly made up by silt and clay fractions (Figure 4.8). The Kayenta Formation consists of ~90.1% sand, ~8.5% silt and ~1.3% clay (Table 4-1). These values correspond to the recorded values of the Cutler- and the Chinle formations of similarly mixed-fluvial origin. The overall thicknesses of bed units in the Kayenta Formation range from ~0.4- to ~10 m; however most of the beds have a thickness of ~1.2- to ~ 2.6 m (25th to 75th percentiles, Figure 4.4). Generally, the thicknesses of the bed units are thus smaller in the Kayenta Formation than in the Cutler- and Chinle formations.

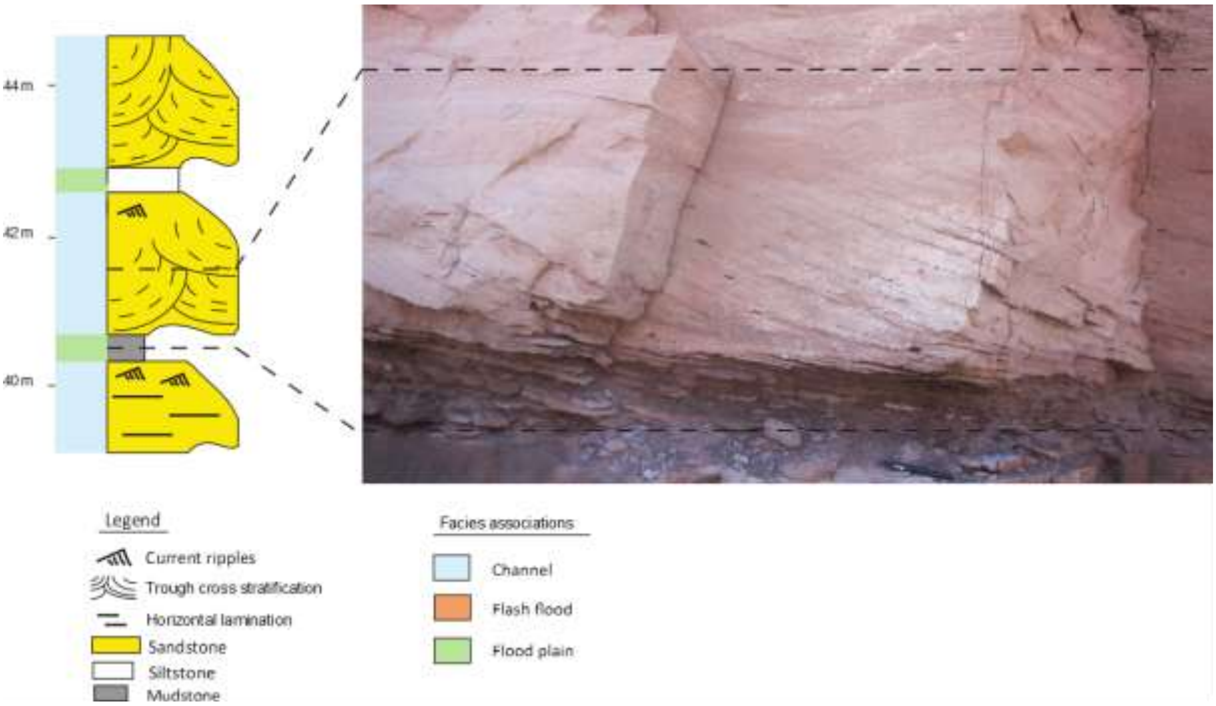

Figure 4.8: Characteristic facies associations (to the left) and example from outcrop (to the right) of the Kayenta Formation. Figure by Tunheim (2015).

The Navajo Sandstone is characterized by large (up to ~19 m thick) trough-cross- and planar-cross stratified aeolian dune facies alternating with smaller interdune facies (with wavy, chaotic lamination) (Figure 4.9). The Navajo Sandstone consists of ~100% sand fractions (Table 4-1). The overall thicknesses of bed units in the Navajo Sandstone range from ~0.3- to ~18.9 m; however most of the beds have a thickness of ~1.3- to ~5 m (25th to 75th percentiles, Figure 4.4). The average bed thicknesses of the Navajo Sandstone are thus slightly larger than for the Wingate Sandstone.

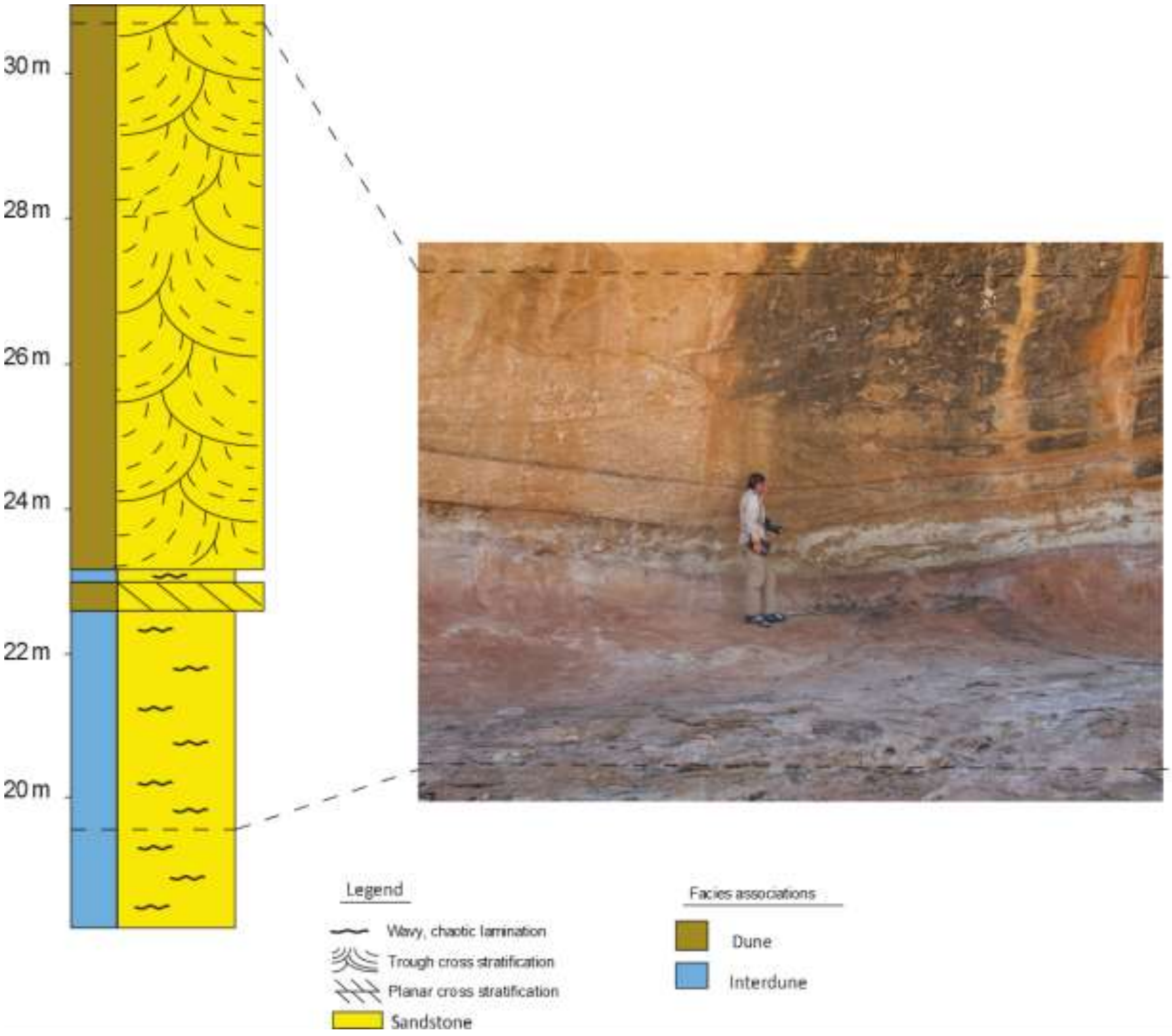

Figure 4.9: Characteristic facies associations (to the left) and example from outcrop (to the right) of the Navajo Sandstone. Figure by Tunheim (2015).

The Slick Rock Member is characterized by trough-cross- and planar-cross stratified aeolian dune facies (up to ~11 m thick) alternating with smaller interdune facies (with wavy, chaotic lamination) (Figure 4.10). Some of the interdune facies consist of interbedded laminations of sand and silt. The Slick Rock Member consists of ~96.5% sand and ~3.5% silt (Table 4-1). The overall thicknesses of bed units in the Slick Rock Member range from ~0.05- to ~10.7 m; however most of the beds have a thickness of ~0.6- to ~1.3 m (25th to 75th percentiles, Figure 4.4). The average bed thicknesses of the Slick Rock Member are thus considerably smaller than for the other formations.

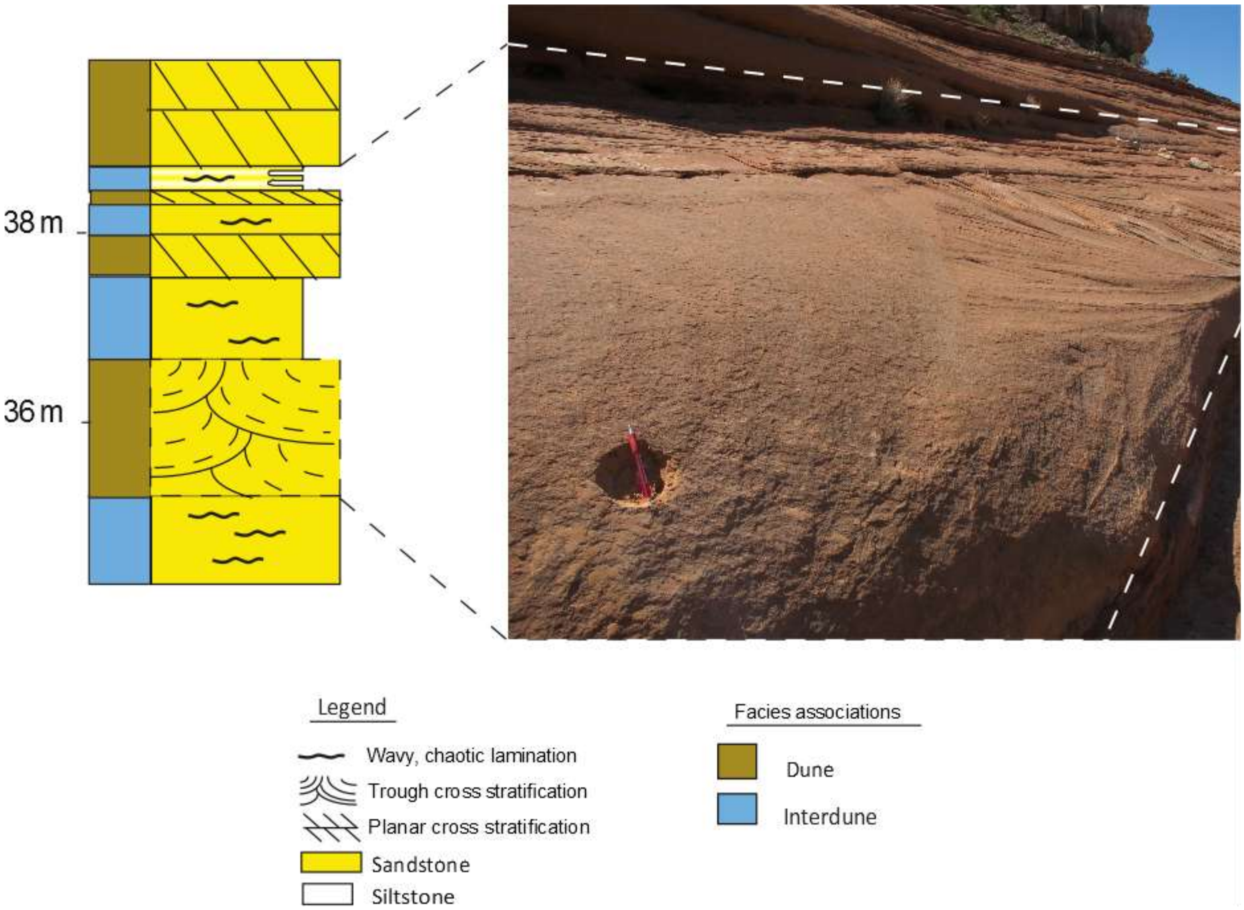

Figure 4.10: Characteristic facies associations (to the left) and example from outcrop (to the right, pen for scale) of the Slick Rock Member. Figure by Tunheim (2015).

The Moab Member is characterized by trough-cross stratified aeolian dune facies (up to ~5.5 m thick) alternating with smaller interdune facies (with wavy, chaotic lamination) (Figure 4.11). The Moab Member consists of ~98.9% sand and ~1.1% silt (Table 4-1). The overall thicknesses of bed units in the Moab Member range from ~0.5- to ~5.5 m; however most of the beds have a thickness of ~0.8- to ~2 m (25th to 75th percentiles, Figure 4.4). The average bed thicknesses of the Moab Member are thus considerably smaller than for other formations of aeolian origins (e.g. the Wingate- and Navajo sandstones).

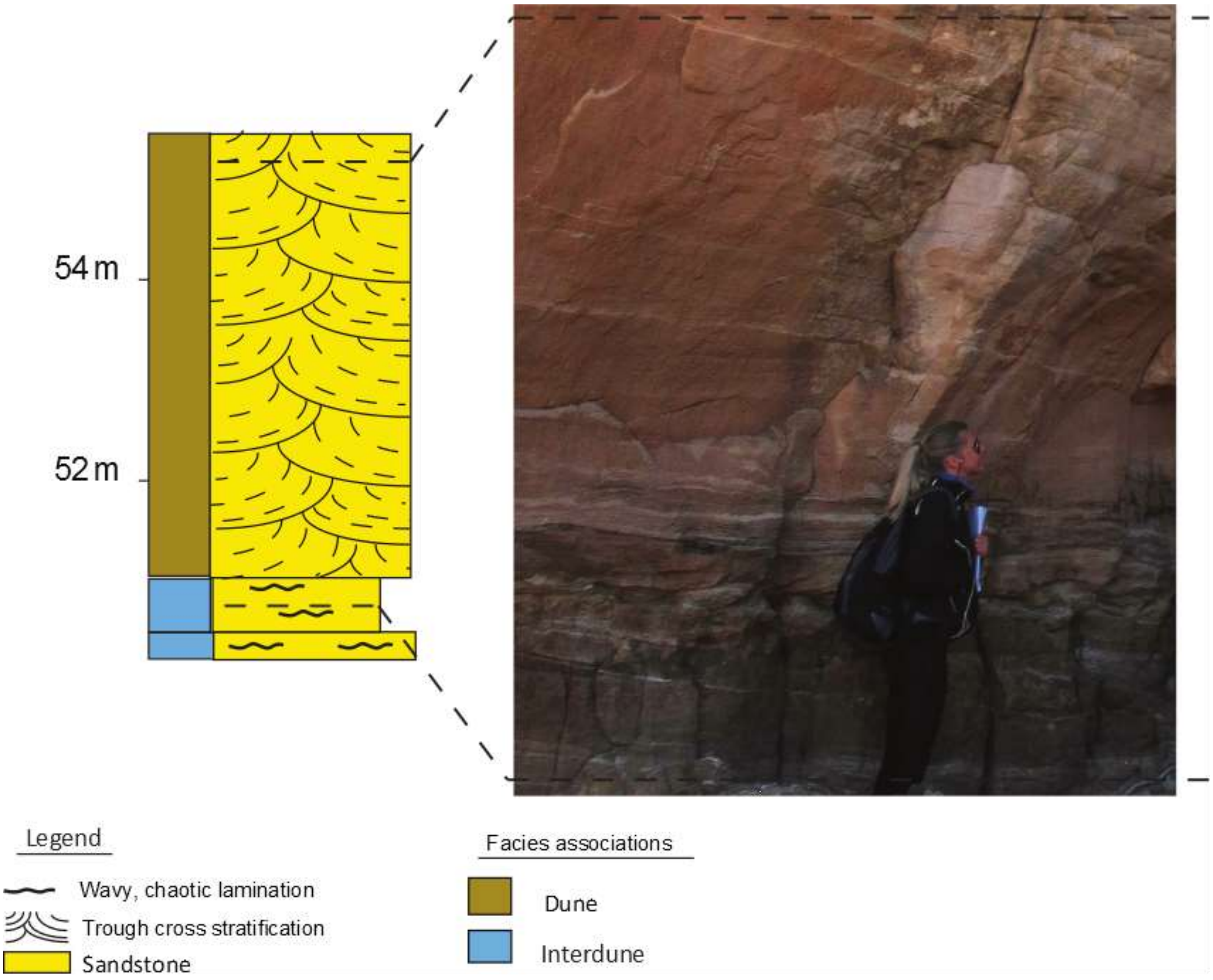

Figure 4.11: Characteristic facies associations (to the left) and example from outcrop (to the right) of the Moab Member. Figure by Tunheim (2015).

4.4 Sedimentological- and mineralogical properties

The sedimentological- and mineralogical properties of the formations have been explored mainly by Ragnhild J. Tunheim by sedimentological logging, looking at thin-sections made from rock samples collected during the field work and by performing point-counting studies. Original minerals present, secondary minerals (cementation and alterations) present, grain properties (grain size, sorting, roundness, shape, and grain contacts) and petroleum properties (porosity) have been studied by Ragnhild. In addition, I have studied the degree of cementation and the degree of pressure solution of the formations by looking at the thin sections. These two properties have been described qualitatively and have been categorized into: very low-, low-, intermediate-, high-, and very high degree. There were often large differences within samples collected from the same formation regarding the degree of cementation and pressure solution visible in thin sections and the description of these two parameters is thus highly generalized. Table 4-2 and Table 4-3 are generalized summaries and trends observed related to sedimentological properties based on the thin-section studies. Figure 4.12 - Figure 4.14 illustrate the degree of cementation and pressure solution observed in thin sections from each formation. Table 4-4 displays average values (in %) of different sedimentological properties for each formation based on point-counting studies and permeability values based on Tiny-Perm II measurements recorded during field work.

The proportion of quartz grains increase stratigraphically from the bottom (the Cutler Formation) to the top (the Moab Member), whereas the content of feldspar grains show the opposite trend. Regarding quartz cement, the most steeply-dipping formations (e.g. the Wingate Sandstone, the Kayenta Formation and the Moab Member) show a high content compared to the gently-sloping formations (e.g. the Cutler- and Chinle formations). The gently-sloping formations such as the Cutler- and Chinle formations generally have high proportions of carbonate cement. However, the steep-sloping formations such as the Wingate Sandstone and Kayenta Formation show relatively high proportions of carbonate cement as well.

There seems to be a strong relation between steep erosional slopes and high porosity values of the formations (e.g. the Moab Member and Wingate Sandstone with average porosities of 19- and 13%, respectively in contrast to the Cutler- and Chinle Formation with average porosities of 4- and 6%, respectively). Further, general trends for the steep-sloping formations based on Table 4-3 are that they are relatively better sorted and have more rounded grains than the gently-sloping formations.

Table 4-2: A generalized summary of the facies association and mineralogy of the formations included in this study. Based on thin section descriptions by Ragnhild J. Tunheim.

Unit	Facies association	Original minerals			Secondary minerals	
		Quartz	F-spar	Other minerals	Cement	Alteration
Moab	Aeolian (dune/ interdune)	Yes, dominating	Yes (plagioclase, microcline and orthoclase)	Lithic fragments, tourmaline, zircon	Quartz and iron oxide	Muscovite
Slick Rock	Aeolian (dune/ interdune)	Yes, dominating	Yes	Muscovite, carbonate, tourmalin, zircon	Quartz and carbonate	-
Navajo	Aeolian (dune/ interdune)	Yes, dominating	Yes (plagioclase)	Muscovite, carbonate, tourmalin, zircon	Dominantly carbonate (and some quartz)	Muscovite
Kayenta	Fluvial	Yes, dominating	Yes (microcline)	Muscovite, carbonate, tourmalin, zircon	Quartz and some carbonate	-
Wingate	Aeolian (dune/ interdune)	Yes, dominating	Yes, (plagioclase)	Muscovite, carbonate, tourmaline, zircon	Some quartz, iron oxide and carbonate	-
Chinle	Fluvial	Yes, dominating	Yes	Muscovite, biotite, carbonate, tourmaline, zircon	Carbonate and some quartz	Some biotite/ chlorite
Cutler	Fluvial/ aeolian	Yes	Yes (plagioclase)	Muscovite, biotite, carbonate, tourmaline	Carbonate and some iron oxide	Some muscovite

Table 4-3: A generalized summary of grain properties and petroleum properties of the formations included in this study. Based mainly on thin section descriptions by Ragnhild J. Tunheim.

Unit	Grain properties					Petroleum properties		
	Avg. Grain size (mm)	**Sorting**	**Roundness**	**Shape**	**Grain contact**	**Porosity**	**Degree of cementation**	**Degree of pressure solution**
Moab	0,18 (fine sand)	Well/ very well	Rounded/ well rounded	Rounded/ well rounded	Point contact/ concavo-convex	Very high	Low/ moderate	Low/ moderate
Slick Rock	0,12 (very fine sand)	Moderate	Subrounded/ rounded	Subrounded/ rounded	Point contact/ concavo-convex	Moderate	Moderate/ high	Moderate
Navajo	0,14 (fine sand)	Moderate/ well	Rounded	Rounded	Point contact/ concavo-convex	High	Moderate	High
Kayenta	0,11 (very fine sand)	Moderate/ well	Subrounded/ rounded	Subrounded/ rounded	Concavo-convex/ sutured contact	Moderate	Moderate/ high	Moderate/ high
Wingate	0,10 (very fine sand)	Moderate/ well	Rounded/ well rounded	Rounded/ well rounded	Concavo-convex/ sutured contact	High	High	Moderate
Chinle	0,08 (very fine sand)	Moderate/ well	Subrounded/ rounded	Subrounded/ rounded	Point contact/ concavo-convex	Very low/ low	High	Moderate
Cutler	0,17 (fine sand)	Poor/ moderate	Subrounded/ subangular	Subrounded/ subangular	Point contact/ sutured contact	Very low	Moderate	Low

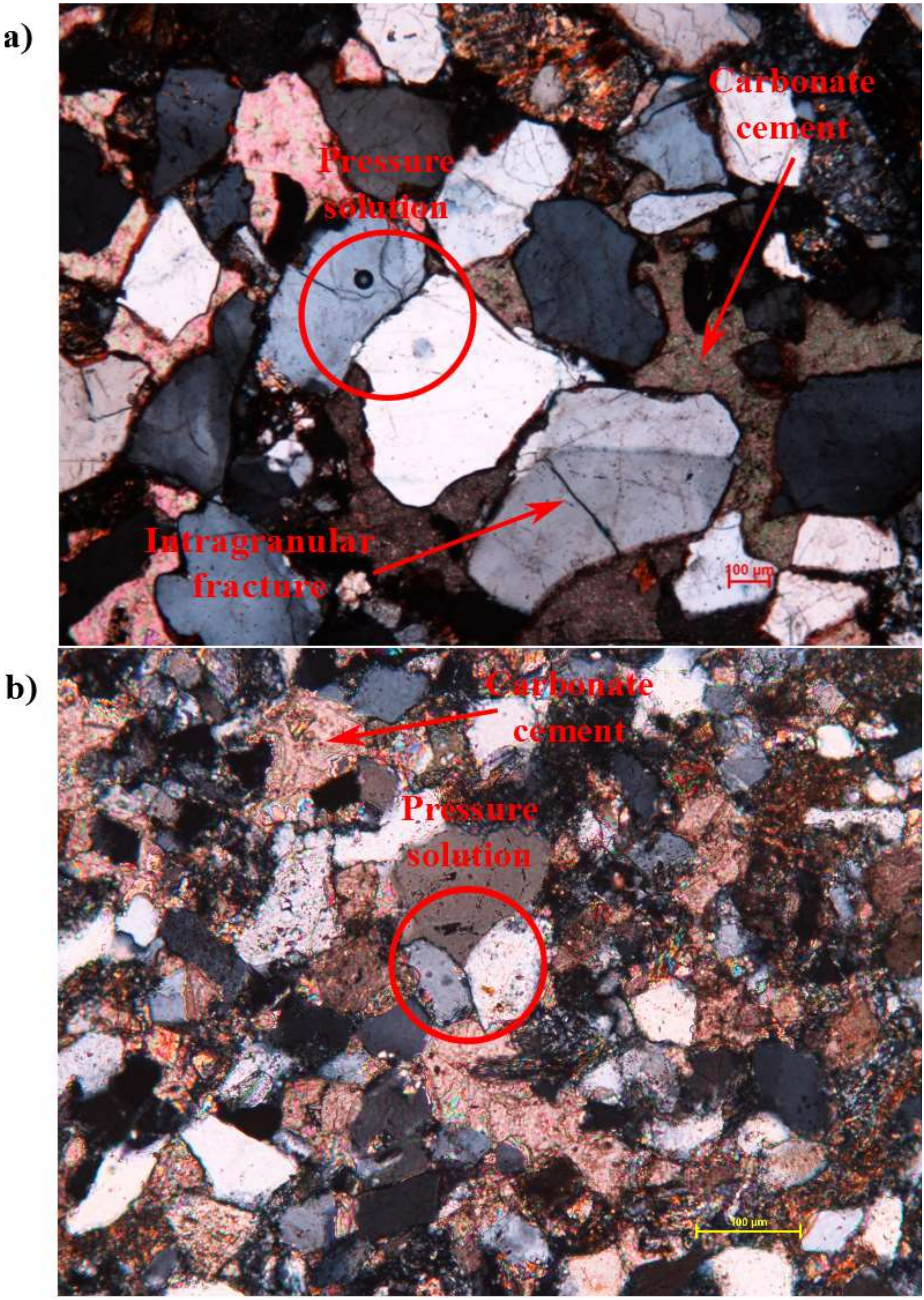

Figure 4.12: Images illustrating the degree of cementation and pressure solution from a thin sections of a) the Cutler Formation and b) of the Chinle Formation (under crossed polars).

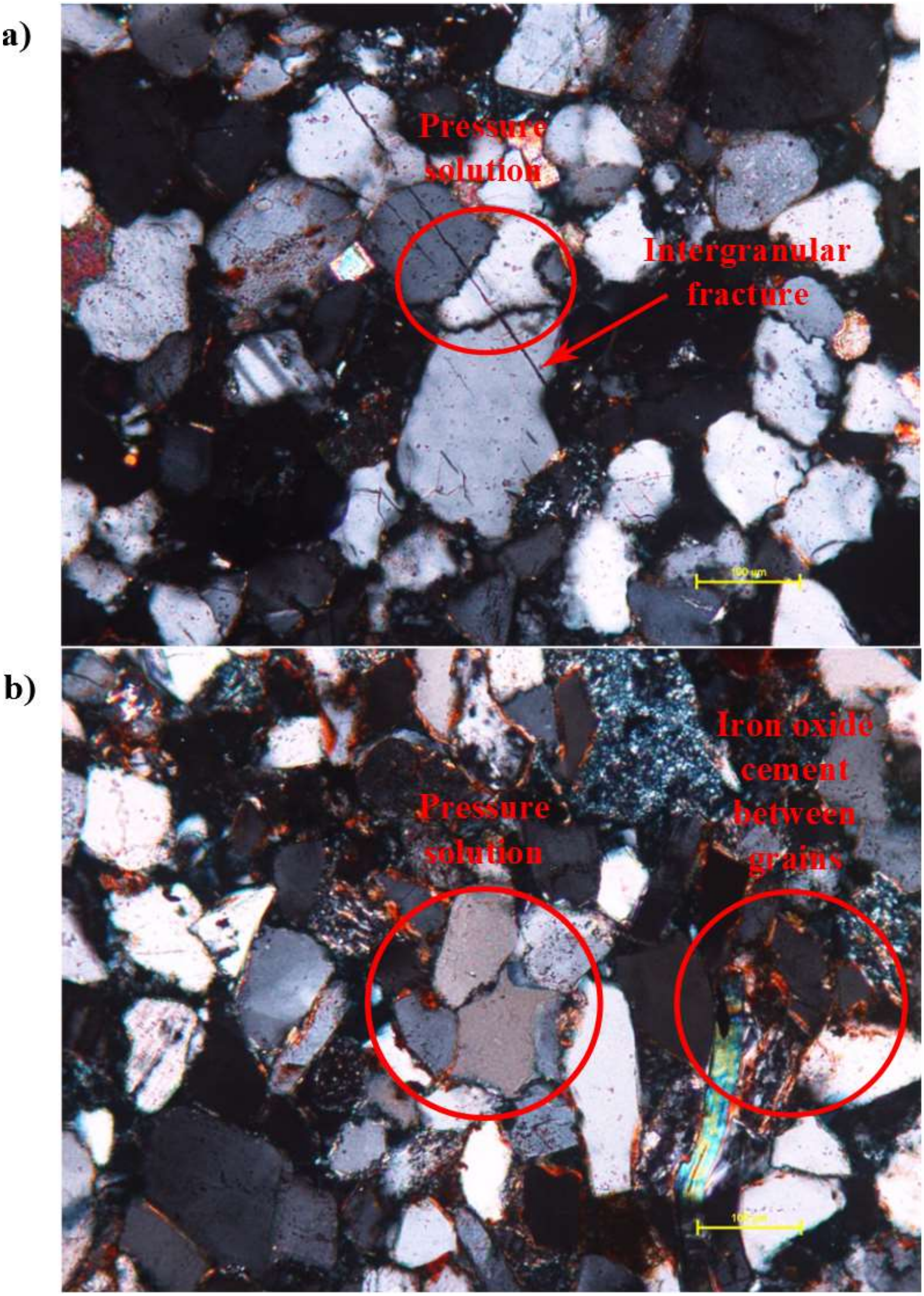

Figure 4.13: Images illustrating the degree of cementation and pressure solution from a thin sections of a) the Wingate Sandstone and b) of the Kayenta Formation (under crossed polars).

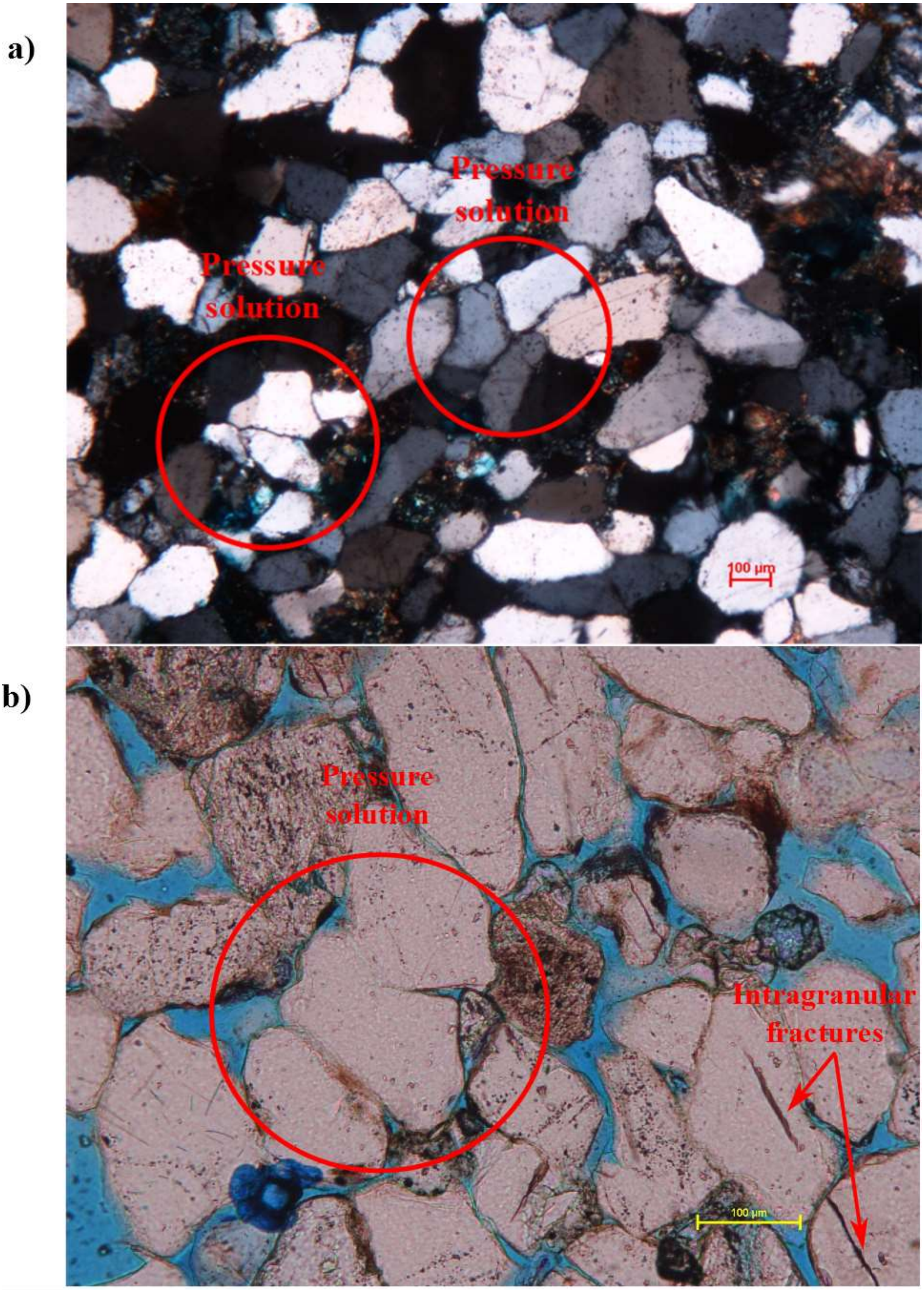

Figure 4.14: Images illustrating the degree of cementation and pressure solution from a thin sections of a) the Navajo Sandstone and b) of the Slick Rock Member (under crossed polars).

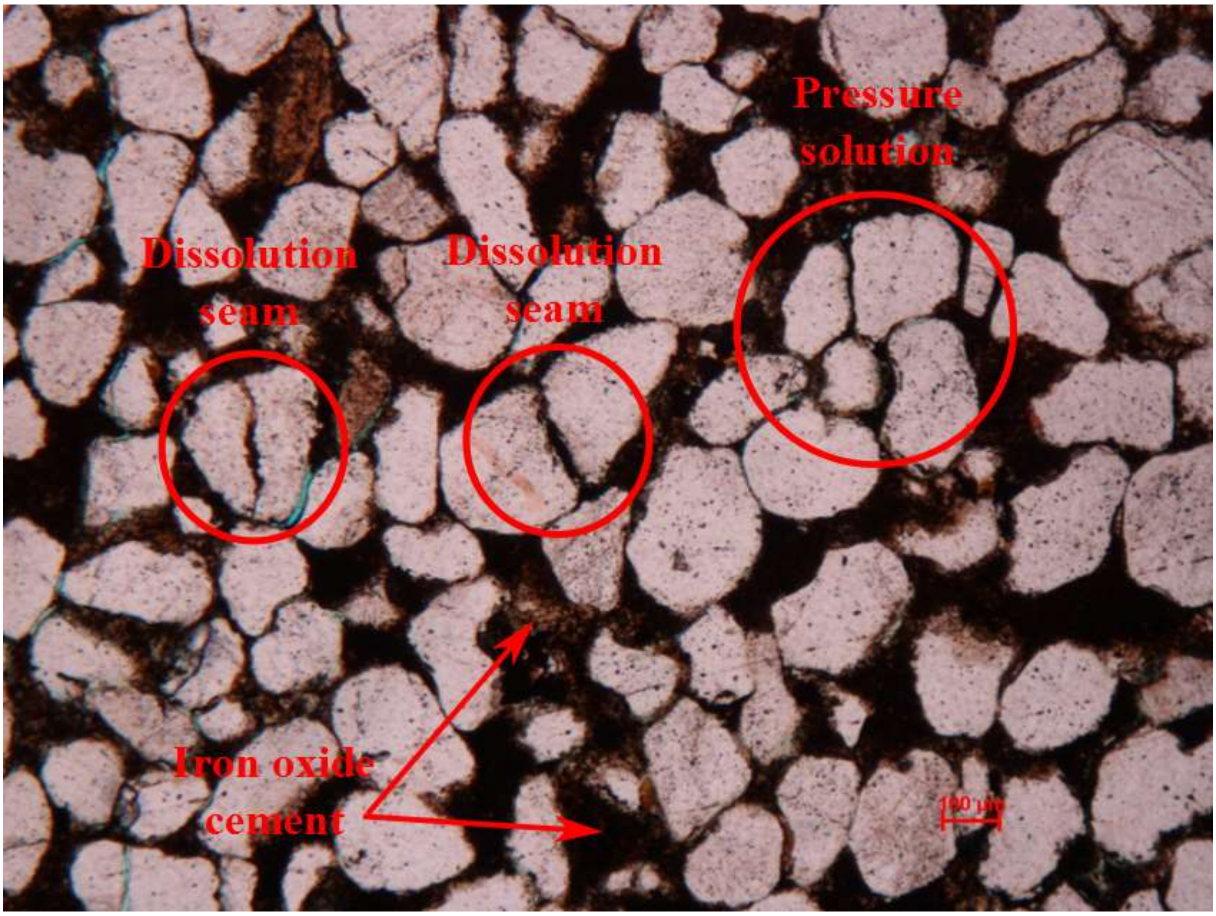

Figure 4.15: Image illustrating the degree of cementation and pressure solution from a thin section of the Moab Member.

Table 4-4: Average values (in %) of different sedimentological properties for each formation. Based on point-counting studies of thin-sections by Ragnhild J. Tunheim. Permeability values are based on TinyPerm II values collected during field work.

Unit	Quartz (%)	Feldspar (%)	Muscovite (%)	Oxide (%)	Carbonate (%)	Biotite (%)	Quartz cement (%)	Carb. cement (%)	Porosity (%)	Permeability (mD)
Moab	69	0	0	4	0	0	5	1	19	3177
Slick Rock	67	1	0	5	2	0	3	10	11	796
Navajo	67	1	0	2	0	0	5	11	13	2058
Kayenta	66	3	0	6	1	0	3	9	9	326
Wingate	64	1	0	4	1	0	4	11	13	1087
Chinle	58	1	1	6	4	0	1	18	6	209
Cutler	52	4	1	12	2	3	0	16	4	198

4.5 Mechanical properties

4.5.1 Permeability

Permeability measurements have been achieved by using a Tiny-Perm II equipment. A complete list of Tiny-Perm II (TP) measurements and the calculated permeability K (mD) for all the formations can be found in Appendix B (Table 8-2 – Table 8-8). The permeability has been measured at a different number of localities for each formation as a result of limited accessibility of proper outcrops for some of the formations and because the aeolian formations had a higher priority than the fluvial formations (18 for the Cutler Formation, 20 for the Chinle Formation, 39 for the Wingate Sandstone, 40 for the Kayenta Formation, 41 for the Navajo Sandstone, 54 for the Slick Rock Member and 35 for the Moab Member). Figure 4.16 is a boxplot illustrating the range, median and 25th to 75th percentile of the calculated permeability values for each formation.

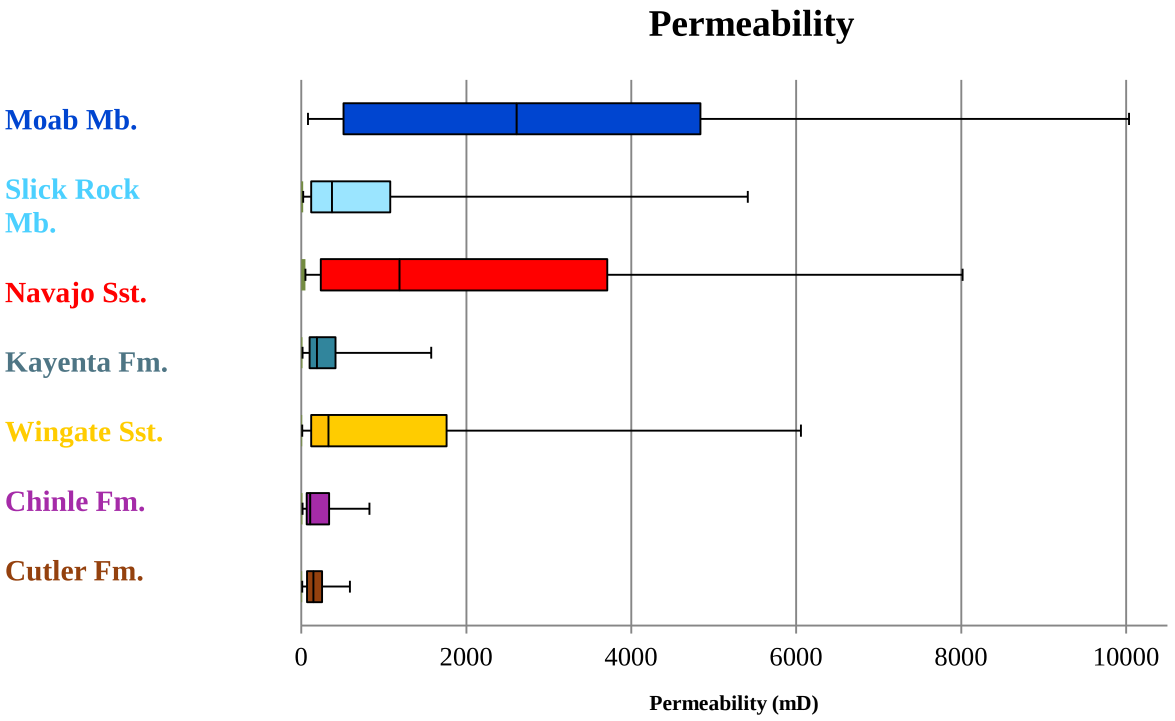

Figure 4.16: Boxplot of the permeability measurements (in mD) (25th to 75th percentile boxplot).

The permeability measurements for the Cutler Formation range from ~0.001- to ~0.6 D (with a mean value of ~0.2 D), for the Chinle Formation from ~0.001- to ~0.8 D (with a mean value of ~0.2 D), for the Wingate Sandstone from ~0.008- to ~6 D (with a mean value of ~1.1 D), for the Kayenta Formation from ~0.01- to ~1.6 D (with a mean values of ~0.3 D), for the Navajo Sandstone from ~0.05- to ~8 D (with a mean value of ~2 D), the Slick Rock Member from ~0.02- to ~5.4 D (with a mean value of ~0.8 D) and for the Moab Member from ~0.08- to ~10 D (with a mean value of ~3.2 D) (Appendix B, Table 8-2 – Table 8-8).

Gently-sloping formations such as the Cutler- and Chinle formations have alternating intervals of slopes and small ledges and it is worth noting that it was only possible to carry out the permeability measurements on the surface of these ledges. The overall result of the permeability values is thus likely misleading to some extent, considering that only the steep/stiff parts of the overall gently-sloping formations could be measured (measured values are likely above average for the entire units).

Formations of aeolian origins such as the Wingate- and Navajo sandstones and the Moab Member show considerably higher permeability values with a much wider range (with a mean value of ~1-, ~2 and ~3.2 D, respectively) than the formations of mixed-fluvial origin (e.g. the Cutler-, Chinle and Kayenta formations, the Cutler- and Chinle formations with a mean value of ~0.2 D and the Kayenta Formation with a mean value of ~0.3 D) (Appendix B, Table 8-2 – Table 8-8).

In general, the recorded permeability values are high for the formations of aeolian origins and low for the formations of mixed-fluvial origins. The Slick Rock Member however, displays considerably lower permeability values than the other sandstone formations, with the bulk of the permeability values ranging from ~0.1- to ~1.1 D (25th to 75th percentiles, Figure 4.16).

4.5.2 Young’s Modulus

Young’s Modulus measurements (σ/ε, a measure of the stiffness/elasticity of a formation) have been achieved by using a Schmidt Hammer equipment (high Young’s Modulus values correspond to stiff formations). A complete list of hammer rebound (HR) measurements and the calculated Young’s Modulus value (GPa) for all the formations can be found in Appendix B (Table 8-2 – Table 8-8). The Young’s Modulus has been measured at a different number of localities for each formation as a result of limited accessibility of proper outcrops for some of the formations and because the aeolian formations had a higher priority than the fluvial formations (18 for the Cutler Formation, 20 for the Chinle Formation, 39 for the Wingate Sandstone, 40 for the Kayenta Formation, 41 for the Navajo Sandstone, 54 for the Slick Rock Member and 35 for the Moab Member). Figure 4.17 is a boxplot illustrating the range, median and 25th to 75th percentile of the calculated Young’s Modulus values for each formation.

The Young’s Modulus measurements for the Cutler Formation range from ~0.5- to ~15.5 GPa (with a mean value of ~5.7 GPa), for the Chinle Formation from ~1.6- to ~27.6 GPa (with a mean value of ~13 GPa), for the Wingate Sandstone from ~1.8- to ~24 GPa (with a mean value of ~13.3 GPa), for the Kayenta Formation from ~1.9- to ~26.5 GPa (with a mean value of ~10.7 GPa), for the Navajo Sandstone from ~1.7- to ~22.1 GPa (with a mean value of ~9.4 GPa), for the Slick Rock Member from ~1.5- to ~18.7 GPa (with a mean value of ~5.3 GPa) and for the Moab Member from ~1.4- to ~24 GPa (with a mean value of ~9 GPa) (Appendix B, Table 8-2 – Table 8-8).

Formations such as the Moab Member, the Kayenta Formation and the Wingate Sandstone all show significantly high Young’s Modulus values (with a mean value of ~9, ~11 and ~13 GPa, respectively) (Appendix B, Table 8-4 – Table 8-8). In contrast to the relatively high Young’s Modulus values recorded for the formations in general, the overall measurements of the Slick Rock Member are considerably lower (with a mean value of ~5.3 GPa).

Gently-sloping formations such as the Cutler- and Chinle formations have alternating intervals of slopes and small ledges and it is worth noting that it was only possible to carry out the Young’s Modulus measurements on the surface of these ledges (Figure 5.1). Considering that the result of the measurements of the Cutler- and Chinle formations are based on only the steep/stiff intervals they are thus probably not representative for these formations. Overall Young’s Modulus values would most likely be considerably lower than those displayed in Figure 4.17.

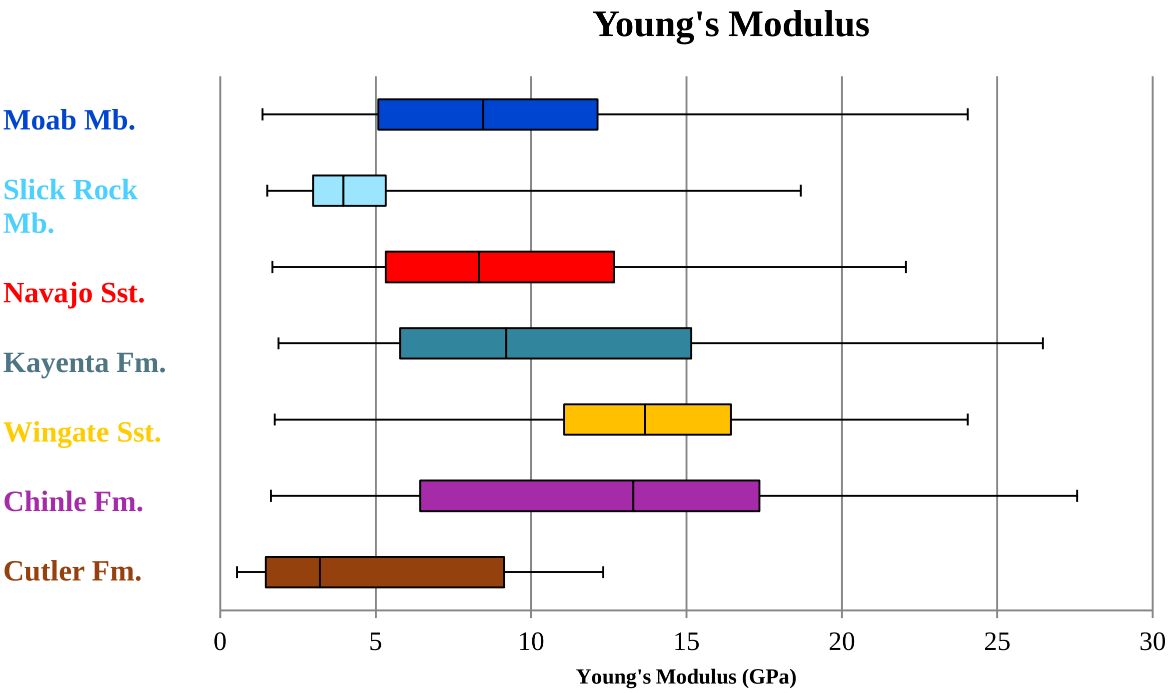

Figure 4.17: Boxplot of the measured Young's Modulus measurements (in GPa) (25th to 75th percentile boxplot).

4.5.3 Permeability versus Young's Modulus

Figure 4.18 is a comparison of the permeability measurements (to the left) and the Young's Modulus values (to the right) of each formation. The permeability- and Young's Modulus were measured at a different number of locations for each formation (18 for the Cutler Formation, 20 for the Chinle Formation, 39 for the Wingate Sandstone, 40 for the Kayenta Formation, 41 for the Navajo Sandstone, 54 for the Slick Rock Member and 35 for the Moab Member). The measured values are illustrated in scatter plots for each formation (Figure 4.19 - Figure 4.21).

Generally, the permeability values have a narrower range (are more consistent) than the Young's Modulus values for all the formations (Figure 4.18). There seems to be a strong correlation between high permeability values and high Young's Modulus values for formations of aeolian origin such as the Wingate Sandstone, the Navajo Sandstone and the Moab Member. In contrast, the overall fluvial Kayenta Formation display low permeability values combined with high Young's Modulus values.

Although the Slick Rock Member displays large lateral differences regarding erosional slopes (Figure 4.3), the permeability and Young's Modulus values are relatively consistent with generally low permeability- and Young's Modulus values. As previously mentioned, the measurements of the Cutler- and Chinle formations were carried out in the steep ledge-intervals of the overall gently sloping formations and such data are likely not representable for the formations as a whole (measured values are likely above average for the entire units).

The scatter plots for the formations of aeolian origins (the Wingate Sandstone, the Navajo Sandstone and the Moab Member, Figure 4.19 c), Figure 4.20 b) and Figure 4.21 b), respectively)) show similar trends, such as a wide scatter of both the permeability- and Young's Modulus measurements. In contrast, the Cutler-, Chinle- and Kayenta formations of fluvial origin show less scatter of the data with generally low permeability values and high Young's Modulus values (Figure 4.19 a) and b) and Figure 4.20 a)).

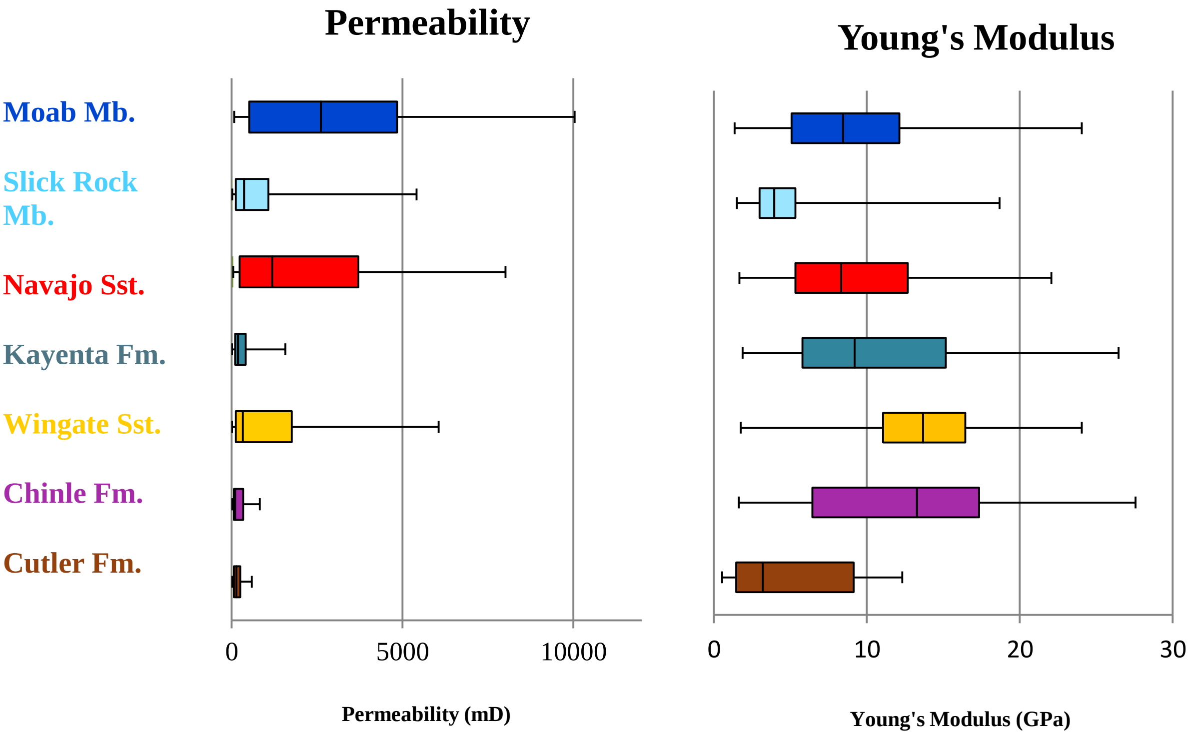

Figure 4.18: Boxplots of the permeability measurements (to the left) and Young's Modulus measurement (to the right) (25th to 75th percentile boxplots).

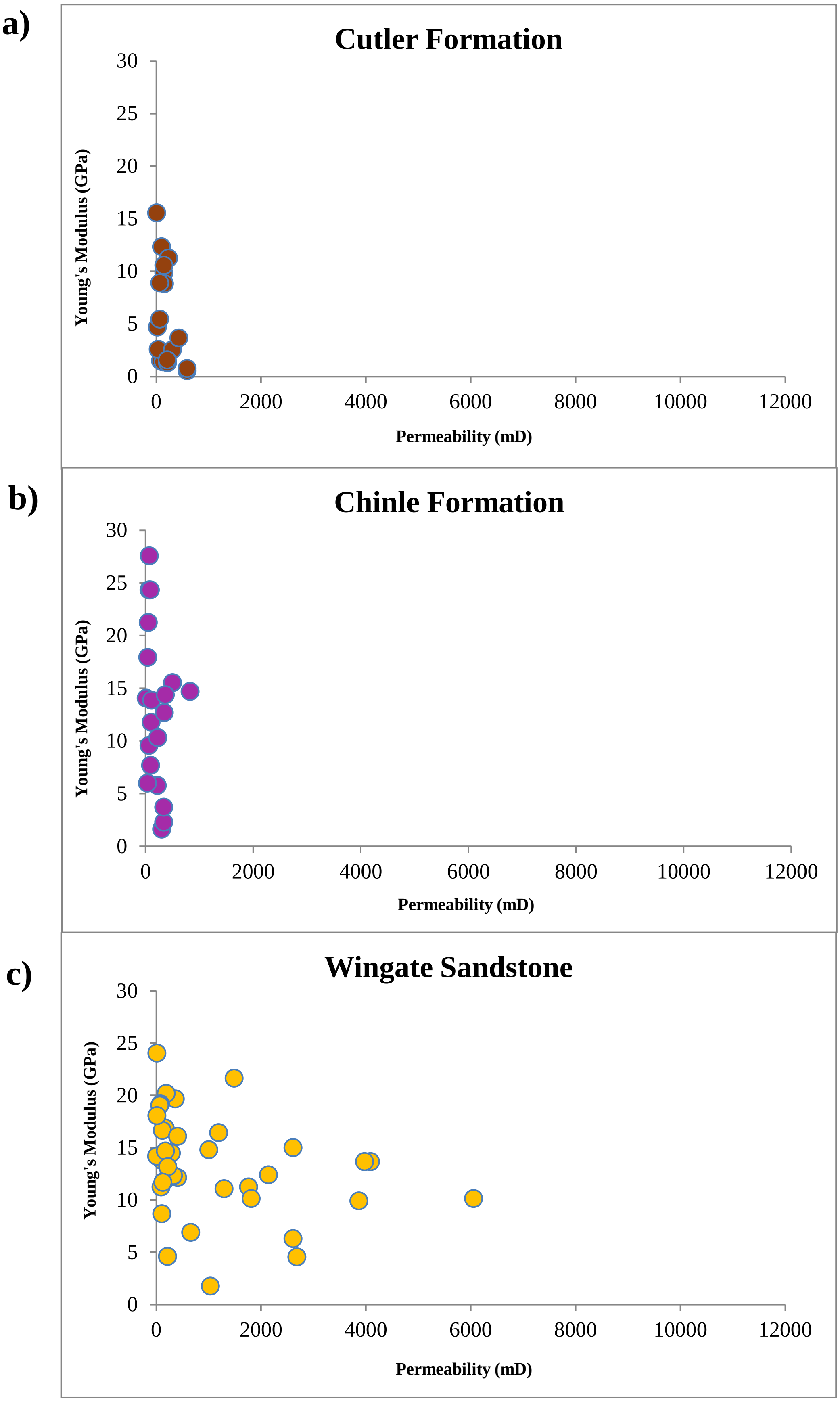

Figure 4.19: Scatter plot illustrating measured permeability- (x axis) and Young's Modulus (y axis) values at each location for a) the Cutler Fm., b) the Chinle Fm. and c) the Wingate Sst.

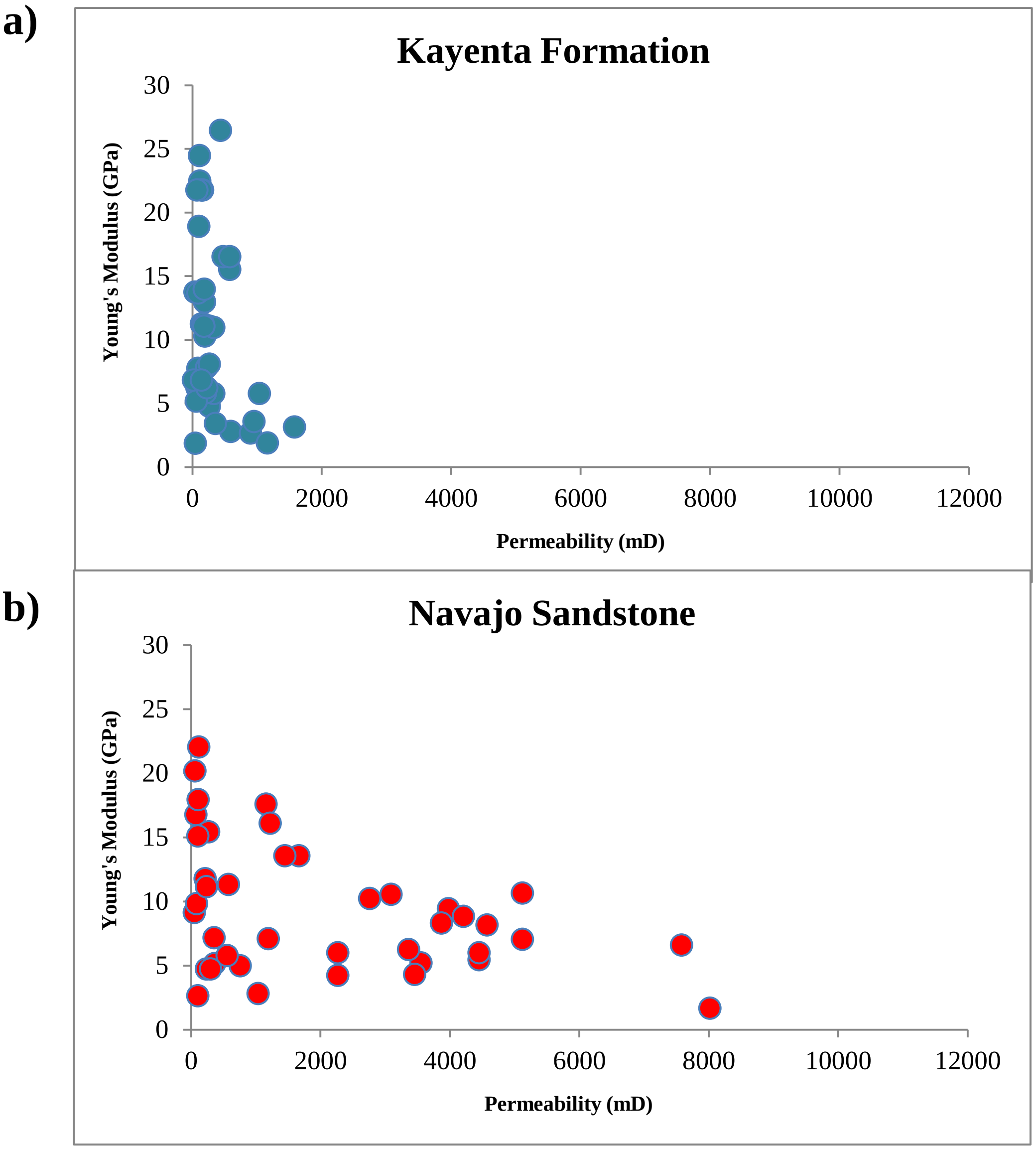

Figure 4.20: Scatter plot illustrating measured permeability- (x axis) and Young's Modulus (y axis) values at each location for a) the Kayenta Fm. and b) the Navajo Sst.

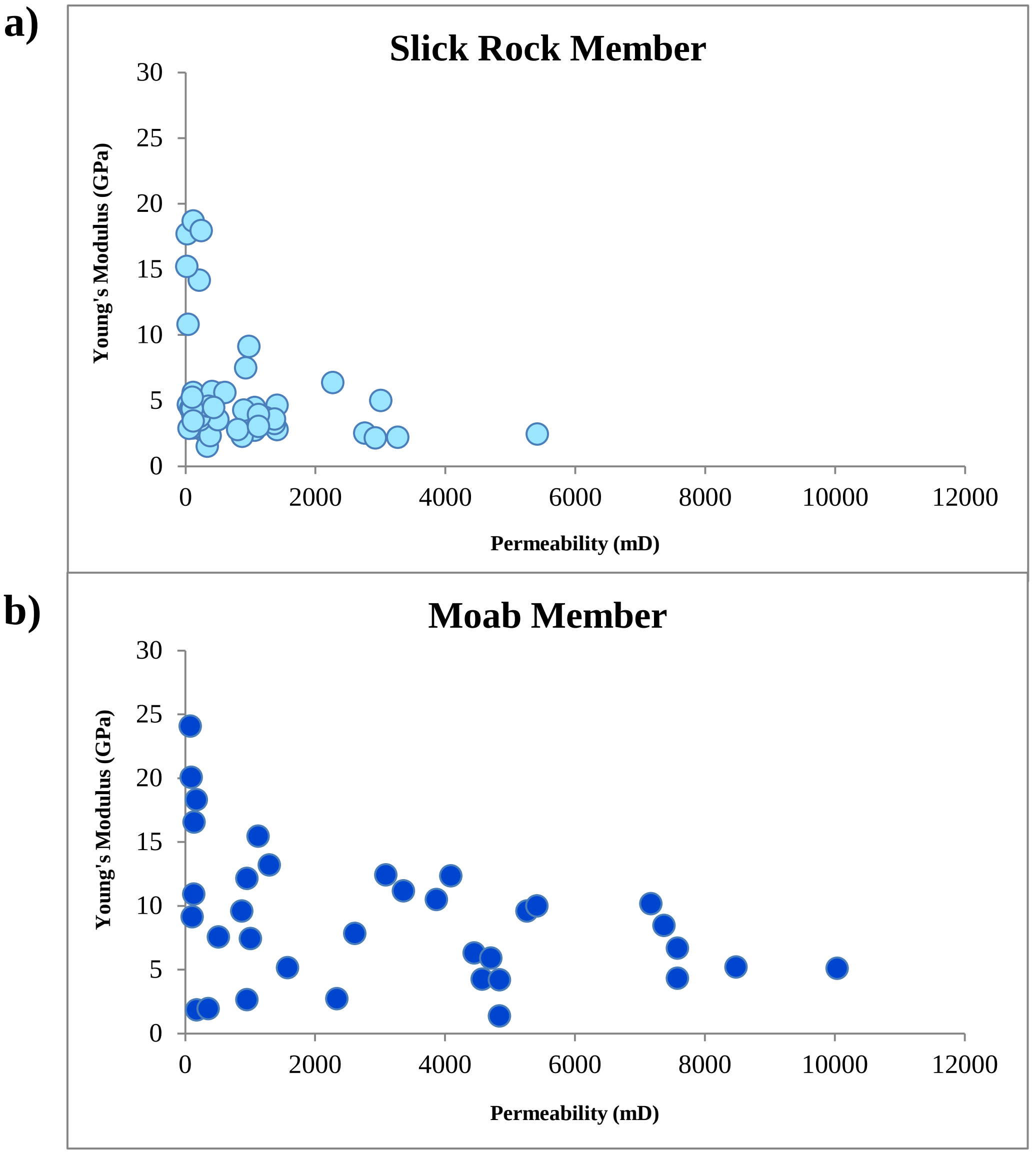

Figure 4.21: Scatter plot illustrating measured permeability- (x axis) and Young's Modulus (y axis) values at each location for a) the Slick Rock Mb. and b) the Moab Mb.

4.6 Erosional slope versus mechanical properties

Figure 4.22 is a comparison of the erosional slopes (to the left) versus the permeability measurements (to the right) of each formation. Figure 4.23 is a comparison of the erosional slopes (to the left) versus the Young's Modulus measurements (to the right) of each formation.

Steeply-dipping formations of aeolian origins such as the Wingate Sandstone, the Navajo Sandstone and the Moab Member show considerably higher permeability values with a much wider range (with a mean value of ~1-, ~2- and ~3.2 D, respectively) than the gently-sloping formations such as the Cutler- and Chinle formations (both with a mean value of ~0.2 D, however, these values are likely above average for the entire units) (Appendix B, Table 8-2 – Table 8-8). In contrast, the also steeply-dipping Kayenta Formation of fluvial origin displays low permeability values.

Regarding the Young's Modulus values, the steep-sloping formations such as the Moab Member, the Kayenta Formation and the Wingate Sandstone all show high Young's Modulus values (with a mean value of ~9, ~11 and ~13 GPa, respectively) (Appendix B, Table 8-4 – Table 8-8). The Slick Rock Member displays large lateral differences in erosional slopes and generally consistently low Young's Modulus values.

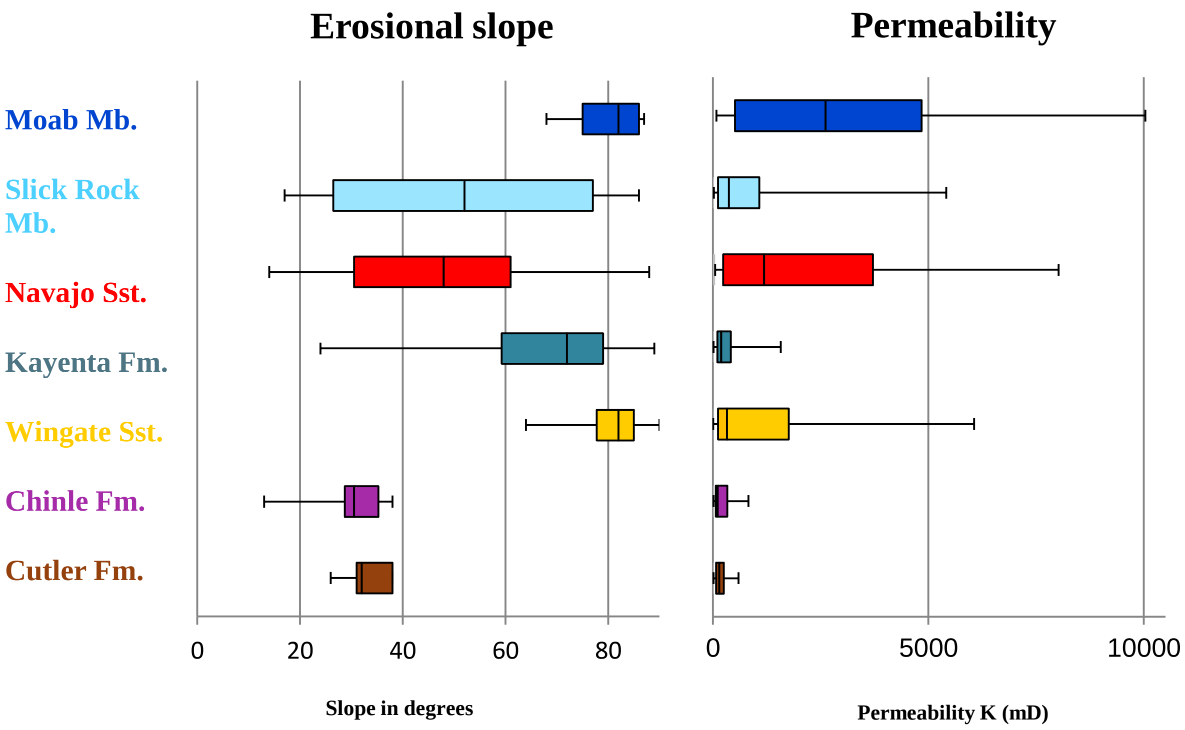

Figure 4.22: Boxplots of the measured erosional slopes of each formation (to the left) and permeability measurement (to the right) (25th to 75th percentile boxplots).

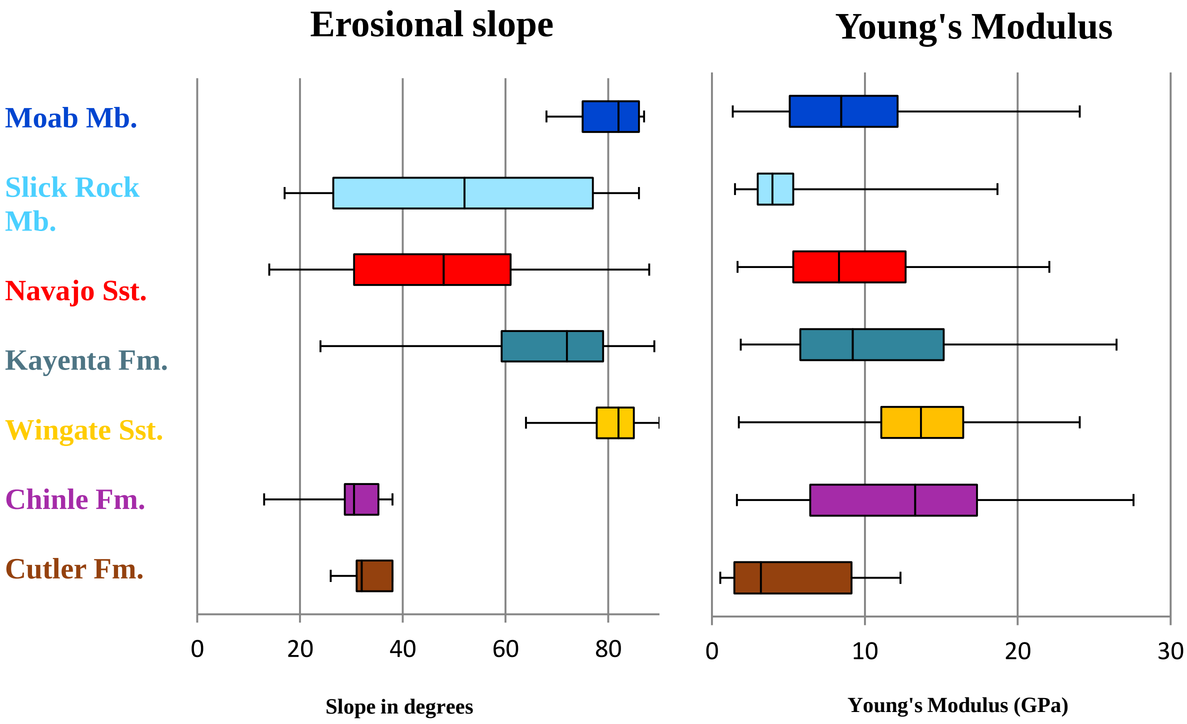

Figure 4.23: Boxplots of the measured erosional slopes of each formation (to the left) and Young's Modulus measurement (to the right) (25th to 75th percentile boxplots).

4.7 Lateral differences within the Slick Rock Member

While most of the formations show roughly the same characteristic slope throughout the study area, the Slick Rock Member looks quite different at three different locations; at Courthouse, Bartlett Wash and Hidden Canyon. Figure 4.24 illustrate the locations and the approximate aerial distance between them. There is about 6 kilometers aerial distance between Courthouse and Hidden Canyon.

Figure 4.24: Aerial photo illustrating the locations of Hidden Canyon-, Bartlett Wash- and Courthouse localities and the approximate aerial distance between them (image from Google Earth).

In Courthouse, Slick Rock is nearly vertical, whereas in Bartlett Wash and Hidden Canyon the Slick Rock Member shows much more gentle erosional slopes (Figure 4.25). Table 4-5 displays sedimentological properties (in %) and mechanical properties (permeability and Young's Modulus) at each location. The sedimentological properties are based on point-counting studies of thin sections from rock samples of dunes in Slick Rock. The mechanical properties are based on measurements achieved during field work.

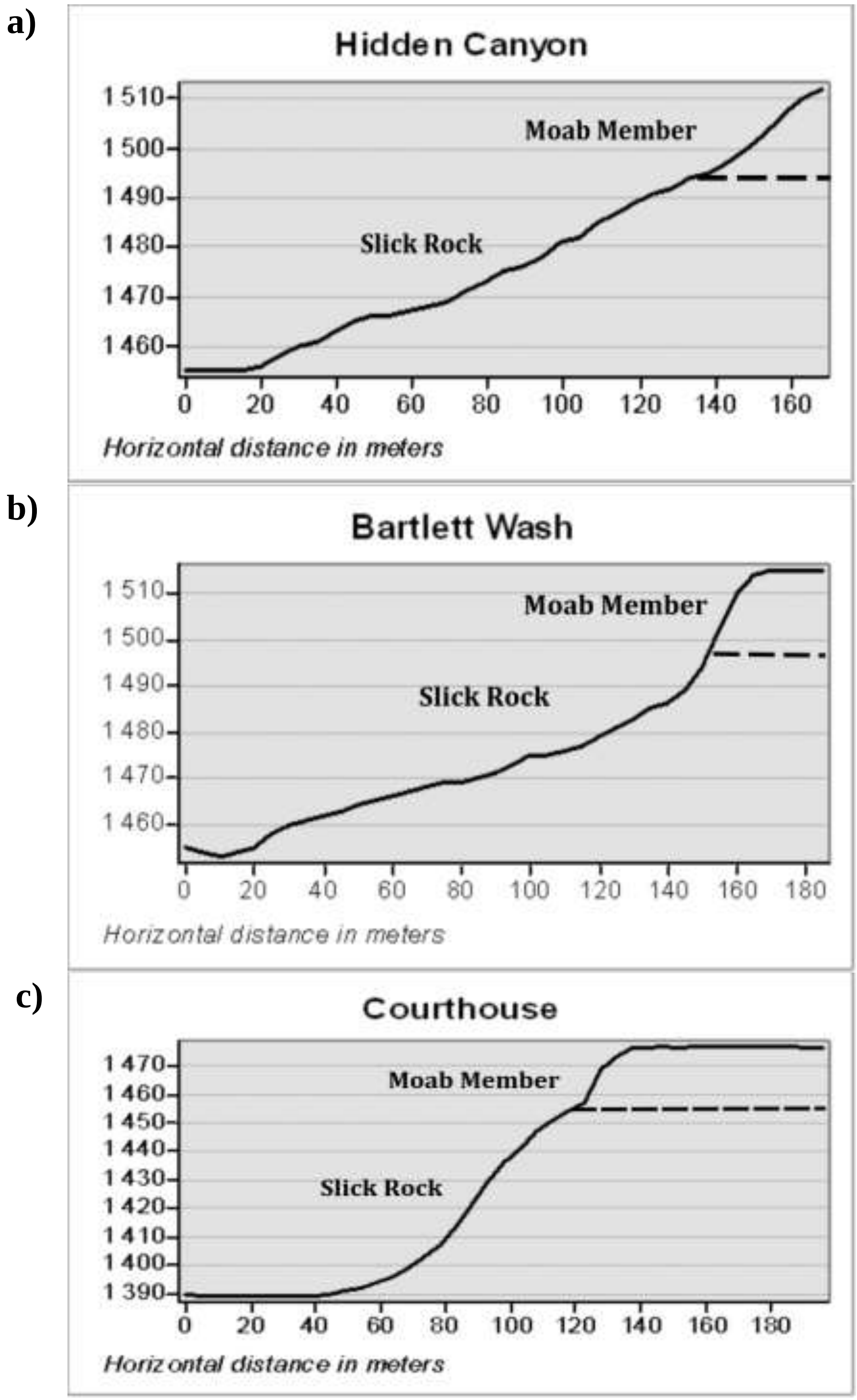

Figure 4.25: Slope profiles illustrating the differences in erosional slopes of the Slick Rock Member at three different localities; in a) at Hidden Canyon (UTM: 12S 603989 4286118), b) at Bartlett Wash (UTM: 12S 605643 4285271) and c) at Courthouse (UTM: 12S 610101 4285245). The profiles have been made based on a DEM created in ArcGIS software.

Table 4-5: Sedimentological properties (in %) and mechanical properties (permeability and Young's Modulus) at each location. The sedimentological properties are based on point-counting studies of thin sections from rock samples of dunes in Slick Rock (7-CH 1: from Courthouse, 23-BW from Bartlett Wash and 27-HIC 1 from Hidden Canyon) by Ragnhild J. Tunheim. The mechanical properties are mean values from each location based on measurements achieved during field work.

Thin section no.	Quartz (%)	Feldspar (%)	Carbonate (%)	Rock fragments (%)	Quartz cement (%)	Carbonate cement (%)	Porosity (%)	Permeability K (mD)	Young's Modulus (GPa)
7 – CH 1	76	1	1	4	0	13	4	787	9
23 - BW	75	0	2	0	3	1	16	739	5
27 - HIC 1	72	1	3	0	2	3	19	614	3

The proportion of quartz cement is generally low at each location whereas at the cliff-forming Courthouse locality, the proportion of carbonate cement is considerably higher (13%, in contrast to 1% and 3% in Bartlett Wash and Hidden Canyon, respectively). Other observations based on this table is that the porosity is remarkably lower (4%, in contrast to 16% and 19% in Bartlett Wash and Hidden Canyon, respectively) and the Young's Modulus values are higher (9 GPa, in contrast to 5 GPa and 3 GPa in Bartlett Wash and Hidden Canyon, respectively) at the Courthouse locality. In contrast, the average permeability values do not differ much at the different localities.

Figure 4.26 display thin section images from dunes at each locality, illustrating different degrees of porosity. Figure 4.26 a) illustrates a relatively low porosity at the Courthouse location, Figure 4.26 b) illustrates a moderate porosity at the Bartlett Wash location whereas a relatively high porosity at the Hidden Canyon location is displayed in Figure 4.26 c).

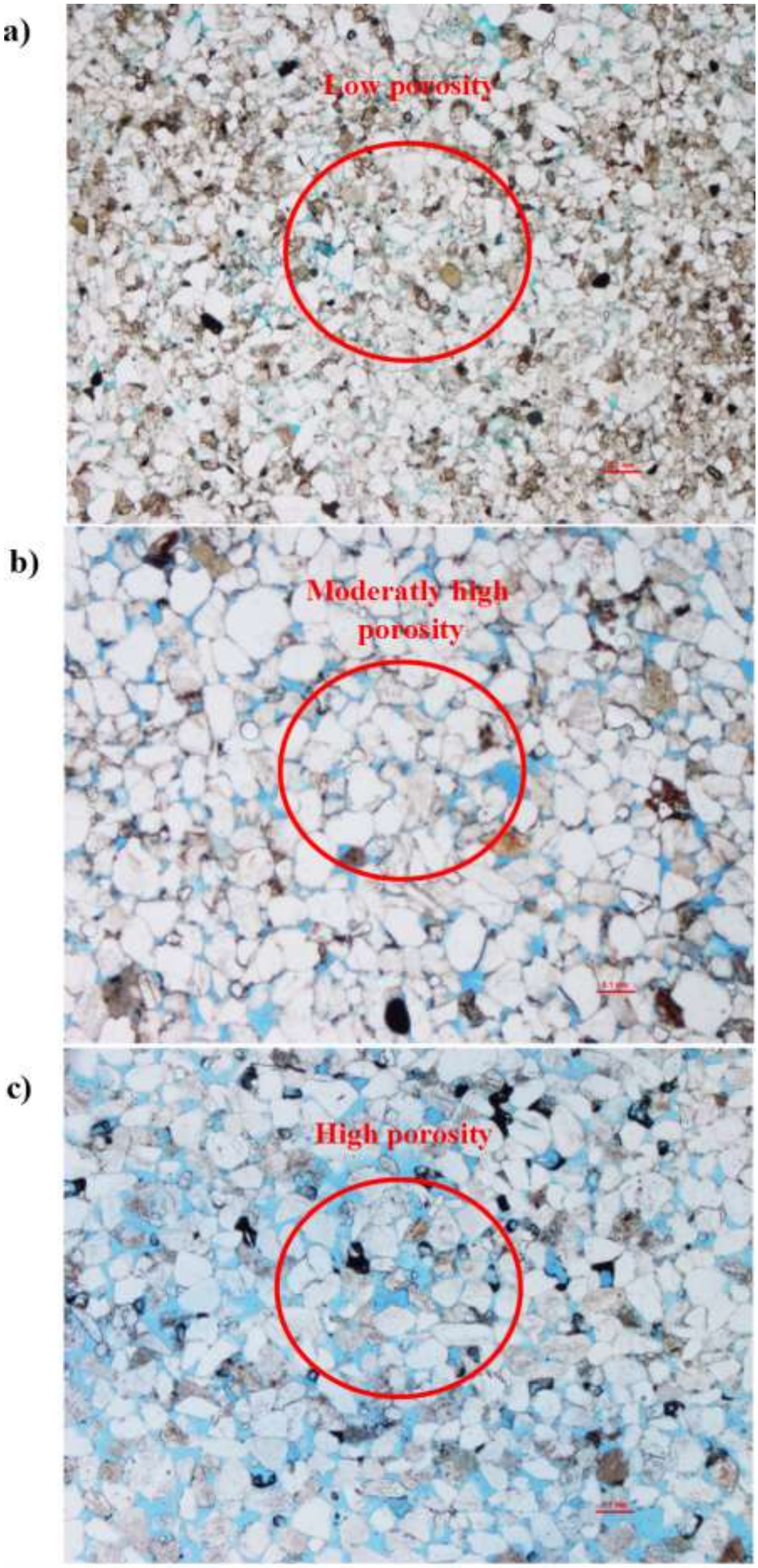

Figure 4.26: Thin section images from dunes in Slick Rock in a) at the Courthouse locality (sample no.: 7-CH 1), in b) at the Bartlett Wash locality (sample no.: 23-BW) and in c) at the Hidden Canyon locality (sample no.: 27-HIC 1). The blue-colored space between the grains highlights the porosity. Images by Ragnhild J. Tunheim.

Figure 4.27 is a comparison of the mechanical properties of the dunes and interdunes at each location. The overall permeability measurements (of dunes and interdunes combined) at the Courthouse locality range from ~0.02- to ~2.8 D (with a mean value of ~0.8 D), at the Bartlett Wash locality from ~0.02- to ~3.3 D (with a mean value of ~0.7 D) and at the Hidden Canyon locality from ~0.08- to ~2.9 D (with a mean value of ~0.6 D) (Appendix C, Table 8-9 – Table 8-11). The overall Young's Modulus measurements (of dunes and interdunes combined) at the Courthouse locality range from ~1.5- to ~18.7 GPa (with a mean value of ~8.7 GPa), at the Bartlett Wash locality from ~2.2- to ~15.2 GPa (with a mean value of ~4.6 GPa) and at the Hidden Canyon locality from ~2.2- to ~4.4 GPa (with a mean value of ~3.2 GPa) (Appendix C, Table 8-9 – Table 8-11).

Generally, the permeability values are higher- and the Young's Modulus values are lower for the dunes compared to the interdunes. The measured permeability values for the dunes and interdunes do not differ considerably between each location (however, the permeability measurements for the dunes at the Bartlett Wash location are generally slightly lower than at the two other locations). In contrast, there are great differences regarding the measured Young's Modulus values. In the steep-sloping Courthouse locality, the values are remarkably higher (both for the dunes and interdunes) than in the more gently-sloping Bartlett Wash and Hidden Canyon localities. On the other hand, the differences in Young's Modulus values between the Bartlett Wash and Hidden Canyon localities are not that great (the values are generally slightly higher for both the dunes and interdunes at the Bartlett Wash locality).

It is worth noting that only one rock sample suited for making a thin section was collected at the Courthouse locality during the field work. Some of the sedimentological- and mineralogical properties recorded for the Courthouse location are thus based on this one rock sample and thereby some degree of uncertainty is related to the data. Further, this rock sample was collected near the boundary between the Slick Rock Member and the underlying Dewey Bridge Member. There is some uncertainty related to whether the sample represents the uppermost part of the Dewey Bridge Member or the lowermost part of the Slick Rock Member.

In addition to the large lateral differences in erosional slopes, the erosional character of the Slick Rock Member stands out from the other formations in two ways; 1) the joints form in the fine-grained interdunes to a higher degree than in the coarse-grained dunes and 2) the

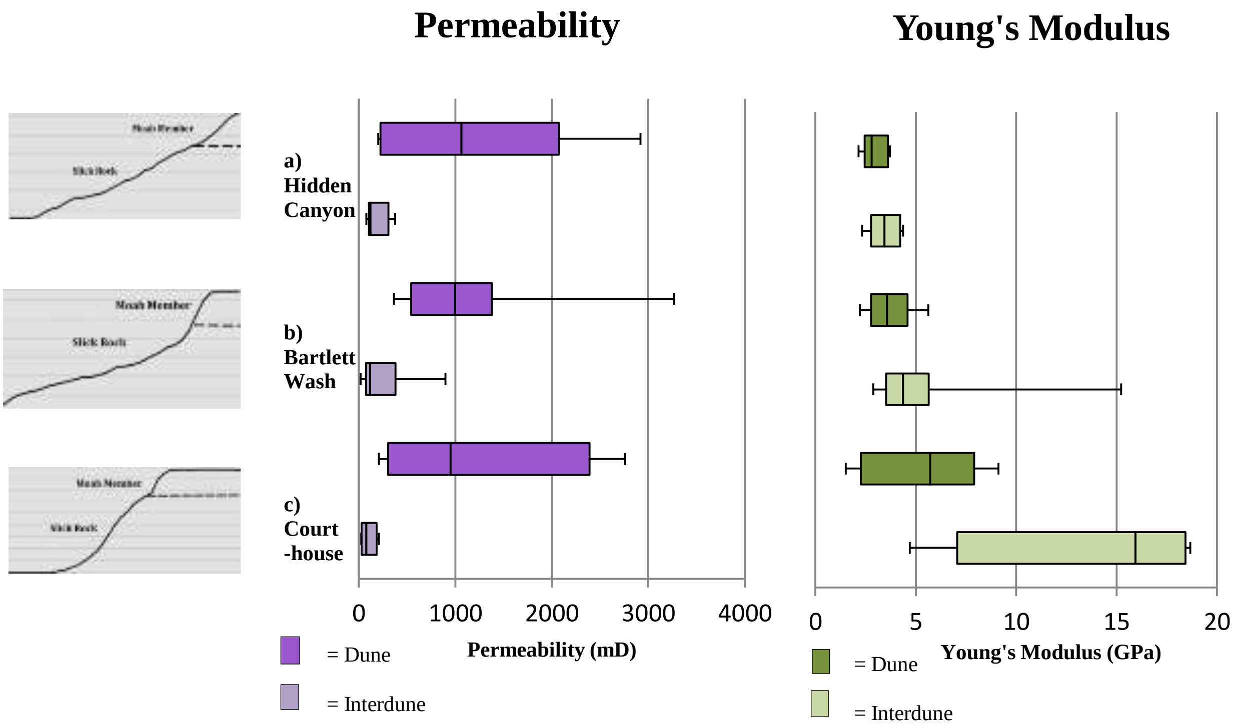

Figure 4.27: Boxplots of the measured permeability- (to the left) and Young's Modulus values (to the right) of the Slick Rock Member at the localities a) Hidden Canyon, b) Bartlett Wash and c) Courthouse (25th to 75th percentile boxplots).

interdunes exhibit steeper erosional slopes than the dunes. These differences are further discussed in the subsequent discussion chapter.

4.8 Joints and joint mechanisms

4.8.1 Fracture-maps

The formations in this study are fractured to a various degree. Fracture-maps from two areas within the study area have been made (Figure 4.28 and Figure 4.29) in order to illustrate the large-scale, dominating fracture orientations in the area near Moab. Based on aerial photos, black lines have been drawn along most of the joint-traces visible in map view (the uppermost image displayed in Figure 4.29 is zoomed in on parts of the fracture-map, illustrating to which extent the joint-traces have been mapped). The black lines represent both the overall joint orientations and the general spacing between the joints. The fracture-map illustrated in Figure

4.28 is located in the proximity of the town Moab and the fractures are mainly developed in the Navajo- and the Wingate sandstones (Figure 4.28 b)). The fracture-map illustrated in Figure 4.29 is located ~24 km northwest of Moab and the fractures are mainly developed in the Moab Member (some fractures are also developed in the underlying Slick Rock Member).

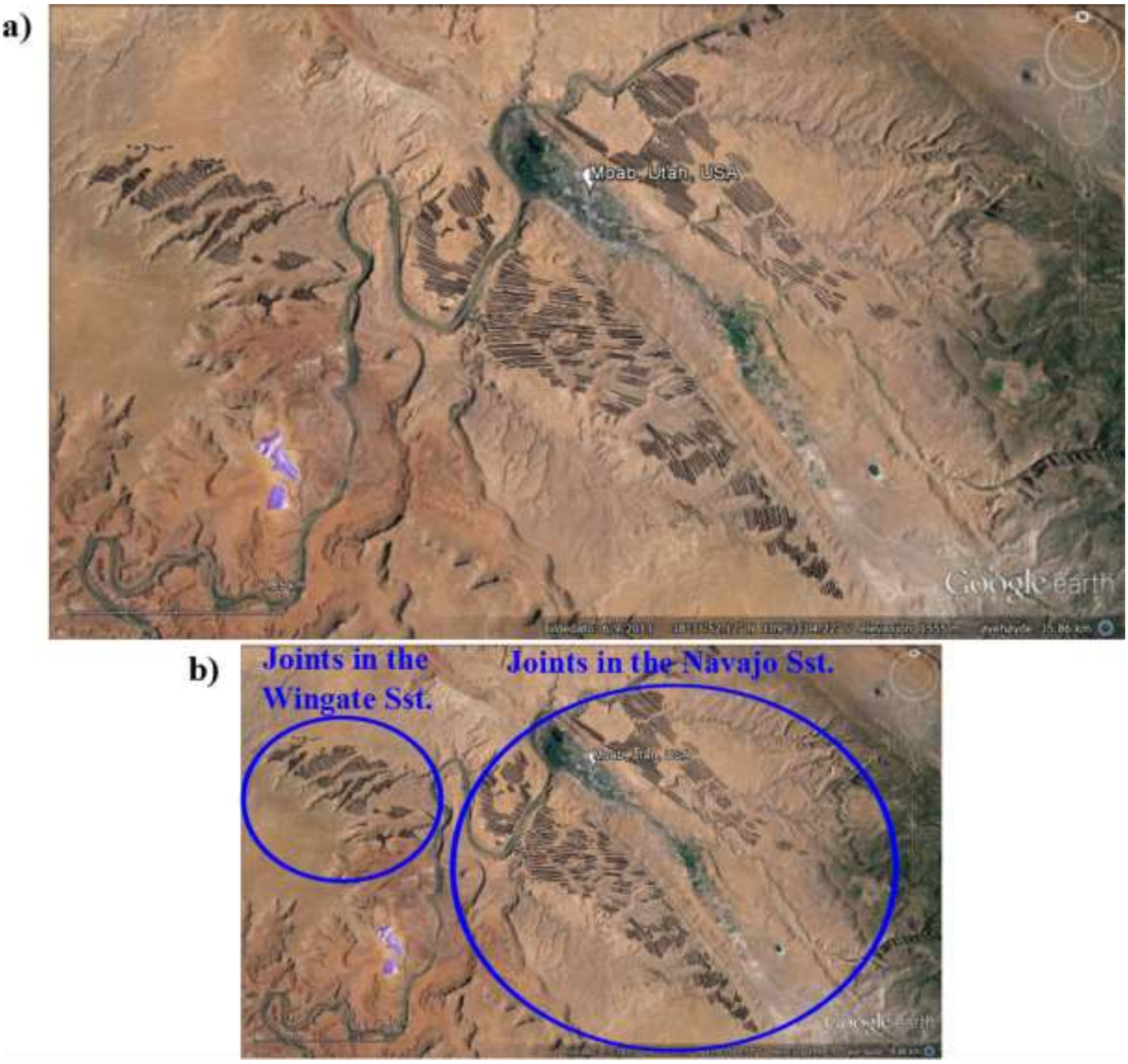

Figure 4.28: Fracture-maps based on aerial photos from Google Earth, in a) illustrating the overall fracture orientations (NW-SE) and fracture density in the area near Moab and in b) illustrating fractures developed in the Wingate- and Navajo sandstones.

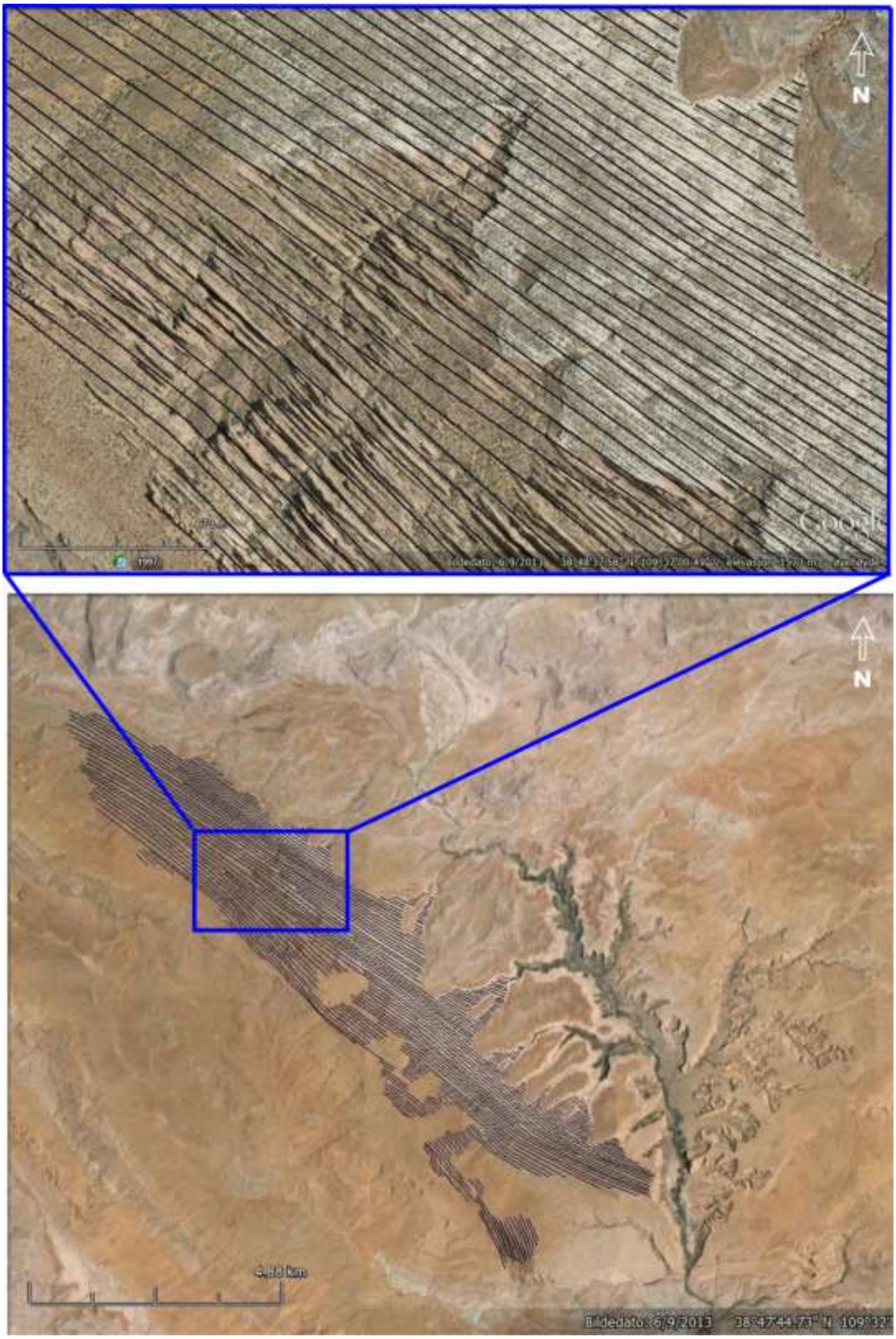

Figure 4.29: Fracture-map based on aerial photos from Google Earth. This map illustrates that the dominating orientation of the fractures in the field area (this area is located ~24 km northwest of Moab) are NW-SE. The uppermost image illustrates to which extent the fractures have been mapped.

4.8.2 Joint interaction- and propagation features

Joint interaction- and propagation features can be used to establish relative age relations between joints and/or other structures and for mapping the deformation history within an area (subchapter 3.5). Observations of joint interaction features (Figure 4.30 and Figure 4.31) and joint propagation features (Figure 4.32 and Figure 4.33) have been made in the field area. These observed features were developed in the Slick Rock Member (Figure 4.30 and Figure 4.31) and the Cutler Formation (Figure 4.32 and Figure 4.33). Figure 4.30 and Figure 4.31 display examples of so-called *hook-geometries*.

In Figure 4.30 the upper two joint tips curve toward the lower, relatively older joint whereas in Figure 4.31 the lower joint tip curves toward the upper, relatively older joint. Figure 4.32 displays *en echelon fractures* and Figure 4.33 illustrates *twist hackles* developed in the fringe zone of a propagating joint. Such features can be used to infer the joint propagation direction at the time of the joint formation.

Figure 4.30: Interacting joint tips observed in the Slick Rock Member at the Hidden Canyon locality (Figure 1.4) (hammer for scale). Coordinates: N38°43’01.8’’ W109°48’09.3’’.

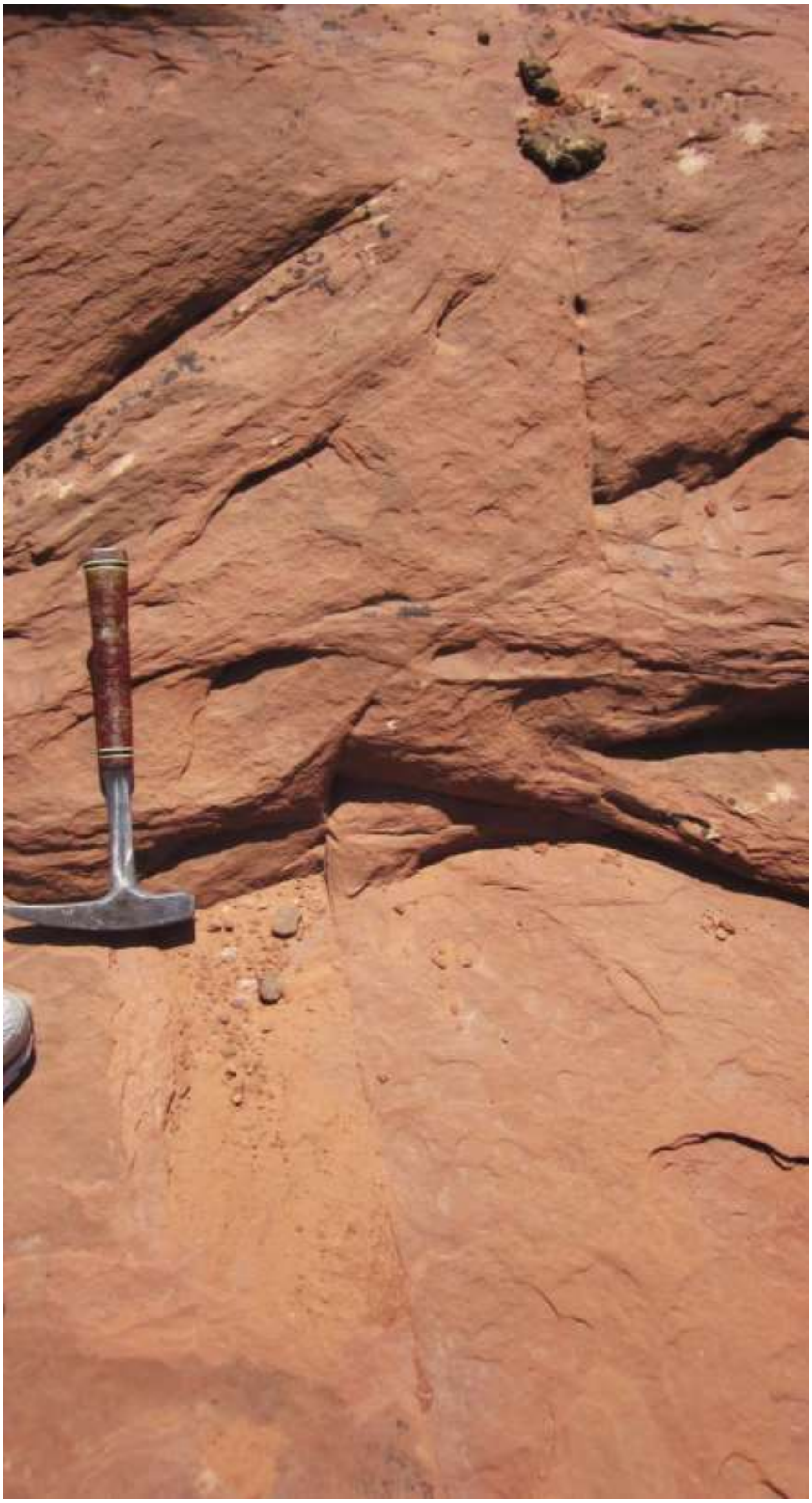

Figure 4.31: Interacting joint tips observed in the Slick Rock Member at the Hidden Canyon locality (Figure 1.4) (hammer for scale). Photo by Ragnhild J. Tunheim. Coordinates: N38°43’01.8’’ W109°48’09.3’’.

Figure 4.32: En echelon fractures observed in the Cutler Formation near the Shafer Trail locality (Figure 1.4) (measuring tape holder for scale). Coordinates: N38°27’55.1’’ W109°46’40.5’’.

Figure 4.33: Twist hackles observed in the Cutler Formation near the Big Bend locality (Figure 1.4) (camera lense cover for scale). Coordinates: N38°36’06.8’’ W109°34’00.4’’.

4.8.3 Joint spacing measured in field

A total of 26 fracture-frequency distribution analyses have been performed (4 of the Cutler Formation, 5 of the Chinle Formation, 4 of the Wingate Sandstone, 6 of the Slick Rock Member and 7 of the Moab Member) in order to explore the degree of fracturing within the formations. Well-developed fracture-patterns that were accessible for joint-spacing studies could only be found for five of the seven formations included in this study. Figure 4.34 - Figure 4.38 illustrates the range, median and 25th to 75th percentile of the measured joint spacing data for each of these formations. The average thickness of the confining layer of each distribution has been calculated and is given in the figure captions. An overview of all 26 fracture-frequency distribution analyses can be found in Appendix D (Table 8-12 – Table 8-37) and joint orientations for each fracture-frequency distribution in Appendix D (Figure 8.1 – Figure 8.26).

The orientations of the joints in each formation are illustrated in stereoplots and rose diagrams in Figure 4.39. The locality of each of the fracture-frequency distributions are shown in Appendix E (Figure 8.27 – Figure 8.31).

The Cutler- and Chinle formations both consist of alternating gently-sloping and steep-sloping intervals (ledges), even though their overall erosional slopes are gently-sloping (28-35°). Fracture-frequency distributions of these two formations have been carried out along the ledge-intervals (Figure 5.1). Fractures have not developed in the gently-sloping intervals and Figure 4.34 and Figure 4.35 thus represent fractures developed in small portions of the formations. Taking this into consideration it would be incorrect to describe these two formations as highly-fractured in comparison to formations such as the Wingate Sandstone and Moab Member.

In general, the spacing between the fractures is more systematic in the formations with small thicknesses of the confining units, such as for the Cutler Formation, the Chinle Formation and the Slick Rock Member (given by the relatively narrow 25th – 75th percentile boxes in the boxplots). There is a wider scatter of the measured spacing for the thicker units (e.g. for the Wingate Sandstone and the Moab Member). The relation between the layer thickness and average fracture spacing is explored in subchapter 4.8.5.

Figure 4.39 illustrates that there are a wide spread of recorded orientations of the joint-trace in some of the formations (e.g. the Chinle Formation, the Wingate Sandstone and the Moab Member), whereas the orientations are more systematic for the Cutler Formation (with two dominant orientations) and the Slick Rock Member (with only one dominant orientation).

Contrary to the common observation that joints preferentially form in the coarser-grained dune units (subchapter 3.4), the joints in the Slick Rock Member are to a high degree distributed in the fine-grained interdune units and to a small degree in the dune units (Figure 5.5) (this observation is further discussed in the subsequent discussion chapter).

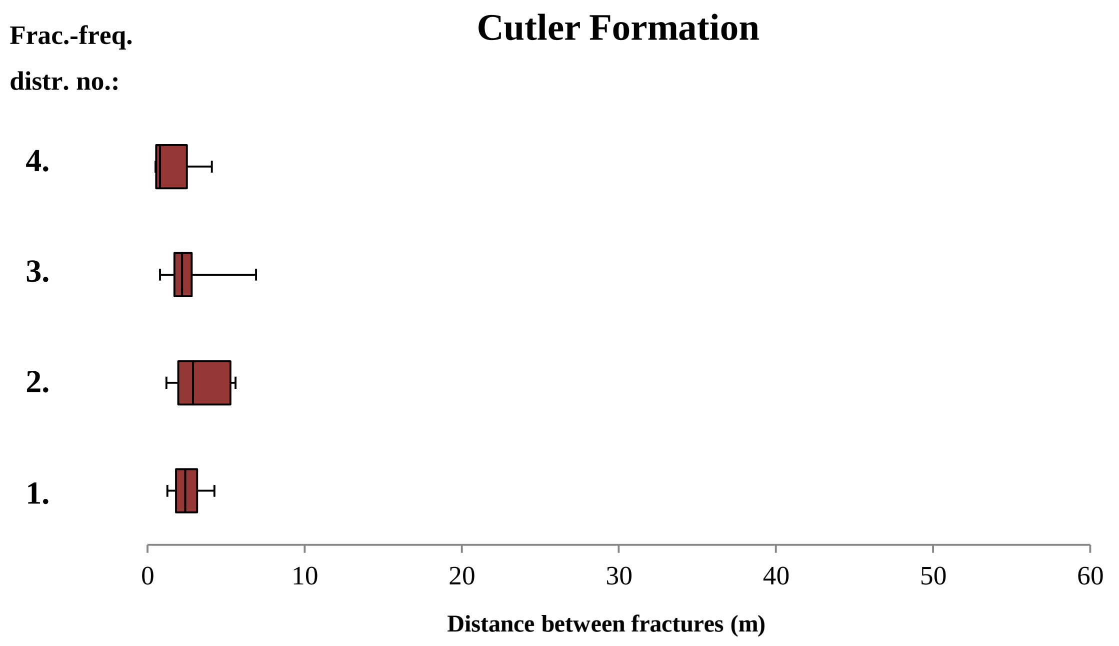

Figure 4.34: Measured spacing (in m) between fractures along 4 different scanlines along the Cutler Formation (25th to 75th percentile boxplot). Average thickness of the confining layer for distribution no. **1.** = 2.2 m, **2.** = 3.7 m, **3.** = 1 m and **4.** = 6.1 m.

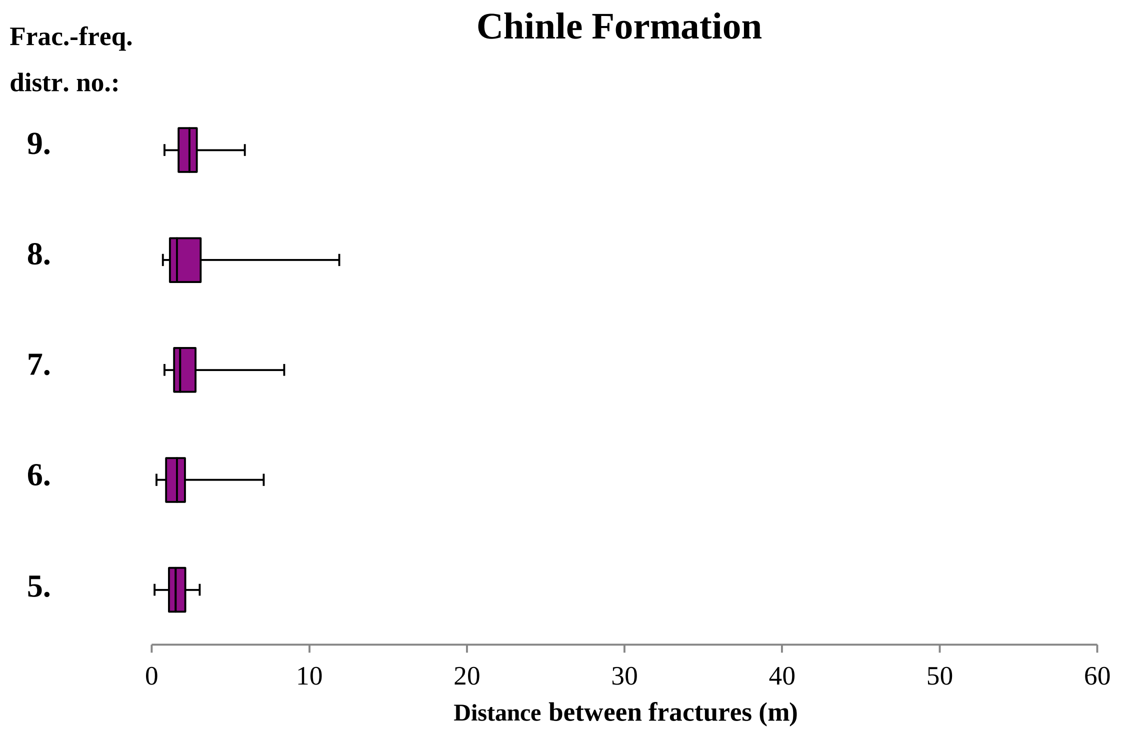

Figure 4.35: Measured spacing (in m) between fractures along 5 different scanlines along the Chinle Formation (25th to 75th percentile boxplot). Average thickness of the confining layer for distribution no. **5.** = 1.2 m, **6.** = 2.1 m, **7.** = 1.2 m, **8.** = 1.1 m and **9.** = 1.5 m.

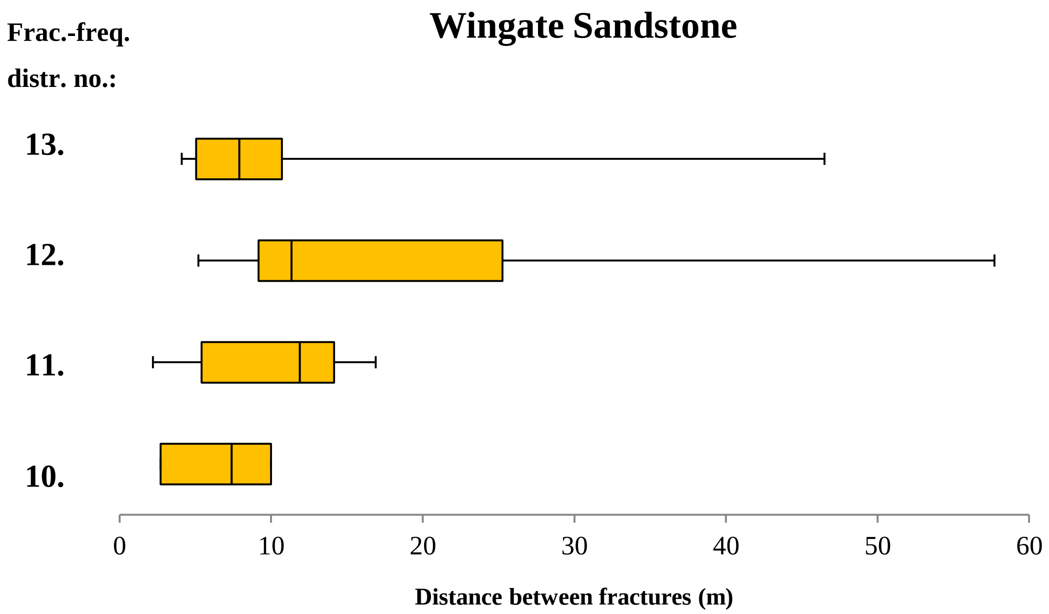

Figure 4.36: Measured spacing (in m) between fractures along 4 different scanlines along the Wingate Sandstone (25th to 75th percentile boxplot). Average thickness of the confining layer for distribution no. **10.** = 42.8 m, **11.** = 39.6 m, **12.** = 43 m and **13.** = 57.8 m.

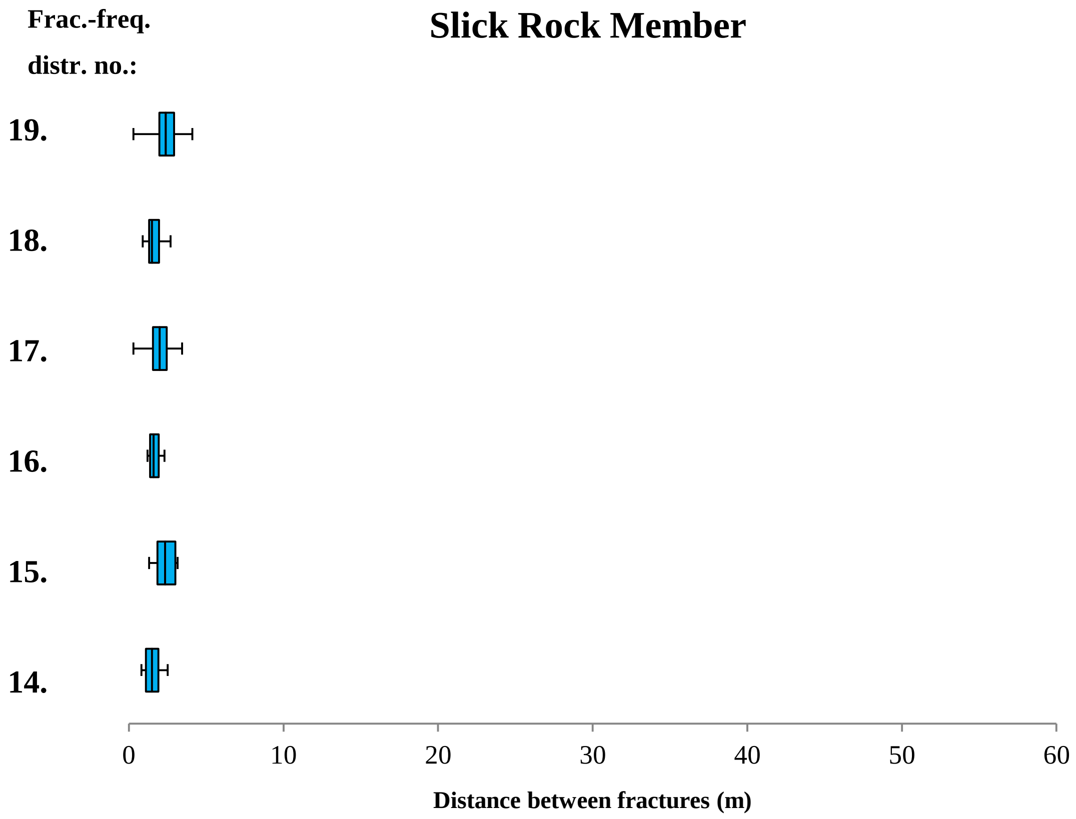

Figure 4.37: Measured spacing (in m) between fractures along 6 different scanlines along the Slick Rock Member (25th to 75th percentile boxplot). Average thickness of the confining layer for distribution no. **14.** = 0.4 m, **15.** = 1.6 m, **16.** = 0.4 m, **17.** = 1.5 m, **18.** = 0.4 m and **19.** = 1.5 m.

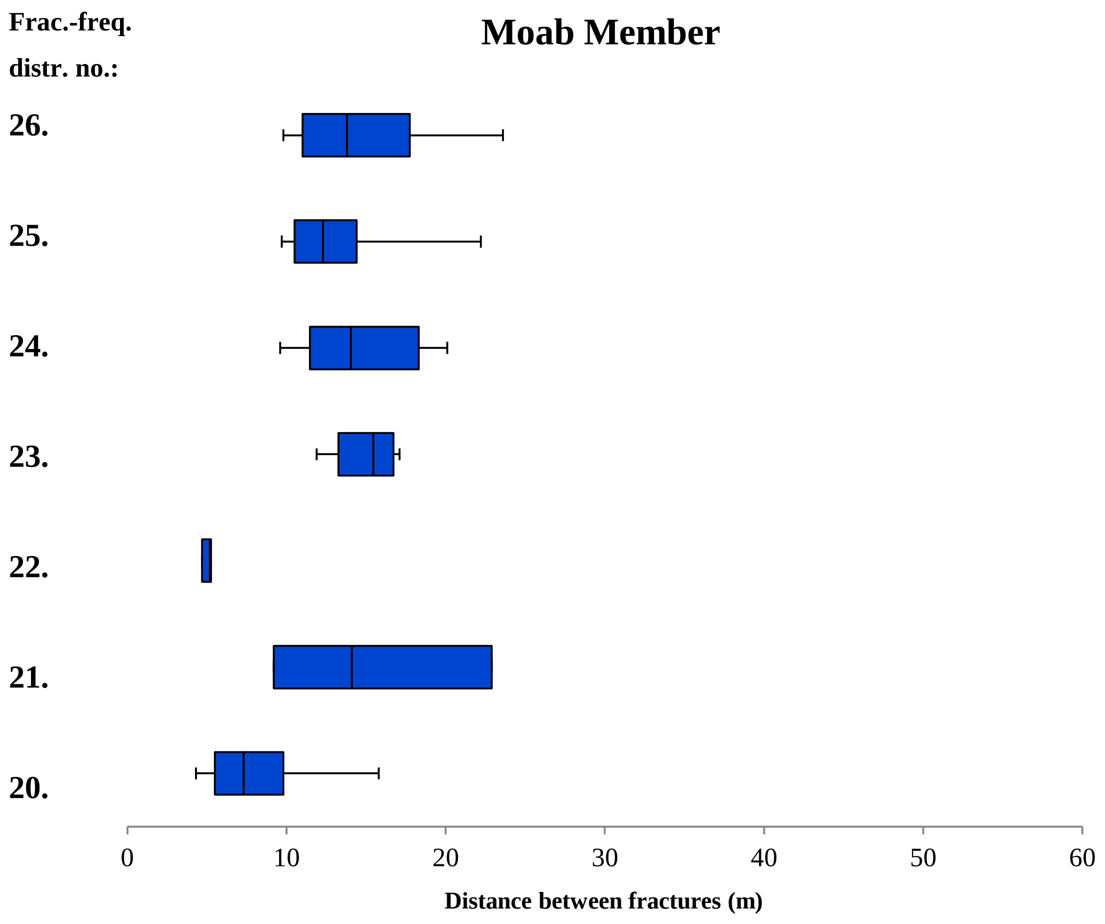

Figure 4.38: Measured spacing (in m) between fractures along 7 different scanlines along the Moab Member (25th to 75th percentile boxplot). Average thickness of the confining layer for distribution no. **20.** = 11.6 m, **21.** = 15 m, **22.** = 7 m, **23.** = 9.4 m, **24.** = 8.9 m, **25.** = 8.5 m and **26.** = 10.9 m.

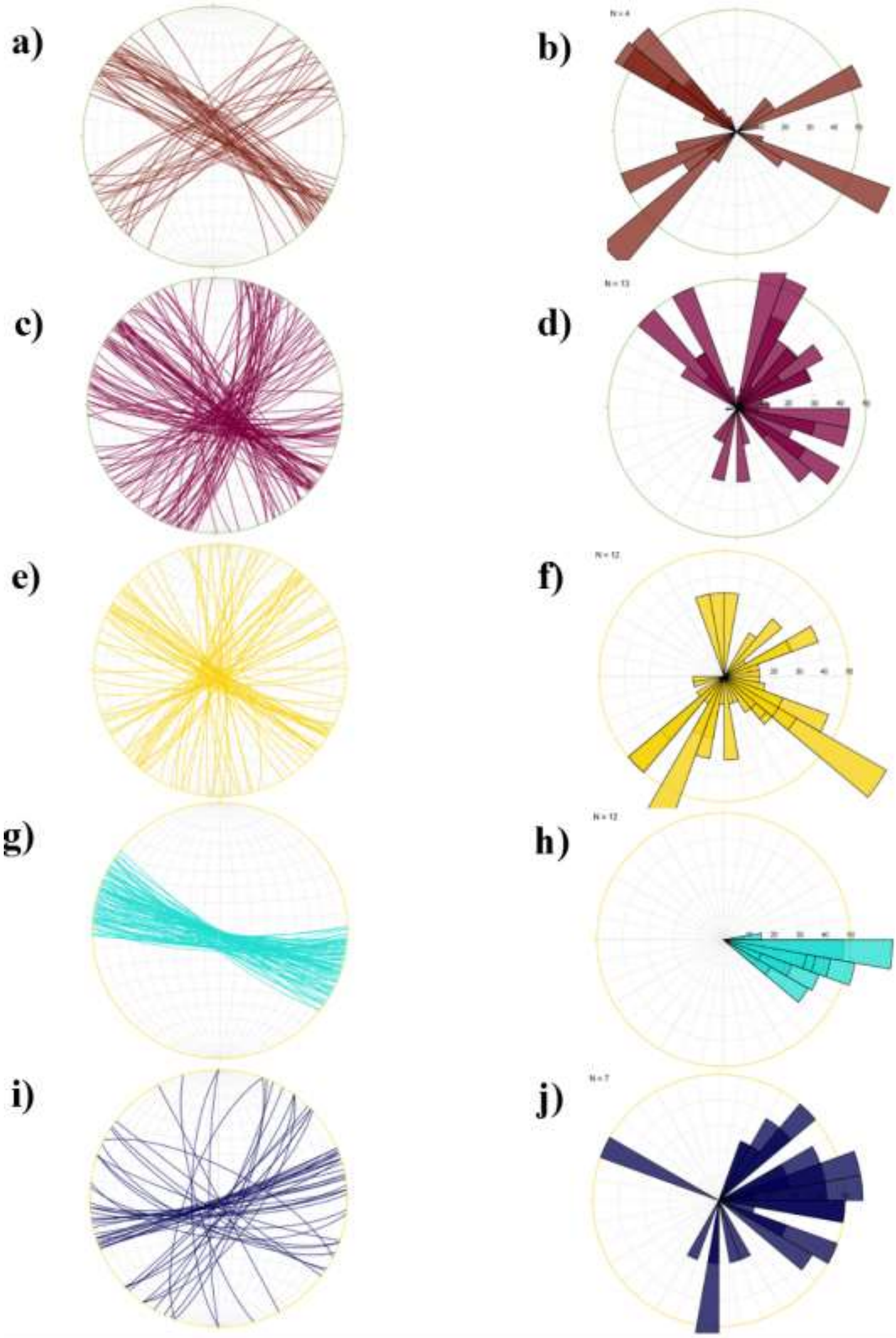

Figure 4.39: Joint orientations recorded for the Cutler Fm. (a, b), the Chinle Fm. (c, d), the Wingate Sst. (e, f), the Slick Rock Mb. (g, h), and the Moab Mb. (i, j), displayed on the left side in stereoplots and on the right side in rose diagrams. Achieved by using Stereonet 8 software by Rick Allmendinger (Allmendinger et al., 2011),(Cardozo and Allmendinger, 2013).

4.8.4 Joint spacing based on aerial photos

Fracture-frequency distributions have been made based on aerial photos from Google Earth. Fractures along 10 scanlines of various lengths have been recorded for each of the Wingate Sandstone, the Navajo Sandstone and the Moab Member. Only these three formations show large-scale, well-developed, systematic fracture-patterns visible on aerial photos. Figure 4.40 - Figure 4.42 illustrates the range, median and 25th to 75th percentile of the measured joint spacing data for each of these formations. An overview of all 30 fracture-frequency distribution analyses can be found in Appendix F (Table 8-38 – Table 8-67). Examples of fractures developed in the Wingate- and Navajo sandstones are illustrated in Figure 4.28 b), and in the Moab Member in Figure 4.29. The overall orientation of these large-scale joint-patterns is NW-SE.

The Wingate Sandstone (Figure 4.40) appears as a relatively consistent formation with a highly systematic fracture spacing (given by the relatively narrow 25th – 75th percentile boxes in the boxplots and a narrow scatter of the boxes from each distribution). The fracture-patterns developed in the Navajo Sandstone and the Moab Member appear similarly systematic, but with a larger difference between the separate distributions. Considering the limited area across which the fractures of the Wingate Sandstone could be recorded (Figure 4.28 b)) in comparison to the Navajo Sandstone (Figure 4.28 b)) and the Moab Member (Figure 4.29, uppermost image), lateral thickness variations across the larger areas have probably influenced the slightly less systematic fracture spacing observed in Figure 4.41 and Figure 4.42. The relation between the fracture spacing and the average layer thickness is further explored in the following subchapter.

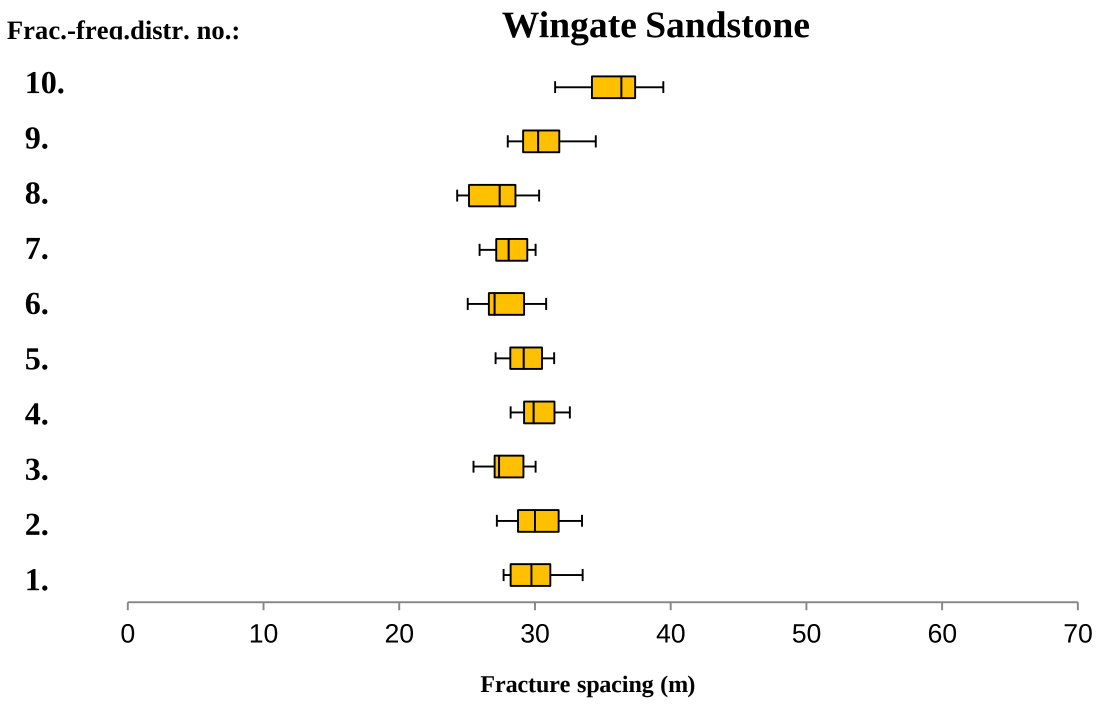

Figure 4.40: Boxplot illustrating the range of spacing between joints in 10 different fracture-spacing analyses in the Wingate Sandstone, based on aerial photos from Google Earth (25th to 75th percentile boxplot).

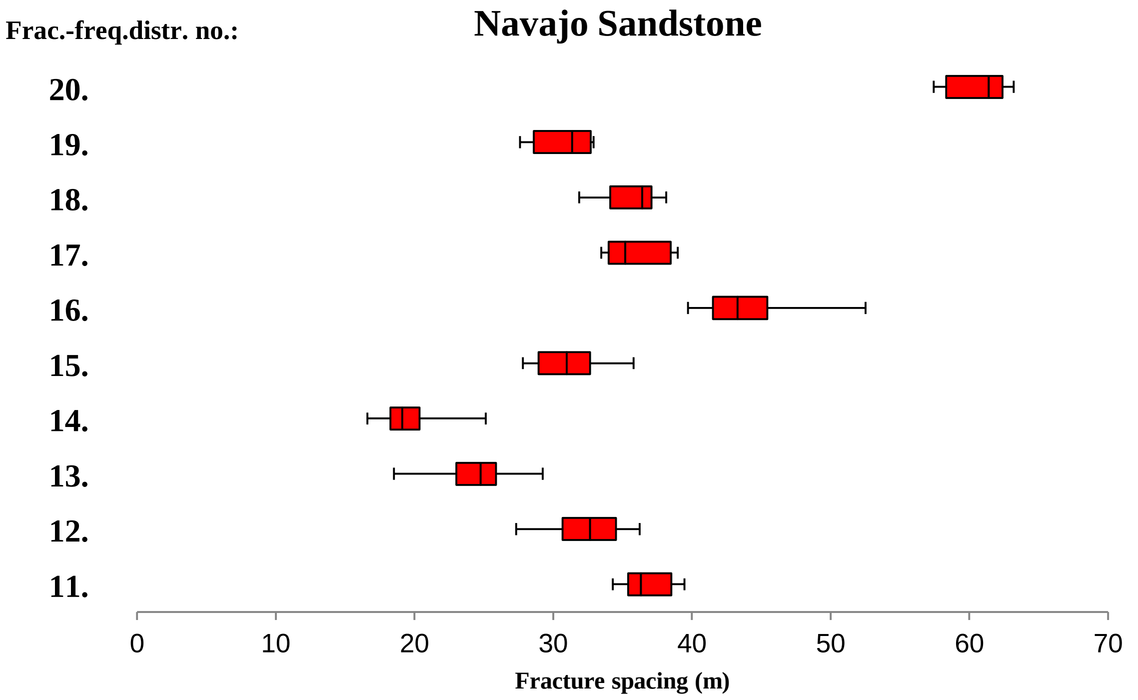

Figure 4.41: Boxplot illustrating the range of spacing between joints in 10 different fracture-spacing analyses in the Navajo Sandstone, based on aerial photos from Google Earth (25th to 75th percentile boxplot).

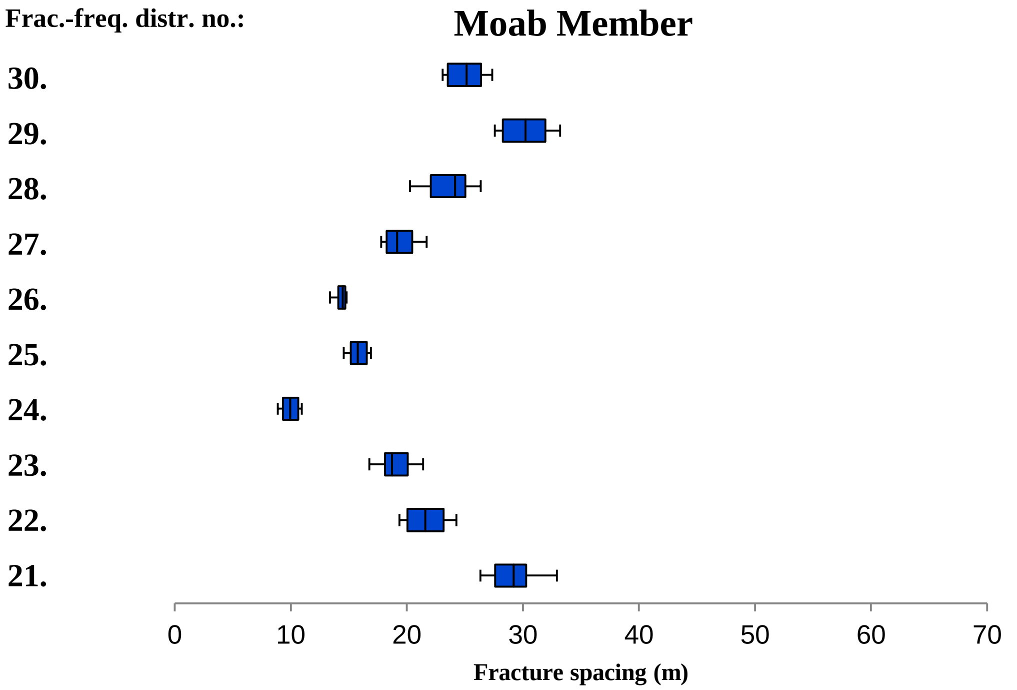

Figure 4.42: Boxplot illustrating the range of spacing between joints in 10 different fracture-spacing analyses in the Moab Member, based on aerial photos from Google Earth (25th to 75th percentile boxplot).

4.8.5 Layer thickness versus joint spacing

The relation between the layer thickness and the average fracture spacing for five of the formations (the Cutler Formation, the Chinle Formation, the Wingate Sandstone, the Slick Rock Member and the Moab Member) has been explored (Figure 4.43). Average layer thickness data have been achieved by using Ragnhild J. Tunheim as a scale next to the outcropping formations. Fracture spacing data are based on fracture-frequency distribution no. 1-26 (Figure 4.34 - Figure 4.38) (Appendix G, Table 8-68).

It seems to be a strong correlation between the average spacing between the fractures and the thickness of the jointed layer (Figure 4.43). Thin layers correlate with a small spacing between the joints (Figure 4.45). This relation is strongest for the thinner layers (such as the layers in the Cutler- and Chinle formations and the Slick Rock Member). The ~60 m thick layers of the Wingate Sandstone generally have a relatively small fracture-spacing compared to the average layer thickness (Figure 4.44).

It is worth noting that along most of the scanlines there were lateral thickness differences within the same confining layer which most often resulted in a narrower spacing for thinner intervals and a wider spacing for thicker intervals. Considering these lateral thickness variations, the relation between the fracture spacing and the layer thickness should be considered more systematic than they appear in Figure 4.43.

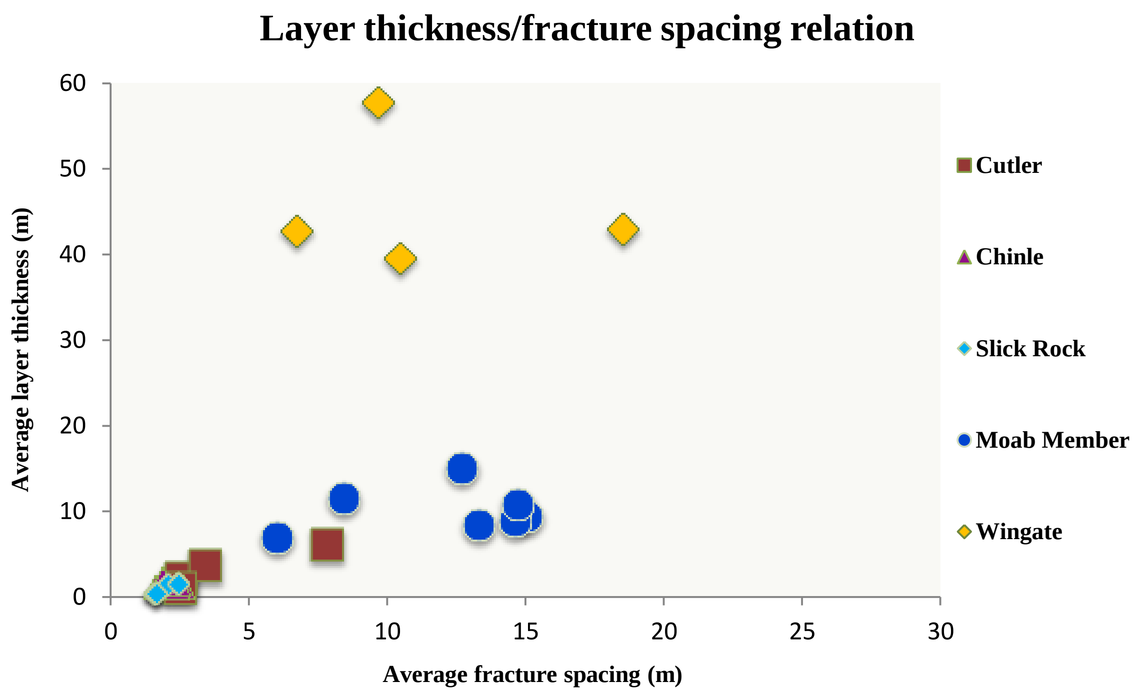

Figure 4.43: The relation between the layer thicknesses of the formations versus the average spacing between the fractures (based on average fracture spacing- and layer thickness data, Appendix G – Table 8-68).

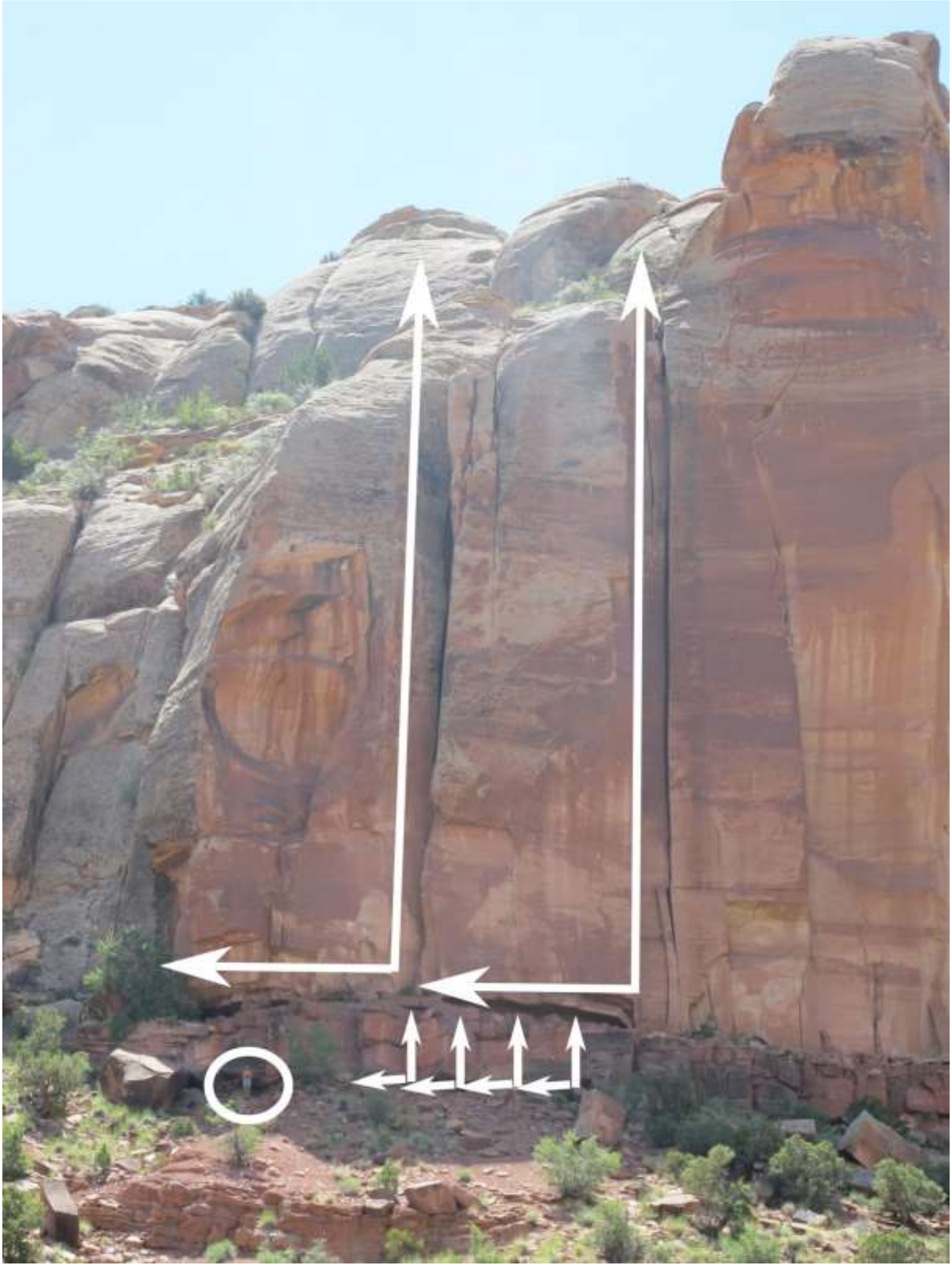

Figure 4.44: Field example of the relation between layer thickness and fracture spacing of the massive Wingate Sandstone overlying the Chinle Formation (Ragnhild J. Tunheim as scale). Note the difference in layer thickness versus fracture spacing correlation between the formations (from the Indian Creek locality, coordinates: N38°02’23.2’’ W109°33’09.7’’),

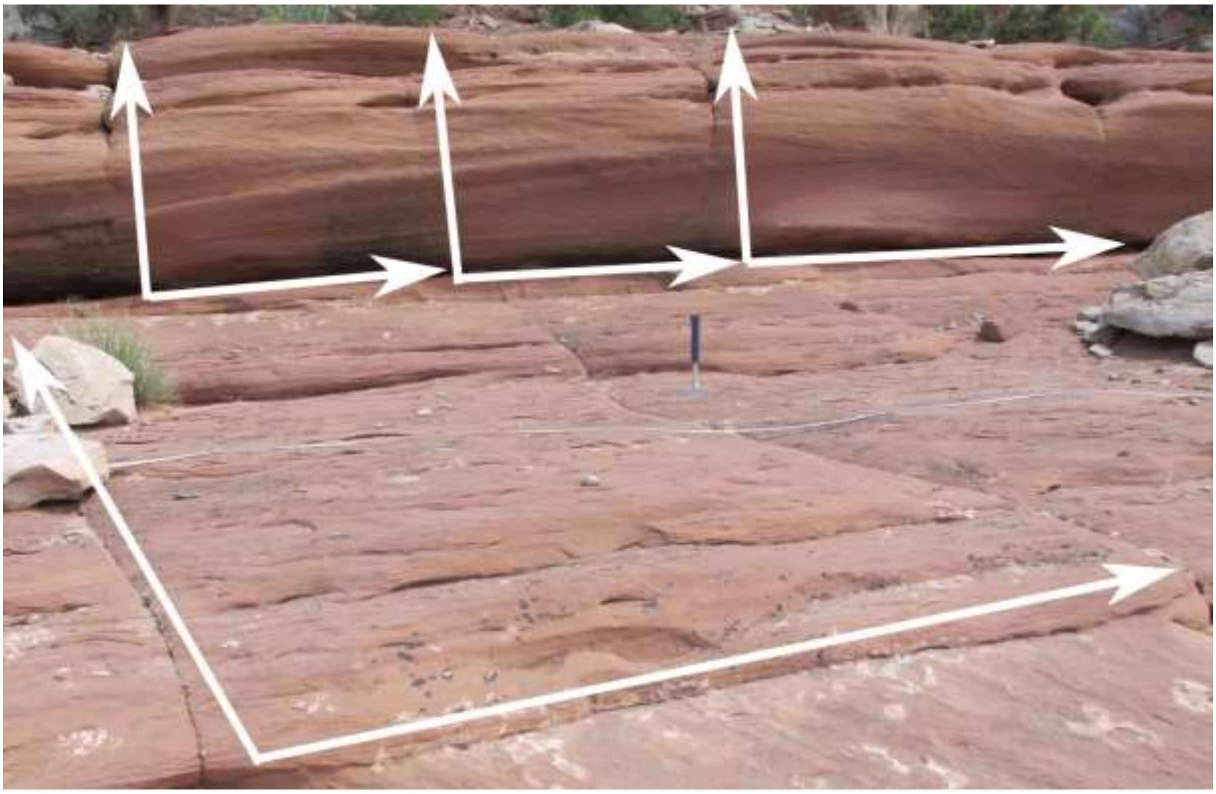

Figure 4.45: Field example of fractures in the Slick Rock Member displaying a high correlation between the layer thickness and the fracture spacing (from the Hidden Canyon locality, coordinates: N38°43’02.6’’ W109°48’08.5’’).

5 Discussion

5.1 Introduction

In the preceding chapter, figures and tables forming the basis of this discussion have been presented. Clearly, many parameters may have contributed to the observed differences in appearances of the continental deposits outcropping in southeastern Utah, USA. Factors such as sedimentological-, mineralogical- and mechanical properties and fracture-patterns may all have affected the observed erosional slopes to a certain degree. The main focus of Tunheim (2015) has been on the sedimentological- and mineralogical properties whereas the main focus of the project presented in this thesis has been on the mechanical properties and fracture-patterns. In order to enlighten which parameters that seem to correlate and should be considered more influencing to the overall erosional signature of the formations, the sedimentological- and mineralogical properties will be briefly discussed in this thesis as well.

In the following discussion, each parameter will be discussed based on the subchapter division in the result chapter (erosional slopes, facies associations, sedimentological- and mineralogical properties, mechanical properties and joints and joint mechanisms) and properties that seem to facilitate steeply-dipping formations (such as the Wingate Sandstone, the Kayenta Formation and the Moab Member) versus gently-dipping formations (such as the Cutler- and Chinle Formation) will be identified. Further, the timing of joint propagation of the joints in the study area is discussed in subchapter 5.7.

5.2 Erosional slopes

The measured values of erosional slopes of each formation displayed in Figure 4.3 are clearly distributed differently for each formation. The variations in erosional slopes are larger for the Slick Rock Member, the Navajo Sandstone and the Kayenta Formation. In contrast, the Cutler Formation, the Chinle Formation, the Wingate Sandstone and the Moab Member show significantly more uniform slope values throughout the study area. Further, it is evident that the Moab Member, the Kayenta Formation and the Wingate Sandstone exhibit the steepest erosional slopes of the formations. The widespread undulating and hummocky surface morphology of the Navajo Sandstone result in the large range of measured slope values. The Cutler- and Chinle Formation are the most gently-dipping formations whereas the Slick Rock Member shows large lateral differences (e.g. gently-dipping in Hidden Canyon versus cliff-forming at Courthouse (Figure 4.24 and Figure 4.25)). Possible explanations for the observed differences in erosional slopes between the formations are discussed in the following subchapters.

5.3 Facies associations, sedimentological- and mineralogical properties

In general, formations of aeolian origins display considerably steeper erosional slopes than those of fluvial origins. All of the formations constitute intervals of coarser- and finer grain-sizes of varying thicknesses. For the formations of aeolian origins (e.g. the Wingate- and Navajo sandstones and the Moab Member), the dunes are remarkably thicker than the interdunes as would be expected regarding their depositional environment. For the formations of mixed-fluvial origins (the Cutler-, Chinle- and Kayenta formations) the coarser-grained intervals are made up by dune deposits (for the Cutler Formation) and channel deposits (for the Chinle and Kayenta formations), whereas the finer-grained intervals are made up by flash-flood-, flood-plain- and intedune deposits. The general thicknesses of the bed units are more consistent for the formations of mixed-fluvial origins. A more thorough comparison of the formations of mixed-fluvial origins and those of an overall aeolian origin is presented in subchapter 5.3.1 and 5.3.2, respectively.

The proportion of quartz grains is found to increase stratigraphically from the bottom (the Cutler Formation) to the top (the Moab Member), whereas the proportion of feldspar grains shows the opposite trend. Regarding quartz cement, the most steeply-dipping formations (e.g. the Wingate Sandstone, the Kayenta Formation and the Moab Member) show high proportions compared to the gently-sloping formations (e.g. the Cutler- and Chinle formations).

Considering the content of carbonate cement, gently-dipping formations such as the Cutler- and Chinle formations generally have high values. However, steeply-dipping formations such as the Wingate Sandstone and Kayenta Formation show relatively high values of carbonate cement as well. The most pronounced relation between erosional slope and type of cement thus seems to be related to quartz cementation and to a much smaller degree carbonate cementation. In addition there seems to be a strong relation between steep erosional slopes and high porosity values for the formations (e.g. the Moab Member and Wingate Sandstone with average porosities of 19% and 13%, respectively in contrast to the Cutler- and Chinle Formation with average porosities of 4% and 6%, respectively). Further, general trends for the steep-sloping formations based on Table 4-3 are that they are relatively better sorted and have more rounded grains than the gently-sloping formations.

5.3.1 Formations of mixed-fluvial origins

The formations of mixed-fluvial origins include the Cutler-, Chinle- and Kayenta formations. Contrary to the overall gently-sloping Cutler- and Chinle formations, the Kayenta Formation of similarly mixed-fluvial origin, display significantly steeper erosional slopes.

The formations of mixed-fluvial origins are generally made up by alternating coarse-grained and fine-grained intervals, the fine-grained intervals usually making up large parts of the formations. The coarser-grained intervals are made up by dune deposits (for the Cutler Formation) and channel deposits (for the Chinle- and Kayenta formations), whereas the finer-grained intervals are made up by flash-flood-, flood-plain- and intedune deposits. The Chinle Formation consist of a high proportion of silt and clay (~75.4% sand, ~22.3 % silt and ~2.3% clay) in comparison to the Cutler Formation (~93.8% sand, ~0.8% silt and ~5.3% clay) and the Kayenta Formation (~90.1% sand, ~8.5% silt and ~1.3% clay) (Table 4-1). Generally, the thicknesses of the bed units are smaller in the Kayenta Formation (~1.2- to ~ 2.6 m) than in the Cutler- (~1- to ~3.5 m) and Chinle (~0.55- to ~3 m) formations (25th to 75th percentiles, Figure 4.4).

The porosity values are all in all higher for the Kayenta Formation (~9%) than for the Cutler- (~4%) and Chinle (~ 6%) formations (Table 4-4). Further, the proportions of quartz grains are generally higher for the steeply-sloping Kayenta Formation than for the overall gently-sloping Cutler- and Chinle formations. The degree of cementation is generally moderate to high for all the formations, but a difference is found regarding the type of cement; quartz cement is dominant within the Kayenta Formation whereas carbonate cement is dominant within the Cutler- and Chinle formations. Considering the hardness and chemical stability of quartz grains, the correspondence of high proportions of quartz- grains and cement along with the steep erosional slopes for the Kayenta Formation seems logical.

Both the Cutler- and Chinle formations are made up by alternating steeply-dipping ledges and gently-sloping intervals. The ledge-intervals represent the coarse-grained facies (dune- and channel facies) whereas the gently-sloping parts represent the fine-grained facies (interdune-, flash-flood- and flood-plain facies). The coarser-grained intervals have resulted in resistant bedrock and steep erosional slopes (Figure 5.1). The small grain size fractions (silt and clay) making up the gently-sloping intervals (mainly covered in screed material) have resulted in significantly less resistant bedrock and highly fragmented erosional surfaces. Such fragmented erosional surfaces covered in screed-material are most evident for the Chinle Formation, corresponding to the large fractions of silt and clay compared to the Cutler- and Kayenta formations.

A possible explanation for the steep erosional slopes of the Kayenta Formation may be linked to the relation between the thicknesses of the fine-grained intervals compared to the coarse-grained intervals. Large intervals of fine-grained facies will likely favor the appearance of an overall gently-sloping erosional surface. Differences in bed thicknesses of fine-grained- and coarse-grained intervals within each formation are further explored by Tunheim (2015).

The average thickness of the Kayenta Formation (ranging from ~30 to ~60 m) are remarkably lower than those of the Cutler (reach up to ~360 m)- and Chinle (reach up to ~275 m) formations. The Kayenta Formation is positioned between the underlying, steeply-dipping Wingate Sandstone and the overlying Navajo Sandstone (many places steeply-dipping). With a considerably larger thickness (of both fine-grained and coarse-grained intervals), not located above the highly fractured, steep-sloping Wingate Sandstone, the erosional expression of the Kayenta Formation might have looked similar to those of the Cutler- and Chinle formations (with alternating ledge- and slope intervals in the coarse-grained- and fine-grained parts, respectively).

Figure 5.1: Image illustrating a steep ledge-interval in the overall gently-sloping Chinle Formation (coordinates: N38°39'02.9'' W109°29'01.5'', Ragnhild J. Tunheim as scale). Note the fragmented, gently-sloping interval covered in screed material below the ledge-interval.

The sedimentological parameters facilitating the steeply-sloping Kayenta Formation in contrast to the gently-sloping Cutler- and Chinle formations of similar mixed-fluvial origin is thus: 1) higher porosity, 2) higher proportions of quartz grains- and cement 3) smaller average thicknesses of bed units and 4) smaller average thickness of entire unit.

Further, three significant variables for the weathering characteristics observed for the formations of mixed-fluvial origins seem to be:

1. Maximum depth of burial (and accompanied cementation)
2. The thickness of the fine-grained- compared to the coarse-grained intervals
3. The thickness of the entire unit

5.3.2 Formations of aeolian origins

The formations of a dominantly aeolian origin include the Wingate- and Navajo sandstones, the Slick Rock Member and the Moab Member. The Wingate Sandstone and the Moab Member are relatively consistently characterized by steep cliffs throughout the study area whereas the Navajo Sandstone and the Slick Rock Member show larger lateral differences in erosional slopes.

Generally, the formations of aeolian origins are characterized by large trough-cross- and planar-cross stratified dunes alternating with smaller interdunes. Whereas the Wingate- and Navajo sandstones both consist of ~100% sand fractions (corresponding to the uniform desert environment in which they were formed), the Slick Rock Member is made up by ~96.5% sand and ~3.5% silt and the Moab Member of ~98.9% sand and ~1.1% silt (Table 4-1). The thicknesses of bed units in the Wingate Sandstone generally range from ~1.2- to ~4.4 m, in the Navajo Sandstone from ~1.3- to ~5 m, in the Slick Rock Member from ~0.6- to ~1.3 m and in the Moab Member from ~0.8- to ~2 m.

The formations of aeolian origins generally have a moderate to high degree of cementation and pressure solution (based on thin-section studies). In general, the aeolian formations show high proportions of quartz grains (~64% for the Wingate Sandstone, ~67% for the Navajo Sandstone, ~67% for the Slick Rock Member and ~69% for the Moab Member). It is not large differences in the content of quartz cement between the formations. Carbonate cement seems to be the dominant type of cement for all the formations of aeolian origin except for the Moab Member (displaying a considerably lower content of carbonate cement than the underlying Slick Rock Member, Table 4-4). Regarding the porosity, the values are greatest for the Moab Member (~19%) in comparison to the Slick Rock Member (~11%), the Navajo Sandstone (~13%) and the Wingate Sandstone (~13%).

Three significant variables for the weathering characteristics observed for the aeolian formations seem to be:

1. Maximum depth of burial (and accompanied cementation)
2. The thickness of the dune-sets
3. Whether the dunes are formed in wet or dry systems

The maximum depth of burial of the formations and accompanied cementation is discussed in subchapter 5.7. In general, the thickness of the dune-sets is clearly larger for the Wingate- and Navajo sandstones, corresponding to the dry, widespread dune-system dominating on the Colorado Plateau in Late Triassic – Early Jurassic time. Further, the smaller thicknesses of the dunes of the Slick Rock- and Moab Member seem to be related to the wetter coastal dune environment in which they were formed.

The interdune-sets as well as the dune-sets are however considered to be relatively “dry” for the Moab Member in comparison to those of the underlying Slick Rock Member. This factor may have influenced the well-developed fracture-patterns formed within the Moab Member, with joints penetrating the entire height of the unit (both through dunes and interdunes). This factor is also applicable for the dry dunes and interdunes (with joints penetrating the entire height of the unit) within the Wingate- and Navajo sandstones.

The Slick Rock Member however, is considered a “wet” dune- and interdune system (deposited in wet/damp environments) and does not display the same fracture characteristics as those of the Moab Member (with joints only penetrating the interdunes). The fracture-patterns again seem to be strongly linked to the weathering characteristics of the formations (subchapter 5.6) and the difference between wet- and dry systems thus seems to be of a great importance for their resulting appearance. The height of the water table in the aeolian deposition environment (strongly affected by the climate) is considered to be the most controlling factor to whether the dune- and interdunes become “wet” or “dry”. A low level of the water table will promote the formation of dry dunes and interdunes. Wet aeolian systems however, are those in which the water table is shallow and the floors of the interdune flats are within the capillary fringe (Crabaugh and Kocurek, 1993).

The mentioned variables of dune-thicknesses and wet- and dry aeolian systems are further explored by Tunheim (2015).

The most pronounced differences in erosional slopes of the formations of aeolian origins involve the undulating and bulbous surface morphology of the Navajo Sandstone (resulting in a wide range of measured slope values) and the lateral differences within the Slick Rock Member (cliff-forming at the Courthouse locality in contrast to gently-sloping at the Bartlett

Wash- and Hidden Canyon localities). Lateral differences within the Slick Rock Member are further discussed in subchapter 5.5.

The differences in sedimentological- and mineralogical properties for the cliff-forming Wingate Sandstone and Moab Member are not that great, corresponding to their relatively similar erosional character.

Considering that the Navajo Sandstone constitute the uppermost exposed surface in large parts of the study area, the resulting undulating surface morphology seems to correspond well. In many areas, the Navajo Sandstone does not have any “protecting” overlying unit and are thus more prone to erosional processes than what is true for the Wingate Sandstone. If the Navajo Sandstone was underlying a “protecting” unit similar to the Kayenta Formation, the erosional expression of the Navajo Sandstone would likely be more similar to the one of the Wingate Sandstone. Further, the differences in erosional signature of the Navajo Sandstone compared to the Wingate Sandstone are likely related to the character of the fracture-patterns developed within the formations (subchapter 5.6).

Figure 5.2: Image illustrating the thin alternating fine-grained- and coarse-grained units making up the Kayenta Formation, likely functioning as a protective "blanket" above the underlying, homogenous and massive Wingate Sandstone. Note the exposed surface of the Navajo Sandstone at the top, clearly more affected by erosional processes. Coordinates: N38°28'30.6'' W109°41'19.2''.

5.4 Mechanical properties

Considering the mechanical properties, a significant factor to keep in mind is that the slope intervals of the overall gently-sloping formations (e.g. the Cutler- and Chinle formations) were highly fragmented and covered in screed-material and as a result there were no such gently-sloping surfaces suitable for performing permeability- and Young's Modulus measurements. Such measurements have thus only been carried out in steep ledge-intervals of all the formations (not including measurements of Slick Rock at the Bartlett Wash- and Hidden Canyon localities) (Figure 5.1). The resulting measurements of the steep parts of the overall gently-sloping Cutler- and Chinle formations would thus likely not be representative for the entire units (the measured permeability values of the Cutler-, Chinle- and Kayenta formations are remarkably lower than those of the other formations, Figure 4.16).

The ledge-intervals in the Cutler- and Chinle formations (of mixed-fluvial origins) are made up by dune- and channel facies, respectively, and the permeability values would thus be expected to correlate to a certain degree to measured permeability values of the formations of aeolian origins (made up by alternating dunes and interdunes). However, formations of fluvial origins are generally expected to have lower permeability values than those of aeolian origins (as a function of differences in porosity, grain size distributions, sorting, rounding etc.). Keeping this in mind, the remarkably low permeability values recorded for the ledge-intervals of the Cutler-, Chinle- and Kayenta formations may be relatively characteristic for these units after all.

In general, steeply-sloping formations (of aeolian origins) would be expected to be stiffer (have higher Young's Modulus values) than gently-sloping formations (as a result of generally larger grain size fractions, higher content of quartz etc.). Contrary to the permeability measurements, the recorded Young's Modulus values for the Cutler- and Chinle formations are likely remarkably higher in the ledge-intervals than what would be characteristic for the entire, overall gently-sloping units.

If a strong correlation exists between erosional slopes and permeability- and Young's Modulus values, the measurements would be expected to be relatively consistent for all the formations considering that only steep parts have been measured. However, the permeability measurements clearly differ between formations of aeolian origins (e.g. the Wingate- and Navajo sandstones and the Moab Member) and formations of mixed-fluvial origins (the Cutler-, Chinle and Kayenta formations) (Figure 5.3). The Young's Modulus measurements on the other hand are generally high for all of the formations which correspond to the steep erosional slopes on which the measurements were performed (not including the gentle slopes of the Slick Rock Member, Figure 5.4). The relation between erosional slopes and permeability values are thus found to be weak, whereas a strong relation is evident between erosional slopes and Young's Modulus values.

The Slick Rock Member (at the Bartlett Wash- and Hidden Canyon localities) comprised the only gentle slopes suitable for performing permeability- and Young's Modulus measurements.

Similar Young's Modulus values as those recorded at the Bartlett Wash- and Hidden Canyon localities (at Bartlett Wash ranging from ~2.2- to ~15.2 GPa (with a mean value of ~4.6 GPa) and at Hidden Canyon ranging from ~2.2- to ~4.4 GPa (with a mean value of ~3.2 GPa)) would likely be applicable as values characterizing the overall gently-sloping formations (the Cutler- and Chinle formations).

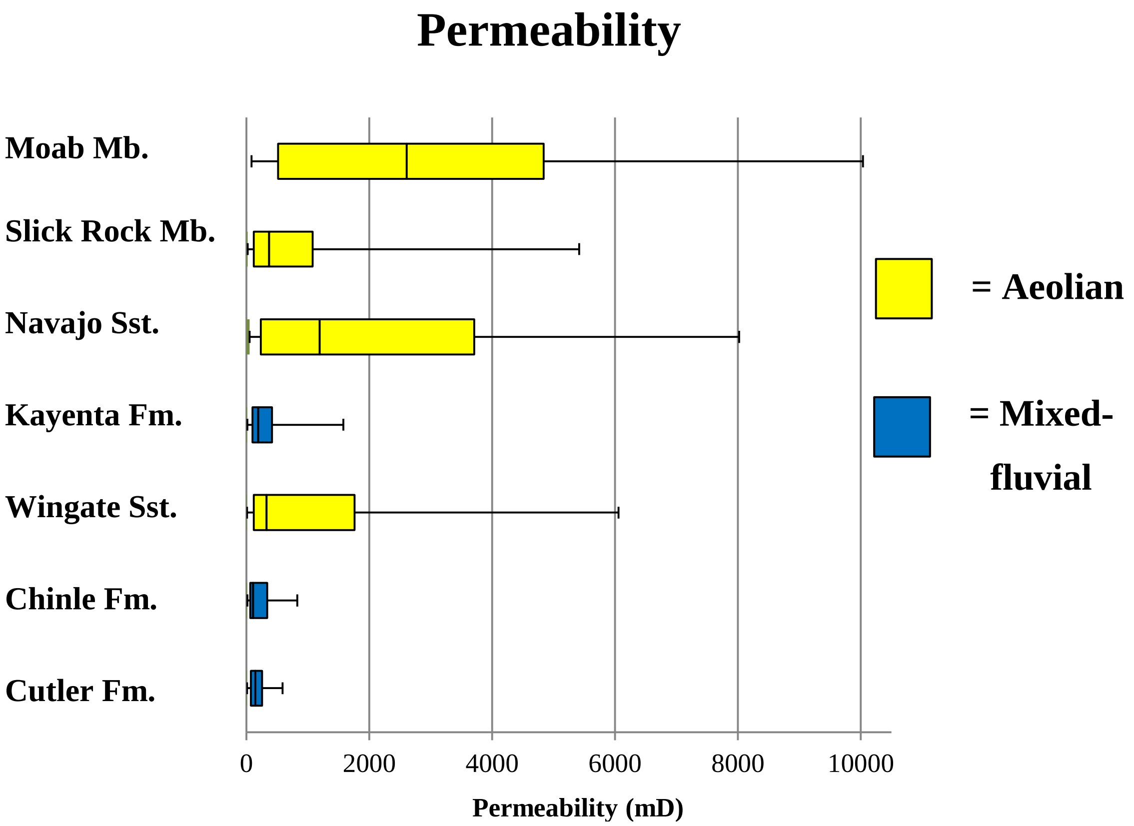

Figure 5.3: Boxplot illustrating measured permeability values (mD) of the formations of aeolian origins versus mixed-fluvial origins (25th- to 75th percentile boxplot).

The relation between permeability (Tiny-Perm II)- and Young's Modulus (Schmidt Hammer) measurements within cemented- and non-cemented parts of the Navajo Sandstone were explored by Alikarami et al. (2013) in the fault core and damage zones of two faults in two localities (in southeast (Cache Valley) and central (San Rafael Swell) Utah). Statistical relations between Tiny-Perm II measurements and Schmidt Hammer values were studied and the statistical results demonstrate that there are correlations between the studied parameters, but the dependencies vary with the degree of calcite cementation in mineralogically similar sandstones (quartz sandstone). Their statistical results demonstrate that the relation is best described by an exponential law for the non-cemented Navajo Sandstone whereas for the cemented Navajo Sandstone the relation is better approximated by a power law.

Differences in degree of cementation (and type of cement) may thus have affected the lack of a strong correlation between the permeability- and Young's Modulus measurements of the formations in this study.

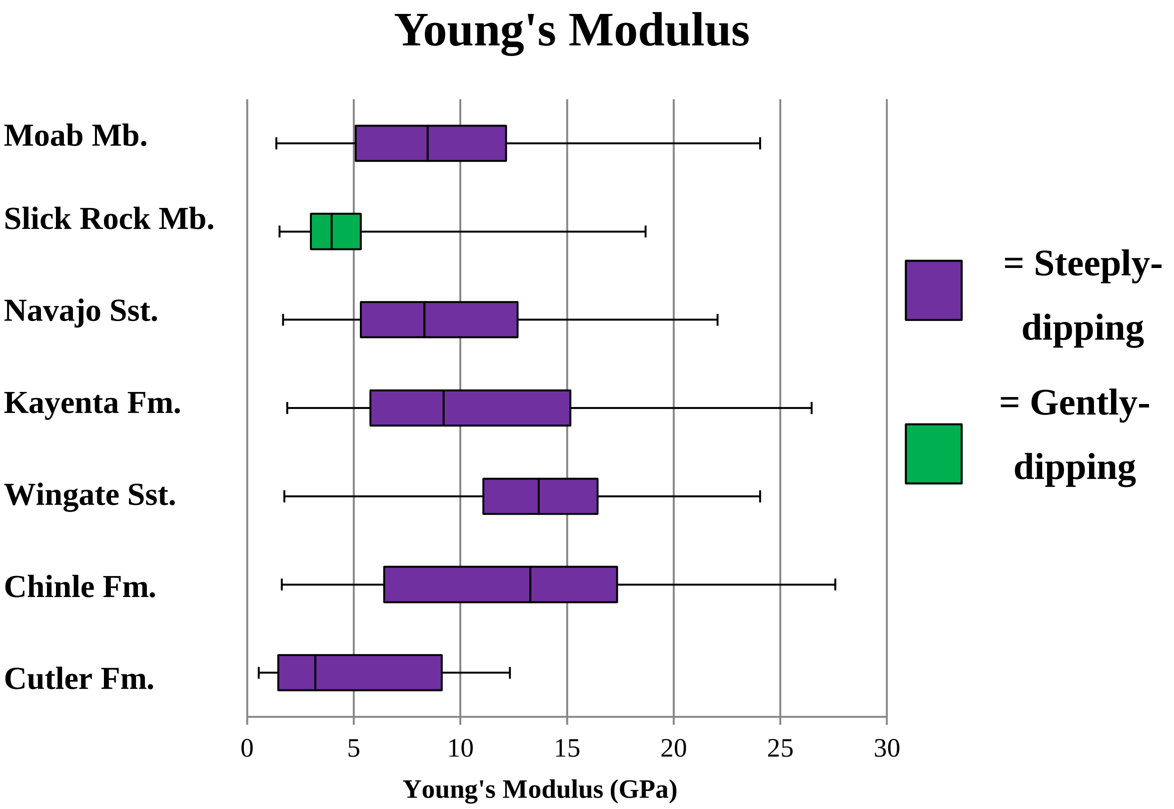

Figure 5.4: Boxplot illustrating measured Young's Modulus values (GPa) of the steeply-dipping intervals versus the gently-dipping intervals of the formations (25th- to 75th percentile boxplot).

5.5 Lateral differences within the Slick Rock Member

The erosional character of the Slick Rock Member stands out from those of the other formations in 3 ways; 1) the Slick Rock Member displays large lateral differences in erosional slopes, 2) the joints form in the fine-grained interdunes to a higher degree than in the coarse-grained dunes (Figure 5.5) and 3) the interdunes exhibit steeper erosional slopes than the dunes (Figure 5.5). The erosional character for the Slick Rock Member thus remarkably deviate from that of the overlying Moab Member (formed in a similar depositional environment), the latter being characterized by consistently steep erosional slopes with well-developed joint-patterns cutting through the entire height of the unit. The dune-sets and the interdune-sets of the Slick Rock Member, contrary to those of the Moab Member, are however considered to represent wet aeolian systems. This factor may have affected the observed differences in appearance between the two formations (this topic is further explored by Tunheim (2015)).

The proportion of quartz cement is generally low at each location whereas at the cliff-forming Courthouse locality, the content of carbonate cement is considerably higher (13%, in contrast to 1% and 3% in Bartlett Wash and Hidden Canyon, respectively). Further, the porosity is remarkably lower (4%, in contrast to 16% and 19% in Bartlett Wash and Hidden Canyon, respectively) and the Young’s Modulus values are higher (9 GPa, in contrast to 5 GPa and 3 GPa in Bartlett Wash and Hidden Canyon, respectively) at the Courthouse locality. In contrast, the average permeability values do not differ much between the different localities.

Generally, the permeability values are higher- and the Young’s Modulus values are lower for the dunes compared to the interdunes. The measured permeability values for the dunes and interdunes do not differ considerably between each location. In contrast, there are great differences regarding the measured Young’s Modulus values. In the steep-sloping Courthouse locality, the values are remarkably higher (both for the dunes and interdunes) than in the more gently-sloping Bartlett Wash and Hidden Canyon localities. On the other hand, the differences in Young’s Modulus values between the Bartlett Wash and Hidden Canyon localities are not that great (the values are generally slightly higher for both the dunes and interdunes at the Bartlett Wash locality).

For the Slick Rock Member, a high degree of carbonate cementation, low porosity values and high Young's Modulus values is thus found to facilitate the steep erosional profiles, whereas a low degree of carbonate cementation, high porosity values and low Young's Modulus values are characteristic for the gently-sloping localities.

The high degree of cementation at the Courthouse location compared to at the Bartlett wash- and Hidden Canyon locations may likely have contributed to the steep erosional slopes visible at Courthouse. Further, the high content of cement has likely affected the low porosity values recorded at this location. For other steep-sloping formations (e.g. the Wingate Sandstone and the Moab Member), high porosity values facilitates the steep erosional slopes. This relation is thus not evident for the Slick Rock Member.

Usually, competent, coarse-grained sand-units would be deformed by brittle deformation mechanisms (fracturing), and fine-grained formations would to a higher degree "give in" to the deformation and not build up a high enough stress level for fracturing to occur (subchapter 3.4). However, the joints in the Slick Rock Member have formed in the fine-grained interdunes to a much higher degree than in the coarse-grained dunes (Figure 5.5). Further, the interdunes display significantly steeper erosional slopes than the dunes (this difference is most evident at the overall gently-sloping Bartlett Wash and Hidden Canyon localities).

These findings are highly abnormal compared to features commonly observed in sandstones similarly made up by dunes and interdunes. However, the measured Young's Modulus values are generally higher for the interdunes than for the dunes in the Slick Rock Member. The explanation for the observed steeply-sloping, fractured interdunes may thus be linked to sedimentological- and mineralogical properties of these interdunes (resulting in relatively stiff, fractured intervals weathering to steep erosional slopes).

The distinct erosional character of the Slick Rock Member may most likely be linked to variations in the depositional environment (coastal dune environment) and differences in the degree of cementation. Another contributing factor may be the relatively large differences in thicknesses of the bed units observed both between the separate locations and between interdunes and dunes at each location (the dunes being considerably thicker than the interdunes, Figure 5.5). The differences in sedimentological- and mineralogical properties between the Courthouse-, Bartlett Wash- and Hidden Canyon locations, and the interdunes versus dunes are further explored by Tunheim (2015).

It is worth noting that a large fault cuts through the strata at the Courthouse locality (Figure 5.6 a)). Considering the proximity to a large fault, the sedimentological properties (e.g. cementation) may likely have been altered to a certain degree. The Bartlett Wash- and Hidden Canyon localities are in contrast not located close to large faults.

Only one rock sample suited for making a thin section was collected at the Courthouse locality during the field work. Some of the sedimentological- and mineralogical properties recorded for the Courthouse location are thus based on this one rock sample and thereby some degree of uncertainty is related to the data. Further, this rock sample was collected near the boundary between the Slick Rock Member and the underlying Dewey Bridge Member. There is some uncertainty related to whether the sample represents the uppermost part of the Dewey Bridge Member or the lowermost part of the Slick Rock Member. The low porosity and high degree of cementation observed on thin sections from this sample could however likely be representative for both the lowermost part of the Slick Rock Member and the uppermost part of the Dewey Bridge Member at this location, given their similar appearance and generally steep erosional slopes.

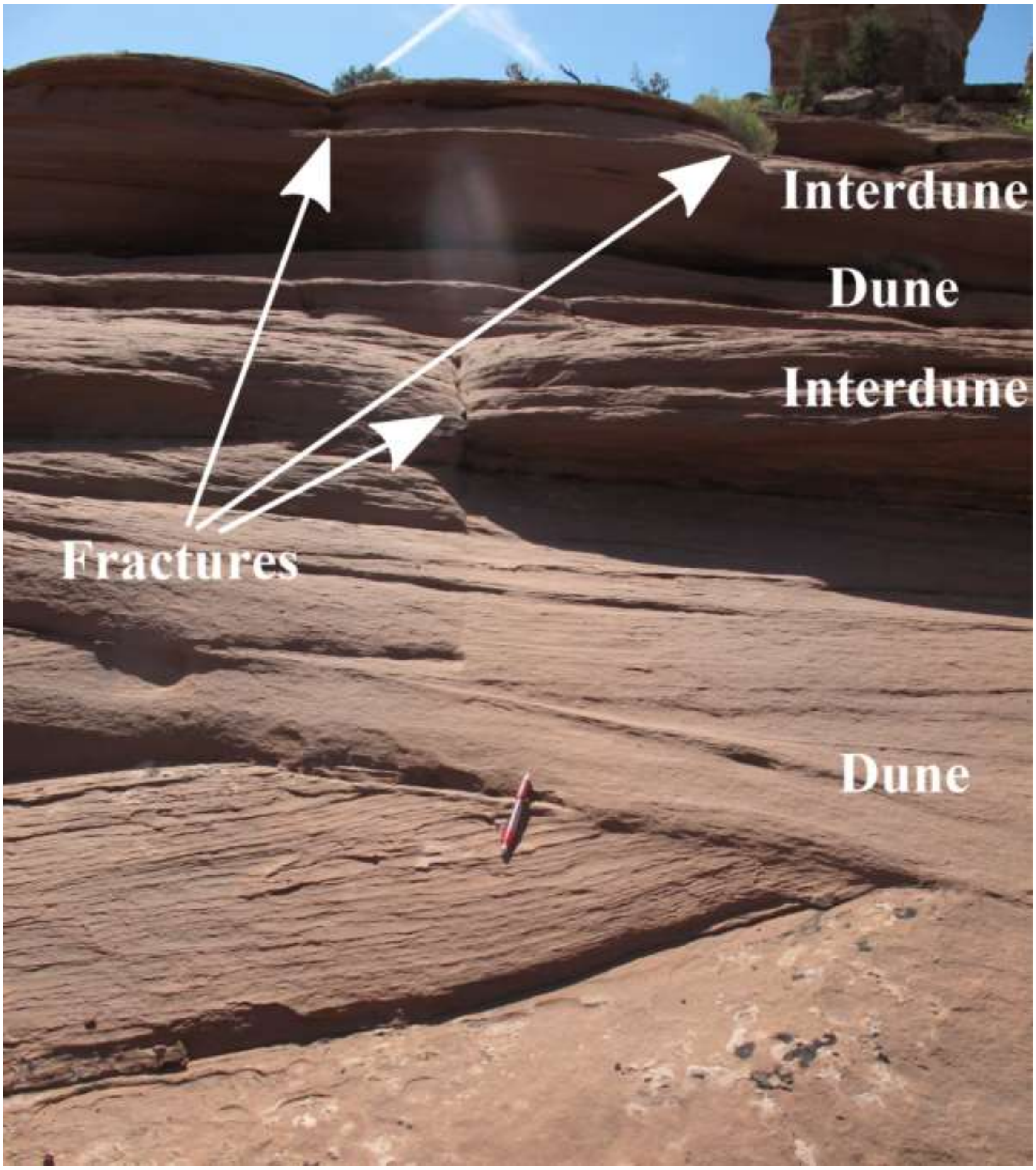

Figure 5.5: Image illustrating differences in degree of fracturing and differences in layer thickness of interdunes and dunes within the Slick Rock Member at the Hidden Canyon locality. Also note the steeper erosional slopes of the interdunes compared to the dunes. Coordinates: N38°43'01.8'' W109°48'09.3''.

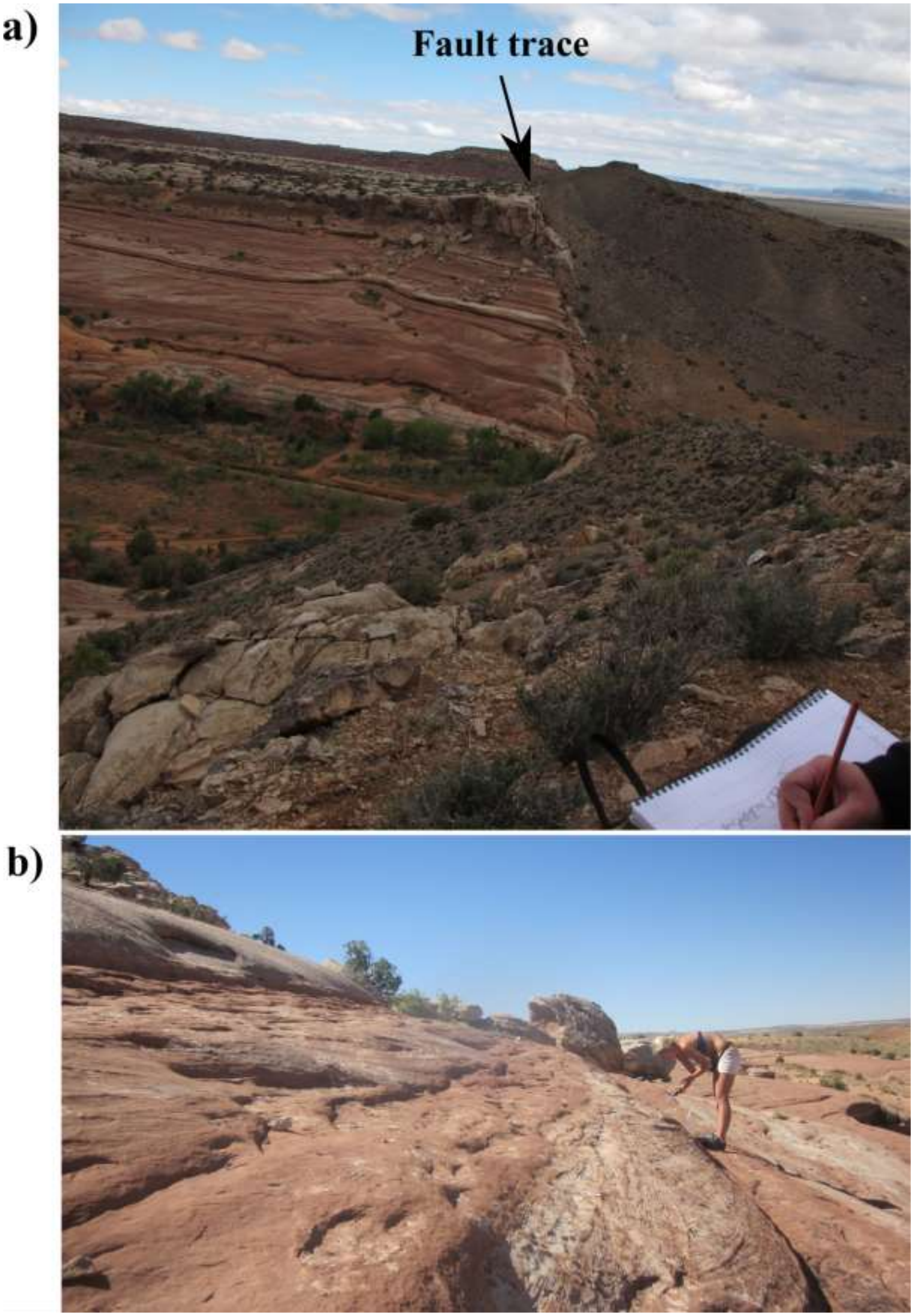

Figure 5.6: Images illustrating the differences in appearance of the Slick Rock Member in a) at the Courthouse location (coordinates: N38°42’29.9’’ W109°43’54.2’’) and in b) at the Hidden Canyon location (coordinates: N38°43’00.5’’ W109°48’10.1’’, photo by Ragnhild J. Tunheim). Note the fault trace cutting the strata at the Courthouse location.

5.6 Joints and joint mechanisms

The formations included in this study are fractured to a various degree. The large-scale, dominating fracture orientations in the area near Moab are relatively consistently trending NW-SE (Figure 4.28). The recorded small-scale fracture orientations are however more deviating (Figure 4.39). Some formations have joint-orientations that can be categorized into one- (the Slick Rock Member) or two (the Cutler Formation) joint-set orientations, whereas others display a wide range of recorded orientations (e.g. the Chinle Formation and the Wingate Sandstone). The small-scale fracture analyses have been carried out along the outcrops; in many places along highly weathered erosional surfaces where the true joint-trace orientation was difficult to measure. Considering that joints commonly develop in joint-sets of similar orientations (subchapter 3.5), the recorded joint-trace orientations should likely more systematically belong to a set of joint-trace orientations.

Large-scale joint-patterns are mainly developed in the Wingate- and Navajo sandstones and the Moab Member visible in map view in the areas of which each of them makes up the uppermost, exposed surfaces. Similar large-scale joint-patterns visible from map view have not developed in the Cutler- and Chinle formations and the Slick Rock Member, despite locations of relatively large areas of which these formations are exposed. The non-existent large-scale fracture-patterns of the overall finer-grained Cutler- and Chinle formations (of mixed-fluvial origins) seem logical. The Slick Rock Member however, formed in a relatively similar depositional environment as the overlying Moab Member, would be expected to display more similar fracture-patterns as those of the Moab Member.

Generally, fractures preferentially form in competent, coarse-grained sandstones (usually made up by large proportions of quartz) as a result of the high level of differential stress that can build up in such units before fracturing occurs (subchapter 3.4). A finer-grained unit consisting of larger proportions of silt and clay would more readily give in to the deformation and not be able to build up a substantial stress level to initiate jointing.

The observed small-scale joint-patterns developed in the coarser-grained intervals (e.g. in dune- and channel facies) for all the formations (except for the Slick Rock Member) thus make sense. A difference in the joint distributions is however found between those developed in formations of aeolian origins and in those of mixed-fluvial origins. The large, more homogenous, coarse-grained dune intervals within the formations of aeolian origins result in more systematic joint-patterns often penetrating the entire height of the unit (also cutting through the relatively thin, fine-grained intervals). When there is a smaller difference in the thickness of the bed units of the coarse-grained- and the fine-grained intervals (such as for the Cutler- and Chinle formations) the joints however become confined within the sand-bodies. Keeping this in mind, the small bed thicknesses observed for the Kayenta Formation of interbedded coarse-grained and fine-grained intervals, may have prohibited systematic joint-sets to form. It may thus seem like a considerable thickness of the sand-bodies compared to the finer-grained bed units is required for small-scale, systematic joint-patterns to develop.

The Kayenta Formation, the Navajo Sandstone and the Slick Rock Member all display certain deviating fracture characteristics. Joint-patterns such as those developed in the coarse-grained ledge-intervals of the Cutler- and Chinle formations (of similarly mixed-fluvial origin) could not be observed for the Kayenta Formation. The Kayenta Formation, displaying the highest content of quartz grains and highest porosity values of the formations of fluvial origins, would be expected to develop fractures in the channel-facies in the same manner as the Cutler- and Chinle formations. However, the generally low content of cement in the Kayenta Formation in comparison to the Cutler- and Chinle formations may have influenced the lack of systematic fracture-patterns (making it generally softer).

The fractures developed within the Slick Rock Member are mainly distributed in the finer-grained interdunes and almost no fractures can be observed in the coarser-grained dunes (Figure 5.5). The measured Young's Modulus values are generally higher for the interdunes than for the dunes and a possible explanation for the fractured interdunes may thus be linked to sedimentological properties of these interdunes (resulting in relatively stiff, fractured intervals). The dune- and interdune-sets of the Slick Rock Member, contrary to those of the Moab Member, are considered to represent wet aeolian systems. The lack of well-developed fracture-patterns (with joints penetrating the entire height of the unit) within the Slick Rock Member may thus be related to sedimentological properties of the "wet" dunes and interdunes (again affecting the level of differential stress building up).

Despite being deposited in a similar widespread, arid, desert environment, the Navajo Sandstone does not display small-scale fracture-patterns visible in outcrop similar to those characteristic for the Wingate Sandstone. However, only widely-spaced, large-scale joint-patterns have developed within the Navajo Sandstone (mainly only visible in map view). A possible contributing factor to this phenomenon may be linked to the sedimentological- and mechanical properties of the overlying Dewey Bridge Member of the Carmel Formation. The Dewey Bridge Member, once covering the Navajo Sandstone, has been removed by erosional processes in large parts of the study area during the uplift and exhumation of the Colorado Plateau. This apparently poorly resistant rock formation, made up by a series of interbedded siltstones and shales (usually 10-20 m thick) (Cruikshank and Aydin, 1995) may have resulted in small build-ups of stress for the underlying Navajo Sandstone (again prohibiting small-scale joint-patterns to form).

The vast exposure of the Navajo Sandstone has likely resulted in extensive erosion along the widely-spaced joint-traces in many places (contributing to the formations of “grooves” (along the joint-traces) and “fins” (between the joint-traces)) and again influenced its bulbous and undulating surface morphology.

The Wingate Sandstone on the other hand, is mostly covered by the Kayenta Formation throughout the study area (Figure 5.2). The protecting “blanket” of the Kayenta Formation may have caused large build-ups of stress within the Wingate Sandstone, resulting in small-scale, systematic fracture-patterns to form. The overall fracture-patterns and related erosional slope values for the Navajo Sandstone may have looked more similar to those of the Wingate Sandstone if it was covered with a more resistant formation such as the Kayenta Formation. Considering the similarities in sedimentological-, mineralogical and mechanical properties of the Wingate- and Navajo sandstones, a possible explanation to their characteristic fracture-patterns may thus be linked to properties of their respective under- and overlying units (again affecting the level of stress building up).

It seems logical that the erosional signature of the modestly fractured, highly exposed Navajo Sandstone looks different than that of the “protected”, highly fractured Wingate Sandstone. If there is a strong correlation between small-scale joint-patterns and steep erosional slopes, the lack of such small-scale joint-patterns within the Navajo Sandstone accompanied by its large variety in erosional slopes seems to make sense.

A common feature observed in the Navajo Sandstone is deformation bands. It may thus seem like small-scale brittle deformation within the Navajo Sandstone is characterized by deformation bands rather than fractures.

The relation between fracture-patterns and erosional slopes seems to be strong. Well-developed, small-scale joint-patterns correlate with steep erosional slopes for the Cutler- and Chinle formations (ledge-intervals), the Wingate Sandstone and the Moab Member. Considering the large surface areas exposed along joint-traces (more prone to erosional processes), the vertical joint-traces will likely favor the formation of steep erosional profiles.

As mentioned, joint-patterns are not distributed in the same manner for the Kayenta Formation as for e.g. the Wingate Sandstone (Figure 5.7). The erosional slopes are however relatively steep for the Kayenta Formation as well. Considering the observed relation between well-developed fracture-patterns and steep erosional slopes, the steep slopes of the Kayenta Formation may be linked to- and affected by the fracture characteristics of the underlying Wingate Sandstone.

The strong correlation between well-developed, small-scale fracture-patterns, steep erosional slopes and high recorded Young’s Modulus values seems logical (e.g. as observed in the ledge-intervals of the Cutler- and Chinle formations, in the Wingate Sandstone and the Moab Member). Further, the relation between well-developed, small-scale fracture-patterns, steep erosional slopes and high Young’s Modulus values will likely correlate strongly to a high degree of cementation (making the formation stiffer and more competent). The lack of small-scale, systematic fracture-patterns in the Kayenta Formation, being the formation of a fluvial origin displaying the lowest content of cement, supports this theory.

Such conclusions are however hard to draw considering that the rock samples, forming the basis for the thin section studies (of which cementation characteristics are described) were collected at a variety of locations at both steeply-sloping and gently-sloping intervals. In order to further explore if there is a link between the fracture-patterns, slopes, Young’s Modulus values and degree of cementation, the cementation properties should be based on rock samples collected consistently from the steep-sloping intervals.

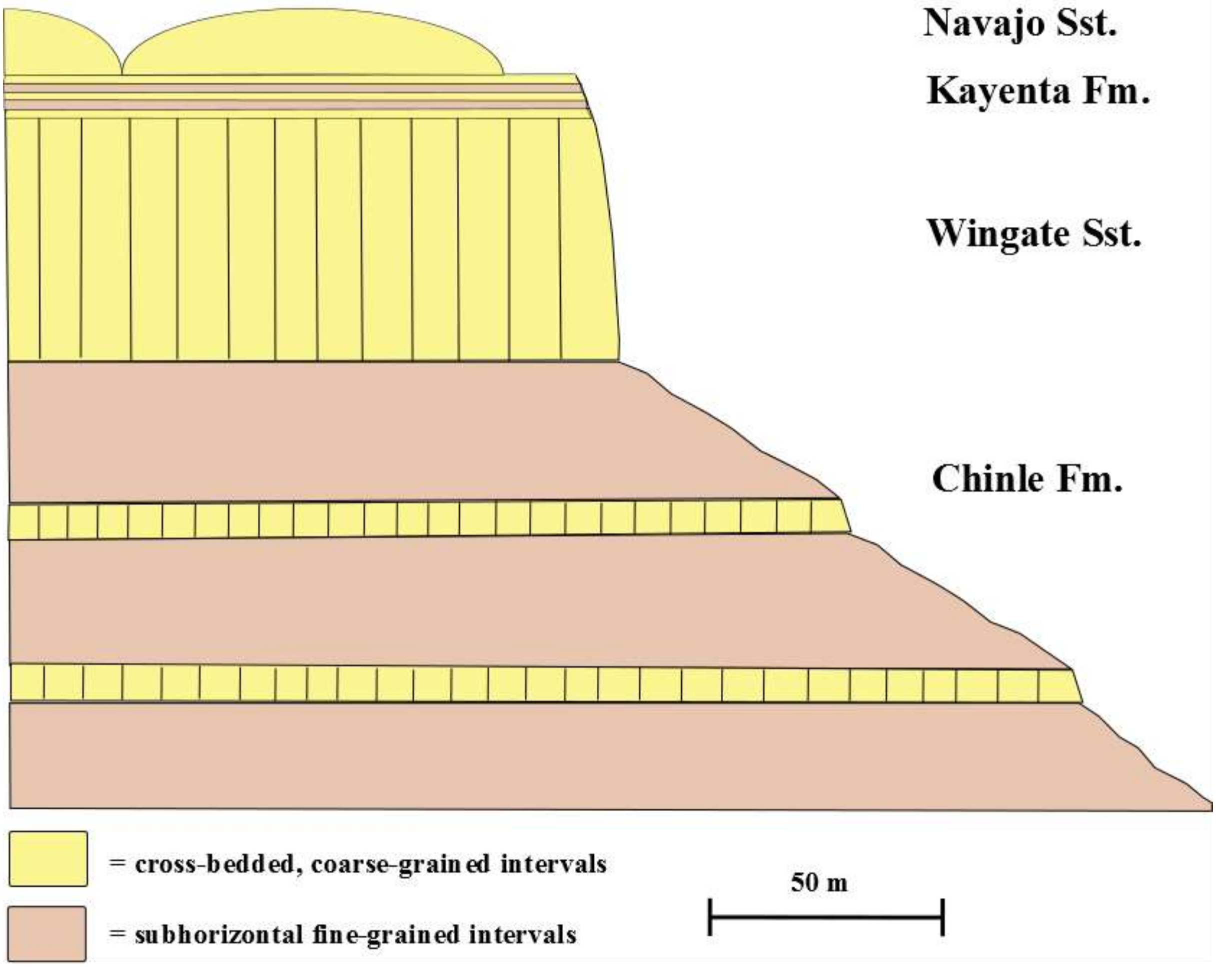

Figure 5.7: Generalized, schematic illustration of the fracture characteristics and erosional slopes of coarse-grained- and fine-grained intervals of the Chinle Fm., the Wingate Sst., the Kayenta Fm. and the Navajo Sst.. The Cutler Fm. would display similar fracture-patterns as those illustrated for the Chinle Fm. The colors are applied to separate between fine-grained- and coarse-grained intervals and do not necessarily reflect the true colors of the formations.

It is worth noting that the fracture frequency distributions of the Cutler- and Chinle formations have been carried out along the ledge-intervals (making up only small parts of the overall gently-sloping formations, Figure 5.1). Fractures have however not developed in the gently-sloping intervals. Taking this into consideration it would be incorrect to describe these two formations as highly-fractured in comparison to formations such as the Wingate Sandstone and the Moab Member.

The characteristic fracture-patterns and erosional slopes for the Chinle Formation, the Wingate Sandstone, the Kayenta Formation and the Navajo Sandstone are illustrated in Figure 5.7 and for the Slick Rock- and Moab Member in Figure 5.8.

Small, fine-grained intervals within the Wingate- and Navajo sandstones and the Moab Member are not indicated in these figures. The fracture-patterns within the Cutler Formation would be similar to those illustrated for the Chinle Formation (Figure 5.7). Note the similarities in surface morphology for the uppermost, exposed formations (the Navajo Sandstone and the Moab Member) compared to the "protected" Wingate Sandstone.

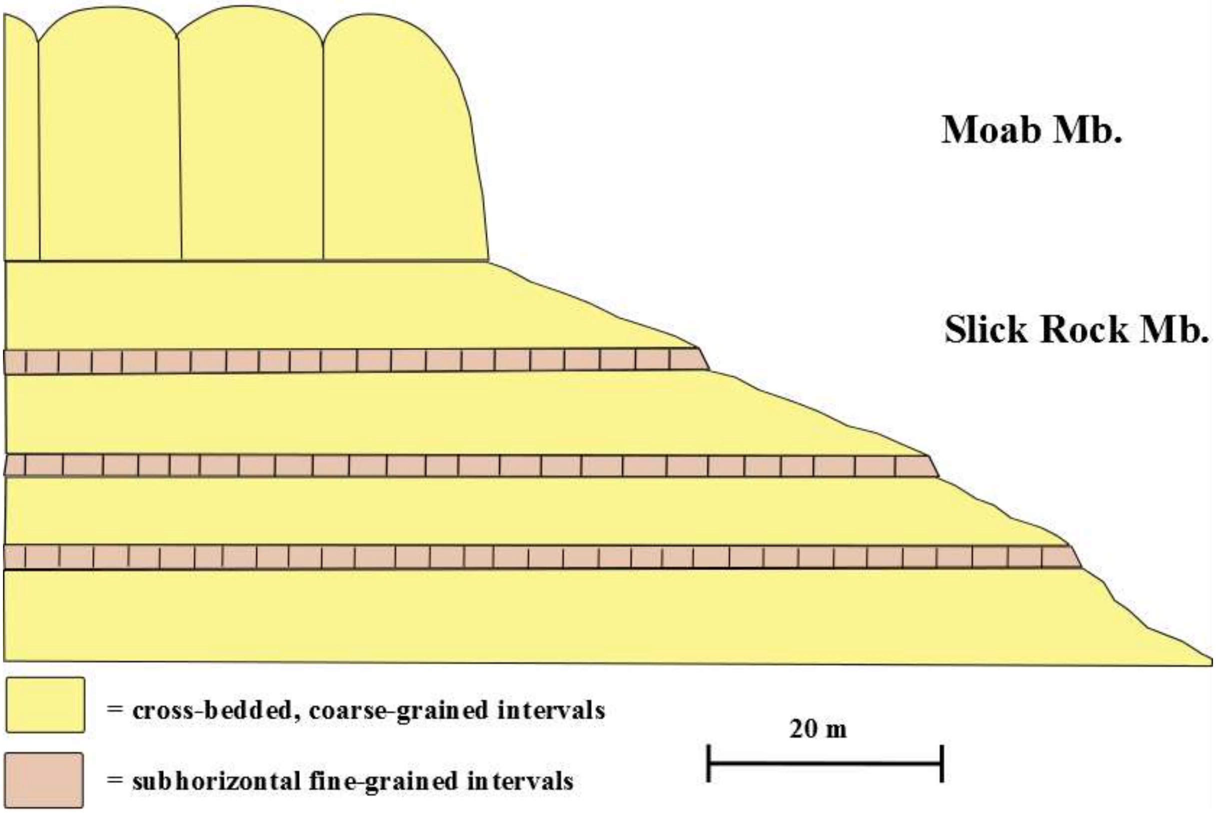

Figure 5.8: Generalized, schematic illustration of the fracture characteristics and erosional slopes of coarse-grained- and fine-grained intervals of the Slick Rock- and Moab Member. Note the fractures preferentially forming in the fine-grained intervals rather than in the coarse-grained intervals for the Slick Rock Member. Further, these fine-grained intervals display significantly steeper erosional slopes than the coarse-grained intervals. The colors are applied to separate between fine-grained- and coarse-grained intervals and do not necessarily reflect the true colors of the formations.

The fractures are formed in a relatively systematic pattern for all of the formations displaying small-scale fracture-patterns. It seems to be a strong correlation between the average spacing between the fractures and the thickness of the jointed layer (Figure 4.43). Thin layers correlate with a small spacing between the joints. This relation is strongest for the thinner layers (such as the layers in the Cutler- and Chinle formations and the Slick Rock Member).

The ~60 m thick layers of the Wingate Sandstone generally have a relatively small fracture-spacing compared to the average layer thickness.

Joints usually form in areas of local stress accumulations (such as near microflaws and microfractures) in the host rock. The bigger the rock volume, the higher is the number of structural weaknesses (microflaws and microfractures) (Fossen, 2010). Keeping this in mind, the relatively narrow fracture spacing compared to the layer thickness observed in the immense rock volume of the Wingate Sandstone may be related to a large number of structural weaknesses along which joints would readily form. Further, the position of the Wingate Sandstone (being situated between the underlying Chinle Formation and covered by the resistant, overlying Kayenta Formation) may have contributed to its high fracture-density.

5.7 Timing of joint propagation

The overall timing of the joint propagation in the study area and the mechanisms involved is unclear and deflecting theories have been expressed. Considering that the overall large-scale joint orientations in the area are parallel to the trend of the large salt structures (trending approximately NW-SE, not reflecting a regional pattern) it seems logical to relate their formation to the growth of the salt structures. However, pointed out by Cruikshank and Aydin (1995), it is important to realize that Salt Valley anticline was well established at the time the Entrada Sandstone (comprising the Slick Rock- and Moab Member among others) was deposited, and that fractures in the Entrada Sandstone can represent only parts of the history of the anticline. Salt diapirism occurred from Middle Carboniferous- through Jurassic time, but did however gradually diminish after Chinle time. Based on studies of angular unconformities resulting from the salt diapirism, continued growth into Cretaceous time is hard to prove (Baars and Doelling, 1987).

At a later time (likely during the Laramide orogeny of Late Cretaceous - Early Cenozoic age), the area was submitted to a west-to-east compressional tectonic event, causing the northwest-trending zones of thick salt to be tightened into true anticlines while adjacent areas became synclines. One interpretation (Baars and Doelling, 1987) is that the joint-patterns developed during this tectonic compression of the strata. However, considering the work of Engelder (1985) (subchapter 3.2) suggesting that a distinction should be made between different types of joints propagating at different times during a tectonic cycle, a classification of the joints as *release-joints* (propagating during the last stages of a tectonic cycle) may seem adequately likely.

Engelder (1985) explored the loading paths of joint propagation during a tectonic cycle (of burial, lithification, deformation and denudation) of clastic rocks within sedimentary basins based on an example from the Appalachian Plateau, USA. A distinction was made between tectonic-, hydraulic-, unloading- and release joints based on the timing of joint propagation during the tectonic cycle. Tectonic- and hydraulic joints form at depth prior to uplift in response to abnormal fluid pressures, whereas unloading- and release joints form near the surface in response to thermal-elastic contraction accompanying erosion and uplift (Engelder, 1985). A distinction is made between unloading- and release joints because a tectonic compression and the fabric it leaves do have a bearing on the orientation of the release joints (in contrast to the unloading joints, with orientations being stress-controlled). In the case of the release joints, the orientation of the future joint plane is normal to the tectonic compression.

The joint-types recognized by Engelder (1985) form at the end of different loading paths and none of them form simultaneous to the active tectonic compressional event. The concept of release joints thus seem applicable for explaining the observed joint-patterns in the area near Moab, considering its history of salt diapirism, tectonic compression, burial, and subsequent uplift and ongoing erosion of the Colorado Plateau.

Nuccio and Condon (1996) constructed a burial and thermal-history model for the Moab area. The area around Moab is in the structurally deeper part of the Paradox Basin. During the Late Paleozoic time, this basin was rapidly subsiding, allowing for thick (up to ~3.6 km) sequences of Carboniferous and Permian strata to accumulate. However, during Triassic and Jurassic time, only a moderate ~0.97 km of strata was deposited in this part of the basin. The timing for the maximum burial is estimated at about 37 Ma in this area. Thus, beginning at about 37 Ma and continuing until the present, uplift and erosion have removed approximately ~3.6 km of rocks from this area.

All of the formations in this study display some degree of quartz- and carbonate cementation. Whereas carbonate cements form at all depth from the soil zone to deep burial (at least 2-3 km) (Morad, 2009), most quartz cement is precipitated by cooling, ascending formation water at burial depths of several kilometers where temperatures range from 60° to 100° C (McBride, 1989). Considering that the cementation (making the formations more competent, possibly "locking in" residual stress in the formations) likely occurred while the formations were buried at certain depths, a subsequent uplift-related origin of the joints seems logical.

The orientation of the joint-traces (parallel to the axis of the large salt structures in the area) may further be linked to the compressional forces acting during the Laramide orogeny. Such forces may have induced anisotropic pressure solution (pressure solution along grain contacts with a preferred orientation) and/or cementation, at a high angle to the east-west oriented $\sigma_{1.}$ A residual stress from the Laramide orogeny may thus have been locked in by cementation in parts of the sandstones during burial and again released close to the surface during uplift, resulting in *release-joints* to form.

Some of the deformation bands distributed in the sandstones in the study area are interpreted to be directly linked to the growth of the salt diapirs and subsequent collapse (Antonellini et al., 1994). Considering that the joints in the study area consistently cut through the deformation bands (and are formed in different stress conditions), the joints may readily have formed considerably later than the deformation bands.

6 Conclusions and future work

6.1 Conclusions

The aim of this study has been to explore possible causes for the different weathering characteristics observed for seven formations (the Cutler Fm., the Chinle Fm., the Wingate Sst., the Kayenta Fm., the Navajo Sst., the Slick Rock Mb. and the Moab Mb.) outcropping in southeastern Utah, USA. In this study, facies associations, sedimentological-, mineralogical- and mechanical properties and fracture-patterns have been investigated and analyzed in an attempt to explain the different appearances of these continental deposits. Further, one of the key questions I have attempted to address in this thesis has been: what is the relation between joint-patterns and observed erosional signatures for the formations?

After studying the distributions of fracture-patterns within the formations, one conclusion seems logical to draw: the degree of jointing (e.g. densely-fractured in the Wingate Sandstone compared to poorly-fractured in the Navajo Sandstone) and the joint-distributions within each formation (e.g. penetrating the entire height of the unit for the Wingate Sandstone and the Moab Member, compared to only developing in coarse-grained intervals of the Cutler- and Chinle formations) seems to have a great impact on the observed erosional slopes (given by the increased erosion along the vertical joint-traces). However, the fracture characteristics are again strongly related to the sedimentological-, mineralogical-, and mechanical properties of the formations.

Further conclusions that can be drawn based on the work of Tunheim (2015) (mainly exploring the sedimentological- and mineralogical properties) and myself (mainly exploring the mechanical properties and fracture-patterns) presented in this thesis include:

- The variations in erosional slopes are clearly highest for the Slick Rock Member (17-86°), the Navajo Sandstone (14-88°) and the Kayenta Formation (24-89°). In contrast, the Cutler Formation (26-38°), the Chinle Formation (13-38°), the Wingate Sandstone (64-90°) and the Moab Member (68-87°) show significantly more uniform slope values throughout the study area.

- In general, formations of aeolian origins (e.g. the Wingate Sandstone and the Moab Member) have considerably steeper erosional slopes than those of fluvial origins (e.g. the Cutler- and Chinle formations).

- The proportions of quartz grains increase stratigraphically from the bottom (the Cutler Formation) to the top (the Moab Member), whereas the proportions of feldspar grains show the opposite trend.

- The most steeply-dipping formations (e.g. the Wingate Sandstone, the Kayenta Formation and the Moab Member) show high proportions of quartz cement compared to the gently-sloping formations (e.g. the Cutler- and Chinle formations).

- A strong correlation is found between steep erosional slopes and high porosity values of the formations (e.g. the Moab Member and Wingate Sandstone with average porosities of 19% and 13%, respectively in contrast to the Cutler- and Chinle Formation with average porosities of 4% and 6%, respectively).

- General trends for the steep-sloping formations are that they are relatively better sorted and have more rounded grains than the gently-sloping formations.

- The recorded permeability values are found to correlate strongly with the overall depositional environment rather than to the observed erosional slopes of the formations. Two observations support the conclusion that the relation between permeability values and erosional slopes are weak;

  1) Large differences in values between formations of aeolian- (display generally high values) and mixed-fluvial (display generally low values) origins regardless that all measurements were carried out on steep intervals, and

  2) Remarkably small differences in permeability values between the cliff-forming Courthouse location and the gently-sloping Hidden Canyon location.

- The recorded Young's Modulus values are found to correlate strongly to the erosional slopes of the formations. Two observations support the conclusion that the relation between Young's Modulus values and erosional slopes are strong;

  1) Similarly high Young' Modulus values for the steep-sloping intervals of all the formations and

2) Considerably higher values at the cliff-forming Courthouse location than at the gently-sloping Hidden Canyon location.

- The erosional character for the Slick Rock Member stands out from those of the other formations in 3 ways;
  1) It displays large lateral differences in erosional slopes,
  2) The joints form in the fine-grained interdunes to a higher degree than in the coarse-grained dunes and
  3) The interdunes exhibit steeper erosional slopes than the dunes.

- For the Slick Rock Member, a high degree of carbonate cementation, low porosity values and high Young’s Modulus values facilitate the steep erosional profiles, whereas a low degree of carbonate cementation, high porosity values and low Young’s Modulus values are characteristic for the gently-sloping localities.

- “Dry” dune- and interdune systems (such as those making up the Wingate- and Navajo sandstones and the Moab Member) seem to favor the formation of joints penetrating the entire height of the unit. In contrast, “wet” dune- and interdune systems seem to result in joints only penetrating certain intervals of the unit.

- The differences in appearance of the Slick Rock Member (mainly gently-sloping) and the overlying Moab Member (consistently steep-sloping) of similar aeolian origin seem to be related to their wet- and dry aeolian systems, respectively, again affecting the joints to partly develop and fully develop within the units, respectively. Consequently, the erosional slopes of the Moab Member (with joints penetrating the entire height of the unit) have become steep whereas those of the Slick Rock Member (with joints only penetrating certain intervals of the unit) have become remarkably more gentle.

- Steep-sloping formations dominantly made up by sand fractions such as the Wingate Sandstone and the Moab Member are generally highly fractured with systematic fracture-patterns. The overall gently-sloping formations (made up by alternating coarse-grained and fine-grained intervals) such as the Cutler- and Chinle formations are fractured to a much lower degree with fractures that only penetrate the steep-sloping (coarse-grained) intervals within the formations. However, relations between layer-thickness and average fracture-spacing are relatively strong for all the formations (the relation is however stronger for the thinner layers).

- The Kayenta Formation, the Navajo Sandstone and the Slick Rock Member all display some degree of abnormal fracture-characteristics;
  1) The Kayenta Formation lacks well-developed joint-patterns (a possible explanation may be linked to the generally small thicknesses of the bed units)
  2) Only widely-spaced, large-scale joint-patterns have developed within the Navajo Sandstone which seems to preferentially deform by deformation-band formation rather than by small-scale fracturing (a possible explanation may be linked to the sedimentological-, mineralogical and mechanical properties of its respective over- and underlying units, affecting the level of stress building up within the Navajo Sandstone), and
  3) The joints in the Slick Rock Member have preferentially formed in the finer-grained interdunes rather than in the coarser-grained dunes (a possible explanation may be linked to sedimentological- and mechanical properties differing between the interdunes and dunes, again being linked to variations in the coastal-dune depositional environment).

- The fracture-characteristics seem to have a great effect on the observed erosional signature of the formations and a strong correlation is found between well-developed, small-scale fracture-patterns, steep erosional slopes and high recorded Young's Modulus values.

- The wide spacing between the joints within the Navajo Sandstone seems to favor the development of more gently-sloping erosional profiles in comparison to the steep slopes of the densely-fractured Wingate Sandstone.

- The timing of the joint propagation of the joints in the study area is unclear. A classification of the joints as *release joints* may seem adequate. The orientation of the joint-traces (parallel to the axis of the large salt structures in the area) may be linked to the compressional forces acting during the Laramide orogeny. Such forces may have induced anisotropic pressure solution and/or cementation at a high angle to the east-west oriented σ_1. A residual stress from the Laramide orogeny may thus have been "locked in" by cementation in parts of the sandstones during burial and again released close to the surface during uplift, resulting in *release-joints* to form.

6.2 Future work

The main aim of the study presented in this thesis has been to explore possible explanations for the differences in appearance of seven continental formations outcropping in southeastern Utah, USA. Working on this project, a few suggestions for future work have come to mind:

- A large fault cut through the strata at the Courthouse location where the Slick Rock Member weathers to form steep erosional slopes. What is the relation between the sedimentological- and diagenetic effects of the fault on the Slick Rock Member and the observed steep erosional slopes?

- The formations in this study do all display varying degrees of quartz- and carbonate cementation and varying degrees of joint distributions. Considering that cementation would make a formation more competent and thus promote fracturing to occur, a strong relation between a high degree of cementation and well-developed fracture-patterns would be expected. Such conclusions are however hard to draw based on this study, considering that the rock samples, forming the basis for the thin section studies (of which cementation characteristics are described) were collected at a variety of locations at both steeply-sloping (fractured) and gently-sloping (not fractured) intervals. In order to further explore if there is a link between these two parameters, the cementation properties should be based on rock samples collected consistently from the fractured intervals. An interesting topic to explore would thus be the relation between the degree of cementation (and type of cement) and the observed joint-patterns developed in sandstone formations. Further, the influence of the timing of the cementation during the diagenetic history of a rock volume could also be explored in this respect.

- The erosional signatures of the Navajo- (displaying undulating surface morphologies) and the Wingate (forming nearly vertical cliffs) sandstones are likely strongly linked to differences in fracture characteristics between the formations (only large-scale fracture-patterns within the Navajo Sandstone in contrast to well-developed, small-scale fracture-patterns within the Wingate Sandstone). However, three intriguing questions can be posed regarding the differences in fracture characteristics between the formations:

  1) Why have the Navajo- and Wingate sandstones (formed in similar depositional environment) developed such deviating fracture-patterns?

2) How big of a role do the sedimentological-, mineralogical- and mechanical properties of their respective under- and overlying units play to the observed fracture-patterns within these formations? and

3) Why is brittle deformation represented by deformation bands within the Navajo Sandstone and not by small-scale joint-patterns such as those observed within the Wingate Sandstone?

7 References

ALIKARAMI, R., TORABI, A., KOLYUKHIN, D. & SKURTVEIT, E. 2013. Geostatistical relationships between mechanical and petrophysical properties of deformed sandstone. *International Journal of Rock Mechanics and Mining Sciences,* 63**,** 27-38.

ALLMENDINGER, R. W., CARDOZO, N. & FISHER, D. M. 2011. *Structural geology algorithms: Vectors and tensors*, Cambridge University Press.

ANTONELLINI, M. & AYDIN, A. 1994. Effect of faulting on fluid flow in porous sandstones: petrophysical properties. *Aapg Bulletin,* 78**,** 355-377.

ANTONELLINI, M. & AYDIN, A. 1995. Effect of faulting on fluid flow in porous sandstones: geometry and spatial distribution. *Aapg Bulletin,* 79**,** 642-670.

ANTONELLINI, M. A., AYDIN, A. & POLLARD, D. D. 1994. Microstructure of deformation bands in porous sandstones at Arches National Park, Utah. *Journal of Structural Geology,* 16**,** 941-959.

AYDIN, A. 1978. Small faults formed as deformation bands in sandstone. *Pure and Applied Geophysics,* 116**,** 913-930.

BAARS, D. & DOELLING, H. 1987. Moab salt-intruded anticline, east-central Utah. *Geological Society of America Centennial Field GuideÐRocky Mountain Section***,** 275-280.

BAARS, D. L. 1983. The Colorado Plateau, a geological history: University of New Mexico Press, 179 p., Albuquerque.

BAARS, D. L. 1993. Canyonlands Country: Geology of Canyonlands and Arches National Parks: University of Utah Press, Salt Lake City, UT, 138p.

BAARS, D. L., AND H. H. DOELLING 1987. Moab salt-intruded anticline, east-central Utah in: S. S. Beus (ed.) Rocky Mountain section of the Geological Society of America, Centennial Field Guide, Volume 2, Geological Society of America, Boulder CO, p. 275-280.

BARBEAU, D. L. 2003. A flexural model for the Paradox Basin: implications for the tectonics of the Ancestral Rocky Mountains. *Basin Research,* 15**,** 97-115.

BLAKEY, R. C. & RANNEY, W. 2008. *Ancient landscapes of the Colorado Plateau*, Grand Canyon Assn.

CARDOZO, N. & ALLMENDINGER, R. W. 2013. Spherical projections with OSXStereonet. *Computers & Geosciences,* 51**,** 193-205.

CRABAUGH, M. & KOCUREK, G. 1993. Entrada Sandstone: an example of a wet aeolian system. *Geological Society, London, Special Publications,* 72**,** 103-126.

CRUIKSHANK, K. M. & AYDIN, A. 1995. Unweaving the joints in Entrada Sandstone, Arches National Park, Utah, U.S.A. *Journal of Structural Geology,* 17**,** 409-421.

CRUIKSHANK, K. M., ZHAO, G. & JOHNSON, A. M. 1991a. Analysis of minor fractures associated with joints and faulted joints. *Journal of Structural Geology,* 13**,** 865-886.

CRUIKSHANK, K. M., ZHAO, G. & JOHNSON, A. M. 1991b. Duplex structures connecting fault segments in Entrada Sandstone. *Journal of Structural Geology,* 13**,** 1185-1196.

DOELLING, H. H. 1985. Geology of Arches National Park, Utah Geological and Mineral Survey, Map 74, Salt Lake City UT, 15p.

DOELLING, H. H. 2001. *Geologic Map of the Moab and eastern part of the san Rafael Desert 30'x60' Quadrangles, Grand and Emery Counties, Utah, and Mesa County, Colorado*.

DOELLING, H. H., OVIATT, C. G. & HUNTOON, P. W. 1988. Geology of Salt Valley anticline and Arches National Park, Grand County, Utah. *Salt Deformation in the Paradox Region, Utah (B-122),* Utah Geol. & Min. Surv. Salt Lake City, Utah. 1-58.

DOELLING, H. H., ROSS, M. L. & MULVEY, W. E. 2002. *Geologic map of the Moab 7.5'quadrangle, Grand County, Utah*, Utah Geological Survey, Utah Department of Natural Resources.

DYER, J. R. 1983. *Jointing in sandstones, Arches National Park, Utah*, Stanford University, Department of Geophysics.

DYER, R. 1988. Using joint interactions to estimate paleostress ratios. *Journal of Structural Geology,* 10**,** 685-699.

ENGELDER, T. 1985. Loading paths to joint propagation during a tectonic cycle - an example from the Appalachian Plateau, U.S.A. *Journal of Structural Geology,* 7**,** 459-476.

FOOS, A. 1999. *Geology of the Moab region (Arches, Dead Horse Point and Canyonlands)* [Online]. Geology Department, University of Akron. Available: http://www.nature.nps.gov/geology/education/Foos/moab.pdf.

FOSSEN, H. 2010. *Structural geology,* Cambridge, Cambridge University Press.

FOSSEN, H., SCHULTZ, R. A. & TORABI, A. 2011. Conditions and implications for compaction band formation in the Navajo Sandstone, Utah. *Journal of Structural Geology,* 33**,** 1477-1490.

HAMBLIN, W. K., AND CHRISTIANSEN, E.H 2004. Earth's Dynamic Systems: Tenth Edition, Pearson Education/Prentice Hall, Upper Saddle River, New Jersey, 759 p.

HINTZE, L. F. 2005. *Utah's spectacular geology: how it came to be*, Department of Geology, Brigham Young University.

HINTZE, L. F. & KOWALLIS, B. J. 2009. *Geologic history of Utah,* Provo, Utah.

HOBBS, D. 1967. The formation of tension joints in sedimentary rocks: an explanation. *Geological Magazine,* 104**,** 550-556.

KATZ, O., RECHES, Z. & ROEGIERS, J.-C. 2000. Evaluation of mechanical rock properties using a Schmidt Hammer. *International Journal of Rock Mechanics and Mining Sciences,* 37**,** 723-728.

KELLEY, V. C. & CLINTON, N. J. 1960. *Fracture systems and tectonic elements of the Colorado Plateau*, University of New Mexico Press.

MCBRIDE, E. F. 1989. Quartz cement in sandstones: a review. *Earth-Science Reviews,* 26**,** 69-112.

MORAD, S. 2009. *Carbonate Cementation in Sandstones: Distribution Patterns and Geochemical Evolution (Special Publication 26 of the IAS)*, John Wiley & Sons.

NARR, W. & SUPPE, J. 1991. Joint spacing in sedimentary rocks. *Journal of Structural Geology,* 13**,** 1037-&.

NUCCIO, V. F. & CONDON, S. M. 1996. Burial and thermal history of the Paradox Basin, Utah and Colorado, and petroleum potential of the Middle Pennsylvanian Paradox Formation.

OLSON, J. 1989. Inferring paleostresses from natural fracture patterns - a new method. *Geology,* 17**,** 345-348.

POLLARD, D. D. & AYDIN, A. 1988. Progress in understanding jointing over the past century. *Geological Society of America Bulletin,* 100**,** 1181-1204.

STOKES, W. L. 1986. *Geology of Utah*, Utah Museum of Natural History Salt Lake City.

TRUDGILL, B. D. 2011. Evolution of salt structures in the northern Paradox Basin: controls on evaporite deposition, salt wall growth and supra-salt stratigraphic architecture. *Basin Research,* 23**,** 208-238.

TUNHEIM, R. J. 2015. Mineralogical controls on the weathering characteristics of arid continental deposits of the Colorado Plateau.

ZHAO, G. & JOHNSON, A. M. 1991. Sequential and incremental formation of conjugate sets of faults. *Journal of Structural Geology,* 13**,** 887-895.

ZHAO, G. & JOHNSON, A. M. 1992. Sequence of deformations recorded in joints and faults, Arches National Park, Utah. *Journal of Structural Geology,* 14**,** 225-236.

URL / websites:

http://geology.utah.gov

https://www2.nau.edu/rcb7/ColoPlatPalgeog.html

http://www.seis.utah.edu

http://www.nature.nps.gov/geology/education/Foos/moab.pdf
http://geology.utah.gov/maps/geomap/interactive/viewer/index.html
http://www2.nau.edu/rcb7/Cap_Reef
http://gis.utah.gov/data/elevation-terrain-data

8 Appendix

Appendix A - Slope values measured in field

Table 8-1: Slope values measured in field.

Member	**Cutler**	**Chinle**	**Wingate**	**Kayenta**	**Navajo**	**Slick Rock**	**Moab**
	32	38	75	55	51	70	80
	36	24	82	65	88	82	68
	38	29	87	39	50	26	85
	26	36	85	76	80	26	87
	31	38	76	72	63	27	84
	38	38	87	88	40	29	86
	32	34	84	76	58	17	75
		22	81	84	25	25	70
		13	86	60	62	59	82
		29	81	79	31	62	86
		20	82	76	32	52	81
		29	86	72	30	74	
		31	83	78	60	52	
		29	85	84	19	51	
		30	77	85	14	46	
		34	84	85	42	24	
		35	84	48	48	80	
		36	76	53		76	
		32	80	84		78	
		34	72	60		78	
		32	82	50		86	
		38	90	64			
		28	67	79			
		28	90	24			
		29	81	69			
		22	82	70			
		38	80	78			
		30	64	48			
		30	84	89			
		32	82	59			
			70	78			
			85	64			
Mean	33,29	30,60	80,94	68,47	46,65	53,33	80,36
Min.	26	13	64	24	14	17	68

Max.	38	38	90	89	88	86	87
Std.dev.	4,35	5,97	6,14	15,55	20,56	23,42	6,59

Appendix B - Tiny-Perm II + Schmidt hammer measurements

Table 8-2: Measured values from Tiny-Perm II equipment (TP), hammer rebound values from Schmidt Hammer equipment (HR) and the calculated permeability (K) and Young's Modulus (E) values for the Cutler Formation. The location abbreviations are explained in Figure 1.4.

Location	**TP**	**Avg. TP**	**K (mD)**	**HR**	**Avg. HR**	**E (Gpa)**
ST1	11,13, 11,44	11,29	85,10	21 21 22 20 21 19 18 22 21 22	20,7	1,49
ST3	10,93, 11,27	11,1	145,03	34 38 36 40 40 36 40 37 41 39	38,1	9,82
ST4	10,69, 10,63, 10,49	10,6	589,90	15 16 16 15 14 14 15 16 13 15	14,9	0,54
ST5	11,75	11,75	23,41	30 26 33 29 34 30 26 36 28 28	30	4,69
ST6	11,13	11,13	133,32	18 20 22 16 18 22 26 18 20 22	20,2	1,38
ST7	10,92, 11,21	11,07	157,77	37 38 36 38 35 39 34 36 39 36	36,8	8,83
ST8	11,08, 11,51, 11,48	11,36	69,92	33 31 30 33 29 31 31 31 31 35	31,5	5,46
ST9	11,56	11,56	39,89	23 25 26 26 23 26 27 22 26 23	24,7	2,57
ST10	10,65, 10,52, 10,64	10,6	589,90	16 16 16 18 17 14 15 16 20 18	16,6	0,75
ST11	11,03, 10,56, 10,91	10,83	309,38	27 27 21 24 24 25 25 26 22 25	24,6	2,54
ST12	11,02, 10,49, 10,62	10,71	433,24	28 29 25 27 27 27 31 28 30 25	27,7	3,67
Po.1	11,37	11,37	67,99	34 38 35 35 39 42 36 35 36 39	36,9	8,90
Po.3	11,07 10,85	10,96	214,82	19 20 18 20 22 21 20 18 18 22	19,8	1,30
Po.4	10,99 10,94	10,97	208,88	21 22 24 20 25 20 20 21 17 21	21,1	1,58
Po.5	12,01	12,01	11,29	42 46 42 45 40 44 43 47 48 45	44,2	15,55
Po.6	11,23	11,23	100,70	40 40 43 43 39 41 40 42 40 42	41	12,33
Po.7	11,23 11,13 10,43	10,93	233,69	43 43 43 39 38 38 42 37 37 38	39,8	11,24
Po.8	11,16 11,03	11,1	145,03	36 38 40 40 42 37 37 38 43 39	39	10,56
Avg.		11,14	197,74		29,31	5,73
Max.		12,01	589,90		44,2	15,55
Min.		10,6	11,29		14,9	0,54

Table 8-3: Measured values from Tiny-Perm II equipment (TP), hammer rebound values from Schmidt Hammer equipment (HR) and the calculated permeability (K) and Young's Modulus (E) values for the Chinle Formation. The location abbreviations are explained in Figure 1.4.

Location	TP	Avg. TP	K (mD)	HR	Avg. HR	E (Gpa)
HC1	11,55	11,55	41,03	45 49 50 46 42 46	46,3	17,95
BB1	11,98	11,98	12,28	46 43 47 45 43 40 39 45 42 38	42,8	14,08
BB2	10,48, 10,44, 10,52	10,48	826,06	47 41 44 39 42 45 44 40 46 46	43,4	14,69
BB3	10,90, 11,02	10,96	214,82	30 36 34 32 30 34 30 29 34 32	32,1	5,78
BB4	10,90 10,77	10,84	300,82	22 20 21 22 20 21 23 23 22 19	21,3	1,63
BB5	11,26	11,26	92,57	30 35 35 31 34 35 42 35 41 34	35,2	7,69
BB6	10,75 10,93 10,71	10,8	336,55	25 24 21 24 26 22 21 22 24 29	23,8	2,29
BB7	11,6	11,6	35,66	32 33 31 31 35 31 33 36 33 30 32	32,5	6,01
BB8	11,4	11,4	62,50	37 39 35 36 36 37 39 43 38	37,8	9,59
BB9	10,79 10,81	10,8	336,55	27 29 28 30 24 28 28 30 26 28	27,8	3,71
BB10	11,49	11,49	48,55	51 47 52 46 49 49 48 52 48 47	48,9	21,25
BB11	11,39	11,39	64,28	49 50 51 48 56 56 52 50 48 51	51,1	24,35
BB12	11,20 11,26	11,23	100,70	39 42 41 40 36 42 37 43 40 44	40,4	11,78
BB0,1	11,36	11,36	69,92	51 53 52 56 51 52 55 53 52 52 52 59	53,2	27,57
DHR 26	11,19	11,19	112,67	46 45 43 44 43 41 39 44 39 42	42,6	13,87
DHR 27	10,66	10,66	498,49	48 42 45 43 41 48 45 42 47 41	44,2	15,55
BB25	10,94 10,94	10,94	227,22	35 40 37 40 35 40 40 40 39 41	38,7	10,31
BB26	10,92 10,72 10,73	10,79	346,13	42 38 40 40 38 45 43 45 43 40	41,4	12,70
BB27	10,88 10,81 10,62	10,77	366,11	44 42 44 40 41 48 42 42 46 42	43,1	14,38
BB28	11,48 11,10	11,29	85,10	50 50 53 54 51 50 48 53 52 50	51,1	24,35
Avg.		11,14	208,90		39,89	12,98
Max.		11,98	826,06		53,2	27,57
Min.		10,48	12,28		21,3	1,63

Table 8-4: Measured values from Tiny-Perm II equipment (TP), hammer rebound values from Schmidt Hammer equipment (HR) and the calculated permeability (K) and Young's Modulus (E) values for the Wingate Sandstone. The location abbreviations are explained in Figure 1.4.

Location	TP	Avg. TP	K (mD)	HR	Avg. HR	E (Gpa)
HC2	10,14, 10,86, 10,38, 11,36, 11,10	10,77	366,11	48 45 52 47 44 46 51 47 49 45 51	47,7	19,68
HC3	11,05, 10,90, 11,05	11	192,01	47 49 48 49 49 48 47 48	48,1	20,19
HC4	11,93	11,93	14,13	48 50 52 51 54 54 53 51 49 50 48	50,9	24,05
HC5	11,28, 11,31	11,3	82,75	46 48 49 47 47 48 44 46 50 48	47,3	19,17
DHR1	10,54 10,58	10,56	659,97	35 35 34 32 36 34 33 34 32 35	34	6,91
DHR2	11,09 11,38	11,24	97,92	43 39 43 40 47 38 39 42 45 50	42,6	13,87
DHR3	10,20 10,19 10,23	10,21	1762,14	39 39 42 38 39 37 42 40 40 42	39,8	11,24
DHR4	11,14 10,95	11,05	166,88	42 43 43 43 43 37 38 38 40 38	40,5	11,87
DHR5	11,04	11,04	171,63	45 44 42 43 41 48 52 49 46 44	45,4	16,89
DHR6	10,76 10,70	10,73	409,60	36 38 40 42 44 40 39 39 48 42	40,8	12,14
DHR7	10,08 10,04	10,06	2684,31	34 28 30 30 29 28 30 25 32 31	29,7	4,55
DHR8	11,18	11,18	115,87	46 46 46 45 44 45 46 46 45 43	45,2	16,66
DHR9	11,17	11,17	119,17	48 41 39 38 45 41 41 40 39 45 46 46 44	42,5	13,77
DHR10	11,36	11,36	69,92	45 48 49 48 47 48 48 45 49 45	47,2	19,05
DHR28	10,96	10,96	214,82	27 27 30 32 32 28 30 32 31 29	29,8	4,60
DHR29	10,73	10,73	409,60	47 42 44 43 42 46 47 48 44 44	44,7	16,10
DHR30	10,27	10,27	1489,09	53 53 47 50 49 51 49 50 45 45	49,2	21,65
DHR31	10,07	10,07	2610,04	46 45 46 45 43 41 44 43 42 42	43,7	15,01
DHR32	10,41	10,41	1005,35	46 46 41 45 43 45 45 40 43 41	43,5	14,80
DHR33	11,26	11,26	92,57	41 40 42 39 40 40 39 40 39 38	39,8	11,24
DHR34	9,77	9,77	6056,65	41 37 37 37 38 40 36 39 40 40	38,5	10,15
DHR35	9,91	9,91	4089,08	43 42 45 46 41 42 40 41 41 43	42,4	13,67
DHR36	9,92	9,92	3975,94	43 44 41 44 42 44 43 40 42 41	42,4	13,67
DHR37	11,89	11,89	15,80	46 43 46 46 46 49 48 49 45 46	46,4	18,07
DHR38	12,11	12,11	8,52	41 40 46 43 46 40 46 41 43 46	42,9	14,18
DHR39	10,4	10,4	1033,95	22 22 20 21 21 21 24 26 20 21	21,8	1,75
DHR40	10,83	10,83	309,38	39 42 42 39 40 39 43 44 40 41	40,9	12,23
I.C1	10,32	10,32	1294,17	37 39 40 40 41 40 43 38 37 41	39,6	11,07
I.C.2	10,35	10,35	1189,69	45 45 46 43 38 45 45 46 49 48	45	16,43
I.C.3	10,2	10,2	1812,28	42 40 40 35 35 38 38 40 39 38	38,5	10,15
I.C.4	10,85	10,85	292,50	42 40 47 45 45 45 40 42 44 42	43,2	14,49
I.C.5	11,03	11,03	176,51	42 42 45 43 41 45 44 44 43 45	43,4	14,69
I.C.6	9,93	9,93	3865,92	37 41 39 35 40 39 37 35 39 40	38,2	9,90
I.C.7	10,81	10,81	327,24	40 40 42 41 40 39 43 42 41 42	41	12,33
I.C.8	10,95	10,95	220,93	40 42 40 44 43 41 46 40 42 41	41,9	13,18
I.C.9	11,15	11,15	126,05	38 40 40 40 41 40 40 42 42 40	40,3	11,69
I.C.10	11,2	11,2	109,55	37 37 36 38 39 37 36 35 35 36	36,6	8,68
I.C.11	10,14	10,14	2144,58	41 41 43 42 38 41 41 42 42 40	41,1	12,42
I.C.12	10,07	10,07	2610,04	36 33 34 34 30 34 32 34 30 33	33	6,30

Avg.		10,75	1086,99		41,27	13,29
Max.		12,11	6056,65		50,9	24,05
Min.		9,77	8,52		21,8	1,75

Table 8-5: Measured values from Tiny-Perm II equipment (TP), hammer rebound values from Schmidt Hammer equipment (HR) and the calculated permeability (K) and Young's Modulus (E) values for the Kayenta Formation. The location abbreviations are explained in Figure 1.4.

Location	**TP**	**Avg. TP**	**K (mD)**	**HR**	**Avg. HR**	**E (Gpa)**
HC5 6	10,59, 10,55, 10,44, 10,56, 10,73, 10,63, 10,74	10,61	573,58	48 48 49 49 51 50 47 50 50 50	44,2	15,55
BB13	10,60 10,62 10,57	10,6	589,90	26 26 29 23 28 24 27 23 26 22	25,4	2,81
BB14	11,20 11,04	11,12	137,12	39 34 38 33 42 45 43 39 40 44 41	39,8	11,24
BB15	10,89 10,97 10,80	10,89	261,44	44 38 36 41 42 41 38 39 40 37	39,6	11,07
BB16	11,19 11,18	11,19	112,67	51 48 46 47 49 52 49 52 49 50 51 53	49,8	22,48
BB17	11,57 11,00	11,29	85,10	36 40 42 36 36 36 30 30 32 35	35,3	7,76
BB18	11,54	11,54	42,20	20 20 20 23 24 24 27 20 21 24	22,3	1,88
BB19	11,24	11,24	97,92	47 49 44 48 48 48 47 45 48 47	47,1	18,92
BB20:	11,56	11,56	39,89	46 43 39 44 52 37 38 42 43 41	42,5	13,77
BB21	11,21	11,21	106,52	49 46 52 54 54 49 53 52 52 51	51,2	24,49
BB22	11,36	11,36	69,92	34 31 39 34 33 30 31 32 35 30	32,9	6,24
BB23	11,07	11,07	157,77	50 53 49 48 45 44 48 54 54 48	49,3	21,79
BB24	10,96	10,96	214,82	32 32 34 34 31 40 38 36 36 41	35,4	7,83
DHR11	11,28	11,28	87,52	34 33 32 33 29 33 36 33 33 30 34	32,7	6,13
DHR12	11,96	11,96	12,99	35 35 37 34 30 31 31 36 33 37	33,9	6,85
DHR13	11	11	192,01	35 36 40 41 38 40 37 40 40 40	38,7	10,31
DHR14	10,45	10,45	898,61	26 27 28 25 25 26 24 23 23 23	25	2,67
DHR15	10,25	10,25	1575,05	28 28 27 26 30 22 23 24 27 29	26,4	3,16
DHR16	11,01	11,01	186,70	34 41 35 39 42 46 46 39 46 43 48	41,7	12,99
DHR17	10,68	10,68	471,29	44 48 35 43 47 51 45 47 47 44	45,1	16,55
DHR18	10,61	10,61	573,58	44 48 35 43 47 51 45 47 47 44	45,1	16,55
DHR19	10,4	10,4	1033,95	32 32 32 30 33 34 31 32 34 31	32,1	5,78
DHR20	10,36	10,36	1156,77	26 20 25 22 25 22 23 20 20 21	22,4	1,90
DHR21	10,43	10,43	950,48	27 24 29 29 28 25 26 26 30 31	27,5	3,59
DHR22	10,89	10,89	261,44	28 30 31 32 28 30 32 30 32 29	30,2	4,79
DHR23:	10,81	10,81	327,24	39 38 39 38 42 41 40 37 42 39	39,5	10,98
DHR24	11,05	11,05	166,88	39 38 40 42 41 40 40 39 40 39	39,8	11,24
I.C.13	10,71	10,71	433,24	54 53 52 53 52 51 53 54 53 50	52,5	26,47
I.C.14	11,3	11,3	82,75	42 40 39 44 44 40 44 44 43 44	42,4	13,67
I.C.15	11,12	11,12	137,12	46 50 46 51 45 48 53 50 51 53 49	49,3	21,79
I.C.16	11,36	11,36	69,92	50 48 50 50 48 48 50 49 50 50	49,3	21,79
I.C.17	11,02	11,02	181,53	44 44 42 44 46 41 39 42 44 41	42,7	13,97

I.C.18	10,89	10,89	261,44	36 35 34 39 33 35 35 37 37 37	35,8	8,10
I.C.19	10,81	10,81	327,24	34 34 34 30 34 31 29 34 29 32	32,1	5,78
I.C.20	10,98	10,98	203,10	30 29 31 33 29 35 33 34 35 33	32,2	5,84
I.C.21:	11,43	11,43	57,45	27 30 32 29 31 30 34 35 30 32	31	5,19
I.C.22	10,78	10,78	355,98	28 29 27 29 27 24 26 25 29	27,1	3,43
I.C.23	11,03	11,03	176,51	39 40 40 38 40 41 39 40 38 41	39,6	11,07
I.C.24	10,95	10,95	220,93	32 34 37 32 30 34 31 36 32 31	32,9	6,24
I.C.25	11,12	11,12	137,12	33 34 35 35 32 35 34 34 34 33 34	33,9	6,85
Avg.		10,98	325,69		37,39	10,74
Max.		11,96	1575,05		52,5	26,47
Min.		10,25	12,99		22,3	1,88

Table 8-6: Measured values from Tiny-Perm II equipment (TP), hammer rebound values from Schmidt Hammer equipment (HR) and the calculated permeability (K) and Young's Modulus (E) values for the Navajo Sandstone. The location abbreviations are explained in Figure 1.4.

Location	TP	Avg. TP	K (mD)	HR	Avg. HR	E (Gpa)
DHR25	11,34	11,34	73,96	46 45 42 42 46 48 43 47 45 49	45,3	16,78
DHR41	10,96 10,79	10,88	268,88	45 43 44 46 44 50 39 45 44 41	44,1	15,44
DHR42	10,96	10,96	214,82	43 43 40 39 42 40 39 40 40 38	40,4	11,78
DHR43	10,77	10,77	366,11	30 35 32 32 29 30 31 30 28 32	30,9	5,14
DHR44	9,92 9,90 9,82	9,88	4448,20	35 33 29 31 30 32 30 31 29 35	31,5	5,46
DHR45	10,48 10,32	10,4	1033,95	26 27 26 26 28 25 24 24 23 25	25,4	2,81
DHR46	10,93	10,93	233,69	29 30 28 30 30 31 31 32 30 30	30,1	4,74
DHR47	10,05 10,05	10,05	2760,70	38 40 40 37 37 40 39 35 40 40	38,6	10,23
DHR48	10,24 10,22	10,23	1665,97	38 38 44 42 42 44 40 47 45 43	42,3	13,57
DHR49	10,39 10,31	10,35	1189,69	34 33 34 34 36 35 34 34 36 33	34,3	7,10
DHR50	10,61 10,60	10,61	573,58	36 34 42 42 39 44 40 43 39 40	39,9	11,33
DHR51	11,18	11,18	115,87	48 45 52 48 49 50 50 52 52 49	49,5	22,07
DHR52	11,23	11,23	100,70	47 43 45 40 41 44 44 46 42 46	43,8	15,12
DHR53	11,48	11,48	49,93	33 37 36 39 34 36 38 38 41 40	37,2	9,12
DHR54	10,55 10,46	10,51	759,37	32 31 32 28 30 32 31 30 29 31	30,6	4,99
DHR55	10,37 10,35	10,36	1156,77	46 46 44 45 48 48 48 45 43 47	46	17,59
DHR56	11,3	11,3	82,75	40 37 38 36 38 40 35 38 39 40	38,1	9,82
DHR57	10,39 10,39 10,23	10,34	1223,54	43 47 45 47 45 46 43 44 43 44	44,7	16,10
I.C.26	10,62	10,62	557,71	34 31 30 33 34 33 30 31 30 33	32,1	5,78
I.C.27	11,22	11,22	103,57	26 24 25 24 27 26 26 24 24 23	24,9	2,64
I.C.28	9,96	9,96	3553,81	25 28 32 32 28 36 31 34 30 34	31	5,19
I.C.29	10,20 10,12 10,03	10,12	2268,38	30 30 30 27 31 29 28 29 28 28	29	4,23
I.C.30	10,31 10,26 10,28	10,28	1447,89	42 46 42 40 46 40 41 44 40 42	42,3	13,57
I.C.31	10,95 10,72	10,84	300,82	32 30 30 29 30 32 30 32 27 29	30,1	4,74
I.C.32	10,86 10,70	10,78	355,98	33 32 33 34 32 36 37 36 34 37	34,4	7,16

I.C.33	9,88 9,85	9,87	4574,78	40 37 38 34 39 31 34 33 40 33	35,9	8,17
I.C.34	9,93 9,93 9,89	9,92	3975,94	43 38 39 40 39 40 35 35 31 36	37,6	9,43
I.C.35	10,97 10,89	10,93	233,69	37 38 40 40 35 42 40 40 43 42	39,7	11,16
I.C.36	11,21	11,21	106,52	45 47 45 43 45 48 49 45 49 47	46,3	17,95
I.C.37	11,42	11,42	59,09	46 50 48 49 47 47 50 45 51 48	48,1	20,19
I.C.38	9,90 9,90 9,84	9,88	4448,20	32 31 32 33 34 36 30 36 30 31	32,5	6,01
I.C.39	9,72 9,68 9,60	9,67	8018,53	27 22 22 20 20 21 20 21 20 22	21,5	1,68
I.C.40	9,81 9,70 9,56	9,69	7580,92	28 35 39 36 30 30 34 34 35 34	33,5	6,60
I.C.41	10,04 10,00 9,94	9,98	3359,87	33 31 31 31 32 34 31 38 33 35	32,9	6,24
I.C.42	9,94 9,88 9,87	9,9	4205,44	38 39 35 35 38 36 39 38 36 34	36,8	8,83
I.C.43	10,16 10,13 10,08	10,12	2268,38	32 33 34 32 34 33 30 32 33 32	32,5	6,01
I.C.44	10,03 9,90 10,01	9,97	3455,48	28 30 30 26 29 28 30 30 30 31	29,2	4,32
I.C.45	9,97 9,91 9,90	9,93	3865,92	39 37 36 37 37 36 38 35 33 33	36,1	8,32
I.C.46	9,88 9,82 9,78	9,83	5118,18	42 38 36 40 45 37 37 42 38 36	39,1	10,64
I.C.47	9,89 9,72 9,89	9,83	5118,18	37 33 34 30 35 31 36 34 40 32	34,2	7,04
I.C.48	10,06 9,96 10,01	10,01	3088,61	34 44 35 36 46 40 36 35 44 40	39	10,56
Avg.		10,46	2058,16		36,38	9,41
Max.		11,48	8018,53		49,5	22,07
Min.		9,67	49,93		21,5	1,68

Table 8-7: Measured values from Tiny-Perm II equipment (TP), hammer rebound values from Schmidt Hammer equipment (HR) and the calculated permeability (K) and Young's Modulus (E) values for the Slick Rock Member. The location abbreviations are explained in Figure 1.4.

Location	**TP**	**Avg. TP**	**K (mD)**	**HR**	**Avg. HR**	**E (Gpa)**
CH1	11,72	11,72	25,46	46 50 40 46 46 45 42 49 50 47	46,1	17,71
CH2	10,89, 10,93, 10,93, 11,04, 11,05	10,97	208,88	30 32 32 29 34 29 30 31 30 31	30,8	5,09
CH3	10,08, 10,06, 9,77, 10,10, 10,43, 10,27	10,12	2268,38	31 32 36 32 34 34 34 38 32 28	33,1	6,36
CH4	11,27, 11,07	11,17	119,17	42 48 52 44 47 54 44 42 48 48	46,9	18,68
CH4,5	11,14, 10,83, 10,94	10,97	208,88	36 38 34 34 44 43 50 50 52 48	42,9	14,18
CH5	10,09, 10,05, 10,03, 10,02, 10,07	10,05	2760,70	22 26 28 24 26 24 26 24 22 22 26 24	24,5	2,51
CH5,5	10,38, 10,48, 10,45	10,44	924,18	39 34 41 35 37 30 31 38 33 31	34,9	7,49
CH5,75	10,95, 10,84, 10,62	10,8	336,55	22 20 21 20 20 20 21 23 19 24 19	20,8	1,51
CH6a	10,38, 10,42, 10,30, 10,58, 10,41	10,42	977,53	42 36 40 35 34 34 36 37 38 36 41	37,2	9,12
CH6b	11,54	11,54	42,20	28 – 32 (snitt 30)	30	4,69
Hi.C 1	10,22, 10,30, 10,34	10,29	1407,83	28 33 32 25 31 28 30 30 32 30	29,9	4,64
Hi.C 2	10,29, 10,44, 10,30, 10,52	10,39	1063,38	30 30 27 28 33 30 27 30 29 31	29,5	4,46
Hi.C3	11,09, 10,99	11,04	171,63	26 26 28 24 24 29 28 25 24 25 28	26,1	3,05
Hi.C4	11,31, 11,06	11,19	112,67	30 30 29 29 28 27 27 28 30 27	28,5	4,01
I1	11,22, 11,16	11,14	129,64	29 28 26 30 26 29 30 30 30 31 29	28,9	4,18
D1	10,88, 10,94	10,91	247,18	22 28 23 27 26 26 26 27 24 25	25,4	2,81
I2	11,31	11,31	80,46	30 28 29 30 30 28 30 27 30 31	29,3	4,36

D2	10,03, 9,99, 10,06	10,03	2920,06	22 23 22 22 24 21 25 24 25 25	23,3	2,15
I3	10,86, 10,86	10,86	284,40	27 28 27 26 25 26 23 26 26 27	26,1	3,05
D3	10,33, 10,35, 10,34	10,34	1223,54	28 27 29 29 30 29 28 26 27 25	27,8	3,71
I4	11,19	11,19	112,67	27 28 28 29 28 29 29 26 28 29	28,1	3,83
D4	11,13, 10,82	10,98	203,10	26 26 28 24 28 30 26 27 30 28	27,3	3,51
I5	11,19	11,19	112,67	26 25 24 26 26 28 27 28 24 23	25,7	2,91
D5	10,33, 10,44, 10,39	10,39	1063,38	22 24 26 24 24 25 25 27 27 27 26	25,2	2,74
I6	10,59, 10,90, 10,80	10,76	376,53	23 23 24 24 25 24 23 24 25 23 25	23,9	2,32
I1	10,67 10,64	10,66	498,49	28 28 28 27 28 29 26 28 27 25	27,4	3,55
D1	10,32 10,25	10,29	1407,83	28 28 27 24 24 26 25 23 24 24	25,3	2,77
I2	10,97 10,93	10,95	220,93	24 26 27 27 30 28 28 26 29 28	27,3	3,51
D2	10,67 10,57	10,62	557,71	32 34 33 34 30 31 30 30 31 32	31,7	5,56
D2,1	10,40 10,18 10,31	10,3	1368,87	30 26 27 26 26 25 28 27 26 25	26,6	3,24
D2,2	10,89 10,78 10,64	10,77	366,11	30 28 31 32 26 29 27 30 30 31	29,4	4,41
I3	11,22 11,12	11,17	119,17	35 30 30 32 30 30 31 33 35 32	31,8	5,62
D3	10,34 10,25	10,3	1368,87	30 28 31 30 29 28 25 24 27 23	27,5	3,59
I4	10,48 10,47 10,41	10,45	898,61	32 29 30 31 30 28 30 26 28 27	29,1	4,27
D4	10,08 10,00 9,98	10,02	3003,15	36 34 31 30 30 30 29 27 30 29	30,6	4,99
I5	10,74 10,71	10,73	409,60	36 32 29 30 30 30 32 32 36	31,9	5,67
D5	10,95 10,88	10,92	240,34	44 45 44 46 46 48 48 47 46 49	46,3	17,95
I6	11,45	11,45	54,32	25 26 26 29 25 26 26 23 24 26	25,6	2,87
D6	10,66 10,66	10,66	498,49	30 30 27 28 29 26 27 26 27 24	27,4	3,55
I7	11,00 10,91	10,96	214,82	27 30 28 30 29 29 27 25 26 29	28	3,79
D7	10,63 10,55	10,59	606,69	34 35 32 31 32 31 30 31 32 30	31,8	5,62
I8	11,8	11,8	20,34	44 46 46 42 42 40 46 44 45 44	43,9	15,22
D8	10,02 9,99 9,95	9,99	3266,90	28 26 24 24 22 24 23 22 22 20	23,5	2,21
I9	10,78 10,77	10,78	355,98	30 31 29 29 27 31 30 29 30 31	29,7	4,55
D9	10,76 10,66	10,71	433,24	30 31 29 27 30 31 30 29 30 28	29,5	4,46
I10	11,55	11,55	41,03	38 39 40 41 40 38 40 36 41 40	39,3	10,81
D10	10,55 10,37	10,46	873,74	24 25 22 26 26 22 25 26 20 21	23,7	2,26
I11	11,23	11,23	100,70	30 30 29 27 30 31 30 28 28 30	29,3	4,36
D11	10,51 10,47	10,49	803,20	24 22 27 26 30 29 22 25 24 24	25,3	2,77
I12	11,22	11,22	103,57	30 30 30 31 32 30 30 34 32 32	31,1	5,25
D12	10,40 10,38 10,34	10,37	1124,76	27 29 28 26 35 29 26 27 27 29	28,3	3,92
I13	11,17	11,17	119,17	28 28 27 25 28 28 29 26 26 26	27,1	3,43
D13	10,40 10,37 10,34	10,37	1124,76	26 22 26 25 26 29 29 24 27	26	3,02
I14	9,86 9,77 9,81	9,81	5413,62	26 25 24 25 23 27 23 22 24 24	24,3	2,45
Avg.		10,76	796,22		29,83	5,27
Max.		11,8	5413,62		46,9	18,68
Min.		9,81	20,34		20,8	1,51

Table 8-8: Measured values from Tiny-Perm II equipment (TP), hammer rebound values from Schmidt Hammer equipment (HR) and the calculated permeability (K) and Young's Modulus (E) values for the Moab Member. The location abbreviations are explained in Figure 1.4.

Location	**TP**	**Avg. TP**	**K (mD)**	**HR**	**Avg. HR**	**E (Gpa)**
CH7a	11,04	11,04	171,63	50 46 44 46 44 51 46 48 49 45 44	46,6	18,31
CH7b	9,84, 9,88, 9,91, 9,88, 9,85, 10,11	9,91	4089,08	40 44 40 41 38 42 38 44 44 39	41	12,33
CH8	9,69, 9,45, 9,72, 9,74, 9,78, 9,75, 9,85	9,71	7167,20	39 38 40 36 38 38 40 38 37 41	38,5	10,15
CH9	10,81, 10,81, 10,78, 10,19	10,65	512,68	30 30 30 34 38 39 36 36 37 40	35	7,56
CH10	10,61 10,40 10,27	10,43	950,48	24 24 25 24 23 27 23 27 23 29	24,9	2,64
CH11	11,05 11,01	11,03	176,51	21 22 23 21 24 23 25 20 21 21	22,1	1,82
CH12	10,86 10,70	10,78	355,98	24 23 23 22 22 23 22 24 22 20	22,5	1,93
CH13	11,22 11,01	11,12	137,12	44 42 49 48 45 44 44 43 45 47	45,1	16,55
CH14	11,33 11,07	11,2	109,55	37 36 38 39 36 36 36 38 37 39	37,2	9,12
CH15	11,15 11,11	11,13	133,32	41 38 38 40 39 38 40 40 39 41	39,4	10,90
CH16	11,25	11,25	95,21	47 48 47 46 46 50 49 51 49 47	48	20,06
CH17	11,31	11,31	80,46	53 45 50 48 46 56 56 50 50 55	50,9	24,05
Hi.C5	9,69, 9,76, 9,69, 9,65	9,7	7371,16	34 36 37 40 37 35 36 36 37 35	36,3	8,46
Hi.C6	9,65, 9,66, 9,70, 9,76	9,69	7580,92	30 29 31 29 28 25 29 30 28 30 32	29,2	4,32
Hi.C7	9,59, 9,62, 9,69, 9,69	9,65	8481,39	35 30 32 31 34 30 29 31 30 28	31	5,19
Hi.C. 7	10,32	10,32	1294,17	45 40 43 43 41 40 40 43 43 41	41,9	13,18
Hi.C. 8	10,01	10,01	3088,61	40 42 43 45 42 40 40 41 39 39	41,1	12,42
Hi.C. 9	9,98	9,98	3359,87	40 42 43 38 39 40 42 39 36 38	39,7	11,16
Hi.C. 10	9,87	9,87	4574,78	24 29 30 30 31 30 30 27 29 30	29	4,23
Hi.C. 11	9,59	9,59	10036,54	30 34 31 31 30 31 32 30 30 29	30,8	5,09
Hi.C. 12	9,93	9,93	3865,92	39 40 42 39 37 39 38 42 37 36	38,9	10,48
Hi.C. 13	9,82	9,82	5263,83	40 39 38 35 42 38 39 35 35 37	37,8	9,59
Hi.C. 14	9,85	9,85	4838,86	20 20 19 20 19 20 21 20 23 19	20,1	1,36
B.W.1	10,46	10,46	873,74	39 35 40 40 41 38 38 38 34 35	37,8	9,59
B.W.2	9,88	9,88	4448,20	39 30 32 35 32 30 32 33 35 32	33	6,30
B.W.3	9,85	9,85	4838,86	29 28 30 30 29 29 28 28 30 28	28,9	4,18
B.W.4	9,81	9,81	5413,62	38 37 42 42 38 34 36 40 38 38	38,3	9,99
B.W.5	10,25	10,25	1575,05	30 34 30 30 30 27 33 31 32 32	30,9	5,14
B.W.6	10,11	10,11	2332,93	28 26 25 25 27 24 23 22 25 25	25,1	2,70
B.W.7	9,86	9,86	4704,97	28 33 35 32 32 31 34 32 34 32	32,3	5,90
B.W.8	10,37	10,37	1124,76	41 45 45 43 45 42 45 47 42 46	44,1	15,44
B.W.9	10,43	10,43	950,48	39 40 44 40 42 41 39 44 40 39	40,8	12,14
B.W.10	10,07	10,07	2610,04	37 35 36 36 37 38 35 31 34 35	35,4	7,83
B.W.11	10,41	10,41	1005,35	38 33 37 39 32 35 35 35 31 33	34,8	7,43
B.W.12	9,69	9,69	7580,92	36 32 34 32 31 34 33 37 30 37	33,6	6,66
Avg.		10,26	3176,98		35,49	8,98
Max.		11,31	10036,54		50,9	24,05
Min.		9,59	80,46		20,1	1,36

Appendix C - Tiny-Perm II + Schmidt hammer measurements at Courthouse-, Bartlett Wash- and Hidden Canyon localities

Table 8-9: Calculated permeability (K)- and Young's Modulus (E) values for dunes and interdunes at the Courthouse locality (Figure 4.24).

Location	Facies association	K (mD)	E (GPa)
CH1	Interdune	25,46	17,71
CH4	Interdune	119,17	18,68
CH4,5	Interdune	208,88	14,18
CH6b	Interdune	42,20	4,69
CH2	Dune	208,88	5,09
CH3	Dune	2268,38	6,36
CH5	Dune	2760,70	2,51
CH5,5	Dune	924,18	7,49
CH5,75	Dune	336,55	1,51
CH6a	Dune	977,53	9,12
Avg.		787,19	8,73
Min.		25,46	1,51
Max.		2760,70	18,68

Table 8-10: Calculated permeability (K)- and Young's Modulus (E) values for dunes and interdunes at the Bartlett Wash locality (Figure 4.24).

Location	Facies association	K (mD)	E (GPa)
I1	Interdune	498,49	3,55
I2	Interdune	220,93	3,51
I3	Interdune	119,17	5,62
I4	Interdune	898,61	4,27
I5	Interdune	409,60	5,67
I6	Interdune	54,32	2,87
I7	Interdune	214,82	3,79
I8	Interdune	20,34	15,22
I9	Interdune	355,98	4,55
I10	Interdune	41,03	10,81
I11	Interdune	100,70	4,36
I12	Interdune	103,57	5,25
I13	Interdune	119,17	3,43
D1	Dune	1407,83	2,77
D2	Dune	557,71	5,56

D2,1	Dune	1368,87	3,24
D2,2	Dune	366,11	4,41
D3	Dune	1368,87	3,59
D4	Dune	3003,15	4,99
D6	Dune	498,49	3,55
D7	Dune	606,69	5,62
D8	Dune	3266,90	2,21
D9	Dune	433,24	4,46
D10	Dune	873,74	2,26
D11	Dune	803,20	2,77
D12	Dune	1124,76	3,92
D13	Dune	1124,76	3,02
Avg.		739,30	4,64
Min.		20,34	2,21
Max.		3266,90	15,22

Table 8-11: Calculated permeability (K)- and Young's Modulus (E) values for dunes and interdunes at the Hidden Canyon locality (Figure 4.24).

Location	**Facies association**	**K (mD)**	**E (GPa)**
I1	Interdune	129,64	4,18
I2	Interdune	80,46	4,36
I3	Interdune	284,40	3,05
I4	Interdune	112,67	3,83
I5	Interdune	112,67	2,91
I6	Interdune	376,53	2,32
D1	Dune	247,18	2,81
D2	Dune	2920,06	2,15
D3	Dune	1223,54	3,71
D4	Dune	203,10	3,51
D5	Dune	1063,38	2,74
Avg.		613,96	3,23
Min.		80,46	2,15
Max.		2920,06	4,36

Appendix D - Joint-spacing and orientations measured in field

Table 8-12: Fracture-frequency distribution no. 1 of the Cutler Formation. Coordinates: N38°27’53.2’’ W109°46’51.3’’.

	Length (m)	Avg. layer thick. (m)	No. of fractures	Av. frac. spacing (m)	Avg. frac. density (fracs/m)	St. dev. of frac. spacing
Total scanline	27	2,24	14	2,53	0,52	0,88
Frac. orient. 1: Avg.: 307/79	27	2,24	7	2,54	0,26	0,69
Frac. orient. 2: Avg.: 223/81	27	2,24	7	2,52	0,26	1,09

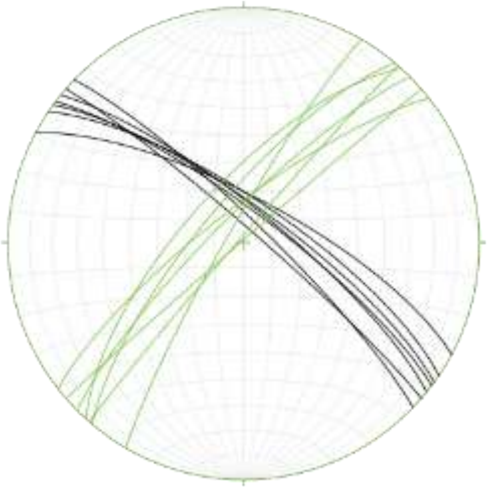

Figure 8.1: Stereographic projection of the joint orientations. The black set represents fracture-set no. 1. Achieved by using Stereonet 8 software by Rick Allmendinger (Allmenndinger 2011, Cardozo 2013).

Table 8-13: Fracture-frequency distribution no. 2 of the Cutler Formation. Coordinates: N38°27’55.1’’ W109°46’40.5’’.

	Length (m)	Avg. layer thick. (m)	No. of fractures	Av. frac. spacing (m)	Avg. frac. density (fracs/m)	St. dev. of frac. spacing
Total scanline	30	3,7	9	3,39	0,3	1,74
Frac. orient. 1: Avg.: 116/85	30	3,7	9	3,39	0,3	1,74

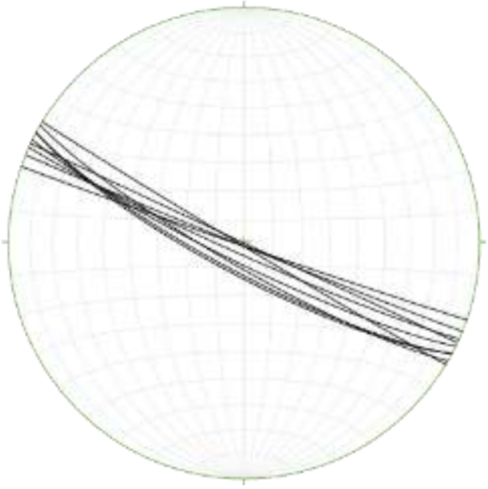

Figure 8.2: Stereographic projection of the joint orientations. Achieved by using Stereonet 8 software by Rick Allmendinger (Allmenndinger 2011, Cardozo 2013).

Table 8-14: Fracture-frequency distribution nr. 3 of the Cutler Formation. Coordinates: N38°27'47.8'' W109°46'23.8''.

	Length (m)	Avg. layer thick. (m)	No. of fractures:	Av. frac. spacing (m)	Avg. frac. density (fracs/m)	St. dev. of frac. spacing
Total scanline	30	1,07	26	2,49	0,87	1,3
Frac. orient. 1: Avg.: 309/83	30	1,07	15	2,14	0,5	0,74
Frac. orient. 2: Avg.: 060/82	30	1,07	11	2,99	0,37	1,75

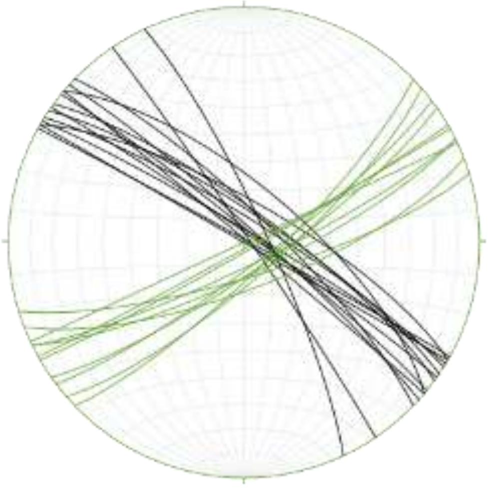

Figure 8.3: Stereographic projection of the joint orientations. The black set represents fracture-set no. 1. Achieved by using Stereonet 8 software by Rick Allmendinger (Allmenndinger 2011, Cardozo 2013).

Table 8-15: Fracture-frequency distribution no. 4 of the Cutler Formation. Coordinates: N38°27’55.3’’ W109°46’39.0’’.

	Length (m)	Avg. layer thick. (m)	No. of fractures	Av. frac. spacing (m)	Avg. frac. density (fracs/m)	St. dev. of frac. spacing
Total scanline	60	6,14	13	7,8	0,22	2,39
Frac. orient. 1: Avg.: 312/84	60	6,14	9	7,45	0,15	2,77
Frac. orient. 2: Avg.: 246/77	60	6,14	4	8,7	0,07	1,62

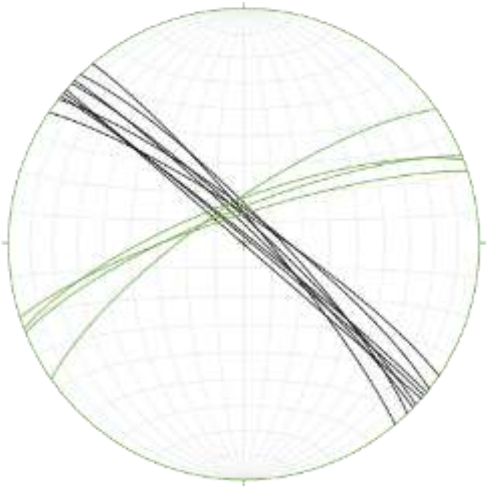

Figure 8.4: Stereographic projection of the joint orientations. The black set represents fracture-set no. 1. Achieved by using Stereonet 8 software by Rick Allmendinger (Allmenndinger 2011, Cardozo 2013).

Table 8-16: Fracture-frequency distribution no. 5 of the Cutler Formation. Coordinates: N38°39'02.9'' 109°29'01.5''.

	Length (m)	Avg. layer thick. (m)	No. of fractures	Av. frac. spacing (m)	Avg. frac. density (fracs/m)	St. dev. of frac. spacing
Total scanline	43	1,19	39	1,61	0,91	0,73
Frac. orient. 1: Avg.: 018/75	43	1,19	22	1,8	0,52	0,77
Frac. orient. 2: Avg.: 098/76	43	1,19	17	1,36	0,39	0,62

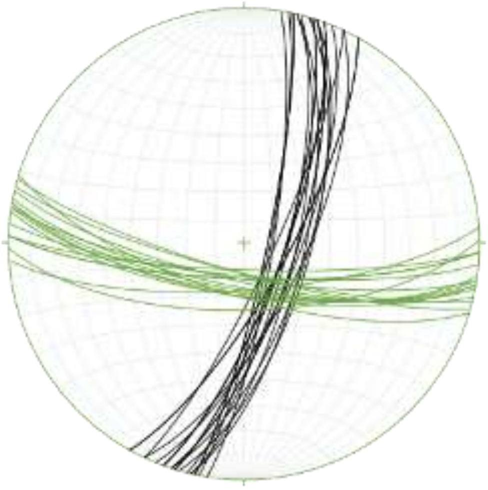

Figure 8.5: Stereographic projection of the joint orientations. The black set represents fracture-set no. 1. Achieved by using Stereonet 8 software by Rick Allmendinger (Allmenndinger 2011, Cardozo 2013).

Table 8-17: Fracture-frequency distribution no. 6 of the Chinle Formation. Coordinates: N38°02’23.2’’ W109°33’09.7’’.

	Length (m)	Avg. layer thick. (m)	No. of fractures	Av. frac. spacing (m)	Avg. frac. density (fracs/m)	St. dev. of frac. spacing
Total scanline	31	2,13	33	1,86	1,06	1,44
Frac. orient. 1: Avg.: 201/82	31	2,13	9	3,33	0,29	2,12
Frac. orient. 2: Avg.: 123/86	31	2,13	24	1,35	0,77	0,59

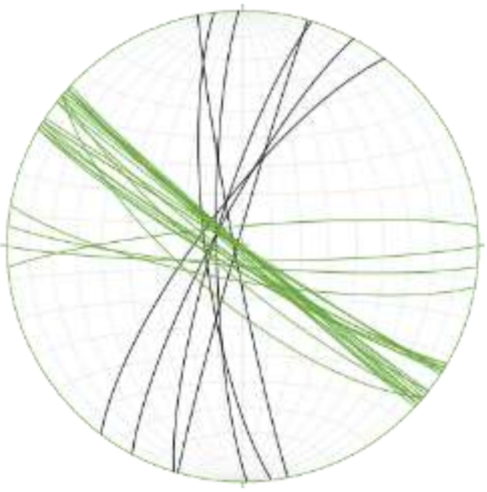

Figure 8.6: Stereographic projection of the joint orientations. The black set represents fracture-set no. 1. Achieved by using Stereonet 8 software by Rick Allmendinger (Allmenndinger 2011, Cardozo 2013).

Table 8-18: Fracture-frequency distribution no. 7 of the Chinle Formation. Coordinates: N38°27'27.6'' W109°48'10.7''.

	Length (m)	Avg. layer thick. (m)	No. of fractures	Av. frac. spacing (m)	Avg. frac. density (fracs/m)	St. dev. of frac. spacing
Total scanline	31	1,22	26	2,58	0,84	1,95
Frac. orient. 1: Avg.: 054/83	31	1,22	13	2,58	0,42	1,96
Frac. orient. 2: Avg.: 330/83	31	1,22	13	2,58	0,42	2,04

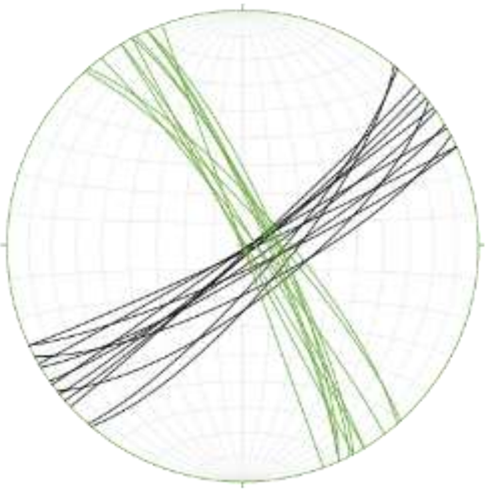

Figure 8.7: Stereographic projection of the joint orientations. The black set represents fracture-set no. 1. Achieved by using Stereonet 8 software by Rick Allmendinger (Allmenndinger 2011, Cardozo 2013).

Table 8-19: Fracture-frequency distribution no. 8 of the Chinle Formation. Coordinates: N38°27’29.4’’ W109°48’07.2’’.

	Length (m)	Avg. layer thick. (m)	No. of fractures	Av. frac. spacing (m)	Avg. frac. density (fracs/m)	St. dev. of frac. spacing
Total scanline	30	1,09	22	2,39	0,73	2,41
Frac. orient. 1: Avg.: 054/82	30	1,09	10	3,24	0,33	3,37
Frac. orient. 2: Avg.: 315/83	30	1,09	12	1,69	0,4	0,85

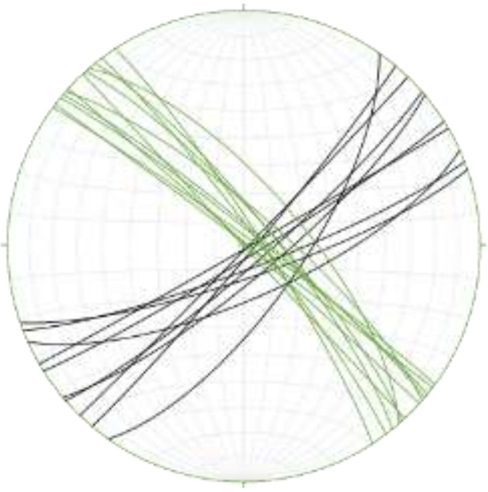

Figure 8.8: Stereographic projection of the joint orientations. The black set represents fracture-set no. 1. Achieved by using Stereonet 8 software by Rick Allmendinger (Allmenndinger 2011, Cardozo 2013).

Table 8-20: Fracture-frequency distribution no. 9 of the Chinle Formation. Coordinates: N38°27’33.4’’ W109°48’03.2’’.

	Length (m)	**Avg. layer thick. (m)**	**No. of fractures**	**Av. frac. spacing (m)**	**Avg. frac. density (fracs/m)**	**St. dev. of frac. spacing**
Total scanline	30	1,54	26	2,41	0,87	1,3
Frac. orient. 1: Avg.: 117/83	30	1,54	13	2,35	0,43	1,38
Frac. orient. 2: Avg.: 027/80	30	1,54	13	2,47	0,43	1,28

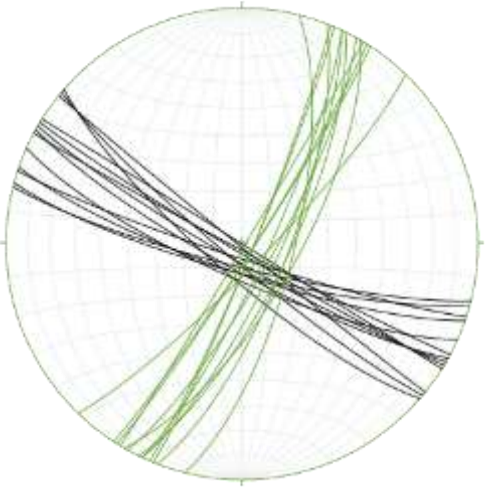

Figure 8.9: Stereographic projection of the joint orientations. The black set represents fracture-set no. 1. Achieved by using Stereonet 8 software by Rick Allmendinger (Allmenndinger 2011, Cardozo 2013).

Table 8-21: Fracture-frequency distribution no. 10 of the Wingate Sandstone. Coordinates: N38°02’23.2’’ W109°33’09.7’’.

	Length (m)	Avg. layer thick. (m)	No. of fractures	Av. frac. spacing (m)	Avg. frac. density (fracs/m)	St. dev. of frac. spacing
Total scanline	31	42,8	8	6,7	0,26	3,31
Frac. orient. 1: Avg.: 214/82	31	42,8	4	6,7	0,13	3,7
Frac. orient. 2: Avg.: 126/89	31	42,8	4	6,7	0,13	3,7

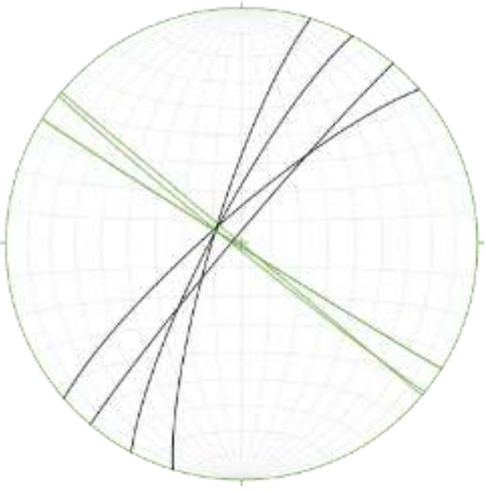

Figure 8.10: Stereographic projection of the joint orientations. The black set represents fracture-set no. 1. Achieved by using Stereonet 8 software by Rick Allmendinger (Allmenndinger 2011, Cardozo 2013).

Table 8-22: Fracture-frequency distribution no. 11 of the Wingate Sandstone. Coordinates: N38°02’18.0’’ W109°32’54.6’’.

	Length (m)	Avg. layer thick. (m)	No. of fractures	Av. frac. spacing (m)	Avg. frac. density (fracs/m)	St. dev. of frac. spacing
Total scanline	100	39,6	19	10,44	0,19	5,04
Frac. orient. 1: Avg.: 125/85	100	39,6	9	11,19	0,09	4,96
Frac. orient. 2: Avg.: 051/86	100	39,6	10	9,84	0,1	5,28

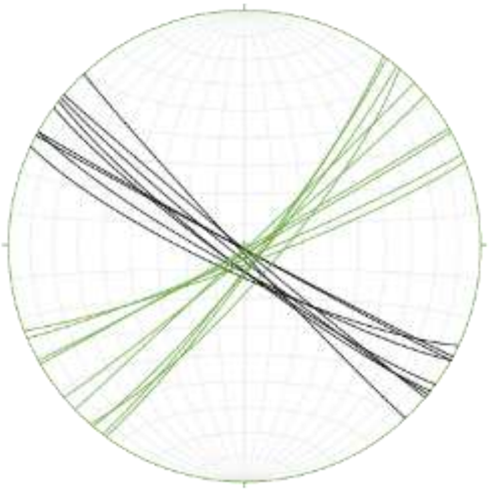

Figure 8.11: Stereographic projection of the joint orientations. The black set represents fracture-set no. 1. Achieved by using Stereonet 8 software by Rick Allmendinger (Allmenndinger 2011, Cardozo 2013).

Table 8-23: Fracture-frequency distribution no. 12 of the Wingate Sandstone. Coordinates: N38°02’22.4’’ W109°32’21.1’’.

	Length (m)	Avg. layer thick. (m)	No. of fractures	Av. frac. spacing (m)	Avg. frac. density (fracs/m)	St. dev. of frac. spacing
Total scanline	100	43	16	18,5	0,16	15,02
Frac. orient. 1: Avg.: 088/82	100	43	7	15,9	0,07	8,94
Frac. orient. 2: Avg.: 210/83	100	43	3	34,1	0,03	33,38
Frac. orient. 3: Avg.: 355/85	100	43	6	15,9	0,06	13,04

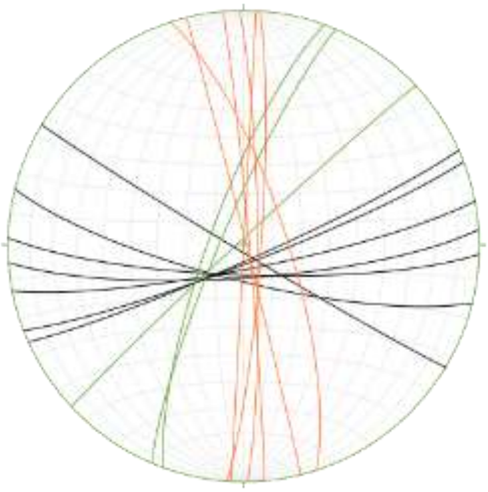

Figure 8.12: Stereographic projection of the joint orientations. The black set represents fracture-set no. 1, the green set no. 2, and the red set no. 3. Achieved by using Stereonet 8 software by Rick Allmendinger (Allmenndinger 2011, Cardozo 2013).

Table 8-24: Fracture-frequency distribution no. 13 of the Wingate Sandstone. Coordinates: N38°02'07.2'' W109°32'43.9''.

	Length (m)	Avg. layer thick. (m)	No. of fractures	Av. frac. spacing (m)	Avg. frac. density (fracs/m)	St. dev. of frac. spacing
Total scanline	100	57,82	29	9,65	0,29	8,22
Frac. orient. 1: Avg.: 233/85	100	57,82	8	12,3	0,08	15,23
Frac. orient. 2: Avg.: 178/86	100	57,82	9	10,22	0,09	5,82
Frac. orient. 3: Avg.: 123/84	100	57,82	12	7,76	0,12	2,37

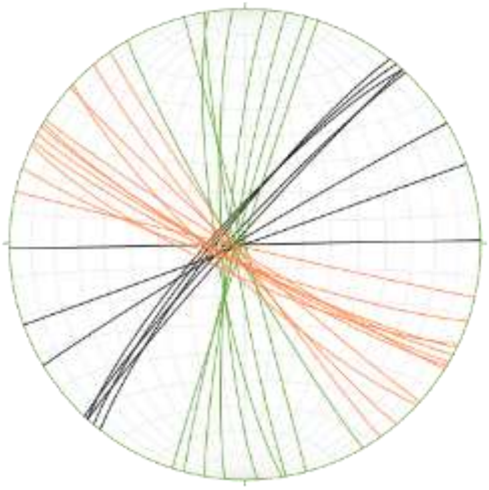

Figure 8.13: Stereographic projection of the joint orientations. The black set represents fracture-set no. 1, the green set no. 2, and the red set no. 3. Achieved by using Stereonet 8 software by Rick Allmendinger (Allmenndinger 2011, Cardozo 2013).

Table 8-25: Fracture-frequency distribution no. 14 of the Slick Rock Member. Coordinates: N38°43’02.6’’ W109°48’08.5’’.

	Length (m)	Avg. layer thick. (m)	No. of fractures	Av. frac. spacing (m)	Avg. frac. density (fracs/m)	St. dev. of frac. spacing
Total scanline	30	0,38	20	1,57	0,67	0,48
Frac. orient. 1: Avg.: 108/86	30	0,38	20	1,57	0,67	0,48

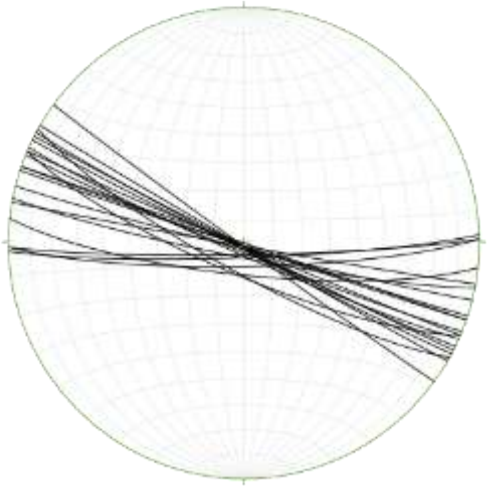

Figure 8.14: Stereographic projection of the joint orientations. Achieved by using Stereonet 8 software by Rick Allmendinger (Allmenndinger 2011, Cardozo 2013).

Table 8-26: Fracture-frequency distribution no. 15 of the Slick Rock Member. Coordinates: N38°43’02.6’’ W109°48’08.5’’.

	Length (m)	**Avg. layer thick. (m)**	**No. of fractures**	**Av. frac. spacing (m)**	**Avg. frac. density (fracs/m)**	**St. dev. of frac. spacing**
Total scanline	30	1,63	13	2,41	0,43	0,62
Frac. orient. 1: Avg.: 112/86	30	1,63	13	2,41	0,43	0,62

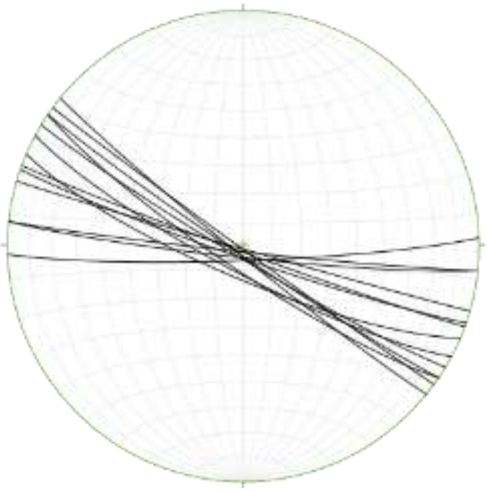

Figure 8.15: Stereographic projection of the joint orientations. Achieved by using Stereonet 8 software by Rick Allmendinger (Allmenndinger 2011, Cardozo 2013).

Table 8-27: Fracture-frequency distribution no. 16 of the Slick Rock Member. Coordinates: N38°43'01.8'' W109°48'09.3''.

	Length (m)	Avg. layer thick. (m)	No. of fractures	Av. frac. spacing (m)	Avg. frac. density (fracs/m)	St. dev. of frac. spacing
Total scanline	30	0,42	19	1,64	0,63	0,35
Frac. orient. 1: Avg.: 110/85	30	0,42	19	1,64	0,63	0,35

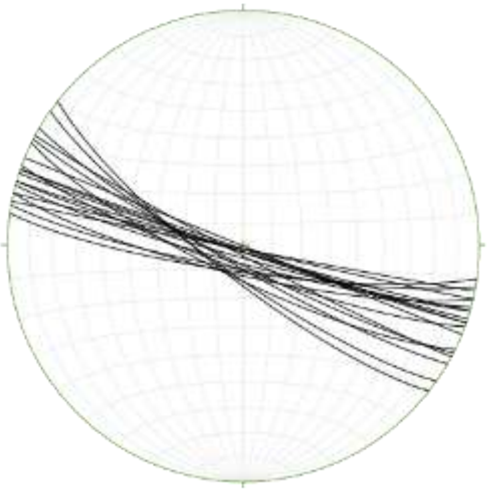

Figure 8.16: Stereographic projection of the joint orientations. Achieved by using Stereonet 8 software by Rick Allmendinger (Allmenndinger 2011, Cardozo 2013).

Table 8-28: Fracture-frequency distribution no. 17 of the Slick Rock Member. Coordinates: N38°43’01.8’’ W109°48’09.3’’.

	Length (m)	Avg. layer thick. (m)	No. of fractures	Av. frac. spacing (m)	Avg. frac. density (fracs/m)	St. dev. of frac. spacing
Total scanline	30	1,52	14	2,04	0,47	0,79
Frac. orient. 1: Avg.: 111/85	30	1,52	14	2,04	0,47	0,79

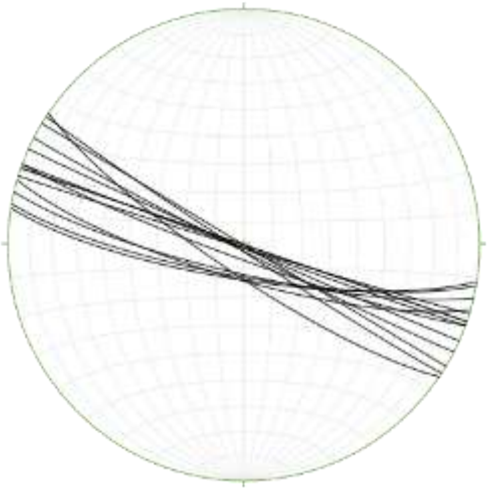

Figure 8.17: Stereographic projection of the joint orientations. Achieved by using Stereonet 8 software by Rick Allmendinger (Allmenndinger 2011, Cardozo 2013).

Table 8-29: Fracture-frequency distribution no. 18 of the Slick Rock Member. Coordinates: N38°43’00.8’’ W109°48’09.9’’.

	Length (m)	Avg. layer thick. (m)	No. of fractures	Av. frac. spacing (m)	Avg. frac. density (fracs/m)	St. dev. of frac. spacing
Total scanline	30	0,43	19	1,62	0,63	0,51
Frac. orient. 1: Avg.: 101/86	30	0,43	19	1,62	0,63	0,51

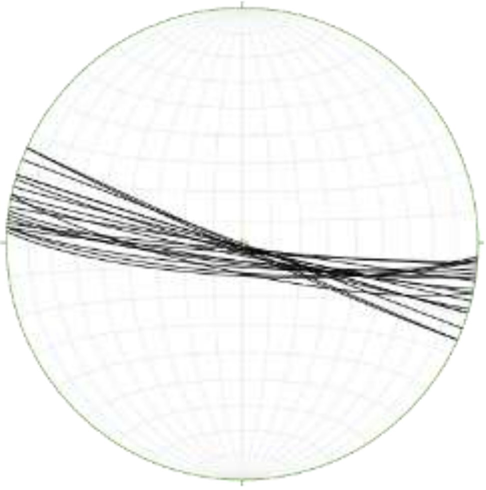

Figure 8.18: Stereographic projection of the joint orientations. Achieved by using Stereonet 8 software by Rick Allmendinger (Allmenndinger 2011, Cardozo 2013).

Table 8-30: Fracture-frequency distribution no. 19 of the Slick Rock Member. Coordinates: N38°43’00.8’’ W109°48’09.9’’.

	Length (m)	Avg. layer thick. (m)	No. of fractures	Av. frac. spacing (m)	Avg. frac. density (fracs/m)	St. dev. of frac. spacing
Total scanline	30	1,55	12	2,43	0,4	1,01
Frac. orient. 1: Avg.: 098/84	30	1,55	12	2,43	0,4	1,01

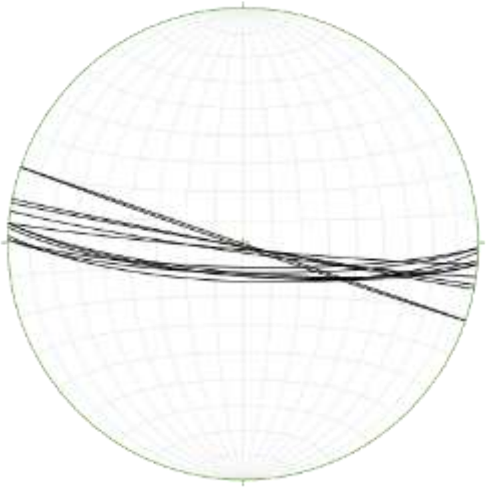

Figure 8.19: Stereographic projection of the joint orientations. Achieved by using Stereonet 8 software by Rick Allmendinger (Allmenndinger 2011, Cardozo 2013).

Table 8-31: Fracture-frequency distribution no. 20 of the Moab Member. Coordinates: N38°43’01.8’’ W109°47’22.7’’.

	Length (m)	Avg. layer thick. (m)	No. of fractures	Av. frac. spacing (m)	Avg. frac. density (fracs/m)	St. dev. of frac. spacing
Total scanline	58,9	11,57	8	8,41	0,14	3,77
Frac. orient. 1: Avg.: 036/80	58,9	11,57	8	8,41	0,14	3,77

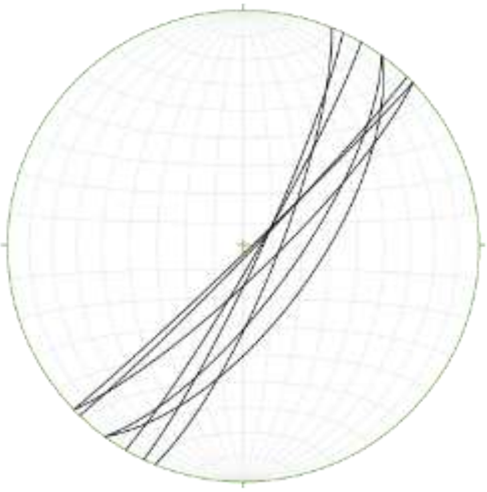

Figure 8.20: Stereographic projection of the joint orientations. Achieved by using Stereonet 8 software by Rick Allmendinger (Allmenndinger 2011, Cardozo 2013).

Table 8-32: Fracture-frequency distribution no. 21 of the Moab Member. Coordinates: N38°43'03.5'' W109°47'24.2''.

	Length (m)	Avg. layer thick. (m):	No. of fractures:	Av. frac. spacing (m):	Avg. frac. density (fracs/m):	St. dev. of frac. spacing:
Total scanline	63,4	15,06	6	12,68	0,09	6,87
Frac. orient. 1: Avg.: 037/78	63,4	15,06	4	15,4	0,06	6,94
Frac. orient. 2: Avg.: 104/69	63,4	15,06	2	8,6	0,03	6,08

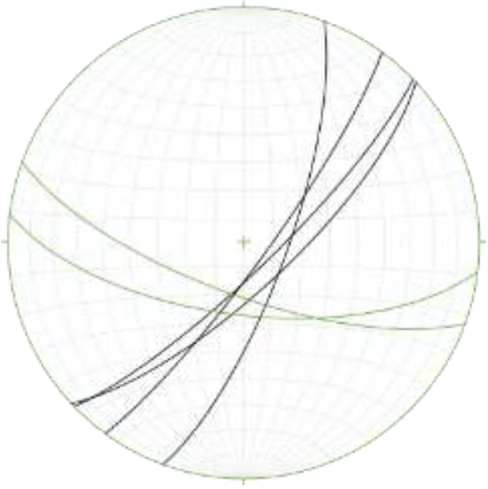

Figure 8.21: Stereographic projection of the joint orientations. The black set represents fracture-set no. 1. Achieved by using Stereonet 8 software by Rick Allmendinger (Allmenndinger 2011, Cardozo 2013).

Table 8-33: Fracture-frequency distribution no. 22 of the Moab Member. Coordinates: N38°43’02.9’’ W109°47’32.1’’.

	Length (m)	Avg. layer thick. (m)	No. of fractures	Av. frac. spacing (m)	Avg. frac. density (fracs/m)	St. dev. of frac. spacing
Total scanline	30	6,97	6	6	0,2	2,08
Frac. orient. 1: Avg.: 174/77	30	6,97	4	5,05	0,13	0,3
Frac. orient. 2: Avg.: 106/72	30	6,97	2	7,43	0,07	3,22

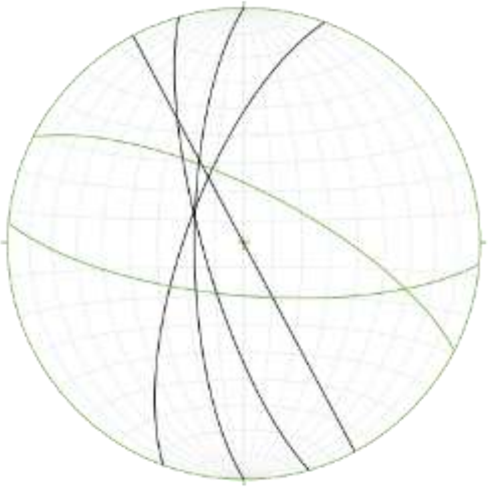

Figure 8.22: Stereographic projection of the joint orientations. The black set represents fracture-set no. 1. Achieved by using Stereonet 8 software by Rick Allmendinger (Allmenndinger 2011, Cardozo 2013).

Table 8-34: Fracture-frequency distribution no. 23 of the Moab Member. Coordinates: N38°42’42.9’’ W109°47’09.8’’.

	Length (m)	Avg. layer thick. (m)	No. of fractures	Av. frac. spacing (m)	Avg. frac. density (fracs/m)	St. dev. of frac. spacing
Total scanline	100	9,43	7	15,03	0,07	1,93
Frac. orient. 1: Avg.: 081/84	100	9,43	7	15,03	0,07	1,93

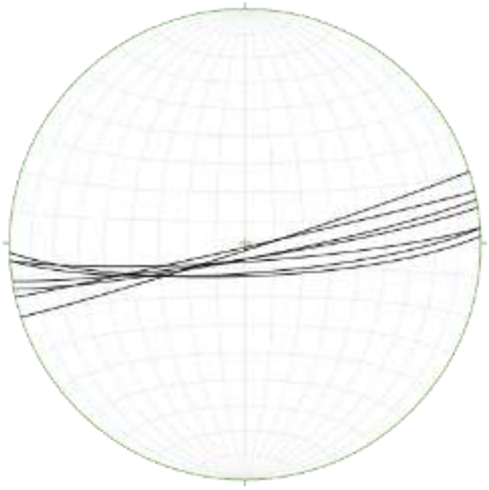

Figure 8.23: Stereographic projection of the joint orientations. Achieved by using Stereonet 8 software by Rick Allmendinger (Allmenndinger 2011, Cardozo 2013).

Table 8-35: Fracture-frequency distribution no. 24 of the Moab Member. Coordinates: N38°42’37.7’’ W109°47’10.8’’.

	Length (m)	Avg. layer thick. (m)	No. of fractures	Av. frac. spacing (m)	Avg. frac. density (fracs/m)	St. dev. of frac. spacing
Total scanline	100	8,91	7	14,6	0,07	3,47
Frac. orient. 1: Avg.: 075/85	100	8,91	7	14,6	0,07	3,47

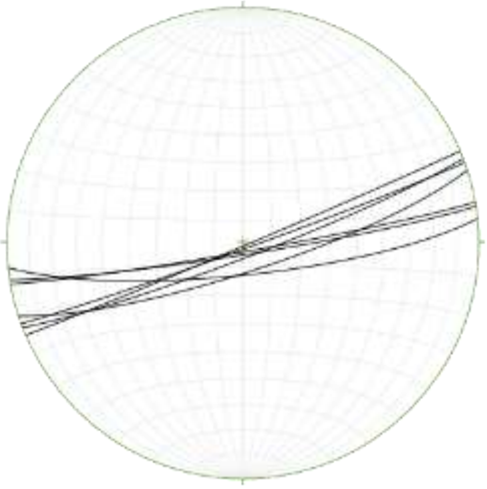

Figure 8.24: Stereographic projection of the joint orientations. Achieved by using Stereonet 8 software by Rick Allmendinger (Allmenndinger 2011, Cardozo 2013).

Table 8-36: Fracture-frequency distribution no. 25 of the Moab Member. Coordinates: N38°42’34.4’’ W109°47’10.4’’.

	Length (m)	Avg. layer thick. (m)	No. of fractures	Av. frac. spacing (m)	Avg. frac. density (fracs/m)	St. dev. of frac. spacing
Total scanline	100	8,45	8	13,29	0,08	4,21
Frac. orient. 1: Avg.: 070/88	100	8,45	7	13,29	0,07	4,21
Frac. orient. 2: Avg.: 180/84	100	8,45	1	-	0,01	-

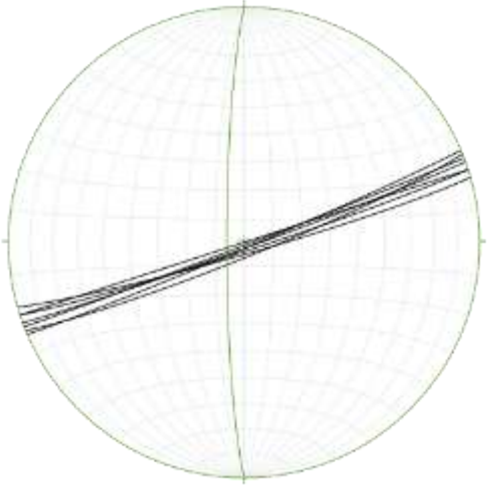

Figure 8.25: Stereographic projection of the joint orientations. The black set represents fracture-set no. 1. Achieved by using Stereonet 8 software by Rick Allmendinger (Allmenndinger 2011, Cardozo 2013).

Table 8-37: Fracture-frequency distribution no. 26 of the Moab Member. Coordinates: N38°42’26.1’’ W109°47’11.2’’.

	Length (m)	**Avg. layer thick. (m)**	**No. of fractures**	**Av. frac. spacing (m)**	**Avg. frac. density (fracs/m)**	**St. dev. of frac. spacing**
Total scanline	100	10,85	7	14,7	0,07	4,92
Frac. orient. 1: Avg.: 113/79	100	10,85	7	14,7	0,07	4,92

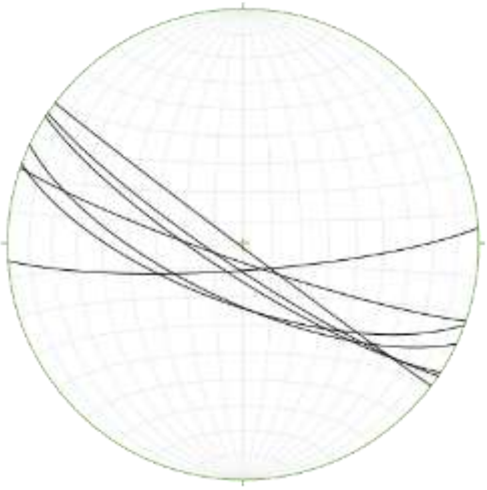

Figure 8.26: Stereographic projection of the joint orientations. Achieved by using Stereonet 8 software by Rick Allmendinger (Allmenndinger 2011, Cardozo 2013).

Appendix E - Locations for fracture-frequency distributions

Figure 8.27: Localities of fracture-frequency distribution no. 1-4 of the Cutler Formation.

Figure 8.28: Localities of fracture-frequency distribution no. 5-9 of the Chinle Formation.

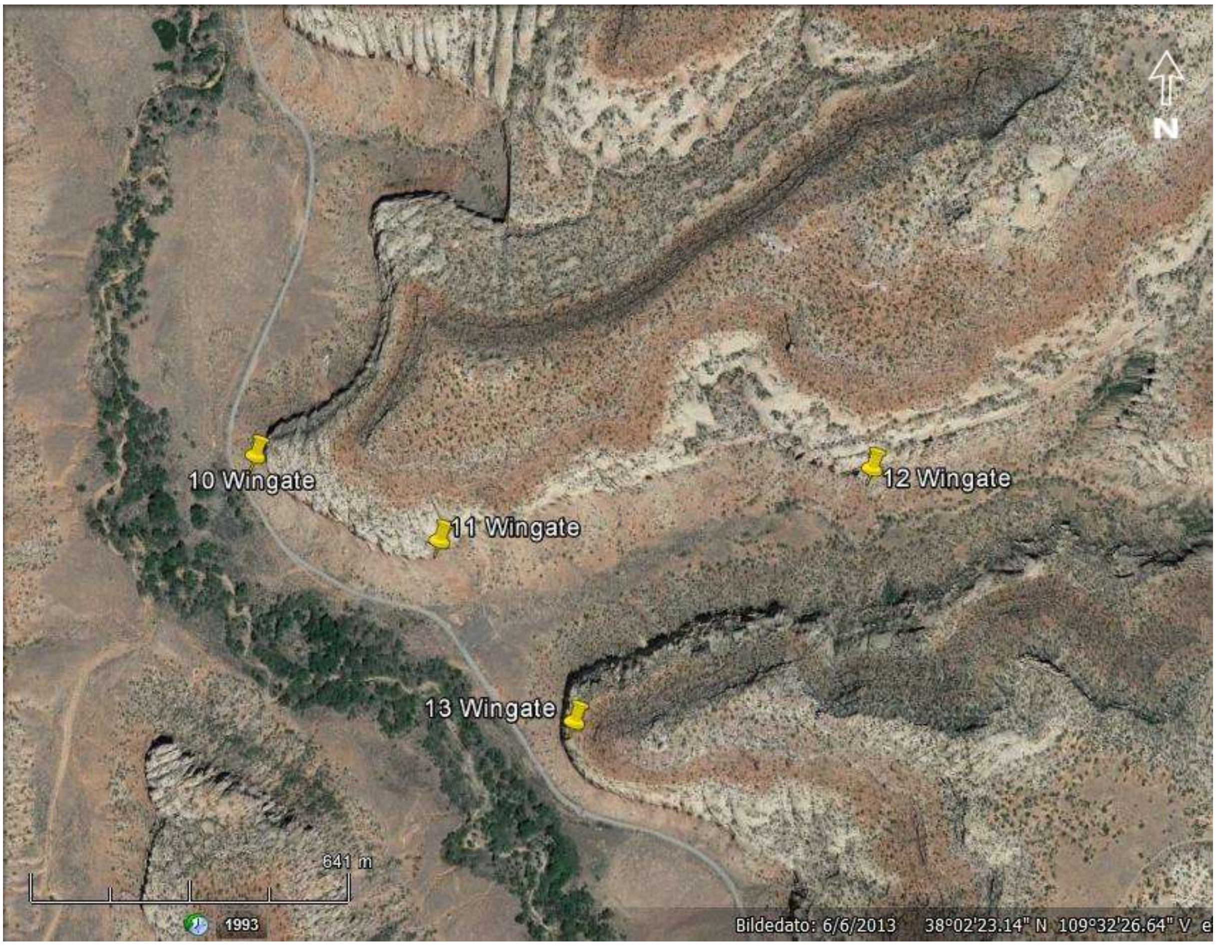

Figure 8.29: Localities of fracture-frequency distribution no. 10-13 of the Wingate Sandstone.

Figure 8.30: Localities of fracture-frequency distribution no. 14-19 of the Slick Rock Member.

Figure 8.31: Localities of fracture-frequency distribution no. 20-26 of the Moab Member.

Appendix F - Joint spacing based on aerial photos

Table 8-38: Fracture-frequency distribution no. 1 of the Wingate Sandstone. Based on aerial photos from Google Earth.

	Length (m)	No. of fractures	Av. frac. spacing (m)	Avg. frac. density (fracs/m)	St. dev. of frac. spacing
Total scanline	358,66	12	29,89	0,03	1,78
Frac. orient. 1: Avg.: 131	358,66	12	29,89	0,03	1,78

Table 8-39: Fracture-frequency distribution no. 2 of the Wingate Sandstone. Based on aerial photos from Google Earth.

	Length (m)	No. of fractures	Av. frac. spacing (m)	Avg. frac. density (fracs/m)	St. dev. of frac. spacing
Total scanline	540,95	18	30,05	0,03	1,69
Frac. orient. 1: Avg.: 139	540,95	18	30,05	0,03	1,69

Table 8-40: Fracture-frequency distribution no. 3 of the Wingate Sandstone. Based on aerial photos from Google Earth.

	Length (m)	No. of fractures	Av. frac. spacing (m)	Avg. frac. density (fracs/m)	St. dev. of frac. spacing
Total scanline	530,6	19	27,93	0,04	1,41
Frac. orient. 1: Avg.: 142	530,6	19	27,93	0,04	1,41

Table 8-41: Fracture-frequency distribution no. 4 of the Wingate Sandstone. Based on aerial photos from Google Earth.

	Length (m)	No. of fractures	Av. frac. spacing (m)	Avg. frac. density (fracs/m)	St. dev. of frac. spacing
Total scanline	453,63	15	30,24	0,03	1,34
Frac. orient. 1: Avg.: 134	453,63	15	30,24	0,03	1,34

Table 8-42: Fracture-frequency distribution no. 5 of the Wingate Sandstone. Based on aerial photos from Google Earth.

	Length (m)	No. of fractures	Av. frac. spacing (m)	Avg. frac. density (fracs/m)	St. dev. of frac. Spacing
Total scanline	410,35	14	29,31	0,03	1,28
Frac. orient. 1: Avg.: 141	410,35	14	29,31	0,03	1,28

Table 8-43: Fracture-frequency distribution no. 6 of the Wingate Sandstone. Based on aerial photos from Google Earth.

	Length (m)	No. of fractures	Av. frac. spacing (m)	Avg. frac. density (fracs/m)	St. dev. of frac. spacing
Total scanline	415,25	15	27,68	0,04	1,70
Frac. orient. 1: Avg.: 127	415,25	15	27,68	0,04	1,70

Table 8-44: Fracture-frequency distribution no. 7 of the Wingate Sandstone. Based on aerial photos from Google Earth.

	Length (m)	No. of fractures	Av. frac. spacing (m)	Avg. frac. density (fracs/m)	St. dev. of frac. spacing
Total scanline	366,38	13	28,18	0,04	1,35
Frac. orient. 1: Avg.: 131	366,38	13	28,18	0,04	1,35

Table 8-45: Fracture-frequency distribution no. 8 of the Wingate Sandstone. Based on aerial photos from Google Earth.

	Length (m)	No. of fractures	Av. frac. spacing (m)	Avg. frac. density (fracs/m)	St. dev. of frac. spacing
Total scanline	298,1	11	27,1	0,04	1,98
Frac. orient. 1: Avg.: 133	298,1	11	27,1	0,04	1,98

Table 8-46: Fracture-frequency distribution no. 9 of the Wingate Sandstone. Based on aerial photos from Google Earth.

	Length (m)	No. of fractures	Av. frac. spacing (m)	Avg. frac. density (fracs/m)	St. dev. of frac. spacing
Total scanline	336,26	11	30,57	0,03	2,07
Frac. orient. 1: Avg.: 141	336,26	11	30,57	0,03	2,07

Table 8-47: Fracture-frequency distribution no. 10 of the Wingate Sandstone. Based on aerial photos from Google Earth.

	Length (m)	No. of fractures	Av. frac. spacing (m)	Avg. frac. density (fracs/m)	St. dev. of frac. spacing
Total scanline	466,86	13	35,91	0,03	2,33
Frac. orient. 1: Avg.: 138	466,86	13	35,91	0,03	2,33

Table 8-48: Fracture-frequency distribution no. 11 of the Navajo Sandstone. Based on aerial photos from Google Earth.

	Length (m)	No. of fractures	Av. frac. spacing (m)	Avg. frac. density (fracs/m)	St. dev. of frac. spacing
Total scanline	699,91	19	36,84	0,03	1,77
Frac. orient. 1: Avg.: 136	699,91	19	36,84	0,03	1,77

Table 8-49: Fracture-frequency distribution no. 12 of the Navajo Sandstone. Based on aerial photos from Google Earth.

	Length (m)	No. of fractures	Av. frac. spacing (m)	Avg. frac. density (fracs/m)	St. dev. of frac. spacing
Total scanline	519,71	16	32,48	0,03	2,52
Frac. orient. 1: Avg.: 110	519,71	16	32,48	0,03	2,52

Table 8-50: Fracture-frequency distribution no. 13 of the Navajo Sandstone. Based on aerial photos from Google Earth.

	Length (m)	No. of fractures	Av. frac. spacing (m)	Avg. frac. density (fracs/m)	St. dev. of frac. spacing
Total scanline	294,97	12	24,58	0,04	2,96
Frac. orient. 1: Avg.: 108	294,97	12	24,58	0,04	2,96

Table 8-51: Fracture-frequency distribution no. 14 of the Navajo Sandstone. Based on aerial photos from Google Earth.

	Length (m)	No. of fractures	Av. frac. spacing (m)	Avg. frac. density (fracs/m)	St. dev. of frac. spacing
Total scanline	488,32	25	19,53	0,05	1,99
Frac. orient. 1: Avg.: 119	488,32	25	19,53	0,05	1,99

Table 8-52: Fracture-frequency distribution no. 15 of the Navajo Sandstone. Based on aerial photos from Google Earth.

	Length (m)	No. of fractures	Av. frac. spacing (m)	Avg. frac. density (fracs/m)	St. dev. of frac. spacing
Total scanline	436,24	14	31,16	0,03	2,43
Frac. orient. 1: Avg.: 133	436,24	14	31,16	0,03	2,43

Table 8-53: Fracture-frequency distribution no. 16 of the Navajo Sandstone. Based on aerial photos from Google Earth.

	Length (m)	No. of fractures	Av. frac. spacing (m)	Avg. frac. density (fracs/m)	St. dev. of frac. spacing
Total scanline	749	17	44,06	0,02	3,55
Frac. orient. 1: Avg.: 098	749	17	44,06	0,02	3,55

Table 8-54: Fracture-frequency distribution no. 17 of the Navajo Sandstone. Based on aerial photos from Google Earth.

	Length (m)	No. of fractures	Av. frac. spacing (m)	Avg. frac. density (fracs/m)	St. dev. of frac. spacing
Total scanline	358,45	10	35,85	0,03	2,11
Frac. orient. 1: Avg.: 100	358,45	10	35,85	0,03	2,11

Table 8-55: Fracture-frequency distribution no. 18 of the Navajo Sandstone. Based on aerial photos from Google Earth.

	Length (m)	No. of fractures	Av. frac. spacing (m)	Avg. frac. density (fracs/m)	St. dev. of frac. spacing
Total scanline	321,15	9	35,68	0,03	1,97
Frac. orient. 1: Avg.: 099	321,15	9	35,68	0,03	1,97

Table 8-56: Fracture-frequency distribution no. 19 of the Navajo Sandstone. Based on aerial photos from Google Earth.

	Length (m)	No. of fractures	Av. frac. spacing (m)	Avg. frac. density (fracs/m)	St. dev. of frac. spacing
Total scanline	277,97	9	30,89	0,03	2,09
Frac. orient. 1: Avg.: 090	277,97	9	30,89	0,03	2,09

Table 8-57: Fracture-frequency distribution no. 20 of the Navajo Sandstone. Based on aerial photos from Google Earth.

	Length (m)	No. of fractures	Av. frac. spacing (m)	Avg. frac. density (fracs/m)	St. dev. of frac. spacing
Total scanline	485,56	8	60,70	0,02	2,18
Frac. orient. 1: Avg.: 091	485,56	8	60,70	0,02	2,18

Table 8-58: Fracture-frequency distribution no. 21 of the Moab Member. Based on aerial photos from Google Earth.

	Length (m)	No. of fractures	Av. frac. spacing (m)	Avg. frac. density (fracs/m)	St. dev. of frac. spacing
Total scanline	291,84	10	29,18	0,03	1,98
Frac. orient. 1: Avg.: 119	291,84	10	29,18	0,03	1,98

Table 8-59: Fracture-frequency distribution no. 22 of the Moab Member. Based on aerial photos from Google Earth.

	Length (m)	No. of fractures	Av. frac. spacing (m)	Avg. frac. density (fracs/m)	St. dev. of frac. spacing
Total scanline	215,7	10	21,57	0,05	1,64
Frac. orient. 1: Avg.: 109	215,7	10	21,57	0,05	1,64

Table 8-60: Fracture-frequency distribution no. 23 of the Moab Member. Based on aerial photos from Google Earth.

	Length (m)	No. of fractures	Av. frac. spacing (m)	Avg. frac. density (fracs/m)	St. dev. of frac. spacing
Total scanline	190,25	10	19,03	0,05	1,33
Frac. orient. 1: Avg.: 117	190,25	10	19,03	0,05	1,33

Table 8-61: Fracture-frequency distribution no. 24 of the Moab Member. Based on aerial photos from Google Earth.

	Length (m)	No. of fractures	Av. frac. spacing (m)	Avg. frac. density (fracs/m)	St. dev. of frac. spacing
Total scanline	119,61	12	9,97	0,10	0,70
Frac. orient. 1: Avg.: 124	119,61	12	9,97	0,10	0,70

Table 8-62: Fracture-frequency distribution no. 25 of the Moab Member. Based on aerial photos from Google Earth.

	Length (m)	No. of fractures	Av. frac. spacing (m)	Avg. frac. density (fracs/m)	St. dev. of frac. spacing
Total scanline	158,04	10	15,80	0,06	0,83
Frac. orient. 1: Avg.: 119	158,04	10	15,80	0,06	0,83

Table 8-63: Fracture-frequency distribution no. 26 of the Moab Member. Based on aerial photos from Google Earth.

	Length (m)	No. of fractures	Av. frac. spacing (m)	Avg. frac. density (fracs/m)	St. dev. of frac. spacing
Total scanline	100,38	7	14,34	0,07	0,48
Frac. orient. 1: Avg.: 121	100,38	7	14,34	0,07	0,48

Table 8-64: Fracture-frequency distribution no. 27 of the Moab Member. Based on aerial photos from Google Earth.

	Length (m)	No. of fractures	Av. frac. spacing (m)	Avg. frac. density (fracs/m)	St. dev. of frac. spacing
Total scanline	174,69	9	19,41	0,05	1,30
Frac. orient. 1: Avg.: 119	174,69	9	19,41	0,05	1,30

Table 8-65: Fracture-frequency distribution no. 28 of the Moab Member. Based on aerial photos from Google Earth.

	Length (m)	No. of fractures	Av. frac. spacing (m)	Avg. frac. density (fracs/m)	St. dev. of frac. spacing
Total scanline	212,53	9	23,61	0,04	1,91
Frac. orient. 1: Avg.: 119	212,53	9	23,61	0,04	1,91

Table 8-66: Fracture-frequency distribution no. 29 of the Moab Member. Based on aerial photos from Google Earth.

	Length (m)	No. of fractures	Av. frac. spacing (m)	Avg. frac. density (fracs/m)	St. dev. of frac. spacing
Total scanline	330,74	11	30,07	0,03	1,89
Frac. orient. 1: Avg.: 097	330,74	11	30,07	0,03	1,89

Table 8-67: Fracture-frequency distribution no. 30 of the Moab Member. Based on aerial photos from Google Earth.

	Length (m)	No. of fractures	Av. frac. spacing (m)	Avg. frac. density (fracs/m)	St. dev. of frac. spacing
Total scanline	250,26	10	25,03	0,04	1,52
Frac. orient. 1: Avg.: 122	250,26	10	25,03	0,04	1,52

Appendix G - Average values of fracture spacing and layer thickness

Table 8-68: Average values of fracture spacing and layer thickness for each of the fracture frequency distributions illustrated in Figure 4.43.

Frac. freq. distr. no.	Unit	Avg. frac. spacing	Avg. layer thickness
1	Cutler	2,53	2,24
2	Cutler	3,39	3,7
3	Cutler	2,49	1,07
4	Cutler	7,8	6,14
5	Chinle	1,61	1,19
6	Chinle	1,86	2,13
7	Chinle	2,58	1,22
8	Chinle	2,39	1,09
9	Chinle	2,41	1,54
10	Wingate	6,7	42,8
11	Wingate	10,44	39,6
12	Wingate	18,5	43
13	Wingate	9,65	57,82
14	Slick Rock	1,57	0,38
15	Slick Rock	2,41	1,63
16	Slick Rock	1,64	0,42
17	Slick Rock	2,04	1,52
18	Slick Rock	1,62	0,43
19	Slick Rock	2,43	1,55
20	Moab	8,41	11,57
21	Moab	12,68	15,06
22	Moab	6	6,97
23	Moab	15,03	9,43
24	Moab	14,6	8,91
25	Moab	13,29	8,45
26	Moab	14,7	10,85